Durham E-Theses

High resolution gamma-ray astronomy in the energy range 0.05 to 10 mev

Owens, Alan

How to cite:

Use policy

HIGH RESOLUTION GAMMA-RAY

ASTRONOMY IN THE ENERGY RANGE

0.05 TO 10 MEV

by

ALAN OWENS B.Sc.

A Thesis

Submitted to the University of Durham

for the Degree of

Doctor of Philosophy

15. APR. 1986

Thesis
1985/OWE

ABSTRACT

An analysis of the detection properties of an actively shielded 86 cm^3 germanium detector is given. Results are presented of observations of the Crab Nebula, its associated pulsar PSR0531+21, the Seyfert galaxy NGC1275, and the COS B source 2CG195+5. Evidence is presented for gamma-ray line emission from the Crab at energies of 404.7 and 1049.8 keV with intensities at the top of the atmosphere of $(7.2 \pm 2.1) \times 10^{-3}$ and $(2.03 \pm 0.46) \times 10^{-2}$ photons cm^{-2} s^{-1} respectively. A line at 78.9 keV has also been detected at the 4.1σ level which shows time variability. The peak flux at the top of the atmosphere was measured to be $(1.1 \pm 0.26) \times 10^{-2}$ photons cm^{-2} s^{-1}.

We report the detection of redshifted annihilation radiation from the type II Seyfert galaxy, NGC 1275. The measured flux at the top of the atmosphere is $(7.1 \pm 2.2) \times 10^{-3}$ photons $cm^{-2} s^{-1}$.

CONTENTS

LIST OF SYMBOLS

The following symbols will be used to denote the physical
quantities expressed in this thesis unless otherwise stated:

Symbol	Parameter	Units
m	Mass	kg
B	Magnetic field strength	gauss
ρ	Density	$gm\ cm^{-3}$
K	Temperature	$^{o}Kelvin$
z	Atomic Number	—
I	Intensity	$cm^{-2}s^{-1}ster^{-1}$
F	Flux	$cm^{-2}s^{-1}$
Ω	Solid Angle	ster
λ	Half Life	s
t	Time	s
υ	Frequency	Hertz
σ	Cross Section	barns
p	Momentum	$kg\ m\ s^{-1}$
v	Velocity	$m\ s^{-1}$
E	Energy	MeV
γ	Lorentz Factor	—
π	Pi	3.142
A	Avogadro's Constant	$6.022 \times 10^{23}mol^{-1}$
c	Velocity of Light	$2.998 \times 10^{8}m\ s^{-1}$
h	Planck's constant	$6.626 \times 10^{-34}J\ s$
ε_{o}	Permittivity of Free Space	$8.854 \times 10^{-12}F/m$
k	Boltzmann Constant	$1.381 \times 10^{-23}J\ K^{-1}$

Symbol	Parameter	Units
α	Fine Structure constant	7.30×10^{-3}
r_o	Classical radius of Electron	5.292×10^{-11} m
e	Charge on an electron	1.602×10^{-19} C
G	Newton's Gravitational Constant	6.67×10^{-11} N m^{2}kg^{-2}
g	Gravitational acceleration	9.807 m s^{-2}

The following suffixes may also be used to explicitly define the parameters listed above:

e	Electron
p	Proton
π	Pion
μ	Muon
γ	Gamma
$\perp$	Perpendicular Component
$\parallel$	Parallel Component
th	Threshold

CHAPTER 1

GAMMA-RAY PRODUCTION MECHANISMS.

1.1 INTRODUCTION.

The electromagnetic spectrum emitted by a celestial body is a useful indication of the physical processes within it. Observations of charged particle radiation can also provide important information but, with the exception of extremely high energy cosmic rays, this information is essentially non-directional.

Uncharged particles which are emitted such as neutrons, neutral mesons and neutrinos could in principle provide directional information. However, the lifetimes of neutrons and mesons are too short to allow significant fluxes to reach earth. Neutrinos on the other hand are stable against decay, but unfortunately their interaction cross section is so low that detection is extremely difficult.

Electromagnetic radiation is undeflected by magnetic fields, has a large range, and can therefore provide directional as well as energetic information. Gamma radiation is particularly powerful because it suffers little attenuation by the interstellar medium (since its mean free path is of the order of the radius of the visible universe) and the full expanse of the cosmic gamma-ray energy spectrum covers roughly sixteen orders of magnitude from 10^5 eV to $\sim 10^{21}$ eV.

Gamma-ray astronomy can contribute to a wide range of cosmological problems. Surveys of the galaxy with instruments measuring photon direction and energy will give indications of

such things as the density of galactic and intergalactic matter, the strength of ambient fields, and the density and distribution of galactic and intergalactic cosmic rays.

Similar observations of the gamma-ray emission of discrete objects will provide information about their origin and nature.

1.2 GAMMA-RAY PRODUCTION MECHANISMS.

Gamma rays are produced by mechanisms involving the interactions of particles and photons. The type of interaction and the flux, is dependent on the density of the particles and photons and the cross-section for the particular mechanism involved. For convenience a method which classifies gamma-ray production mechanisms as particle–field or particle–matter interactions, will be adopted here (cf. Ginzburg, 1969, Lust and Pinkau, 1967). Since this thesis is essentially experimental in nature, only a brief synopsis of the main production methods will be given.

1.3 PARTICLE-FIELD INTERACTIONS.

1.3.1 INVERSE COMPTON SCATTERING.

A relativistic electron which collides with a low energy photon, for example starlight or the 3K microwave background, can give rise to a gamma-ray photon. In the particles rest frame this process can be analyzed in much the same way as forward Compton scattering but the relativistic transforms of the photon both into and out of this frame enhance the photon energy by a factor of γ^2

where,

$$\gamma = E_e / m_o c^2 \qquad (1.1)$$

and E_e is the energy of the electron. Thus the energy of the scattered photon is given by,

$$E_\gamma = \gamma^2 \varepsilon_o \qquad (1.2)$$

where ε_o and E_γ denote the initial and scattered photon energies respectively. In the case when $\gamma \varepsilon_o \gg m_o c^2$ the cross-section for this mechanism is given by the Klein-Nishina formula, set in the electrons rest frame.

In actual fact, until the energy of the electron is extremely high ($\sim 10^{11}$ eV) the process in the electron's rest frame is simple Thompson scattering and the effective cross-section for this process is given by the Thompson formula:

$$\sigma_T = 8 \pi r_0^2 / 3 \qquad (1.3)$$

where r_o is the classical radius of the electron. The average energy of the scattered photon is given by,

$$\langle E_\gamma \rangle = 4\gamma^2 \langle \varepsilon_o \rangle / 3 \qquad (1.4)$$

In the astrophysical case, the electrons are assumed to have a power law energy distribution of the form,

$$I_e(E)dE = kE^{-\alpha}dE \qquad (cm^{-2}s^{-1}sr^{-1}MeV^{-1}) \qquad (1.5)$$

The resulting gamma-ray spectrum for an electron intensity spectrum, $I_e(E)$, isotropically incident on a photon field, has been given by Felten and Morrison (1966);

$$I(E_\gamma)dE_\gamma = 10^9 (56.9)^{3-\alpha} n_o L_{eff} \rho \; T^{(\alpha-3)/2} E_\gamma^{-(\alpha+1)/2} dE_\gamma \qquad (1.6)$$

$$(\text{photons cm}^{-2} \text{ s}^{-1} \text{ sr}^{-1} \text{ MeV}^{-1})$$

where ρ is the photon energy density, L_{eff} is the effective path length for gamma-ray production in light years, and n_o is a constant related to the incident number of electrons. Thus the differential intensity spectrum for the gamma-rays depends only on the effective path length L_{eff} and the electron spectral exponent α.

1.3.2 SYNCHROTRON AND CYCLOTRON RADIATION.

Classically an electron moving in a magnetic field will execute a spiral trajectory and radiate as a dipole. Its mathematical description has been given by Schwinger (1949). The emission is isotropic at the Larmor frequency.

$$\nu_L = \frac{eB}{2\pi m_o c} = 2.8 \text{ MHz per Gauss} \qquad (1.7)$$

where B represents the magnetic field component perpendicular to the particles velocity vector. If the electron is non-relativistic the radiation is isotropic and is emitted only at the Larmor frequency. This is known as cyclotron radiation.

In the relativistic case, synchrotron radiation is emitted in a relativistically narrow cone (angle $\theta \sim 1/\gamma$). The frequency distribution of the emitted radiation is no longer discrete as in the nonrelativistic case but is actually an asymmetric distribution with a maximum of the envelope at,

$$\nu_m = 3/2\gamma^2\nu_L \qquad (1.8)$$

A photon emitted at the peak of this distribution will have an energy E,

$$E_\gamma = 5 \times 10^{-15}\gamma^2 B \qquad (MeV) \qquad (1.9)$$

Therefore extremely energetic electrons or very strong magnetic fields are needed to produce gamma-ray photons in the MeV region.

The total power P_s emitted due to synchrotron radiation, over all frequencies, by a single particle of a mass M and charge z is given by (Ginzburg, 1969),

$$P_s = 9.8 \times 10^{-2} B_\perp^2 \left(\frac{z^2 m_o}{M}\right)^2 \left(\frac{E}{Mc^2}\right)^2 \qquad (eV \ s^{-1}) \qquad (1.10)$$

For an electron z = 1 and M = m_e this expression reduces to:

$$P_s = 10^{-3}B_\perp^2\gamma^2 \qquad (eV \ s^{-1}) \qquad (1.11)$$

Equation 1.10 implies that a proton with the same energy as an electron will emit a total synchrotron power P_s^p which is a factor of 10^{13} lower than the power emitted by the electron. Hence it

may be understood that electrons rather than protons are the primary source of synchrotron radiation.

In application to the astrophysical environment it is again necessary to consider a spectrum of electron energies and, as with the case for Inverse Compton radiation, a power law spectrum is assumed (Equation 1.5). For a uniform but randomly orientated magnetic field B of dimension L and volume V, the gamma ray-flux at distance R is given by (Ginzburg, 1969):

$$\frac{dN_\gamma}{dE_\gamma} = 3.27 \times 10^{-2} \frac{a(\alpha)kVB^{(\alpha+1)/2}}{R^2} \left(\frac{2.59 \times 10^{-2}}{E_\gamma}\right)^{(\alpha+1)/2} \quad (1.12)$$

$$(\text{photons } cm^{-2}s^{-1}MeV^{-1})$$

where a(α) is a function of the order of 0.1 for 1.5 < α < 5.

Synchrotron radiation appears to be most important in the ultra-violet and radio regions. However in the postulated co-rotating magnetosphere of a neutron star sufficiently high magnetic fields should be present for the production of both synchrotron and cyclotron radiation. Indeed synchrotron radiation seems to be responsible for the general x-ray emissions (<30 keV) from the Crab pulsar and recently cyclotron lines have been reported from Hercules Xl.

1.3.3 PHOTOMESON π^0 DECAY.

Neutral π^0 mesons are unstable against decay with a mean lifetime of 10^{-16}s;

$$\pi^O \rightarrow \gamma + \gamma \qquad\qquad (1.13)$$

The available rest energy of the π^O meson is shared between the two gamma-rays which consequently show a fairly broad peaked distribution centered at ~70 MeV in the laboratory frame. In the terrestrial observer's frame of reference the two gamma rays will have unequal energies determined by the relativistic Lorentz transformation. The maximum and minimum photon energies are given by,

$$E_{max} = E_\pi (1 + \beta_\pi)/2$$
$$\qquad\qquad (1.14)$$
$$E_{min} = E_\pi (1 - \beta_\pi)/2$$

where E_π is the total energy of the pion, and β_π = is its velocity in the observers frame divided by the speed of light. The dominant production mechanisms for neutral pions are proton-proton and proton-antiproton interactions which will be described in the next section. However, a process which may be important in producing gamma-rays of energies in the 10^{19} eV range is that of photomeson production. The basic process is;

$$\gamma + p \rightarrow p + \pi^O \qquad\qquad (1.15)$$

The proton threshold in the laboratory system for creating a single π^O meson is given by (Jackson, 1962; Fazio, 1967),

$$E_p^{th} = \frac{m_\pi c^2(m_\pi c^2 + 2m_p c^2)}{2\varepsilon_o(1 + \cos\theta)} \; ; \quad m_\pi c^2 \quad 135 \text{ MeV} \qquad (1.16)$$

where θ is the angle between the initial photon direction and the proton's direction. For thermal radiation the average photon energy is,

$$\varepsilon_0 = 2.7 \times 10^{-4} T(K) \qquad (eV) \qquad (1.17)$$

which for starlight ($\varepsilon_0 \sim 1$ eV) gives a proton threshold of $\sim 10^{18}$ eV and for the 3K background ($\varepsilon_0 \sim 6 \times 10^{-4}$ eV), a threshold of 10^{20} eV. A typical gamma-ray produced by reaction 1.15 carries away about 10% of the primary energy of the cosmic ray (Stecker, 1973). The gamma-rays produced may themselves be attenuated by pair production processes of the type;

$$\gamma_{2.7} + \gamma \rightarrow e^+ + e^- \qquad (1.18)$$

and this process, along with Compton scattering of the electrons and positrons with the 2.7K radiation may lead to a cascade process which has been treated in detail by Wdowczyk et al. (1972), and Stecker (1973).

1.4 PARTICLE-MATTER INTERACTIONS.

1.4.1 COLLISIONAL BREMSSTRAHLUNG.

A charged particle can suffer a large de-acceleration in encounters with the coulomb field of a nucleus. The energy lost is radiated as photons. The cross section for emission of a photon of energy E_γ by relativistic electrons is given by

(Heitler, 1954);

$$\sigma_b(E,E_\gamma) = 4\alpha z^2 \, \sigma_T \ell n \left(\frac{2E}{m_o c^2} - \frac{1}{3} \right) \frac{E}{E_\gamma} \qquad (1.19)$$

where α is the fine structure constant and z is the charge of the nucleus. In the ultra-relativistic case, where the cross-section is calculated by taking into account the screening of the charge of the atomic nucleus by atomic electrons, the resultant cross-section is given by;

$$\sigma_b(E,E_\gamma) = 4\alpha z^2 \, \sigma_T \ell n \left(183 z^{-0.3} + \frac{1}{18} \right) \frac{E}{E_\gamma} \qquad (1.20)$$

Note that the cross-section given by Equations 1.20 has only a linear dependence on E. Indeed Equation 1.20 can be written in the form (Stecker, 1971);

$$\sigma_b(E,E_\gamma) = \frac{\langle m \rangle}{\langle x_o \rangle} \frac{E}{E_\gamma} \qquad (cm^2) \qquad (1.21)$$

where $\langle m \rangle$ is the average mass of the target atoms and $\langle x_o \rangle$ the average radiation length. For an incident power law electron spectrum, Fazio (1967) has shown that the resulting differential gamma-ray spectrum is given by;

$$I(E_\gamma)dE_\gamma = \frac{\langle m \rangle \, N(L)}{\langle x_o \rangle} \frac{dE_\gamma}{E_\gamma} \int_{E_\gamma}^{\infty} I_e(E)dE \qquad (1.22)$$

where $I_e(E)dE$ is the incident electron spectrum given by Equation 1.5 i.e,

$$I_e(E)dE = kE^{-\alpha}dE$$

therefore;

$$I(E_\gamma)dE_\gamma = \frac{\langle m \rangle \ N(L)}{\langle x_0 \rangle} \left(\frac{k}{\alpha - 1} \right) E_\gamma^{-\alpha}dE_\gamma \qquad (1.23)$$

where $N(L)$ is the integrated number of target nuclei in the line of sight. The spectral shape given in Equation 1.23 refers to the case of relativistic electrons, although Ramaty et al. (1975) have pointed out that this spectrum should be $\sim E^{-\alpha + 0.1}$ which is slightly flatter. Refinements must also be made for the case of non-relativistic electrons (Brown, 1971). Scattering in the rest frame of the particle is almost isotropic and the inverse transform yields $\gamma \tan \theta \sim 1$. Thus for $\gamma \gg 1$, the angular distribution of the radiation in relation to the particle is peaked around,

$$\theta = mc^2/E \qquad (1.24)$$

independent of the photon energy.

Bremsstrahlung by fast protons has been considered by many authors (Hayakawa, 1970; Brown, 1970) as a possible source of cosmic gamma-rays. Jones (1971) has extended these calculations and concluded that the resulting gamma-ray spectrum above 5 MeV would have a power law spectrum that is approximately one power steeper than that of the incident proton spectrum. Consequently

proton bremsstrahlung would not seem to make a significant contribution to the galactic cosmic gamma-ray spectrum.

1.4.2 PION DECAY.

Whenever proton energies are high enough meson production can occur. At the lower gamma-ray energies (say ~30 MeV) the proton-proton interaction is the most dominant. The threshold kinetic energy a cosmic ray proton must have to produce a secondary particle of mass M in such an interaction is;

$$T_{th} = M(2 + M/2m_p) \qquad (1.25)$$

Thus to produce a single π^o meson of rest mass 135 MeV requires a threshold kinetic energy of 280 MeV. The relative cross-section for this mechanism is a factor of 10^2 greater than the proton-thermal photon interaction described in the penultimate section. Proton-antiproton interactions can also produce π^o mesons but this does not appear to be significant, at least on the galactic scale. At incident energies greater than 172 MeV the proton-alpha particle interaction becomes a possible contributor, the cross-section being twice that of the proton-proton interaction. At much higher energies, tens of GeV, π^o mesons are produced in proton-proton interactions via K-meson and hyperon decays. These numerous modes of production have been treated quite generally by Stecker (1971).

By using production cross sections and multiplicities obtained from accelerator data, Stecker (1971) has derived the production rate, $q(E_\gamma, \underline{r})$, from a unit volume at distance $\underline{r}$ from

the earth:

$$q(E_\gamma, \underline{r}) = 4\ n(\underline{r}) \int dE_p I(E_p, \underline{r}) \int_{E_{\pi,min}}^{E_{\pi,max}} dE_\pi \sigma(E_\pi, E_p) 2f(E_\gamma, E_\pi) \qquad (1.26)$$

$$cm^{-3} s^{-1}$$

where $n(\underline{r})$ is the hydrogen number density (cm^{-3}) at $\underline{r}$, $I(E_p, \underline{r})$ is the mean directional intensity of cosmic rays ($cm^{-1} s^{-2} sr^{-1}$) of energy E_p in the source volume, $\sigma(E_\pi, E_p)$ is the cross section for the production of a π^o meson with energy E, and $f(E_\gamma, E_\pi)$ is the normalized gamma-ray distribution function from a single π^o decay (Stecker, 1971; p.19),

$$f(E_\gamma, E_\pi) = (E_\pi^2 - m_\pi^2)^{-\frac{1}{2}} \qquad (1.27)$$

The energies $E_{\pi,min}$ and $E_{\pi,max}$ are $E_\gamma + m_\pi^2/4E_\gamma$ and ∞ respectively. The predicted cosmic-ray π^o gamma-ray spectrum at the earth, is shown in Figure 1.1 (taken from Stecker, 1970).

For convenience a summary of formulae for the various possible differential gamma-ray spectral shapes is shown in Table 1.1 (from Chupp, 1976). Only the dependencies of the spectra on photon energy are indicated.

1.5 GAMMA-RAY LINE PRODUCTION MECHANISMS.

Gamma-ray lines are the most direct probe of cosmic nuclear processes. Whilst it has been recognized for two decades that nuclear gamma-ray spectroscopy could provide basic information on such problems as solar activity, supernova dynamics and nucleo-synthesis, only recently have positive identifications of
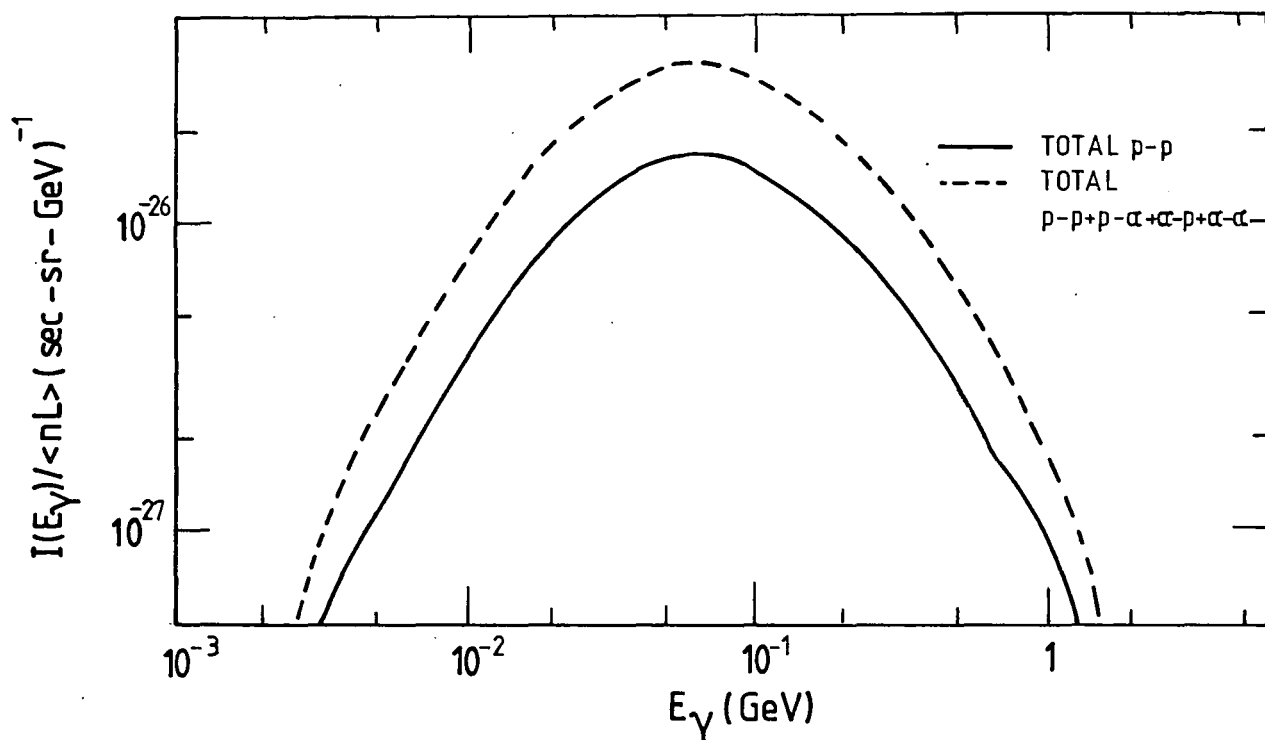
Figure 1.1 The predicted π^0 gamma-ray spectrum at the earth (from Stecker, 1970)

TABLE 1.1 Summary of differential photon spectral shapes from various mechanisms. Taken from Chupp (1976), and references therein. For electrons $k_e E^{-\alpha}$, > 1, and for protons $k_p E^{-m}$, $m > 1$.

Mechanism	Spectral Shape		References
Nonthermal electron bremsstrahlung	$I_b(E_\gamma) \propto E_\gamma^{-\alpha}$	$v_e \sim c$	Fazio (1967)
Nonthermal proton bremsstrahlung	$I_b(E_\gamma) \propto E_\gamma^{-(m+1)}$	$v_p \sim c$	Stecker (1974)
Nonthermal electron bremsstrahlung;			
(nonrelativistic electron < 200 keV)	$I(E_\gamma) \propto E_\gamma^{-(\alpha+1)/2}$	for thin target	Brown (1971)
	$I(E_\gamma) \propto E_\gamma^{-(\alpha-1)}$	for thick target	Brown (1971)
Inverse Compton (electrons)	$I_c(E_\gamma) \propto E_\gamma^{-(\alpha+1)/2}$		Ginzburg and Syrovatskii (1964)
			Felton and Morrison (1966)
Synchrotron radiation (electrons)	$I_s(E_\gamma) \propto B^{(\alpha+1)/2} E_\gamma^{-(\alpha+1)/2}$		Fazio (1967);
			Ginzburg and Syrovatskii (1964)
			Felton and Morrison (1966)
Thermal bremsstrahlung			
Optically thin	$P_{ff}(E_\gamma) \propto 1/E_\gamma \exp(-E_\gamma/kT)$		Hayakawa (1969)
Optically thick	$I(E_\gamma) \propto E_\gamma^2 [\exp(E_\gamma/kT)-1]^{-1}$		Hayakawa (1969)

celestial gamma-ray lines been made.

The principal mechanisms for gamma-ray line production (decay of radioactive products from processes of nucleosynthesis, excitation of nuclei by energetic particle reactions, positron annihilation, neutron capture and cyclotron line emission) are expected to occur at many astrophysical sites.

1.5.1 NUCLEAR GAMMA-RAYS FROM SUPERNOVAE.

Galactic supernovae are potentially the strongest discrete sources through the nucleosynthesis of relatively long lived radionuclei that decay either into excited states of daughter nuclei by gamma-ray emission; or by emitting positrons which subsequently interact with electrons in the interstellar medium to produce the characteristic 511 keV positron annihilation line. Similarly energetic particles in the interstellar medium or close to supernova remnants may suffer inelastic collisions which produce excited nuclei.

Extensive calculations have been carried out on the various emission mechanisms by Ramaty, Kozlovsky and Lingenfelter (1978). Table 1.2 shows (after Ramaty, 1978) the principle radionuclei and some of the important isotopic decay chains that may produce detectable line fluxes occurring in supernovae and novae explosions. The supernovae yields given in Table 1.2, relative to the ^{56}Ni yield, are based on solar system abundances (Cameron, 1973), and the assumption that all the ^{56}Fe, ^{57}Fe and ^{44}Ca in the galaxy, and 2%, 1% and 0.1% of the galactic ^{22}Ne, ^{60}Ni and ^{26}Mg respectively are produced via the decay chains shown in this Table. The lifetimes of the chains are important, for if the

TABLE 1.2

Gamma Ray Producing Decay Chains from Supernovae and Novae.

(from Ramaty, 1978)

Decay Chain	Mean Life (yr)	Nuclei/ Supernova	Photon Energy (MeV)	Photons or positrons per disintegration
$^{56}Ni-^{56}Co-^{56}Fe$	0.31	3×10^{54}	0.847	1
			1.238	0.70
			2.598	0.17
			1.771	0.16
			1.038	0.13
			e^+	0.2
$^{57}Co-^{57}Fe$	1.1	7×10^{52}	0.122	0.88
			0.014	0.88
			0.136	0.12
$^{22}Na-^{22}Ne$	3.8	3×10^{52} (10^{48}/nova)	1.275	1
			e^+	0.9
$^{44}Ti-^{44}Sc-^{44}Ca$	68	6×10^{51}	1.156	1
			0.078	1
			0.068	1
			e^+	0.9
$^{60}Fe-^{60}Co-^{60}Ni$	4.3×10^5	5×10^{50}	1.332	1
			1.173	1
			0.059	1
$^{26}Al-^{26}Mg$	1.1×10^6	4×10^{50}	1.809	1
			1.130	0.04
			e^+	0.85

times are too short then the gamma-rays will be emitted in regions of dense matter and hence may be absorbed. However, even though nucleosynthesis takes place in dense regions which are opaque to gamma-rays, the expanding envelope can become transparent if there is sufficient delay between the synthesis of the isotopes and the emission of the photons. For the de-excitation lines, the delay is due only to the lifetime of the parent isotope, but for the 0.511 MeV line, the delay can be longer because of the finite duration of the positron slowing down and annihilation. Thus although the lifetime of ^{56}Co may not be long enough for the supernova to become transparent to its own de-excitation lines, a significant fraction of the positrons from ^{56}Co may escape from the supernova and annihilate in regions which are transparent to the gamma-rays. It has been estimated (Colgate, 1970) that $\sim 10\%$ of the positrons from the decay of ^{56}Co could escape the supernova. This fraction would make ^{56}Co the dominant positron source from processes of nucleosynthesis. Positrons resulting from the decay of ^{22}Na produced in nova explosions should also annihilate in the interstellar medium, on time scales longer than the interval between nova explosions.

As there are other potential positron sources, a test of the explosive nucleosynthesis origin would be the detection of the associated de-excitation gamma-ray lines. A good prospect is ^{60}Fe which has a long half-life of 9×10^5 years, and the subsequent decay of its ^{60}Co daughter is accompanied by a two gamma-ray cascade with energies E_γ = 1.17 MeV and 1.33 MeV. The flux of gamma-rays having an energy of E_i at the earth is given by,

$$F_i = \frac{g_i \lambda N_o e^{-\lambda t}}{4\pi R^2} \qquad (\text{cm}^{-2}\text{s}^{-1}) \qquad (1.28)$$

where N_o is the initial number of nuclei having a mean lifetime $1/\lambda$, g_i is the number of gamma-rays having energy E_i emitted per decay, and R is the distance of the explosive galactive remnant in kpc. Clayton (1971) has estimated the average explosive yield of ^{60}Fe to be 1×10^{-5} of a solar mass. Using this figure then the expected flux of the 1.17 and 1.33 MeV lines is,

$$F_{60} = \frac{1.3 \times 10^{-7}\exp(-t/(4.3 \times 10^5 \text{ yr}))}{R^2(\text{kpc})} \qquad (\text{cm}^{-2}\text{s}^{-1}) \quad (1.29)$$

To be detectable from balloons a line flux should exceed $\sim 2 \times 10^{-3}$ cm^{-2}s^{-1} and to be detectable from satellites it should exceed 4×10^{-5} cm^{-2}s^{-1}. For comparison the 1.156 MeV line flux from the de-excitation of ^{44}Sc is expected to be,

$$F_{44} = \frac{2.1 \times 10^{-2}\exp(-t/68 \text{ yr})}{R^2(\text{kpc})} \qquad (\text{cm}^{-2}\text{s}^{-1}) \qquad (1.30)$$

which is five orders of magnitude greater than ^{60}Fe immediately after the explosion, but decays more rapidly. After 800 years the ^{60}Fe flux would exceed the ^{44}Sc flux.

Ramaty and Lingenfelter (1977) suggested that the decay of ^{26}Al could be another intense source of gamma-ray lines resulting from processes of nucleosynthesis. ^{26}Al decays with a half life of 7.4×10^5 years by positron emission or electron capture into excited states of ^{26}Mg with ensuing line emission at 1.809 MeV

(100%) and 1.130 MeV (4%). They estimate the flux at the earth, from a supernova explosion at the galactic centre to be $\sim 10^{-4}$ photons $cm^{-2}s^{-1}$. While the short lived isotopes listed in Table 1.2 lead to essentially point sources of gamma-ray lines, the much longer lived ^{26}Al and ^{60}Fe are likely to produce diffuse emission from the interstellar medium. With a supernova rate of one every 30 years and a galactic volume of 4×10^{66} cm^3, Ramaty and Lingenfelter estimate that the total emissivity of lines from ^{26}Al and ^{60}Fe would be comparable to the local emissivity of photons of energies >100 MeV in the galaxy.

The widths of gamma-ray lines from nucleosynthesis are determined by Doppler broadening due to the velocity of the expanding medium. An ejected velocity of 10^4 km/sec would result in line widths of about 6%. The isotopes ^{60}Fe and ^{26}Al essentially come to rest before they decay because of their long mean lives and the resulting line widths are $\sim 0.2\%$, mainly due to galactic rotation.

All the de-excitation lines given in Table 1.2 should be detectable above the diffuse background for some time after the explosion. Figure 1.2 shows the predicted variation in intensity of the various decay lines at the earth as a function of time after a supernova explosion near the galactic centre (from Clayton et al. 1969). Also shown is the diffuse background at 0.1 and 1 MeV for a detector with an angular acceptance of 0.1 steradian.

It is clear that the chance of observing these events depends upon the frequency with which supernovae may be expected to occur within a given distance and upon the likelihood that they will be detected early enough. Zwicky (1964) has estimated the supernova frequency to be 0.03 per year per mean galaxy (10^{11}
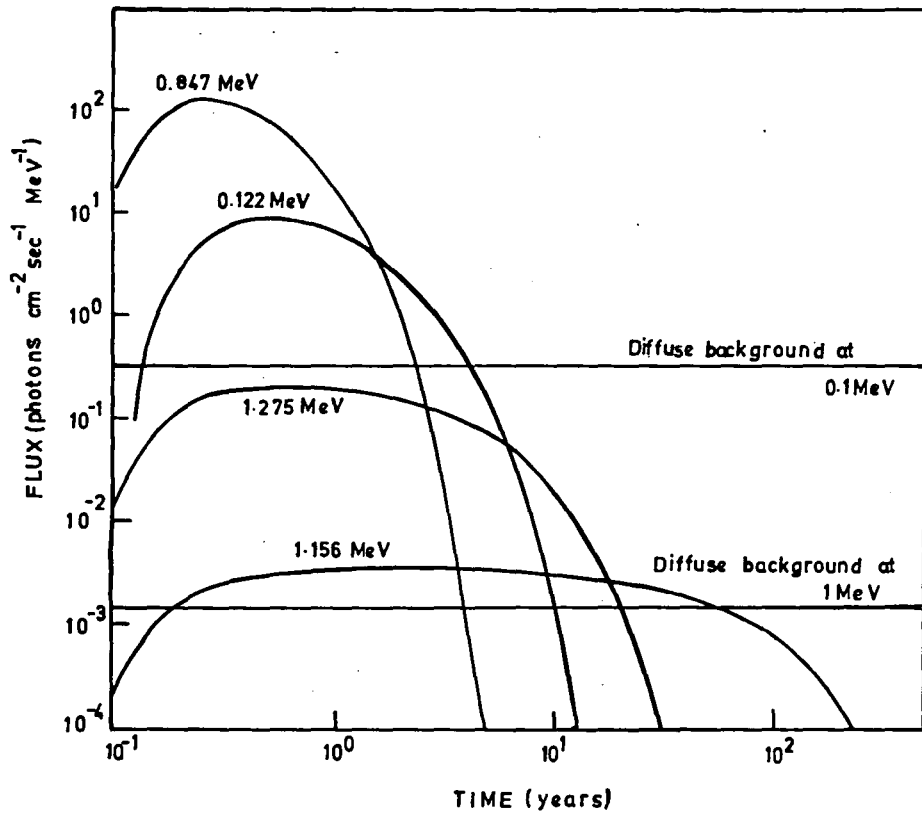
Figure 1.2 Intensities of γ-ray lines from the decay
of radionuclei in the nebula of young
supernova 10kps away as a function of
the time after the explosion.
(from Clayton et al., 1969)

stars), or about 1 every 30 years. Table 1.3 summarizes the expectations regarding the observational possibilities. For the relevant decay chains, the approximate number of supernovae per year detectable at the flux thresholds of both balloon and satellite detectors are listed. The second column shows the period of time during which the supernova should be detectable at the distances indicated. It can be seen that with a balloon borne detector one would only expect to observe a supernova once every 10 years, while with a satellite detector the detection rate is approximately 3 a year.

1.5.2 NUCLEAR GAMMA-RAYS FROM NOVAE.

The most successful theoretical models for common nova events involve thermonuclear runaways proceeding in accreted hydrogen envelopes from a cool companion onto the white dwarf component of a nova binary system. Continued accretion of hydrogen rich matter must inevitably give rise to nuclear burning and consequently to detectable fluxes of gamma-rays. Hydrodynamic calculations of thermonuclear runaways leading to nova eruptions have been reviewed by Starrfield et al. (1976). All studies to date are concerned with hydrogen thermonuclear runaways; the dominant hydrogen burning reactions being those involving carbon, nitrogen and oxygen (CNO) nuclei. The thermonuclear processing of nova ejecta is expected to give rise to production of relatively long lived ^{22}Na nuclei. This represents perhaps the most promising avenue for the detection of gamma-rays from novae. The expected flux of the resulting 1.275 MeV gamma-rays is,

TABLE 1.3 Detectability Summary.

Gamma-ray lines Energies in MeV	Time after Outburst	Balloon-borne Detector Sensitivity 2×10^{-3} γ $cm^{-2}s^{-1}$		Satellite-borne Detector Sensitivity 4×10^{-5} γ $cm^{-2}s^{-1}$	
		Supernova distance (Mpc)	Approximate no. detectable per year	Supernova distance (Mpc)	Approximate no. detectable per year
^{56}Ni(0.812, 0.748)	10-20 days	1.3	0.1	9.0	2 - 5
^{56}Co(0.84,1.24)	15-40 days	1.0	0.1	7.0	2
^{56}Co(weaker lines);					
^{48}V(0.983,1.31)	15-30 days	0.1	0.03	0.7	0.1
^{44}Sc(1.156)	15 days-50 years	0.003	0.003	0.02	Continuous

$$F_{22} = \frac{1.1 \times 10^{-3} \exp(-t/3.75)}{R^2 (\text{kpc})} \quad (\text{cm}^{-2}\text{s}^{-1}) \quad (1.31)$$

if we take $R = 1.1$ kpc for the specific case of Nova Cygni 1975, the predicted flux is 10^{-5} photons $\text{cm}^{-2}\text{s}^{-1}$. The limit of 8 x 10^{-4} photons $\text{cm}^{-2}\text{s}^{-1}$ set by the observations of Leventhal et al. (1977) 9 months after the explosion is larger by an order of magnitude than the expected flux and therefore is consistent, at least in a negative sense.

An additional source of gamma-ray lines from novae is provided by the decay of ^{7}Be. Starrfield et al. (1978) estimate the concentration of ^{7}Li in nova ejecta might be enhanced by a factor of 1000 following the decay of ^{7}Be formed in thermonuclear burning sequences. Novae thus represent a potential source of ^{7}Li in galactic matter. However Starrfield et al. estimate the resulting gamma-ray flux for a nova at one kpc to be significantly less than 10^{-5} photons $\text{cm}^{-2}\text{s}^{-1}$.

The estimated nova rate is 40 per year (Allen, 1976), so a few close nova should occur during a two year gamma-ray satellite mission. With a detector sensitivity of 2 x 10^{-5} photons $\text{cm}^{-2}\text{s}^{-1}$, for a line width of 10 keV FWHM at 1 MeV, an individual nova could be detected from a distance of ~ 2 kpc. But because the time between nova explosions is much shorter than the ^{22}Na mean life (Table 1.2) a detector with a broad field of view observing the galactic plane in the direction of the galactic centre would probably observe diffuse radiation at 1.275 MeV.

1.5.3 NUCLEAR GAMMA-RAYS FROM THE INTERSTELLAR MEDIUM.

Nuclear gamma-ray lines can originate from the interstellar medium in two ways:

1. From the decay of long-lived radionuclei ejected into the interstellar medium after nucleosynthesis processes in supernovae novae, which has been discussed in the previous two sections. The bulk of these nuclei ($^{60}Fe, ^{26}Al, ^{22}Na$) should be fairly well mixed in the interstellar medium before their decay. They should produce a diffuse source of very narrow line emission (less than about 3 keV wide at half maximum) concentrated along the galactic plane. Since these nuclei essentially come to rest before decay, the widths of the lines are primarily due to the galactic rotation which Doppler shifts them by about 2 keV. Assuming that about 0.1% of the present galactic ^{26}Mg results from ^{26}Al decay, and about 1% of ^{60}Ni results from ^{60}Fe, and that the rate of nucleosynthesis has decreased by a factor of ten over the age of the galaxy, Ramaty (1978) has calculated the decay line intensities of ^{60}Fe and ^{26}Al. He finds that they are about the same and equal to 7×10^{-5} photons $cm^{-2} s^{-1} rad^{-1}$ (see Table 1.4). For the 1.275 MeV ^{22}Na line from unresolved novae, he assumes a nova rate larger by a factor of 10^3 than the supernovae rate and a yield of 10^{48} ^{22}Na nuclei per nova. This yields a 1.275 MeV line emissivity larger by a factor of 2.5 than the ^{60}Fe or ^{26}Al line emissivities. Recently the HEAO C-1 satellite gamma-ray experiment has searched the galactic plane for the diffuse emission resulting from the decay of nucleonsynthetic ^{60}Fe, ^{26}Al and ^{22}Na (Mahoney et al., 1982). The measured 3σ upper limit line intensities for ^{60}Fe and ^{22}Na are listed in Table 1.4 and are

TABLE 1.4 Approximate local emissivities and diffuse Galactic fluxes from the direction
of the Galactic Centre. Adapted from Ramaty (1978). All Upper limits are at
the 3σ level.

Mechanism	Photon Energy MeV	FWHM keV	Local Emissivity (Photons/H atom sec)	Predicted Flux γ cm^{-2}s^{-1}rad^{-1}	Measured Flux γ cm^{-2}s^{-1}rad^{-1}	Reference
Inelastic	4.44	100	3×10^{-26}	6×10^{-5}	$(5.4 \pm 1.5) \times 10^{-3}$	(1)
Collisions	6.13 (grain)	8	5×10^{-27}	1×10^{-5}		
(w=1ev/cm^3)	6.13 (gas)	150	1×10^{-26}	2×10^{-5}		
	0.85 (total)	2	6×10^{-27}	1×10^{-5}		
e$^+$ annihilation	0.511	5	2×10^{-25}	1×10^{-4}	$< 3.3 \times 10^{-4}$	(1)
^{26}Al-^{26}Mg	1.809	3	1×10^{-25}	7×10^{-5}	$(4.8 \pm 1.0) \times 10^{-4}$	(2)
^{60}Fe-^{60}Co-^{60}Ni	1.332	2	1×10^{-25}	7×10^{-5} }	$< 1.8 \times 10^{-4}$	(3)
	1.117	2	1×10^{-25}	7×10^{-5} }		
	0.059	0.1	1×10^{-25}	7×10^{-5}		
^{22}Na-^{22}Ne	1.275	10	2×10^{-25}	1×10^{-4}	$< 4.4 \times 10^{-4}$	(3)
π^o decay +	> 100	-	2×10^{-25}	1×10^{-4}	$(1.1 \pm 0.1) \times 10^{-4}$	(4)
bremsstrahlung					$(0.7 \pm 0.1) \times 10^{-4}$	(5)

(1) Haymes et al. (1975), (2) Mahoney et al. (1984), (3) Mahoney et al. (1982), (4) SAS 2, Stephens (1979),
(5) COS B, Stephens (1979).

found to be consistent with the calculations of Ramaty (1978). If the measured intensity of the 1.809 MeV ^{26}Al line does indeed represent a finite flux, then it is a factor of 10 greater than that predicted. However it should be noted that the average galactic fraction of ^{26}Mg resulting from the decay of ^{26}Al used in the calculations is about a factor of 100 below the largest estimate (Woosley and Weaver, 1980) and about a factor of 20 below the more probable value (Arnould et al., 1980; Wallace and Woosley, 1981).

2. Nuclear reactions between energetic charged particles and the ambient interstellar gas and dust grains can lead to gamma-ray line emission following the excitation of nuclear levels both in the accelerated particle and the ambient medium. Table 1.5 lists the most intense de-excitation lines for nuclear interactions in materials with compositions roughly similar to the sun and kinetic energies ranging from a few to a few hundred MeV/nucleon.

Ramaty and Lingenfelter (1979) have calculated the gamma-ray spectrum from the direction of the galactic centre assuming a low energy cosmic ray density of 1 eV/cm^3 and exponential size distribution with a characteristic radius of 5 x 10^{-5} cm for the dust grain size. The results are shown in Figure 1.3 and the predicted line intensities listed in Table 1.4. As can be seen, quite a number of lines are resolvable above the background and at least one line, that at 6.129 MeV (^{16}O) should be resolvable over the background even if the cosmic ray energy density were as low as 0.1 eV/cm^3. The detection of these lines could give a wealth of information on the interstellar medium and the first measure of the energy density of low energy cosmic rays.

TABLE 1.5

Principle deexcitation gamma-ray lines.
From Lingenfelter and Ramaty (1978).

Photon Energy (MeV	Emitting state	Principle production Processes	Mean life (sec)
0.431	$^7\text{Be}^*(0.431)$	$^4\text{He}(\alpha,n)^7\text{Be}^*$	2.7×10^{-13}
0.478	$^7\text{Li}^*(0.478)$	$^4\text{He}(\alpha,p)^7\text{Li}^*$	10^{-16}
0.847	$^{56}\text{Fe}^*(0.847)$	$^{56}\text{Fe}(p,p')^{56}\text{Fe}^*$	9.7×10^{-12}
		$^{56}\text{Fe}(p,n)^{56}\text{Co}(e^+,e)^{56}\text{Fe}^*(100\%)$	9.6×10^{6}
1.238	$^{56}\text{Fe}^*(2.085)$	$^{56}\text{Fe}(p,n')^{56}\text{Fe}^*$	1.0×10^{-12}
	$\to \, ^{56}\text{Fe}^*(0.847)$	$^{56}\text{Fe}(p,n)^{56}\text{Co}(e^+,e)^{56}\text{Fe}^*(67\%)$	9.6×10^{6}
1.369	$^{24}\text{Mg}^*(1.369)$	$^{24}\text{Mg}(p,p')^{24}\text{Mg}^*$	1.8×10^{-12}
1.634	$^{20}\text{Ne}^*(1.634)$	$^{20}\text{Ne}(p,p')^{20}\text{Ne}^*$	1.2×10^{-12}
1.779	$^{28}\text{Si}^*(1.779)$	$^{28}\text{Si}(p,p')^{28}\text{Si}^*$	6.8×10^{-13}
2.313	$^{14}\text{N}^*(2.313)$	$^{14}\text{N}(p,p')^{14}\text{N}^*$	8.5×10^{-14}
		$^{14}\text{N}(p,n)^{14}\text{O}(e^+)^{14}\text{N}^*(100\%)$	102
4.438	$^{12}\text{C}^*(4.438)$	$^{12}\text{C}(p,p')^{12}\text{C}^*$	5.6×10^{-14}
		$^{16}\text{O}(p,x)^{12}\text{C}^*$	5.6×10^{-14}
5.105	$^{14}\text{N}^*(5.105)$	$^{14}\text{N}(p,p')^{14}\text{N}^*$	1.2×10^{-11}
6.129	$^{16}\text{O}^*(6.129)$	$^{16}\text{O}(p,p')^{16}\text{O}^*$	2.4×10^{-11}
6.878	$^{28}\text{Si}^*(6.878)$	$^{28}\text{Si}(p,p')^{28}\text{Si}^*$	2.5×10^{-12}

The de excitation is to the ground state unless otherwise noted.
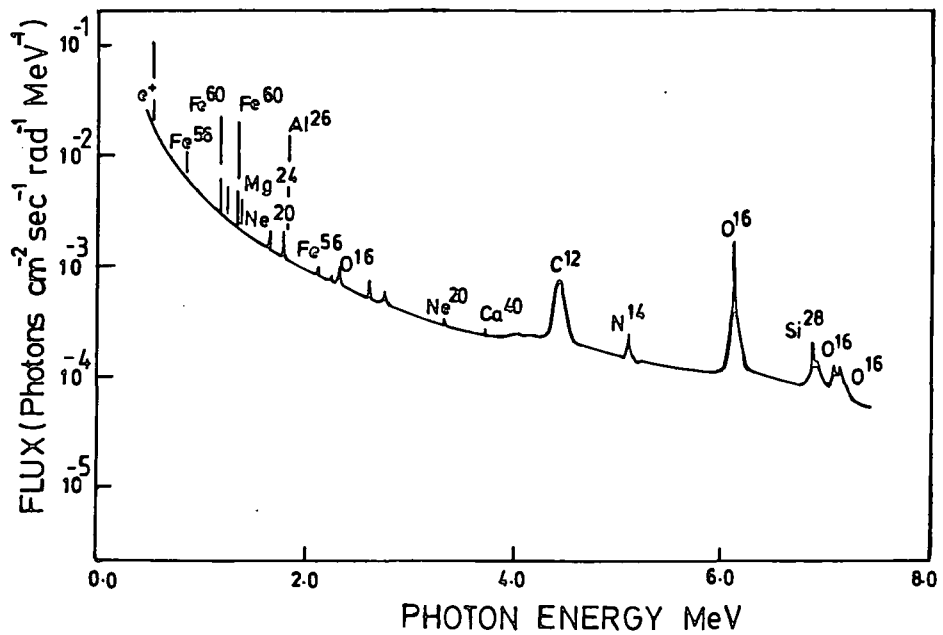
Figure 1.3 Predicted gamma ray spectrum from galactic centre, assuming a low energy cosmic ray density of $1eV cm^{-3}$ and an exponential size distribution with a characteristic radius of 5×10^{-5} cm for dust grains. (from Ramaty and Lingenfelter, 1979)

1.5.4 NUCLEAR GAMMA-RAYS FROM NEUTRON STARS AND BLACK HOLES.

Accretion of matter onto neutron stars and black holes has frequently been suggested as a mechanism for continuum x-ray and gamma-ray emission, both steady state and transient. Because of the small size of a neutron star ($\simeq 10$ km) the gravitational potential energy of a particle of matter of nucleon mass can be quite large. Neglecting magnetic field effects, the gravitational energy of free fall of an ion at the surface of the star is given by,

$$E_i \simeq 1350 \left(\frac{M}{M_\Theta} \right) / R(km) \quad \text{(MeV per nucleon)} \quad (1.32)$$

where M and R are the neutron star's mass and radius respectively. Gamma-ray lines are consequently produced by inelastic collisions induced by the accreted particles which can reach the surface with energies in the range 10 to 100 MeV/nucleon. For a line to be resolvable above the continuum with practical observing times, the nuclear line emissivity must be at least of the order of the continuum emissivity. Consequently for line emission at, say 1 MeV to be stronger than the associated radiative electron bremsstrahlung background, the effective electron and ion energies must be such that,

$$\langle E_e \rangle \ < \ 1 \text{ MeV} \ < \ \langle E_i \rangle \qquad (1.33)$$

or equivalently as a two-temperature quasi-thermal distribution,

$$\langle T_e \rangle \quad < \quad 10^{10} \quad < \quad \langle T_i \rangle \tag{1.34}$$

This will occur if thermalization of the infalling matter is incomplete since the gravitational energy released in the accreting matter is originally almost entirely in the nuclei,

$$\langle E_i \rangle \simeq \frac{m_i}{m_e} \langle E_e \rangle \tag{1.35}$$

If the mean energies or temperatures of the electrons and ions were equal, then the bremsstrahlung emissivity greatly exceeds the nuclear line emissivity for nearly all lines and all compositions. However dynamical models of accretion processes suggest that the effective ion temperatures may be an order of magnitude or more greater than the electron temperatures.

Assuming that continuum bremsstrahlung emission is the principal radiative loss process for the electrons, Ramaty et al. (1978) have shown that in order to observe gamma-ray line emission above the bremsstrahlung continuum from a black hole,

$$\frac{T_e}{T_i - T_e} \quad < \quad 10^{10} \tag{1.36}$$

The principal nuclear gamma-ray lines expected from energetic particle interactions in general have been reviewed by Ramaty and Lingenfelter (1978), and have been discussed in the previous sections. These include the 6.13, 4.44, 2.31, 1.78, 1.63 and 1.37 MeV lines from de-excitation of excited ^{16}O, ^{12}C, ^{14}N, ^{28}Si, ^{20}Ne and ^{24}Mg respectively, the 0.511 MeV line from

annihilation of positrons from the decay of radioisotopes and the 2.223 MeV line from capture on hydrogen of neutrons, all produced in inelastic collisions. They should be thermally broadened to a few hundred keV and gravitationally reshifted by as much as an MeV. The expected gamma-ray flux is difficult to estimate due to the uncertainties in the chemical composition of the accreting star. Brecher (1978), has examined the problem of gamma-ray emission from a gas with normal cosmic abundance accreting spherically symmetrically onto a rigid neutron star surface. The gamma-ray line fluxes obtained as functions of accreted proton energy or equivalently, surface redshift z are given in Figure 1.4. The results are given relative to the continuum x-ray flux, and essentially represent upper limits to the expected yields. For a specific x-ray source such as SCO X1 the expected fluxes at the earth for the positron annihilation line at 0.511 MeV and the Deuterium line at 2.22 MeV are 4×10^{-6} and 2×10^{-5} photons $cm^{-2}s^{-1}$ respectively, assuming an accretion energy E_p = 300 MeV. These fluxes should just be detectable during a two year satellite mission.

Neutron stars could be strong sources of quantized cyclotron emission as the observations of Her X1 by Trumper et al. (1977) would suggest. Cyclotron and synchrotron radiation are due to transitions in the energy levels of electrons in the presence of a magnetic field. The total energy of the electron E_e is quantized and is given by (e.g. Bussard, 1980),

$$E^2 = p^2c^2 + m^2c^4 (1 + 4.5 \times 10^{-14}B_j) \qquad (1.36)$$

$$j = n + s + \tfrac{1}{2}; \quad n = 0, 1, 2; \quad s = \pm \tfrac{1}{2}$$
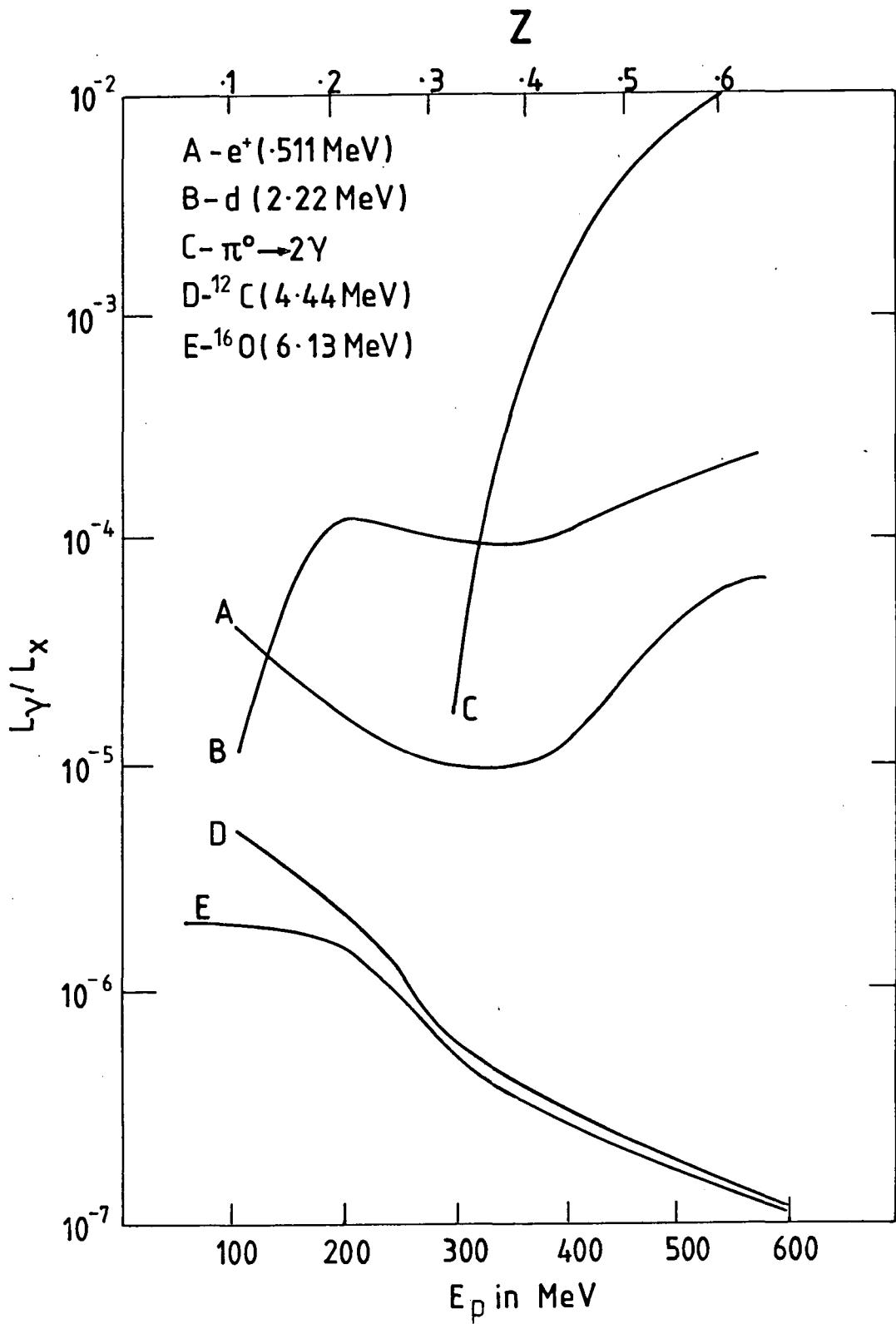
Figure 1.4 Expected gamma-ray line fluxes as a function of neutron star redshift z or accreted proton energy E_p. (from Brecher, 1978)

where p is the electron's momentum parallel to the magnetic field,
B is the magnetic field in gauss and j is the transverse energy
quantum number which has a contribution from the Landau level n
and the electron's spin s. In the presence of strong magnetic
fields (B > 10^{12}G), the energy level separation is large and can
lead to discrete gamma-ray line emission.

The detection of cyclotron lines provides a unique method of
determining neutron star magnetic field strengths. Interpreting
the 58 keV line feature from Her X1 reported by Trumper et al.
(1977) as the first harmonic emission line yields a value for the
magnetic field strength of 5.3 x 10^{12} gauss uncorrected for
gravitational redshift.

CHAPTER 2

CURRENT DETECTION METHODS IN GAMMA-RAY ASTRONOMY

2.1 INTERACTION OF GAMMA-RAYS WITH MATTER.

Unlike charged particles, a well collimated beam of gamma-rays shows a truly exponential absorption in matter. This is because photons can only be absorbed or scattered in a single event. A catalogue of the possible processes by which the electromagnetic field of the gamma-ray may interact with matter has been put in the following systematic form by Fano (1953, a,b),

Interaction	Effects
1. Interaction with electrons	a) Complete absorption
2. Interaction with nuclei	b) Elastic Scattering (coherent)
3. Interaction with the electric field surrounding nuclei or electrons	c) Inelastic scattering (incoherent)
4. Interaction with the meson field surrounding nucleons	

There are 12 ways of combining columns 1 and 2, thus in theory there are 12 different processes by which gamma-rays can be absorbed or scattered. Many of these processes are quite infrequent and indeed some have not yet been observed. It turns out that in the energy domain met most frequently in gamma-ray line astronomy, say 50 keV to 10 MeV, the bulk of gamma-rays interact through only three of the twelve processes listed. These are the photoelectric effect 1(a), the Compton effect 1(c), and pair production 3(a). Each type of interaction will be discussed in the next sections.

2.1.1 PHOTOELECTRIC EFFECT.

The photoelectric process involves the complete transfer of the incident photon energy to an atomic electron. Photoelectrons may be ejected from any of the K,L,M, ... shells of an atom, but a free electron cannot absorb a photon and become a photoelectron, since a third body (the nucleus) is necessary for conserving momentum. It is found both experimentaly and theoretically that about 80% of the photoelectric absorption processes take place in the K-shell, provided that the incident photon energy, $h\upsilon$, exceeds the K-shell binding energy. Because the entire atom participates, the photoelectric process may be visualized as an interaction of the primary photon with the atomic electron cloud in which the entire photon energy is absorbed and an electron is ejected from the atom with a kinetic energy,

$$E = h\upsilon - \phi \qquad (2.1)$$

where ϕ is the binding energy of the particle. The remainder of the energy appears as characteristic x-rays or Auger electrons from the filling of the vacancy in the inner shell. The former process is of particular importance in detectors of small size since the K x-ray can escape giving rise to the K electron escape peak. If the energy of the photon is sufficiently small so that relativistic effects are not important, but large enough so that the binding energy of the electrons in the K-shell may be neglected, the cross section per atom for photoelectric absorption is given by (Heitler, 1954),

$$\alpha^{\tau}\kappa = \sigma_T z^5 \alpha^4 2^{5/2} \left(\frac{m_o c^2}{h\nu} \right)^{7/2} \quad (cm^2 \text{ per atom}) \quad (2.2)$$

where σ_T is the Thompson cross section, α is the fine structure constant, $h\nu$ is the energy of the incident photon, $m_o c^2$ is the rest energy of the electron, and z is the atomic number of the absorbing material. The most important property of the cross section is the strong dependence on the atomic number z and on the energy of the incident photon.

2.1.2 COMPTON SCATTERING.

At energies much greater than the binding energies of the electrons, photons can be scattered as if the electrons were free and at rest. This is the Compton effect, and around 1 MeV it is the dominant mode of interaction. Figure 2.1 shows the scattering geometry for a Compton interaction at a point 0 (taken from Evans, 1955). The energy of the scattered photon is given by,

$$E_\gamma' = h\nu' = \frac{E_{\gamma o}}{1 + (E_{\gamma o}/m_o c^2)(1 - \cos\theta)} \quad (2.3)$$

where θ is the angle through which the photon is scattered. The kinetic energy of the scattered electron is then,

$$K_e = E_{\gamma o} - E_\gamma' = \frac{E_{\gamma o}^2 (1 - \cos\theta)}{m_o c^2 [1 + (E_{\gamma o}/m_o c^2)(1 - \cos\theta)]} \quad (2.4)$$
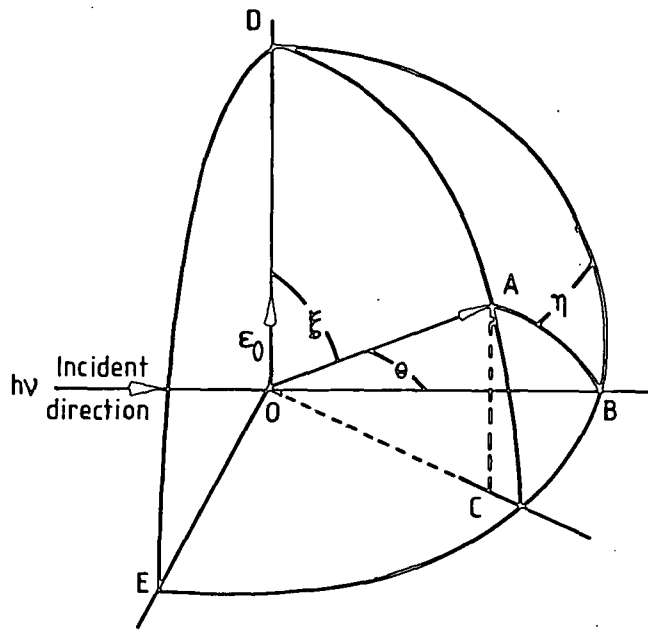
Figure 2.1　Compton interaction scattering geometry. ε_0 is the incident photon electric vector. (From R.D. Evans, 'The Atomic Nucleus,' McGraw-Hill book company)
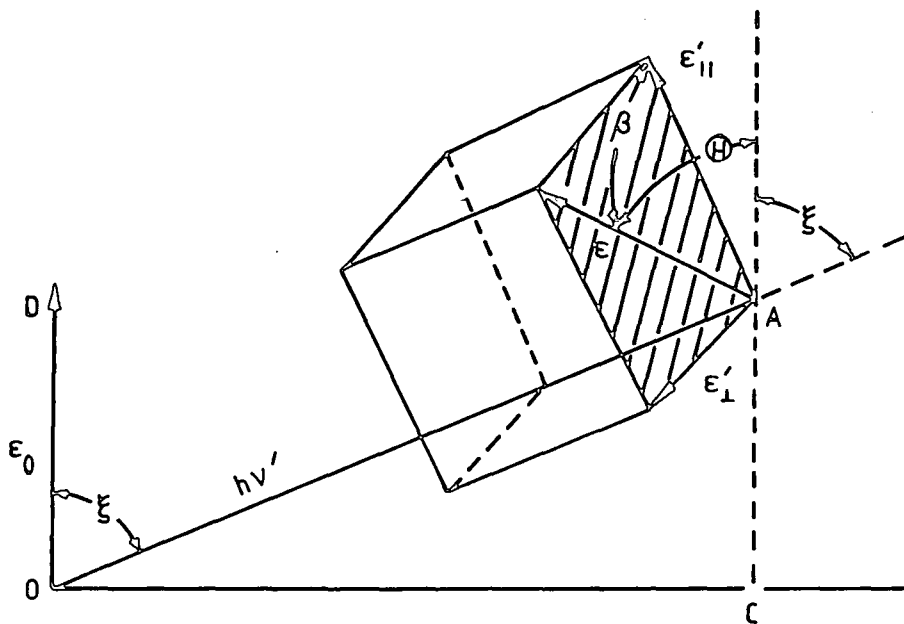
Figure 2.2　Compton interaction in the OADC plane of figure 2.1 giving the polarisation of the scattered photon by the direction of the electric vector ε'. (From R.D. Evans, 'The Atomic Nucleus,' McGraw-Hill book company)

The kinetic energy of the electron has its maximum value when $\cos \theta = -1$ or $\theta = 180°$, and the photon is scattered directly backward. The electron energy, in this case is,

$$K_e^{max} = \frac{E_{\gamma 0}}{1 + (m_0 c^2 / 2 E_{\gamma 0})} \qquad (2.5)$$

To obtain the cross-section for Compton scattering Klein and Nishina (1929) have carried out a quantum mechanical treatment of the problem using the Dirac equation for the electron. Figure 2.2 defines the geometry for the process following the discussion by Evans (1955). The differential collision cross-section is given by,

$$d(_e\sigma) = \frac{r_0^2 d\Omega}{4} \left(\frac{\nu'}{\nu_0}\right)^2 \left(\frac{\nu_0}{\nu'} + \frac{\nu'}{\nu_0} - 2 + 4\cos^2\Theta\right) \qquad (2.6)$$

$$(cm^2 \text{ per electron})$$

Here Θ is the angle between the electric vectors of the incident radiation and the scattered radiation, ε_0 and ε'. Physically, $d(_e\sigma)$ is the effective area which a free electron presents to a photon of initial energy $h\nu_0$, such that the photon is scattered into a solid angle, $d\Omega = 2\pi \sin \theta \, d\theta$ with a new energy $h\nu'$ and with the electric vector rotated by an angle Θ. Since the polarization of the scattered photon is unimportant in practical cases equation 2.6 can be summed over all possible scattered photon polarization directions. Thus for a Compton scattering at angle θ (Evans, 1955),

$$d(_e\sigma) = \frac{r_o^2 d\Omega}{2} \left(\frac{\nu'}{\nu_o}\right)^2 \left(\frac{\nu_o}{\nu'} + \frac{\nu'}{\nu_o} - 2\sin^2\theta\cos^2\eta\right) \tag{2.7}$$

where η is the projection of the angle ξ (Figure 2.2) onto the plane normal to the incident photon direction. For a given value of θ, Equation 2.7 shows that for $\eta = 90°$ the scattered intensity will be maximum and therefore the scattered photon and electron tend to be ejected at right angles to the electric vector of the incident radiation. This fact, emerging from Equation 2.8, forms the operational basis for practical γ-ray polarimeters (eg Metzger and Deutsch, 1950).

More theoretical attention has been paid to the case of unpolarized radiation rather than the polarized case. The differential collision cross-section for unpolarized radiation (Heitler, 1954; Evans, 1955) is given by,

$$d(_e\sigma) = \frac{r_o^2 d\Omega}{2} \left(\frac{\nu'}{\nu_o}\right)^2 \left(\frac{\nu_o}{\nu'} + \frac{\nu'}{\nu_o} - \sin^2\theta\right) \tag{2.8}$$

which has the same physical interpretation as Equation 2.6. Figure 2.3 is a polar plot of Equation 2.8 and indicates a strong increase in the fraction of forward scattered photons with increasing energy. The Compton total cross-section is found by integrating Equation 2.8 over all values of the angular co-ordinates and is found to be (Evans, 1955),
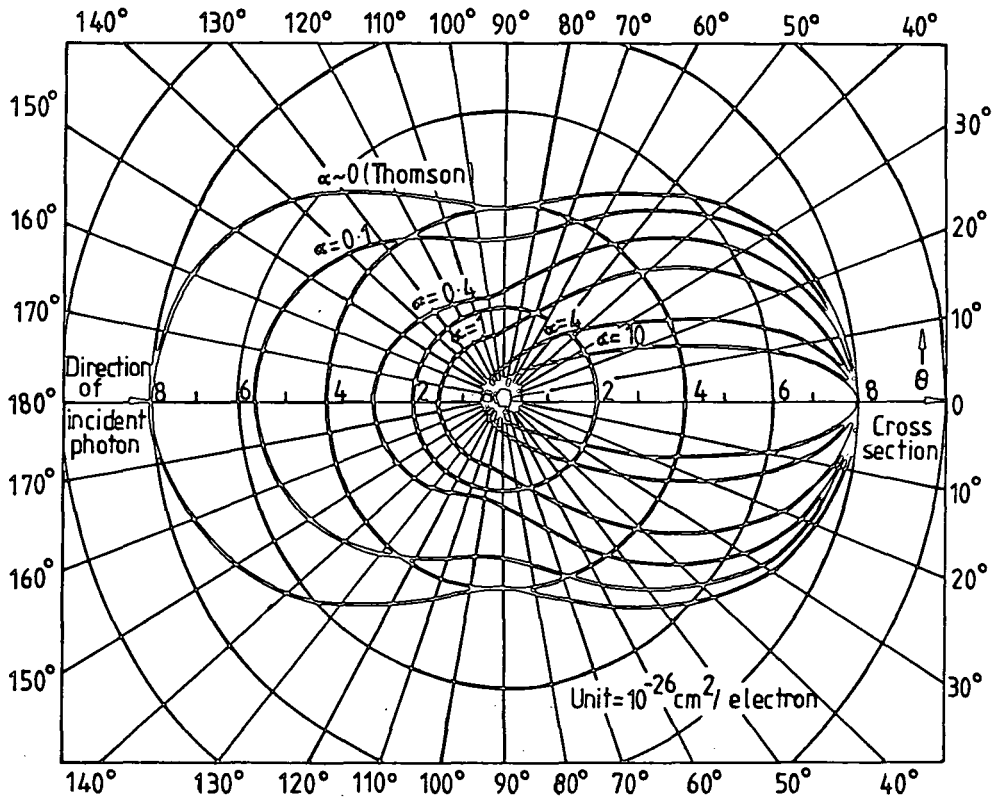
Figure 2.3 The number of photons scattered into unit solid angle $d(e^\sigma)/d\Omega$, at a mean scattering angle θ. (From R.D. Evans, 'The Atomic Nucleus,' McGraw-Hill book company)

Here $\alpha = E_{\gamma_0}/m_o c^2$

$$e^{\sigma} = 2\pi r_0 \left\{ \frac{1 + \alpha}{\alpha^2} \left(\frac{2(1 + \alpha)}{1 + 2\alpha} - \frac{\ln(1 + 2\alpha)}{\alpha} \right) \right.$$

$$\left. + \frac{\ln(1 + 2\alpha)}{2\alpha} - \frac{(1 - 3\alpha)}{(1 + 2\alpha)^2} \right\} \quad (\text{cm}^2 \text{ per electon}) \quad (2.9)$$

where $\alpha = E_{\gamma O}/m_0 c^2$. This then represents the probability of removal of the photon from a collimated beam while passing through an absorber containing one electron cm^{-2}.

2.1.3 PAIR PRODUCTION.

In the coulomb field of a nucleus a photon of energy $E_\gamma > 2 m_0 c^2$ may be converted into an electron positron pair such that,

$$E_\gamma = (E_- + m_0 c^2) + (E_+ + m_0 c^2) \quad . \quad (2.10)$$

where E_- and E_+ denote the energies of the electron and positron respectively. The cross-section is difficult to derive and is obtained by use of a quantum mechanical treatment. Marmier and Sheldon (1969) summarize the useful forms of the total cross-section as,

$$_a\kappa_p = \frac{r_0^2 z^2}{137} \left[\frac{28\ln}{9} \left(\frac{2h\nu}{m_0 c^2} \right) - \frac{218}{27} \right] \quad (\text{cm}^2/\text{atom}) \quad (2.11)$$

for $1 \ll E_\gamma \ll 1/\alpha z^{1/3}$ and for complete screening,

$$a\kappa_p = \frac{r_o^2 z^2}{137} \left[\frac{28\ell n}{9} \left(\frac{183}{z^{0.3}} \right) - \frac{2}{27} \right] \quad (cm^2/atom) \qquad (2.12)$$

when $E_\gamma/m_o c^2 \gg 1/\alpha z^{1/3}$. It is interesting to note that the latter expression is independent of energy.

2.1.4 ATTENUATION AND ABSORBTION OF ELECTROMAGNETIC RADIATION.

The probability of a photon traversing a given amount of absorber without any kind of interaction is just the product of the probabilities of survival for each particular type of interaction. Thus a collimated gamma-ray beam of initial intensity I_o after traversing a thickness x of absorber will have a residual intensity I of unaffected primary photons equal to,

$$I = I_o \exp(-\mu_o x) \qquad (2.13)$$

where $\mu_o = \sigma + \tau + \kappa$ and σ, τ and κ are the total Compton, photo-electric, and pair production cross-sections. μ_o is known as the total linear attenuation coefficient. The attenuation coefficient is a measure of the number of primary photons which have interactions. For any type of interaction, the mass attenuation coefficient is the linear coefficient divided by the density, ρ g/cm^3. As Evans (1955) points out, mass attenuation coefficients are of more fundamental value for gamma-ray detector work than the linear coefficients because all mass attenuation coefficients are independent of the actual density or physical state of the absorber whether it be gaseous, liquid or solid form. This is because the fundamental interactions are expressible as cross-

sections per atom, $_a\sigma$, $_a\tau$ and $_a\kappa$ and when these are multiplied by the number of atoms per gram, the mass absorption coefficient is obtained directly. Figure 2.4 shows the gamma-ray mass absorption coefficients for NaI and Ge; typical detector materials.

2.2 CURRENT DETECTION METHODS.

In this section a review of several instruments that are now, or have been in operation will be given. All the instruments discussed, have made important gamma-ray line measurements. Only a preliminary assessment of the capabilities of the instruments is possible based on design specifications given in various publications.

2.2.1 ACTIVELY SHIELDED NaI(Tℓ) DETECTORS.

Figure 2.5 shows diagrammatically the Rice University instrument which has observed the Galactic Centre on four balloon flights between the years 1969 and 1974 (Haymes et al. 1969; Johnston et al. 1972; Johnston and Haymes, 1973; and Haymes et al. 1975). It consists of a 6" diameter x 2" NaI(Tℓ) detector collimated to 15° FWHM by an active NaI(Tℓ) anticoincidence shield. The shield is at least two interaction mean free paths thick at all gamma-ray energies and complete 4π protection against data contamination by charged particles is provided by a thin sheet of plastic scintillator that covers the aperture. The function of the active shield is twofold. Firstly, to provide suppression of Compton and pair events that scatter into the shield, and secondly, to define the aperture which reduces the
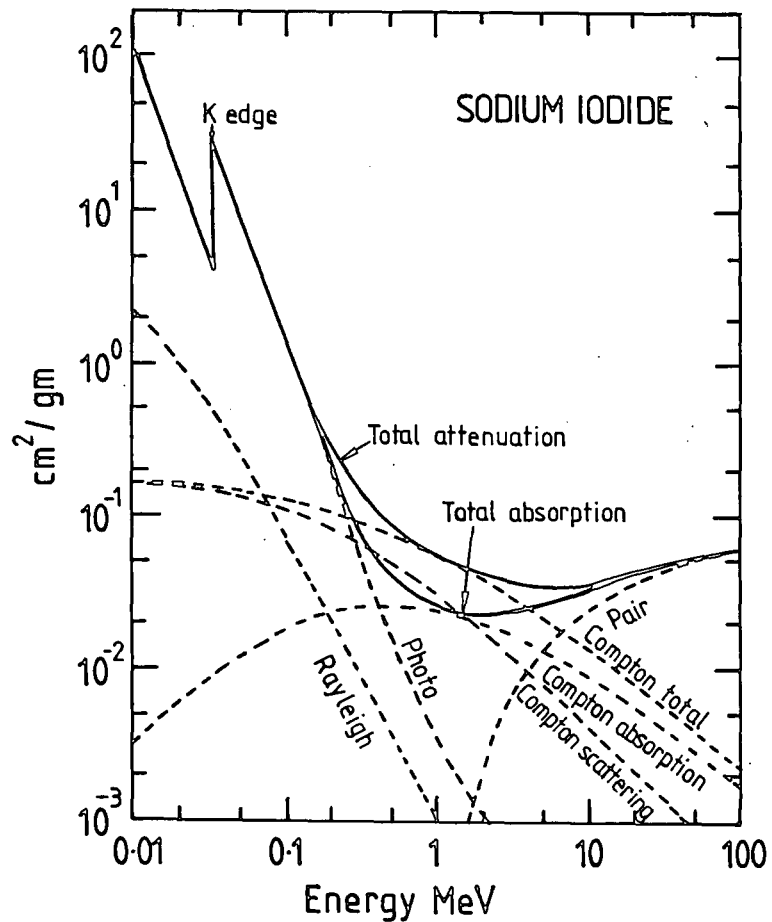
Figure 2·4 The mass attenuation coefficients ($cm^2 g^{-1}$) for γ-rays in Sodium Iodide.
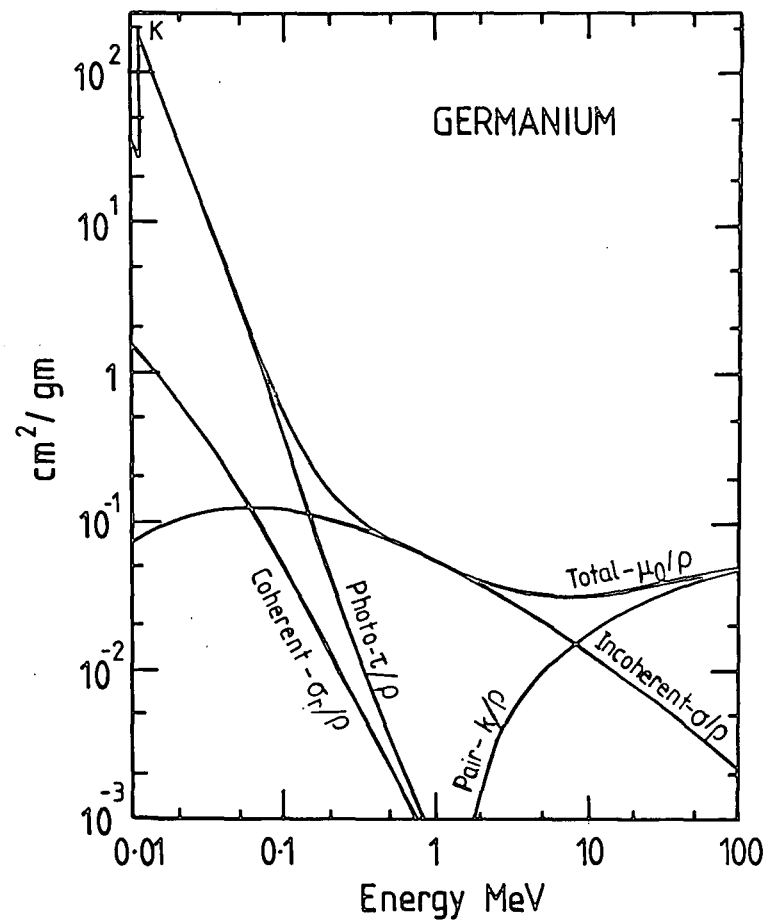
The mass attenuation coefficients ($cm^2 g^{-1}$) for γ-rays in Germanium.

contribution of the atmospheric and cosmic diffuse sources of background in the central detector and also helps to resolve discrete sources. The central detector is viewed by a single 3" photomultiplier tube. The shield is viewed by six photomultiplier tubes, the outputs of which are electronically connected in anticoincidence with the central detector's output.

Pulses from the central detector are analyzed by two 256 channel PHA's covering the energy ranges 56 keV to 1.0 MeV and 1.0 to 12.11 MeV. The instrumental resolution is 11% at 662 keV. The detector is equatorially mounted and pointed by command from the ground.

The first reported evidence for gamma-rays associated with solar flares was obtained during the August 4th and 7th 1972 solar eruptions with the University of New Hampshire's gamma-ray spectrometer onboard the OSO-7 satellite (Chupp et al., 1973). The basic sensor is a 3" x 3" diameter NaI(Tℓ) crystal mounted directly on the face plate of a ruggedized photomultiplier and hermetically sealed in a thin-walled stainless steel housing (Figure 2.6). The central detector is shielded by a thick, cup-shaped CsI(Na) shield and a thin front slab of the same material. Charged particle interactions in either of these shields initiate anticoincidence logic signals. Gamma rays have a high probability of passing through the thin front shield without interaction. The cup is approximately 5 cm thick nearest the central detector and attenuates 1 MeV gamma-rays by at least 60%. The entire instrument is located in a compartment of a rotating wheel section of the OSO-7 spacecraft, with the crystal and cup axis colinear with the wheel radius. Data is accumulated over 90 wheel rotations (taking approximately 3 minutes) when the instrument axis lies within 45°

ACTIVE
COLLIMATOR

NaI(Tl)

NaI(Tl)

HOLLOW THIN-WALL
LIGHT PIPE

NaI

RCA 8054
PMT

0.6cm

25.4cm

NaI(Tl)

15.2cm

15°

12.7cm   5cm

40.6cm

PLASTIC
SCINTILLATOR

NaI(Tl)

NaI(Tl)

25.4cm   30.5cm

CENTRAL
DETECTOR
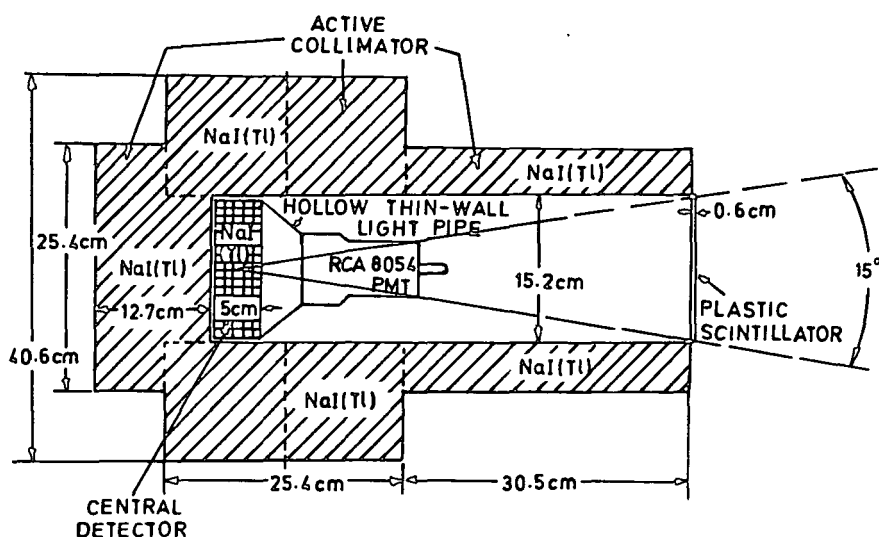
Figure 2.5 A cross sectional view of the Rice
University gamma-ray spectrometer.
(from Walraven et al., 1975)

X-RAY

X-RAY CALIBRATION
(Am 241 LIGHT
PULSER)

FRONT SLAB
CsI(Na)

CALIBRATION
(Co[60] SOURCE AT END
OF LIGHT PIPE)

CsI(Na) CUP

3x3" NaI(Tl) INTEGRAL LINE CRYSTAL
AND PHOTOMULTIPLIER ASSEMBLY
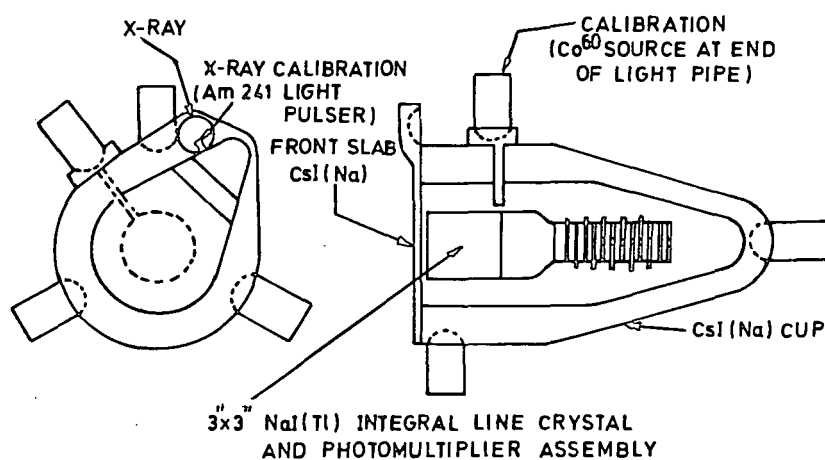
Figure 2.6 A schematic drawing of the γ-ray spectrometer
onboard the OSO -7 satellite. (Chupp et al. 1973)

of either the solar or antisolar direction. The instrument was designed to operate in the energy range 0.3 to 10 MeV and has an energy resolution of ~8% at 662 keV.

2.2.2 ACTIVELY SHIELDED GERMANIUM DETECTORS.

The first line observation using a balloon borne actively shielded Ge(Li) detector was made by the JPL group (Jacobson et al., 1975) using a cluster of four Ge(Li) detectors with a present combined volume of 180 cm^3. The detectors are surrounded by a CsI(Na) scintillation shield of thickness 6.4 cm defining a solid angle of 0.2 sr. Figure 2.7 shows an exploded view of the sensor elements and the sensor assembly. Four Ge(Li) crystals are arranged in a four leaf clover pattern and housed in a single vacuum cryostat. Each of the crystals is a right circular cylinder in a closed-end coaxial drift configuration, with the closed end pointing in the forward direction. The closed end coaxial configuration was chosen to maximize the active volume per crystal and to minimize the interaction between adjacent crystals by keeping the electric fields more confined within the crystal volume. Each crystal functions as an independent detector with its own amplifiers and 8192 channel pulse height analyzer. The resolution of the system is 2.8 keV at 1.33 MeV (0.22%). Collimation and background rejection for the Ge(Li) crystals is provided by a four piece CsI(Na) scintillation shield. Two pieces are the halves of a split annulus, the third is a plug for the rear of the annulus, and the last is a collimator which lies on top of the annulus. The collimator is 7.62 cm thick with four holes axially aligned with the Ge(Li) crystals below. Located
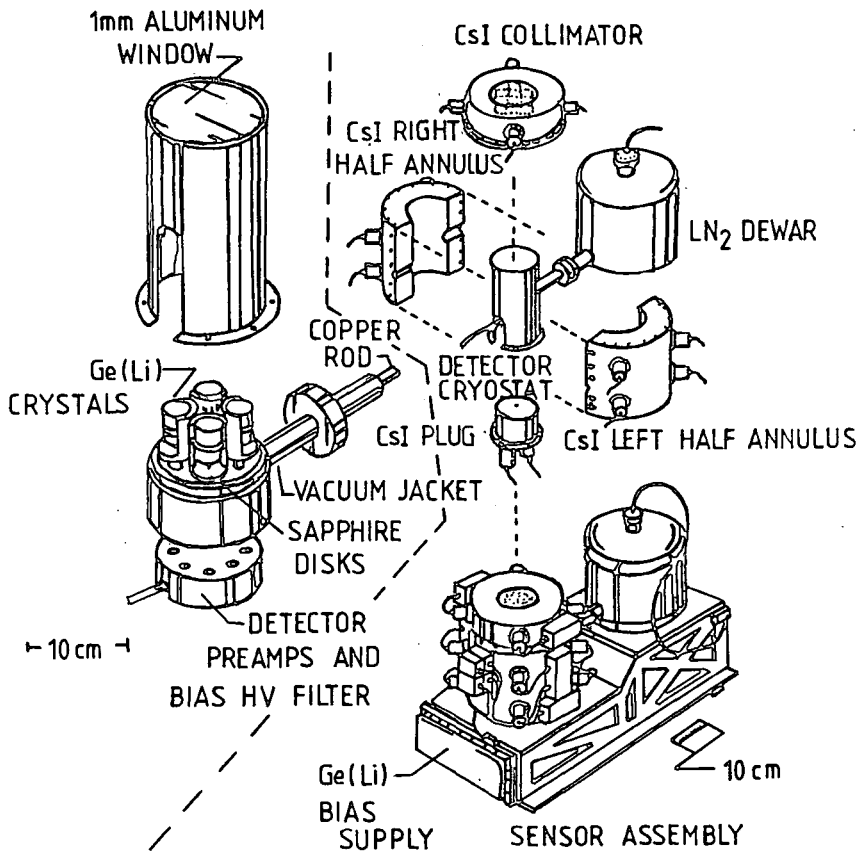
Figure 2.7 The Jet Propulsion Laboratory four-headed
gamma-ray spectrometer. [Jacobson et al (1978)]
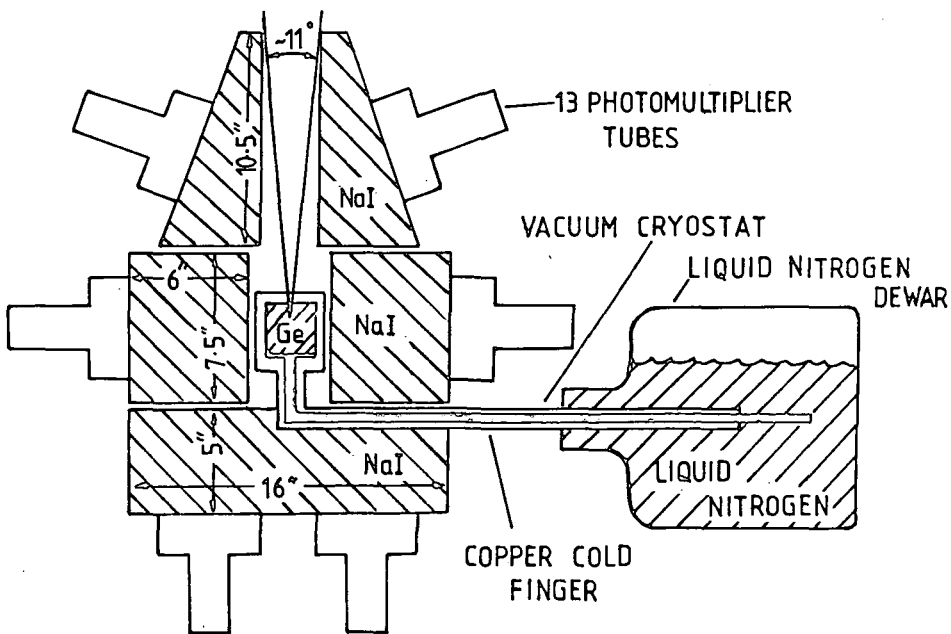
Figure 2.8 A cross sectional view of the Bell-Sandia instrument
apparatus. (Leventhal et al., 1977)

above the sensor, on a commandable turntable, are a radioactive calibration source and a 20.3 cm diameter by 10.2 cm thick NaI(Tℓ) detector used as a blocking crystal, or shutter, for the sensor. This is not shown in the diagram. The blocking crystal allows the study of the background properties of the instrument. A later version of this instrument was launched into low Earth orbit as part of the Third High Energy Astronomy Observation, (HEAO-3) satellite (Mahoney et al., 1980).

There have been reports of cosmic gamma-ray line observations by the Bell/Sandia Laboratories (Leventhal et al., 1977) using a balloon borne actively shielded Ge(Li) detector. The gamma-ray telescope is shown in Figure 2.8 and is designed around a single 92 cm^3 Ge(Li) crystal. Surrounding the central detector assembly are 184 kg of active NaI(Tℓ) acting as an anticoincidence shield. The shield is in three sections, an annulus of 15cm thickness, a plug of 12.7 cm thickness, and a collimator. The effective entrance aperture of the collimator increases slowly with energy from 11° FWHM at 50 keV to 13° FWHM at 1.33 MeV. The energy resolution of the individual sections of the shield is approximately 20% at 0.662 MeV. Ge(Li) pulses, not vetoed by a coincident shield pulse, pass through a preamplifier and a shaping amplifier, and are finally analysed and stored in the memory of a 4096 channel pulse height analyser. The energy range of the instrument is 0.1 to 5 MeV and the energy resolution below 2 MeV is 3.4 keV FWHM.

2.3 DISCUSSION OF SENSITIVITY.

The limiting source flux that can be detected by any

gamma-ray detector depends ultimately on two parameters of the detection element; the sensitive area exposed to the source and the level of background counts induced in the detector. For a gamma ray source in a direction θ and ϕ, the minimum source flux seen at a statistical significance of n standard deviations is given by;

$$F_{min} \geq \frac{n}{A(E,\theta,\phi)\epsilon(E)G(E,\theta,\phi)} \left[\frac{2[dB(E)/dE]\Delta E}{T} \right]^{\frac{1}{2}} \quad (2.14)$$

$$(cts\ sec^{-1})$$

assuming a null source count rate. dB(E)/dE is the differential background counting rate observed in the detector in counts s^{-1} keV^{-1}, T is the observation time on the source, ΔE is the width of the energy range in keV, $A(E,\theta,\phi)$ is the sensitive area exposed to the source in cm^2, $\epsilon(E)$ is the detection efficiency and $G(E,\theta,\phi)$ is the transmission of the overlying atmosphere at energy E.

It can be seen that to improve sensitivity, the observation time, detector area, efficiency and photon transmission into the instrument may all be increased while the detector background should be decreased. However it should be pointed out that an increase in area also increases the background, and thus impacts the sensitivity approximately as the square root of itself. For continuum source flux measurements scintillation detectors generally have sensitivities an order of magnitude better that of solid state detectors as their area's are usually a factor of ten greater. However with respect to narrow gamma-ray line measurements they must have ⴰ20 times the effective area to match the sensitivity of germanium detectors because of their much larger FWHM resolution. It should be noted that many of the lines

predicted from astrophysical sources are expected to exhibit broadening, and whenever significant broadening occurs, the relative sensitivity of a scintillation detector will be improved while that of a germanium detector will be impaired by a factor of approximately the square root of the ratio of the line width to the instrumental resolution. Table 2.1 lists the sensitivities at 3σ level for various recent gamma-ray detectors. The sensitivities are quoted for narrow line emission at 511 keV and source and background observing times of one hour. For comparison the sensitivity of the Durham 86 cm^3 actively shielded germanium detector is also included. This instrument has been described in Ayre et al. (1981a; 1984).

TABLE 2.1

The 511 keV line sensitivities[+] at the 3σ level for various experiments.
Observation time = 3600 seconds.

EXPERIMENT	RESOLUTION	MINIMUM DETECTABLE FLUX Photons $cm^{-2}s^{-1}$
Walraven et al. (1975) 4" x 2" NaI (Tl)	15% at 511 keV	1.5×10^{-3}
Chupp et al. (1973) 3" x 3" NaI (Tl)	8% at 662 keV	7.5×10^{-3}
Jacobson et al. (1975) 4 headed Ge 150 cm^3	2.9 keV at 1.33 MeV	1.0×10^{-3}
Leventhal et al. (1977) 130 cm^3 Ge	3.2 keV at 511 keV	1.9×10^{-3}
Nakano et al. (1973) 50 cm^3 Ge	3.5 keV at 1.33 MeV	1.2×10^{-2}
Graml et al. (1978) Double Compton Telescope	10% at 1 MeV	1.4×10^{-3} (at 1 MeV)
HEAO-C Mahoney et al. (1980) 4 headed Ge, 400 cm^3	2.5 keV at 511 keV	1.6×10^{-3}
LEGS Paciesas et al. (1983) 3 headed Ge, 258 cm^3	2.2 keV at 511 keV	8.6×10^{-4}
Ayre et al., (1981a) 86 cm^3 Ge	2.1 keV at 511 keV	2.2×10^{-3}

+ These calculations implicity assume that no continuum flux is observed
  from the hypothetical target. Also the instrumental β^+ background
  line has been ignored.

CHAPTER 3

OBSERVATIONAL STATUS OF GAMMA-RAY LINE ASTRONOMY.

3.1   THE GENERAL APPEARANCE OF THE GAMMA-RAY SKY.

The most comprehensive gamma-ray surveys have been made in the high energy region by the SAS-2 and COS-B satellites covering most of the galactic plane in the energy range 50 MeV to 5 GeV (Fichtel et al., 1977; Bignami et al., 1978). Since such a survey has yet to be made in low energy gamma-rays the COS-B and SAS-2 data will be discussed here. The results related to high energy galactic gamma-ray emission show a strong correlation with galactic structure seen at other wavelengths, when the known gamma-ray sources are subtracted (Haslam et al., 1981; Strong et al., 1982; Lebrun et al., 1983). In the Galactic Centre region the emission appears to be dominated by a broad band of radiation extending over the galactic longitude range (Mayer-Hasselwander, 1983). Evidence for localised excesses appear in several regions along the galactic plane. Excluding the Galactic Centre, each of these enhancements corresponds to the tangential direction of a spiral arm which in turn have been localised by intensity maxima in the radio continuum and neutral hydrogen (see Fichtel et al., 1977 and references therein). This has led to the conclusion that the high energy gamma-rays are revealing data on galactic spiral structure and the dynamics of galactic cosmic rays (Bignami et al., 1975). Localised sources could, however, account for some proportion of these excesses in the central region but their actual contribution is unknown (Frye et al., 1974). More sensitive measurements with improved spatial resolution are

required (Carter et al., 1983). Away from the Galactic Centre localised enhancements are seen to be associated with the quasar 3C273, the ρ Ophiucus cloud and the Crab and Vela pulsars.

3.2 GAMMA-RAY LINE OBSERVATIONS.

3.2.1 INTRODUCTION.

In general gamma-ray spectroscopy experiments can be carried out using various techniques depending on the energy region of interest. The gamma-ray line measurements that will be discussed here have all been carried out using actively shielded scintillation or solid-state detectors. Some of the individual instruments have already been discussed in some depth in the previous chapter. For the sake of brevity, and since the theoretical interpretation of many of these observations appear to be as transient as the lines themselves, the reader is referred to the excellent theoretical reviews of Ramaty and Lingenfelter (1981, 1982).

3.2.2 SOLAR GAMMA-RAY LINES.

One of the most likely expected sources of gamma-ray lines is the Sun, especially during periods of high solar activity when energetic particles (solar cosmic rays) are known to be produced. For early predictions of solar gamma-ray lines, see Lingenfelter and Ramaty (1967). The first reported observations were made by Chupp et al. (1973) on the solar flares of August 4th and 7th 1972. They used an actively shielded 3" x 3" NaI(Tℓ) detector

onboard the OSO-7 satellite. Figure 3.1 shows the spectrum obtained during the rising phase ($\sim$ 9 mins) of the large flare that erupted at 0624 UT on August 4th 1972, the onset of which closely coincided with the H_α flash, x-ray and radio bursts. The dotted curve shows the background spectra (anti-solar direction) obtained during three full accumulations of 9 minutes duration. Besides the ^{60}Co calibration lines, the solid curve shows strong spectral emission features at 0.511 and 2.22 MeV and weaker features at energies 4.4 and 6.1 MeV with the following average intensities: (6.3 ± 2.0) x 10^{-2}, (2.8 ± 0.2) x 10^{-1}, (3.9 ± 1.0) x 10^{-2} and (3.0 ± 1.0) x 10^{-2} photons cm^{-2} s^{-1} respectively. All of these lines result from nuclear reactions of flare accelerated particles most probably in the chromosphere or lower corona, athough at this time there is still controversy over whether these particles are ions or protons. The measured intensities of these four lines are consistent with the earlier calculations of Lingenfelter and Ramaty which show that the strongest flare produced lines should be at 2.22 MeV from the capture of flare produced neutrons on photospheric hydrogen and at 0.511 MeV from the annihilation of solar cosmic ray produced positrons with the ambient electrons in the solar atmosphere. The weaker lines at 4.4 at 6.1 MeV are the result of inelastic scattering of energetic protons and alpha particles on ambient ^{12}C and ^{16}O nuclei. The latter lines are prompt so that their production varies as the instantaneous number of energetic particles while the lines at 2.22 and 0.511 MeV are delayed because of the finite neutron capture and positron annihilation times. Indeed only the 0.511 and 2.22 MeV lines were seen by the OSO-7 instrument during the decaying phase of another large flare which erupted on August 7th
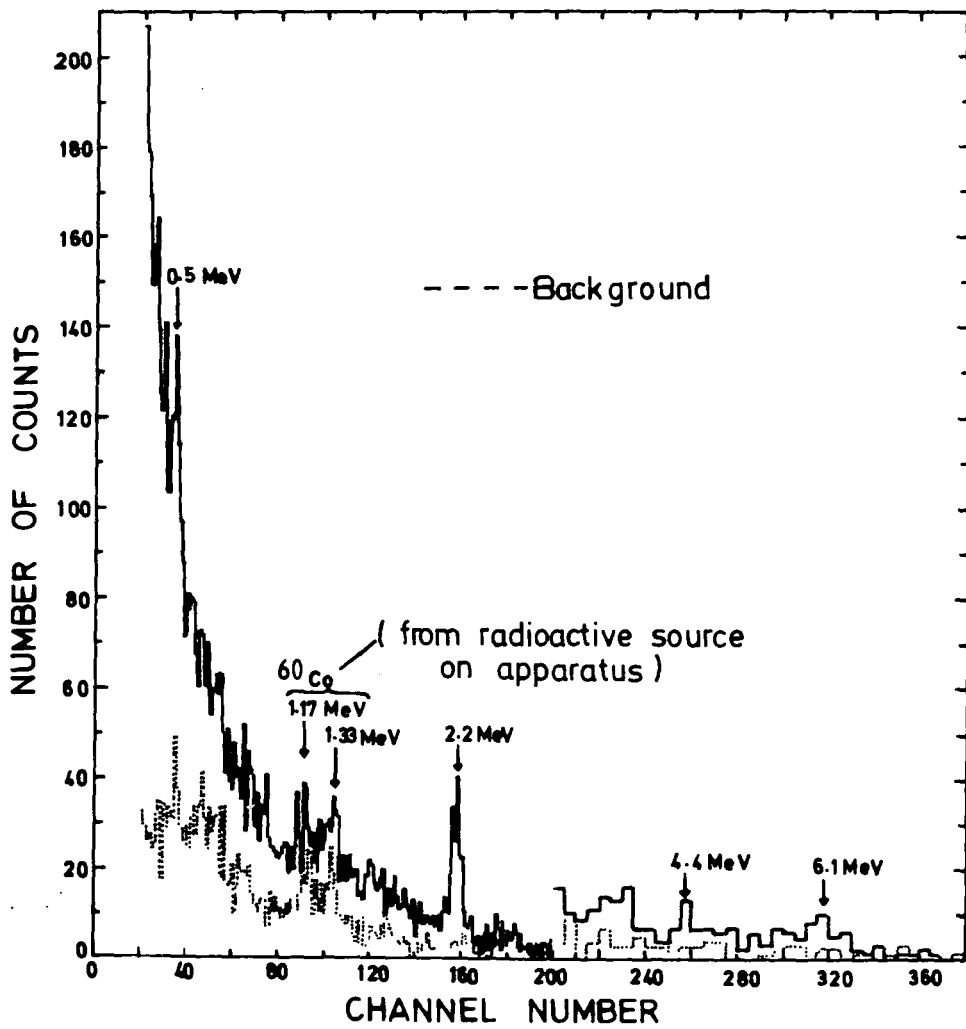
Figure 3·1 The Solar Spectrum obtained by Chupp et al (1975)

1972. Ramaty et al. (1975) attribute the continuum to bremsstrahlung produced by relativistic electrons accelerated in the flare region.

Gamma-ray line emission has also been detected by the HEAO 1 satellite borne spectrometer during a white light flare which occurred on July 11th 1978 (Hudson et al., 1980). This instrument had an energy range of 1 to 5 MeV and consisted of an array of 7 collimated actively shielded NaI(Tℓ) scintillation counters (Matteson, 1978). The energy resolution at 1.33 MeV was ∿ 23% FWHM. The flare erupted at approximately 1035 UT and produced an excess over the entire spectral range. Strong spectral features were found at energies (2.26 ± 0.07) and (4.39 ± 0.13) MeV. The observed fluxes were (1.0 ± 0.29) and (0.18 ± 0.07) photons cm^{-2} s^{-1} respectively, which are about 5 to 6 times greater than those reported by Chupp et al. (1973). However the ratio of the line intensities is the same and agrees with the calculations of Ramaty and Lingenfelter (1975). The line at 4.43 MeV was found to be prompt while the line at 2.2 MeV was delayed by 90 seconds, in agreement with the observations of the August 1972 flares. The clear delay of the 2.2 MeV line is also consistent with the time needed for the slowing and capture of fast neutrons (Wang and Ramaty, 1974) assuming that the neutron production rate had a time profile matching that of the integral flux > 1 MeV.

3.2.3 LINES FROM THE GALACTIC CENTRE.

Probably the first report of a cosmic gamma-ray line was by Johnston et al. (1972) of Rice University who observed the Galactic Centre during a balloon flight of an actively shielded

NaI(Tℓ) detector from Parana, Argentina in November 1970. The
instrument had an energy resolution of 15% FWHM at 511 keV and an
angular resolution of 24°. Using an orientatable gondola, source
and background spectra were taken for alternate 10 minute periods
by rotating the azimuth of the telescope through 180°. The source
spectrum was determined for a particular source observation by
subtracting the average background spectrum obtained during two
adjacent background accumulations, assuming the background to be
independant of azimuth. The total observation time was 7 hours.
The resulting differential source spectrum after correcting for
atmospheric absorption is shown in Figure 3.2. Also shown are the
data for the 1969 and 1971 flights along with the data points
obtained by Leventhal et al. (1978). The two important results
indicated by the 1970 flight are the apparent continuum flux
expressed by,

$$dN(E) = (10.5 \pm 2.2)E^{-(2.37 \pm 0.05)} \text{ photons cm}^{-2} \text{ s}^{-1} \text{ keV}^{-1} \quad (3.1)$$

and a Gaussian shaped line feature centred at (473 ± 35) keV with
an intensity of $(1.8 \pm 0.5) \times 10^{-3}$ photons cm^{-2} s^{-1}. The
existence of this spectral line was reportedly confirmed by an
additional balloon flight of the same apparatus in November 1971
which detected a Galactic Centre feature centred at (485 ± 24) keV
(Johnson and Haymes, 1973). In April 1974 the same group flew a
similar instrument to that flown previously from Rio Cuarto in
Argentina (Haymes et al., 1975). This detector had only
marginally better efficiency and energy resolution, but a
significantly smaller angular resolution (15° as opposed to 24°).
A total of 219 minutes of source and background data were
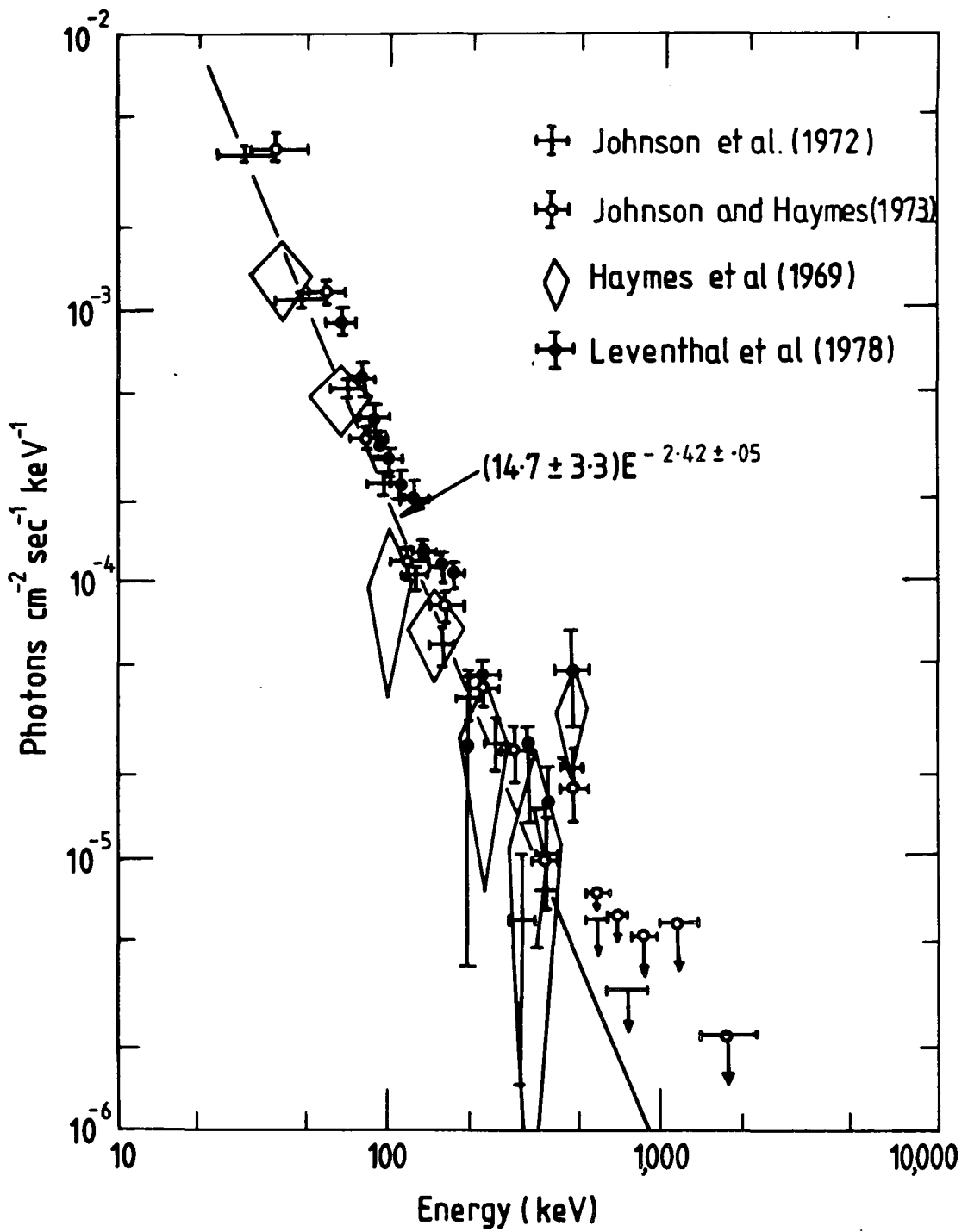
Figure 3·2   Differential photon spectrum from the galactic centre.

obtained. On this occasion several spectral lines were recorded
including one at (530 ± 11) keV at a confidence level of 3.5σ.
They believe this to be the same as the feature observed in 1970
and 1971 in spite of a quantitative difference in average energy
of 3.4σ (which pratically excludes the possibility of a
statistical fluctuation).   Haymes et al. (1975) suggest that the
average energy of the excess is a function of the galactic
longitude coordinates observed, which in 1970 extended from ℓ =
354° to 17°, in 1971 ℓ = 351° to 15° and in 1974 ℓ = 353° to 8°.
Leventhal et al.   (1978) observed the Galactic Centre with a
balloon borne 130 cm^3 actively shielded germanium detector
launched from Alice Springs, Australia in November 1977.   The
instrument had an energy resolution of 3.2 keV (FWHM) and an
angular acceptance of 15° at 511 keV.   The differential flux
obtained is shown in figure 3.3 and was determined by forming
target-background pair difference rates on a channel by channel
basis and correcting to the top of the atmosphere. A 4.5σ
enhancement in counting rate was found in the energy region 509 to
512 keV with a corresponding line flux of (1.22 ± 0.22) x 10^{-3}
photons cm^{-2} s^{-1}. Figure 3.4 shows an expanded version of Figure
3.3 in the vicinity of 511 keV. The line centre is at (510.7 ±
0.5) keV with a width limited by the instrumental resolution at <
3.2 keV.

A detailed study of the continuum spectrum seems to reveal
the presence of a three photon positronium continuum. Stecker
(1969) and Leventhal (1973) have pointed out that positrons
stopping in the interstellar gas should annihilate predominately
from one of the two ground state configurations of positronium.
Should this be the case, 25% of the annihilations will be from the
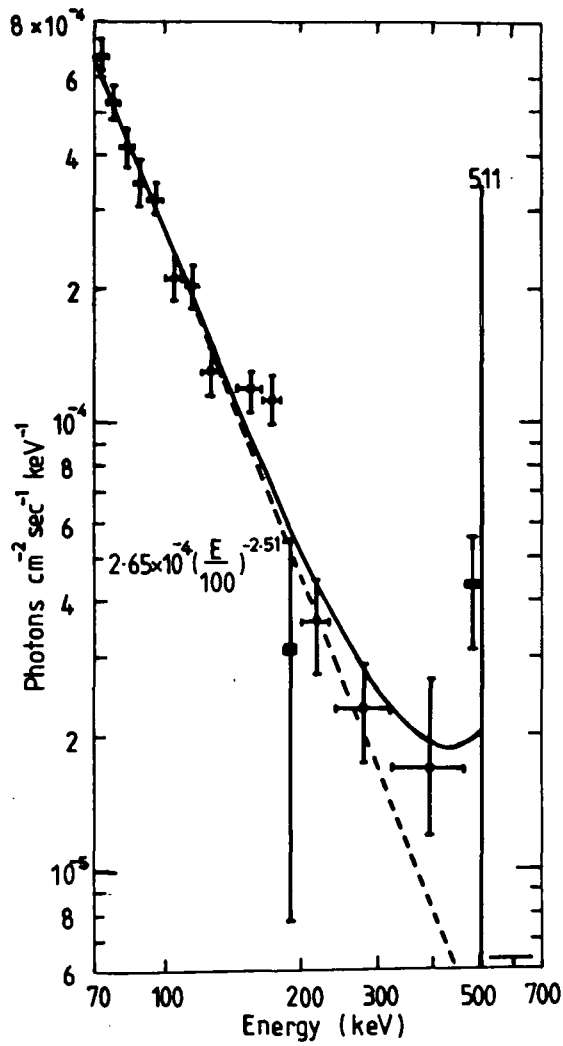
Figure 3·3 Differential photon spectrum from the galactic centre. From Leventhal et al. (1978)
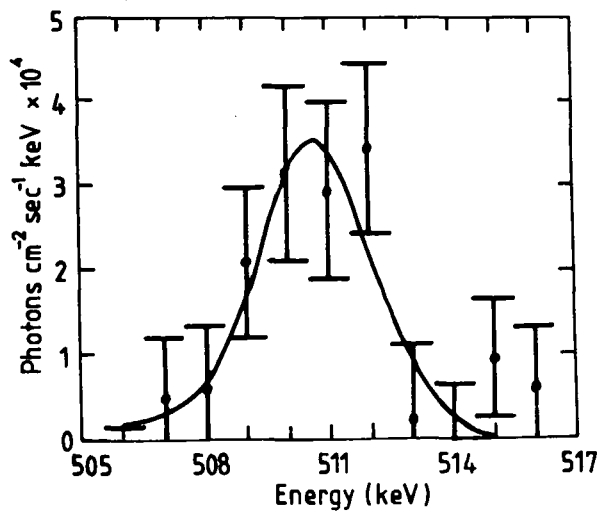
Figure 3·4 An expanded version of Fig. 3·3 in the vicinity of 511 keV. From Leventhal et al. (1978)

para-state yielding two anti-parallel 511 keV photons whereas 75% of the annihilations will be from the ortho-state yielding three gamma-rays in a plane. Leventhal et al. (1978) have concluded that $\sim$ 90% of the positrons must annihilate via positronium and that the detected spectrum can therefore be fitted by the sum of three functions: a) an inverse power law continuum (which is most likely a composite spectrum from the many sources in the field of view), b) a Gaussian line near 511 keV and c) a three photon positronium continuum as determined by Ore and Powell (1949). Meagan (1978) in reassessing the Rice University results of 1971 and 1974 conclude that the discrepancy concerning the energy variability of the $\sim$500 keV feature is resolved in view of the Bell/Sandia results.

Confirmation for the Galactic Centre emission at 511 keV was provided by the high resolution germanium spectrometer onboard the HEAO 3 satellite during observations performed in the fall of 1979 and the spring of 1980 (Reigler et al., 1980). A 3.5σ decrease in line intensity is apparent between these two observation periods thereby strongly indicating temporal behaviour. Furthermore the HEAO 3 data are consistent with a point source located at the Galactic Centre, and a maximum source size of 10^{18} cm is inferred from the apparent 6 month variability (Reigler et al., 1981). A subsequent flight by the Goddard Low Energy Gamma-ray Spectrometer (LEGS) from Alice Springs, Australia on November 20 1981 failed to detect line emission at 511 keV (Paciesas et al., (1982). This instrument consists of an actively shielded 3-headed Ge detector of total active volume 250 cm^3. The energy resolution is 2.2 keV at 511 keV with a field of view of 15° FWHM. The 98% confidence upper limit of 1.2×10^{-3} photons cm^{-2} s^{-1} derived by this

experiment is consistent with the HEAO 3 1980 results.

The 511 keV line is interpreted as being due to electron positron annihilation though the source of the positrons is unclear. Suggestions include supernova and nova explosions, radio pulsars and cosmic ray interactions. Calculations by Ramaty et al. (1979) indicate that cosmic ray positron production should account for only a few percent of the detected flux. In view of the recent infra-red data (Lacy et al., 1979,1980), Lingenfelter et al. (1981) suggest that a massive singularity within the central parsec of the Galaxy is necessary to explain the $\sim 10^{43}$ positron electron pairs required by the present observations.

Apart from the 511 keV line, there have been several unsubstantiated reports of line emission from the direction of the Galactic Centre. During their 1974 flight, Haymes et al. (1975) found evidence for an additional spectral line at an energy of (4.4 ± 0.1) MeV with an intensity of (9.5 ± 2.7) x 10^{-4} photons cm^{-2} s^{-1}. The line, shown in Figure 3.5, appears to be broadened and is attributed to the first excited state of ^{12}C at 4.43 MeV. The early results of the HEAO 1 satellite seemed to confirm the presence of this line during observations of the Galactic Centre in August 1977. However more recent results (Matterson et al., 1978) yielded a 3σ upper limit for broadened emission of 5.7 x 10^{-4} photons cm^{-2} s^{-1}, well below that reported by Haymes et al. Similarly, null results were also found by the Apollo 16 (Gilman et al., 1979) and CESR (Mandrou, 1979) gamma-ray detectors. Since the galactic coordinates covered in these observations were not exactly the same, several authors have pointed out that if the 4.4 MeV line exists, it is limited to longitudes between ± 12° and emanates from within 2 kpc of the Galactic Centre (Vedrenne, 1979;
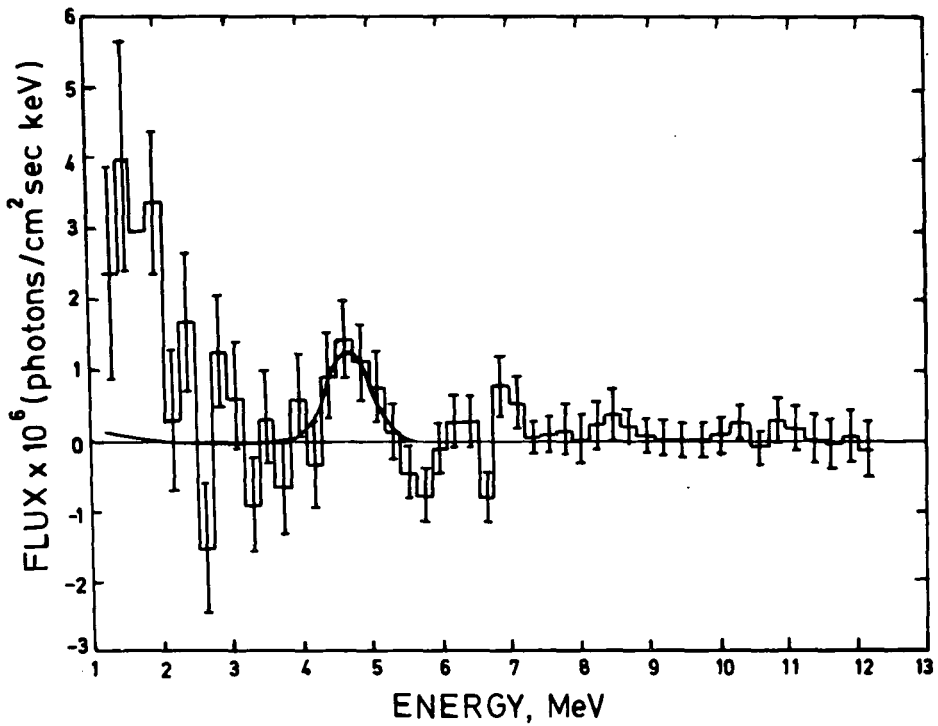
Figure 3·5 Measured differential energy spectrum of the Galactic Centre region for energies greater than 1·0 MeV. (From Haymes et al.,(1975))
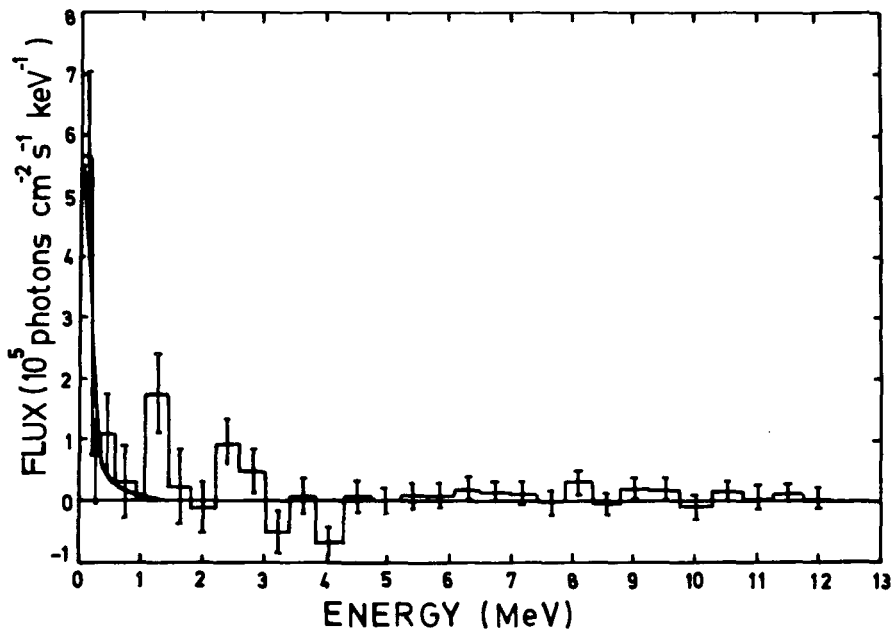
Figure 3·6 A spectrum of gamma rays obtained from a possible source in the galactic plane. A possible spectral line exists ~ 1·15 MeV (From Walraven and Haymes (1976)

Audouze et al., 1979).

Walraven and Haymes (1976) have analysed the background scans taken during the 1974 observations. They found that one particular background segment had anomalously high counts in one part of the spectrum. The segment in question was near the galactic plane but centred 15° away from the Galactic Centre. The line, shown in Figure 3.6, is marginally significant at an energy of (1.15 ± 0.07) MeV and a flux of $(3.4 \pm 1.5) \times 10^{-3}$ photons cm^{-2} s^{-1}. Calculations by Clayton et al. (1969) on explosive nucleosynthesis predict a line at 1.156 MeV from the decay of ^{44}Ca. Thus the presence of this line is considered by Walraven and Haymes to be more than coincidence even though the statistical significance is marginal. However it should be pointed out that Leventhal et al. (1978) also observed this region of the galactic plane and failed to detect line emission at 1.16 MeV, quoting a 2σ upper limit of 1.8×10^{-3} photons cm^{-2} s^{-1}.

Imhof and Nakano (1977) scanned the galactic plane using a satellite borne 50 cm^3 Ge(Li) detector with an energy resolution of 3.5 keV and an angular acceptance of 90°. Two portions of the galactic plane were scanned in the energy range 38 to 2700 keV; from 100° to 170° and 260° to 330°. The minimum sensitivity at 511 keV was just sufficient to resolve the gamma-ray flux detected by Haymes et al. (1975). They found no strong evidence for gamma-ray emission at this energy from either scan, however it should be remembered that the Galactic Centre was not covered in these observations. Peaks at 1121 and 1358 keV were detected at the 3.1 and 2.9σ levels respectively and are suggested to be two of the lines considered by Lingenfelter and Ramaty (1976) from the de-excitation of ^{46}Ti and ^{24}Mg.

3.2.4 LINES FROM CENTAURUS A.

Centaurus A is the nearest radiogalaxy to us. The intense radio, infrared and x-ray emission emanating from Cen. A and associated optical Galaxy NGC5128 which surrounds it, imply the existence of relativistic electrons which in turn suggest there may be a large flux of high energy atomic nuclei as well. Consequently it is expected to be one of the brightest sources of nuclear radiation. X-ray and low energy gamma-ray observations since 1969 show long term variability of a factor of 5 with 1973-1975 being a period of particularly high flux (Baity et al., 1981 and references therein). Although gamma-ray emission is not seen in the $30-10^3$ MeV region of the spectrum by either SAS 2 or COS B, a strong indication of very high energy ($E \geq 3 \times 10^{11}$ eV) γ-ray emission has been found (Grindlay et al., 1975).

Hall et al. (1976) observed Cen. A during the same balloon flight that made the Galactic Centre observations. Source and background spectra were taken in a manner indentical to that described previously and a total of 85 minutes source observing time and 109 minutes background observing time were recorded. The resulting differential photon spectrum is shown in Figure 3.7. By excluding deviant points around 1.6 and 4.5 MeV, the best fit continuum was found to be,

$$dN(E) = (0.86 \pm 0.17) \, E^{-(1.9 \pm 0.04)} \text{photons cm}^{-2} \text{ s}^{-1} \text{ keV}^{-1} \quad (3.2)$$

Superimposed on this continuum were two positive deviations. These are shown in more detail in Figure 3.8. The first line is a
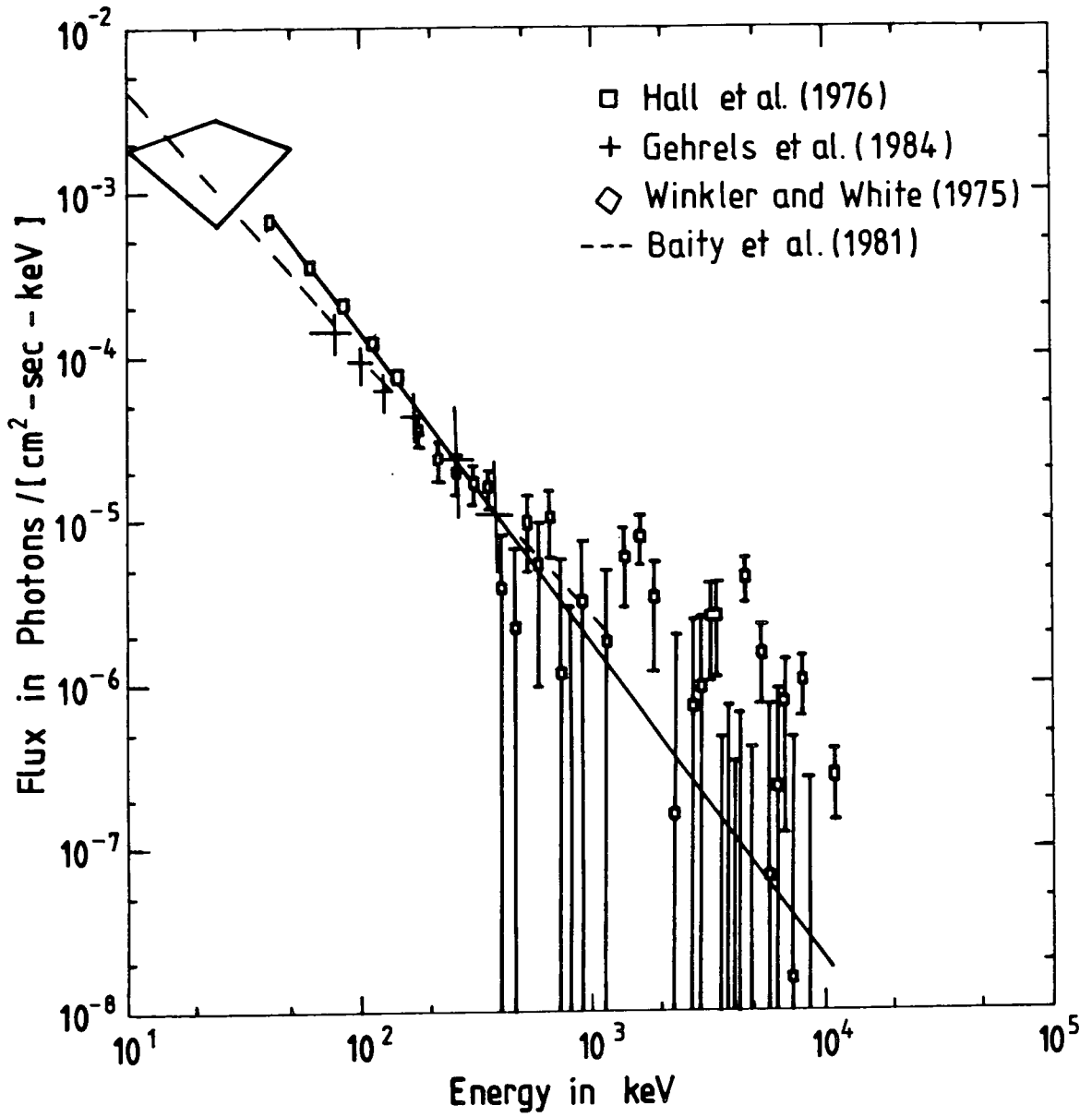
Figure 3·7 Differential photon spectrum of Centaurus A
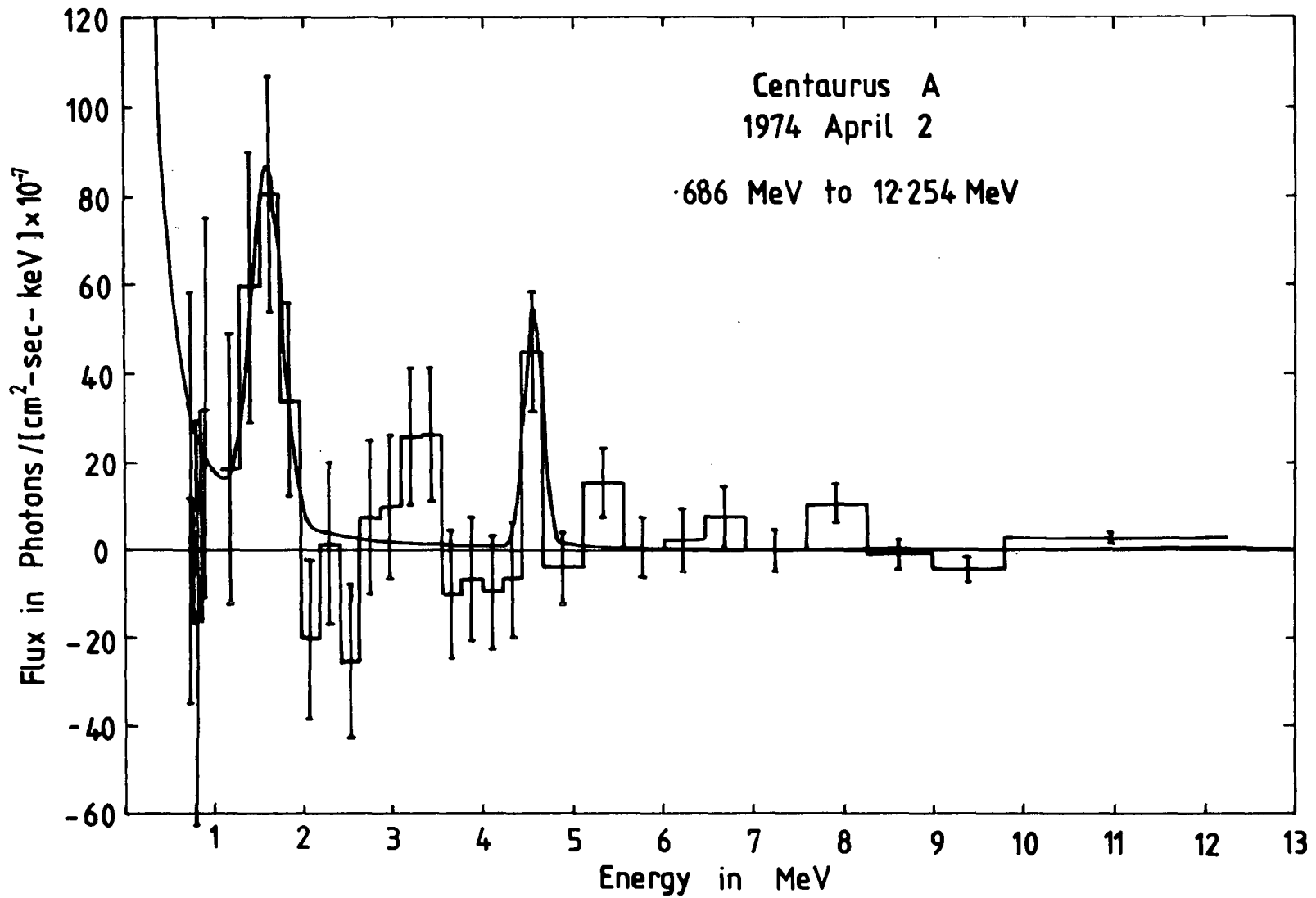
Figure 3·8   The Centaurus A spectrum at energies above 0·686 MeV. [Hall et al (1976)]

broad feature centred at 1.6 MeV extending from 1.27 to 1.95 MeV, a range much larger than the FWHM resolution of 0.12 MeV at this energy. The line flux for this feature is $(3.4 \pm 1.0) \times 10^{-3}$ photons cm^{-2} s^{-1}. The feature centred at 4.5 MeV has an intensity of $(9.9 \pm 3.0) \times 10^{-4}$ photons cm^{-2} s^{-1} and a width approximately equal to the instrumental energy resolution and is therefore likely to be unbroadened. The latter line is suggested to be a result of excitation of ambient ^{12}C to its first excited state by low energy cosmic rays and the broad feature at 1.6 MeV is suggested to be a blend of nuclear lines from excited states of $^{24}Mg^{*}$ (1.37 MeV), $^{20}Ne^{*}$ (1.63 MeV) and $^{28}Si^{*}$ (1.78 MeV). All three nuclides are relatively abundant in cosmic rays as observed from the Earth (cf. Goret et al., 1981). It is proposed that the nuclear excitation could be due to either cosmic ray bombardment of the intersellar medium of Cen. A or to nucleosynthesis within the Centaurus A/NGC5128 system.

Subsequent observations by the HEAO 1 satellite during January and July 1978 failed to detect line emission in the energy range 2 to 2300 keV (Baity et al., 1981). Upper limits to unresolved lines at 511 keV and 1.6 MeV were found to be 6.5 x 10^{-4} and 2.2×10^{-4} photons cm^{-2} s^{-1} respectively at the 90% confidence level. These results are consistent with the later observations of the LEGS detector on November 19 1981 (Gehrels et al., 1984) who report 2σ upper limits of 9.9×10^{-4}, 4.1×10^{-4} and 9.4×10^{-4} photons cm^{-2} s^{-1} for narrow line emission at 511 keV, 1.6 MeV and 4.5 MeV respectively. For the case of the 1.6 MeV line both the HEAO and LEGS upper limits are a factor of 10 lower than the line flux reported by Hall et al. (1976) and therefore if the 1974 line was real, source variablity would be

indicated over a time scale of less than a few years.

3.2.5. LINES FROM THE CRAB NEBULA.

There have recently been several reports of possible gamma-ray line emission from the Crab Nebula region. Leventhal et al. (1977) observed the Crab during a balloon flight in May 1976. Data were accumulated in alternate 20 minute target-background segments with the telescope rotated in azimuth 180° for the background measurements. A total of 7.4 Crab target and background segments were obtained. The differential spectrum obtained after correcting to the top of the atmosphere is shown in Figure 3.9. A careful study of the data was made for sharp line features by searching both the target and background data for 5 keV wide bins which contained greater than a 3σ excess number of counts over what would be expected (based upon the two 10 keV wide bins on either side of the 5 keV bin in question). One potential line feature was detected at (400 ± 1) keV in the target data but not in the background data (Figure 3.10). When the Crab target spectrum is extrapolated to the top of the atmosphere the feature represents a 3.5σ deviation over the telescope continuum corresponding to a line flux of $(2.24 \pm 0.65) \times 10^{-3}$ photons cm^{-2} s^{-1} and a width < 3 keV. It has been suggested by Leventhal et al. (1977) that this line could be the result of gravitationally redshifted annihilation radiation from the surface of a neutron star. The value of the deduced redshift is 0.28 which implies a neutron star mass of ~ 1.6 $M_\odot$. Confirmation for this line was provided, albeit with small statistical significance, by Yoshimori et al. (1979) who flew a balloon borne Ge(Li) spectrometer on
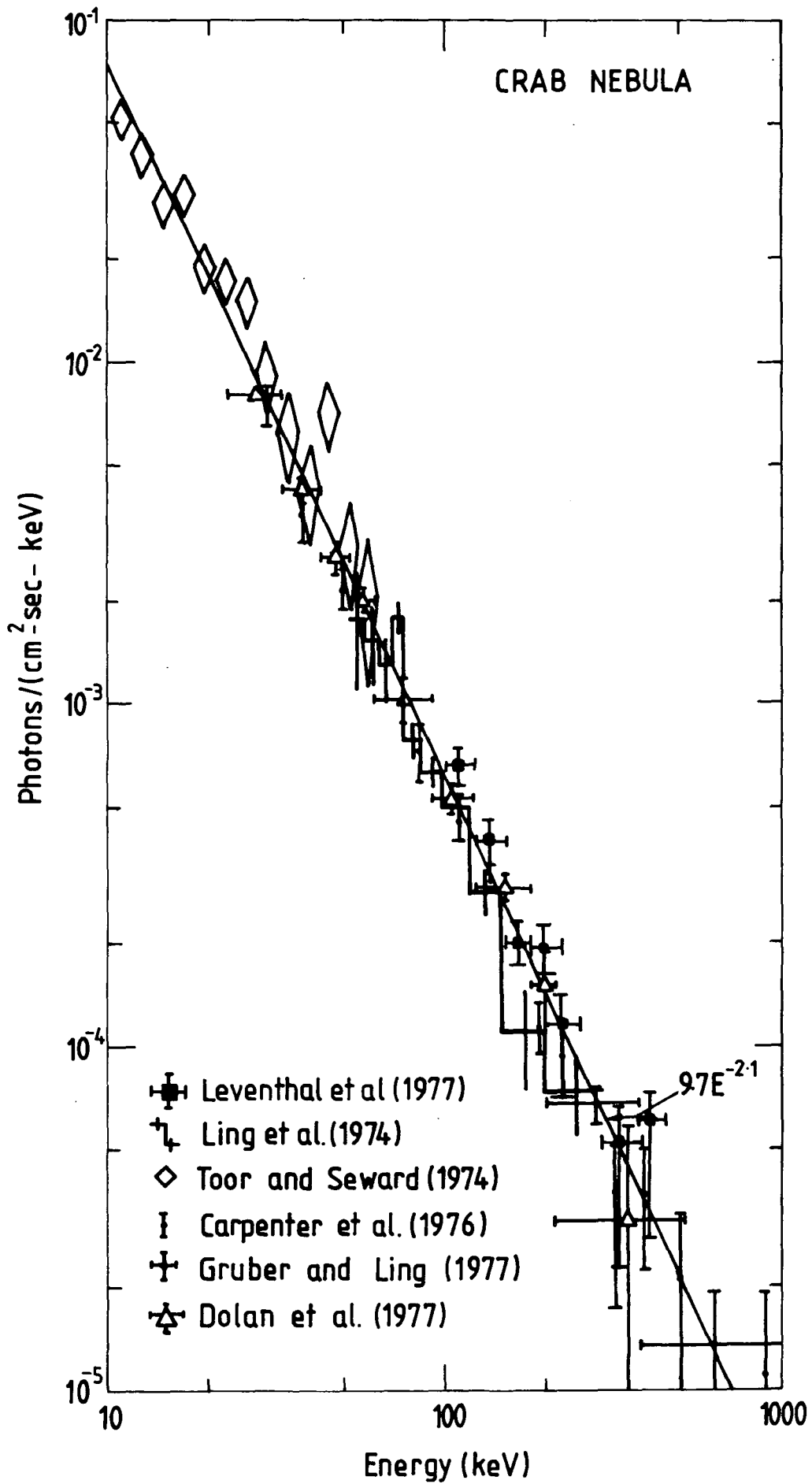
Figure 3·9 Differential photon spectrum from the Crab Nebula
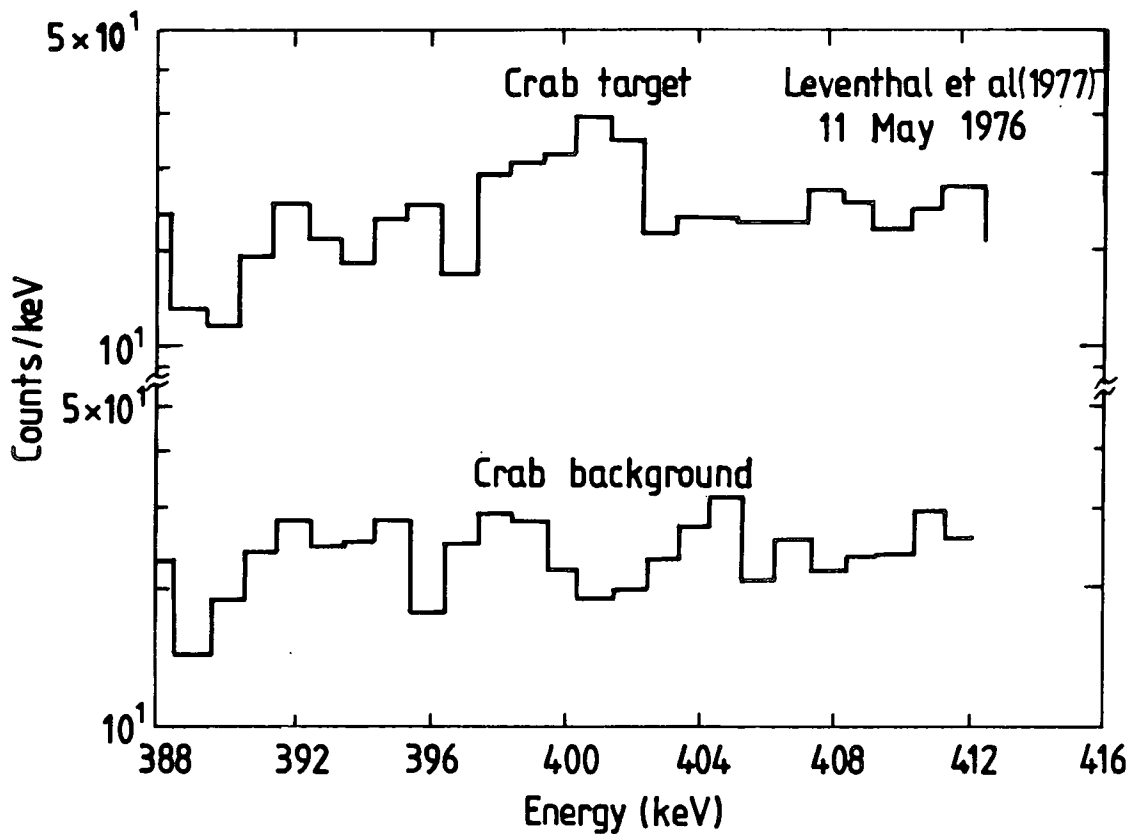
Figure 3·10 The Crab target energy spectrum in the vicinity of 400 keV. From Leventhal et al. (1977)
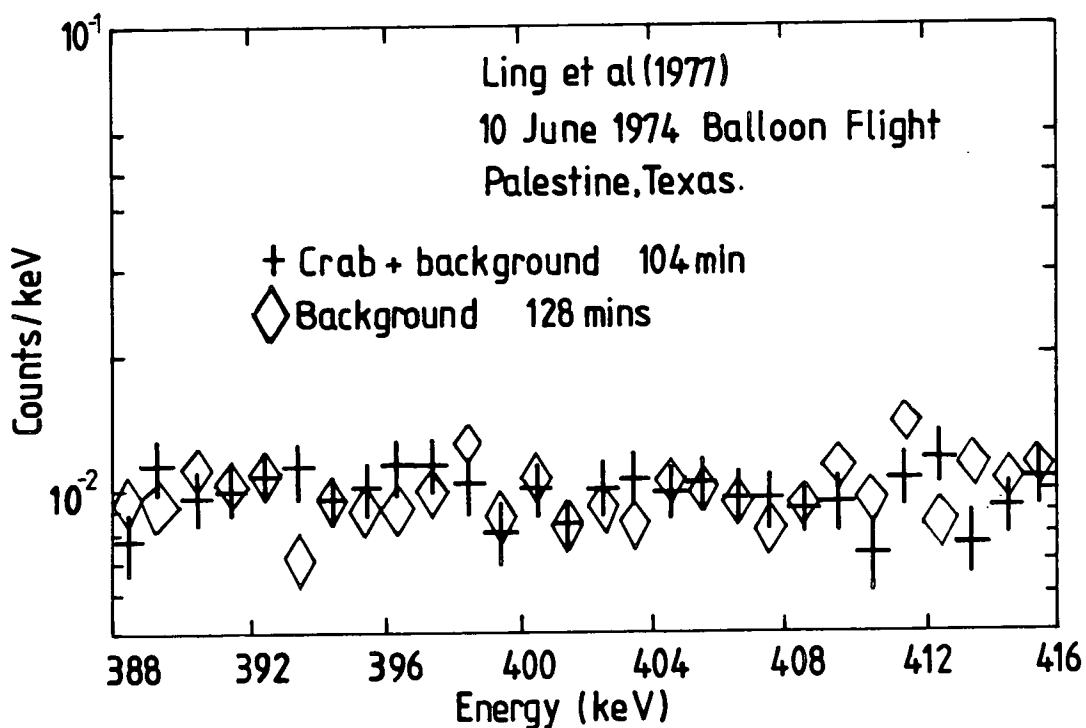
Figure 3·11 The Crab target energy spectrum in the vicinity of 400 keV. From Ling et al. (1977)

September 30 1977 and observed a flux of $(7.4 \pm 5.4) \times 10^{-3}$ photons $cm^{-2} s^{-1}$ at a centre energy of (400 ± 1) keV.

Ling et al. (1977) observed the Crab during a balloon flight over Palestine Texas on June 10th 1974. The instrument consisted of a cluster of four Ge(Li) detectors with a combined volume of 180 cm^3. The detectors were surrounded by a CsI(Na) scintillation shield of thickness 6.4 cm defining a solid angle of 0.2 sr. The spectral resolution of the Ge(Li) cluster was 2.9 keV at 1.33 MeV. In viewing sources with this instrument the telescope viewing axis was kept at a fixed altitude and azimuth and thus the Crab Nebula made a transit of the field of view. In this way source and background observations were made under identical (or nearly identical) conditions, unlike the observational technique used by the Bell/Sandia and Rice University groups. Spectra were accumulated for about 100 minutes during the Crab's transit and for about 130 minutes before and after the transit for background data. Figure 3.9 shows the measured differential spectrum they obtained. A 3.9σ signal should have been measured in their Crab spectra for the 400 keV line flux reported by Leventhal et al. (1977). Instead Ling et al. (1977) deduced a 3σ upper limit of 1.75 $\times 10^{-3}$ photons $cm^{-2} s^{-1}$. Figure 3.11 shows the spectrum obtained in the region of 400 keV. As the two observations were separated by 2 years, Ling et al. were careful not to rule out the possibility that the reported feature could vary with time. Earlier experiments (for example Walraven et al., 1975) had also produced a negative result even though they had had the required sensitivity to observe at least a 2σ effect.

Ling et al. also found evidence for a spectral feature at 73.3 keV with a line flux above the continuum of $(3.8 \pm 0.86) \times$

10^{-3} photons cm^{-2} s^{-1} and a width of 2.5 keV FWHM. The total Crab spectrum in the region 50 to 300 keV observed by Ling et al. is shown in Figure 3.12. The excess counts in the line represent a 3.8σ effect over the continuum. Jacobson (1977) suggests that this line may be produced by the decay of transbismuth elements in the Crab Nebula or cyclotron radiation in the strong magnetic field at the polar cap of the Crab pulsar, as proposed by Trumper et al. (1978) in the case of line emission from Hercules X1. If the 73 keV line is interpreted as the first harmonic, and is redshifted by 20%, then the magnetic field strength would be 8 x 10^{12} gauss over the emitting region.

Several efforts were made to observe this line and apparent confirmation was provided by Strickman et al. (1982). Using data from a balloon flight in May 1976, Strickman et al. initially reported no line feature near 73 keV from the Crab Nebula or its pulsar, however further analysis revealed flaring line emission from the pulsar at a centre energy of (76.6 $\pm$ 2.5) keV. The detector consists of an actively shielded 5 mm thick NaI(Tℓ) crystal of energy resolution 24% FWHM at 60 keV and a field of veiw of 10° FWHM. The 77 keV line was detected only during the first 25 minutes of a 3 hour observation with a phase averaged flux at the top of the atmosphere of (3.0 $\pm$ 0.9) x 10^{-3} photons cm^{-2} s^{-1} and a line width of (8 $\pm$ 18) keV FWHM. A second confirmation of this line was reported by Manchanda et al. (1982). They report an unpulsed line feature centred around 73 keV with an intensity at the top of the atmosphere of (5.8 $\pm$ 1.5) x 10^{-3} photons cm^{-2} s^{-1} and a width less than 4 keV. This experiment was carried out using two balloon borne multiwire, high pressure xenon proportional counters flown from Sicily on August 26 1979. The
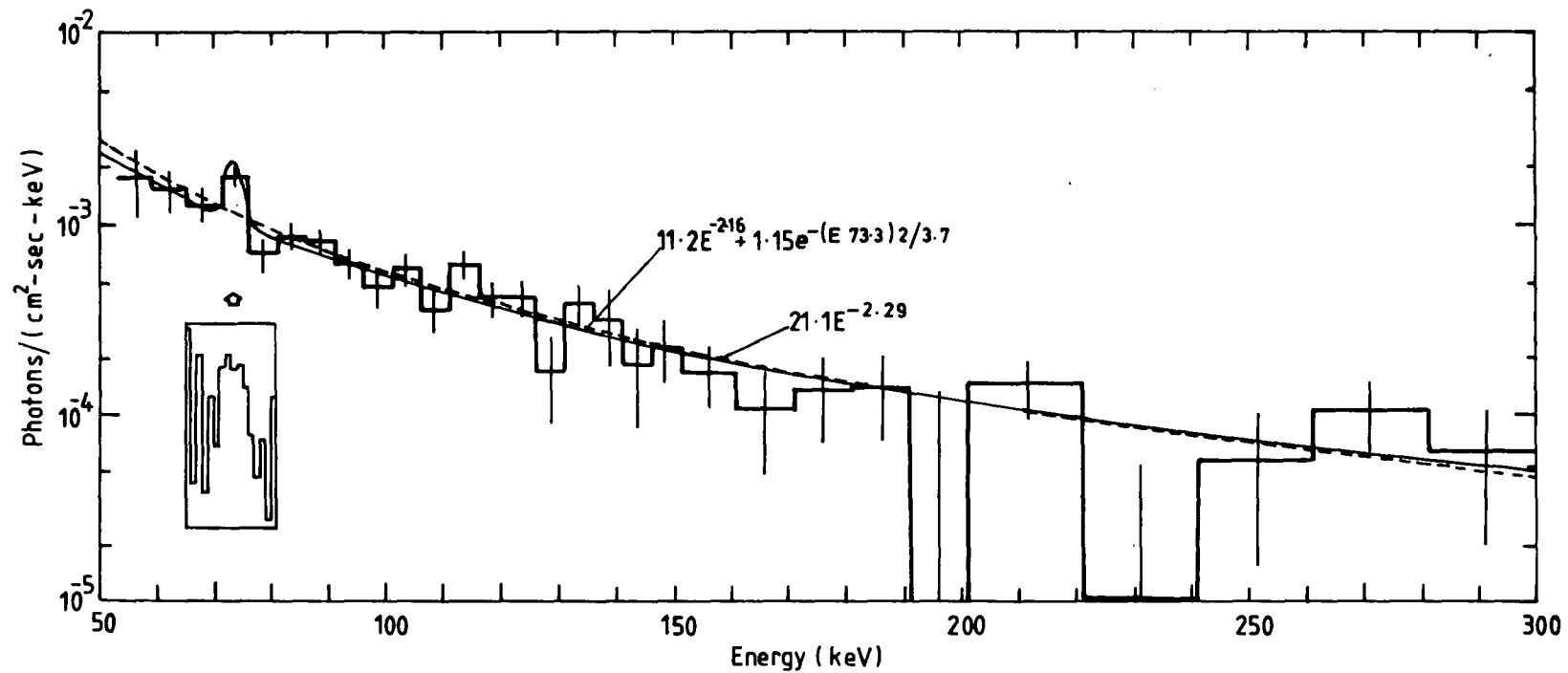
Figure 3·12 The net photon spectrum from the Crab Nebula in the energy range 50keV to 300keV, measured on June 10, 1974. From Ling et al. (1979).

fields of veiw defined by these detectors were 7.5° x 7.5° and 5° x 5° FWHM. The Crab was observed in the energy range 20 to 150 keV in a single transit scan from 0524 UT to 0624 UT yielding a total of 30 minutes of usable data. A search to detect pulsations of the 73 keV line failed, primarily due to poor statistics and timing uncertainties.

On the other hand, there have been several observations of the Crab during which no line emission near 73 or 400 keV was detected. During a balloon flight on October 17 to 18 1979, Schwartz et al. (1980) observed the Crab with an array of planar germanium detectors. They saw no evidence for line emission in the energy range 30 to 300 keV and were able to place a 3σ upper limit of 2 x 10^{-3} photons cm^{-2} s^{-1} on any feature near 73 keV. Hameury et al. (1983) observed the Crab using the LEGS high resolution spectrometer on a balloon flight on September 25 1980. The reported 3σ upper limits on unpulsed emission at 73 and 400 keV are 6.2 x 10^{-3} and 1.7 x 10^{-3} photons cm^{-2} s^{-1} respectively. While they quote no upper limits, there is no evidence for line emission in the published gamma-ray spectrum obtained by the HEAO 1 satellite detector (Knight, 1982) during the observation periods, 24-25 March and 28-29 September 1978. Similarly the HEAO 3 satellite reported a null result from observations during the fall of 1979 and the spring of 1980 (Mahoney et al., 1984). The reported 3σ upper limits for phase averaged narrow line emission at 73 and 400 keV are 2.8 x 10^{-4} and 1.8 x 10^{-4} photons cm^{-2} s^{-1} respectively. It should be noted however that their data corresponds to 2 day integrations over both observation periods and, as Mahoney et al. point out, a line flaring on a time scale of 25 minutes would not have been detected. Finally Hasinger et

al. (1981) observed the Crab on September 28 1980 with a balloon borne scintillation detector and deduced a 2σ upper limit on narrow line emission at 77 keV of 1.9 x 10^{-3} photons cm^{-2} s^{-1}. A summary of the observations made to date is given in Table 3.1.

3.2.6 LINES FROM HERCULES X1.

Hercules X1 is a highly variable binary x-ray source exhibiting periodicities, a) 1.24 second pulsations, b) 1.7 days due to binary eclipse and c) 34.4 days of currently unknown origin. Many observations of the continuum spectrum have been made in the keV range and a summary of the results prior to 1976 can be found in Manchanda (1977).

Recently gamma-ray line observations were reported by the Max Planck Institute group (Trumper et al., 1976). The instrument used had an effective area of 107 cm^2 and an energy resolution of 23% FWHM at 60 keV. The main detector consisted of 4 phoswich detectors, 5.7 x 5.7 cm^2 in area, collimated by an outer active plastic anticoincidence shield and an inner lattice of passive lead shielding. In total, 4 balloon flights from Palestine, Texas were undertaken in which pointed observations of Her X1 were performed for typically a few hours duration each. The first of these flights was on May 3 1976 (5 days after turn on of the 35 day cycle; binary phase 0.77). A total of 4 hours source and background measurements were obtained. From the data they found that the heliocentric pulsation period of Her X1 was 1.24 seconds, and for ease of analysis, the count rates of each energy channel during this period were folded into 40 separate bins. The spectrum was subsequently obtained by subtracting the background

TABLE 3.1 Reported spectral line observations from the Crab Nebula.
All upper limits are at the 3σ level.

OBSERVER	DATE	73 - 80 keV Photons $cm^{-2}s^{-1}$	400 - 405 keV Photons $cm^{-2}s^{-1}$
Ling et al. (1979)	10 June 1974	$(3.8 \pm 0.9) \times 10^{-3}$	$< 1.7 \times 10^{-3}$
Leventhal et al. (1977)	10 May 1976	-	$(2.2 \pm 0.9) \times 10^{-3}$
Strickman et al. (1982)	11 May 1976	$(3.0 \pm 0.9) \times 10^{-3}$	-
Yoshimori et al. (1979)	30 Sept. 1977	-	$(7.4 \pm 5.4) \times 10^{-3}$
Knight (1980)	29 March 1978 } 29 Sept. 1878	$< 1.0 \times 10^{-3}$	-
Manchanda et al. (1982)	26 Aug. 1979	$(5.0 \pm 1.5) \times 10^{-3}$	-
Mahoney et al. (1984)	23 Sept. to 10 Oct. 1979 and 24 Feb. to 4 April 1980	$< 2.8 \times 10^{-4}$	$< 1.8 \times 10^{-4}$
Schwartz et al. (1980)	17 Oct. 1979	$< 2.0 \times 10^{-3}$	-
Hameury et al. (1983)	25 Sept. 1980	$< 6.2 \times 10^{-4}$	-
Ayre et al. (1983)	6 June 1981	$(1.1 \pm 0.3) \times 10^{-2}$	$(7.2 \pm 2.1) \times 10^{-3}$
Hasinger et al. (1981)	28 Sept. 1981	$< 2.9 \times 10^{-3}$	-

counts from the counts in a 10 bin wide phase interval around the pulse maximum of the 1.24 s period. The results shown in Figure 3.13 show clear enhancements at 58 keV and 110 keV. A Gaussian line fitted to these points yeilded peak energies at (58 ± 5) keV and (110.6 ± 10) keV with intensities of $(3.0^{+3.0}_{})$ x 10^{-3} and (1.4 ± 0.6) x 10^{-3} photons cm^{-2} s^{-1} respectively. Since it is difficult to explain a 58 keV line by atomic or nuclear emission due to energy and intensity reasons, Trumper et al. (1977) believe the most likely interpretation to be in terms of a cyclotron emission line which has been predicted to occur in the x-ray spectra of binary neutron stars by Gnedin and Sunyaev (1974) and Basco and Sunyaev (1975). If the 58 keV line is the first harmonic then the corresponding magnetic field strength is 5.3 x 10^{12} gauss. Consequently the second harmonic should appear at 110.7 keV which is very close to the energy where the second enhancement is observed. In September and October, Trumper et al. (1978) flew an improved detector from Palestine, Texas. The four main phoswich detectors were increased in size by a factor of 6.5 to give an effective area of 730 cm^2. The energy resolution was marginally better at 21% FWHM at 60 keV. The flights covered three interesting phases of the Her X1 35 day cycle:

> September 3 1977 on state   (phase 0.12)
>
> September 20 1977 short on state (phase 0.61)
>
> October 18   1977 off state   (phase 0.41)

The phases are measured with respect to 'turn on'. The pulsed spectrum was derived from the light curve in the same way as before. Voges et al. (1979) found that there were two major differences from the May 3 1976 results. Firstly the continuum and 58 keV line fluxes were approximately a factor of 2 lower than
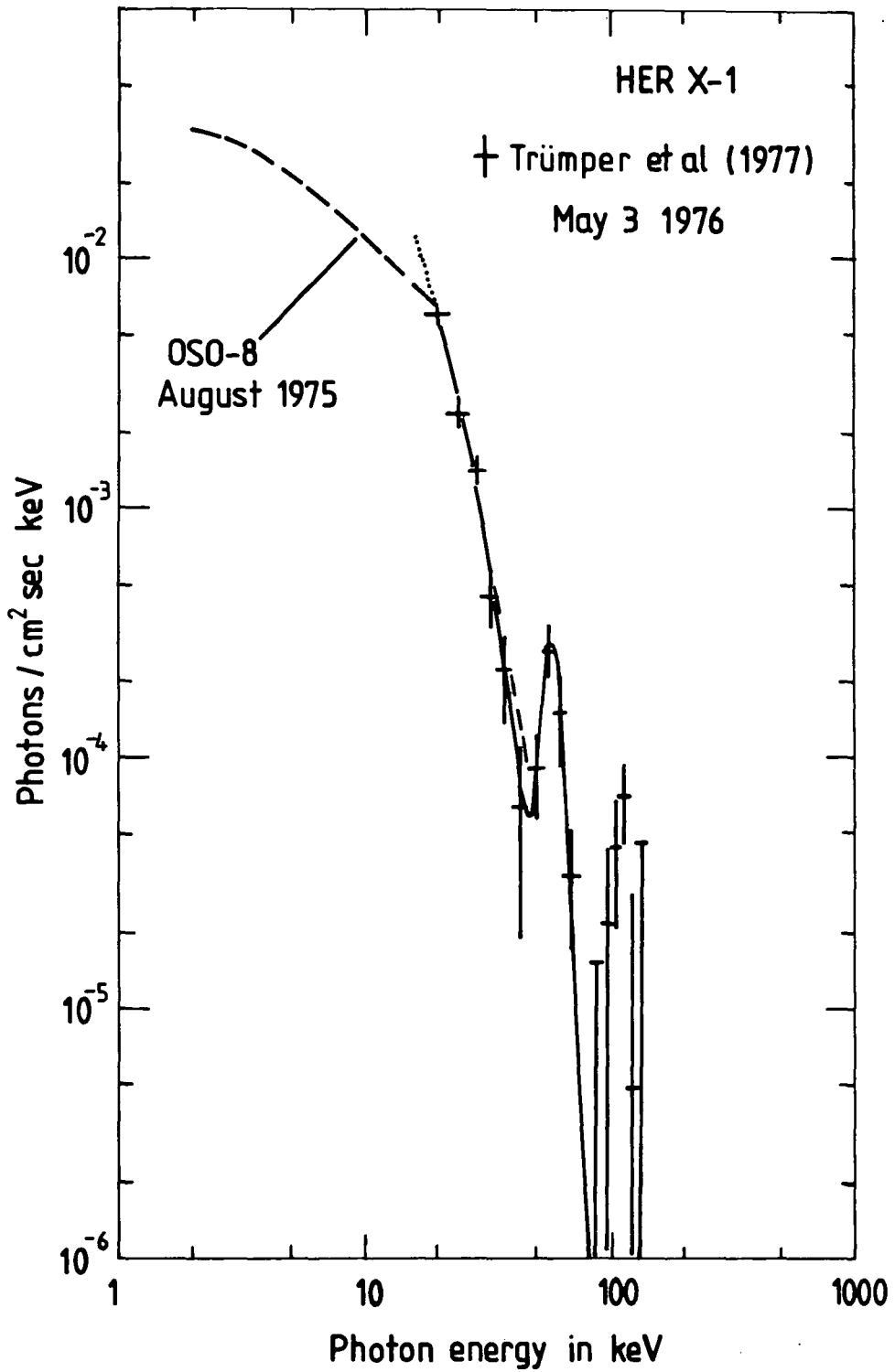
Figure 3·13 Pulsed spectrum derived from the May 3 ,1976 flight, (Trümper et al,1977)

at the beginning of the May 3 1976 flight, and secondly they were unable to detect the second harmonic at 110 keV. By fitting a Gaussian profile to the feature at 58 keV the measured line energy was found to be 55.4 keV with an intensity of (1.1 ± 0.1) x 10^{-3} photons cm^{-2} s^{-1}.

Coe et al. (1977) observed Her X1 with an alkali-halide detector onboard the Ariel 5 satellite during the on period, February 3 to 13 1977. The instrument covered the energy range 26 keV to 1.2 MeV and consisted of an actively shielded CsI(Na) crystal. Her X1 was observed for two days on the rising side of the light curve and 4 days on the falling side. Since the data had a time resolution of 8 minutes only a time averaged spectrum could be obtained. Data from both epochs were summed to obtain the best statistics and the resulting pulse height spectrum shows a significant flux excess in the 56 to 94 keV region. Coe et al. (1977) have determined the peak energy to be (64 ± 6) keV with an intensity of (1.7 ± 0.7) x 10^{-2} photons cm^{-2} s^{-1}. Although the line energy agrees with that derived by Voges et al. (1979), the flux is a factor of 10 times higher. The authors offer no explanation. Later observations by the HEAO 1 satellite during 3 days in Febuary 1978 provide confirmation of these results and show evidence for variations of both the continuum and line fluxes by a factor of 2 on time scales of one day (Matterson et al., 1978).

The only observations using a high resolution spectrometer occurred on September 24 1980 during a balloon flight of the LEGS detector (Tueller et al., 1981). The observations took place when the source was near the maximum of its 35 day cycle. No narrow lines were observed in the spectrum and a 3σ upper limit of 2.2 x

10^{-4} photons cm^{-2} s^{-1} was given for line emission in the region 50 to 60 keV. The pulsed continuum flux could not be well fitted by a simple power law or thermal spectrum. Acceptable fits were only obtained with a thermal spectrum plus either a 43.9 keV emission line or a 34.8 keV absorption line. The line energies are systematically lower than that suggested by previous experiments indicating variability in energy as well as intensity. The width of these features are typically 13 keV and so they are clearly resolved by this instrument (FWHM $\simeq$ 2 keV). It is interesting to note that the addition of a second emission line at (62 ± 2) keV provides a substantial improvement to the fit and is noteworthy in that the second emission line is consistent in energy with the lines reported previously by Trumper et al. (1977) and Coe et al. (1977) but is a factor of 5 less intense. Tueller et al. (1981) conclude that either the line feature is variable in energy or there exist two features in the emission spectrum both variable in intensity.

3.2.7 TRANSIENT GAMMA-RAY LINES.

Temporal variability is a common property of a large fraction of the astronomical sources of high energy radiation. In fact with the possible exception of the diffuse nucleosynthesis lines (Mahoney et al., 1984) all gamma-ray lines detected to date exhibit some degree of variability on time scales ranging from a few seconds to 6 months. In this section we consider those events which do not appear to originate from any indentifiable source. The most common class of these transients, known as gamma-ray bursts, are impulsive and persist for times ranging from

a fraction of a second to a few minutes. The observed
distribution of the number of bursts as a function of apparent
luminosity (log N versus log S) favours a galactic origin for the
bulk of these events (Fishman et al., 1978; Jennings and White,
1980), but it is not clear what population or populations of
galactic objects are responsible for them. The principle
continuum emission processes are also unclear in view of the lack
of knowledge of the precise nature of the sources, and
bremsstrahlung, Comptonisation or gyrosynchrotron radiation have
all been suggested (Lingenfelter et al. 1982, and references
therein). Recently, emission lines and absorbtion features have
been detected in their energy spectra (see Teegarden, 1982 for
review). The absorption features, observed at energies < 100 keV
(Mazets et al., 1981), are probably due to cyclotron absorption in
an intense magnetic field of order 10^{12} gauss, which in turn
suggests a neutron star origin. The most commonly observed
emission line lies in the energy range 400 to 470 keV as observed
by Mazets et al. (1980) in 7 gamma-ray bursts. This is generally
interpreted as gravitationally redshifted annihilation radiation
which again suggests a neutron star origin.

There is apparently another class of gamma-ray transients in
which essentially all the observed radiation is in the form of
lines. Such an event was observed with a balloon borne Ge(li)
detector on June 10 1974 (Jacobson et al., 1978). The JPL
experiment was intended to study line emissions from the Crab
Nebula and this aspect has been discussed in a previous section.
Near the end of the flight, a transient burst was recorded which
lasted for 20 minutes and was characterised by strong emission in
four relatively narrow energy bands, or lines, with no detectable

continuum. Figure 3.14 shows the spectra obtained in 3 energy intervals containing the four lines during the time interval for which the transient source was present (2020 UT to 2041 UT). The average background spectra based on earlier and later intervals are also shown for comparison. Table 3.2 lists the centroid energy location of each feature, the error in its position, the approximate width and the flux intensity (Jacobson, 1977). The time intervals given are those which maximise the statistical significance of the line and can be taken as a rough measure of the onset and end of the event.

Table 3.2 Properties of the lines observed in the transient burst spectrum of June 10 1974 (from Jacobson, 1977).

| Line energy | Flux | FWHM | Time interval |
| | | | spanned |
keV	photons cm^{-2} s^{-1}	keV	UT
413.2 ± 1.8	(7.0 ± 2.0) x 10^{-3}	15	2020 - 2041
1789.7 ± 6.0	(3.2 ± 0.7) x 10^{-2}	95	2026 - 2041
2216.6 ± 6.3	(1.5 ± 0.5) x 10^{-2}	70	2020 - 2041
5946.5 ± 3.7	(1.5 ± 0.5) x 10^{-2}	25	2006 - 2041

One unique aspect of these features is that they are all much broader than the instrumental energy resolution. The belief that this is a true extraterrestrial transient event is greatly strengthened by the fact that the anticoincidence shield elements of the detector also registered simultaneous counting rate increases, corresponding to 3 to 5σ deviations on the average. Information on the direction of the source is highly uncertain and seems to lie within 20° of RA 7h and dec. 20°. Because of the
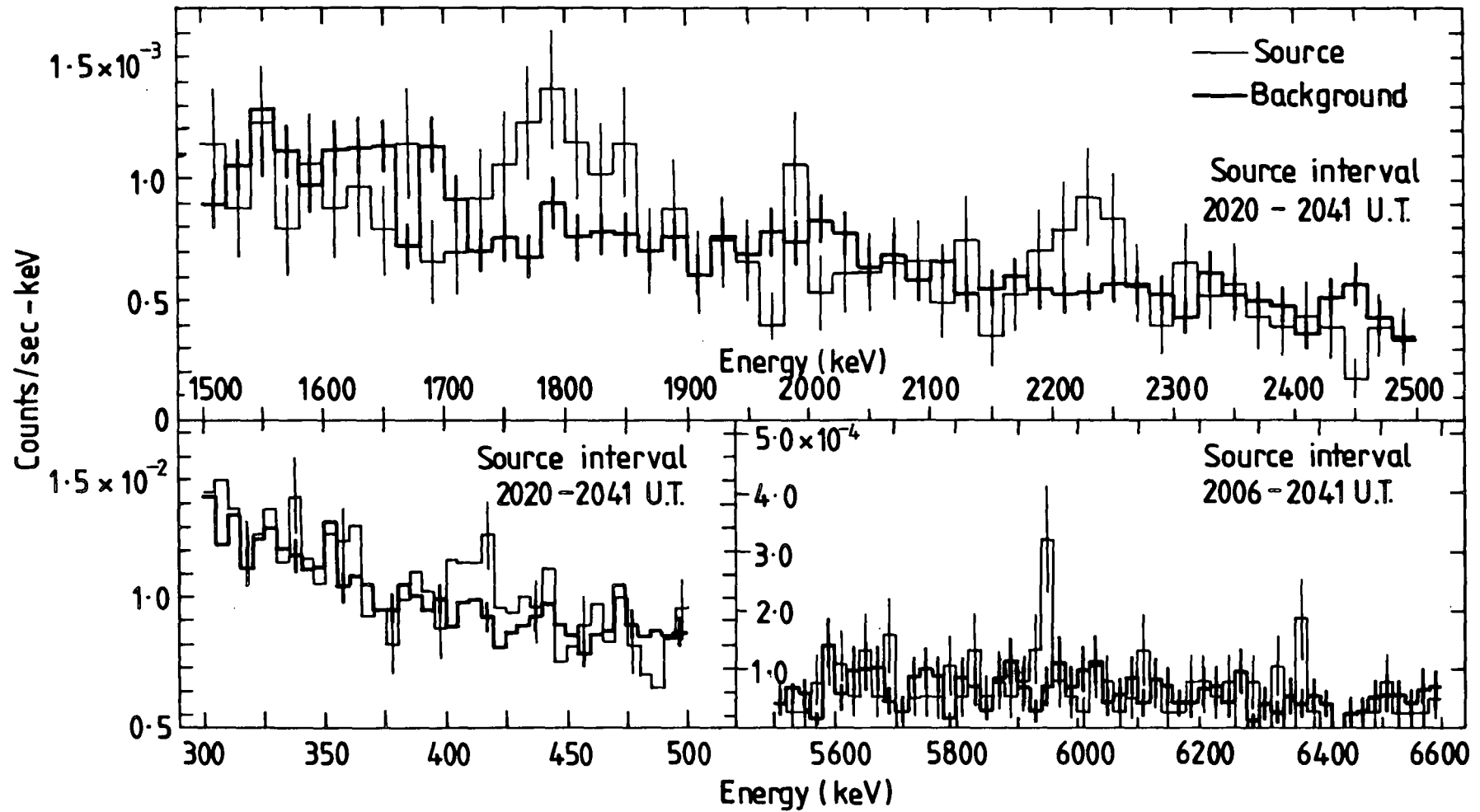
Figure 3·14 Those portions of the spectrum containing the lines measured during the transient event of June 10, 1974. From Jacobson et al. (1978).

large difference between the relative solid angles viewed by the Ge(Li) detectors and the collimator crystal, the relative count rates rule out a source extending over a solid angle greater than about 0.1 sr which again lends support to the conclusion that the source is probably extraterrestrial. Figure 3.15 shows the portion of the sky viewed during the event. The concentric circles represent the FWHM fields of view at the energies of the lines detected. Within this field of view are the planets Mercury and Saturn, the SN remnant 1C443 and the pulsar PSR0611+22 which may be associated with it, and the high energy COS B source CG195+5. At the edge of the field are the Crab Nebula and the Sun. The numbered dots represent stars less than 6 pc from the Earth.

There are no simple nuclear schemes that can account for all four lines. The line at 1790 keV is within 1.8σ of the most prominate line of $^{28}Si^{\star}$ and 3.2σ from that of $^{26}Mg^{\star}$. The 2220 keV line is less than 1σ from the Deuterium formation line. There are no such obvious associations for the remaining two lines. Lingenfelter et al. (1978) have suggested that the observed lines could result from episodic accretion onto a neutron star from a binary companion. The observations could then be understood in terms of neutron capture and positron annihilation, which are also the dominant production mechanisms in solar flares. If the 1.79 MeV line was considered to be a redshifted component of the 2.22 MeV line (and both were emitted in the source region) then the resulting redshift of 0.28 would shift the 511 keV positron annihilation line to within 1σ of the observed line at 413 keV. This redshift factor is typical of a neutron star of 1.5 $M_{\odot}$. The unshifted 511 keV from the companion star could not have been
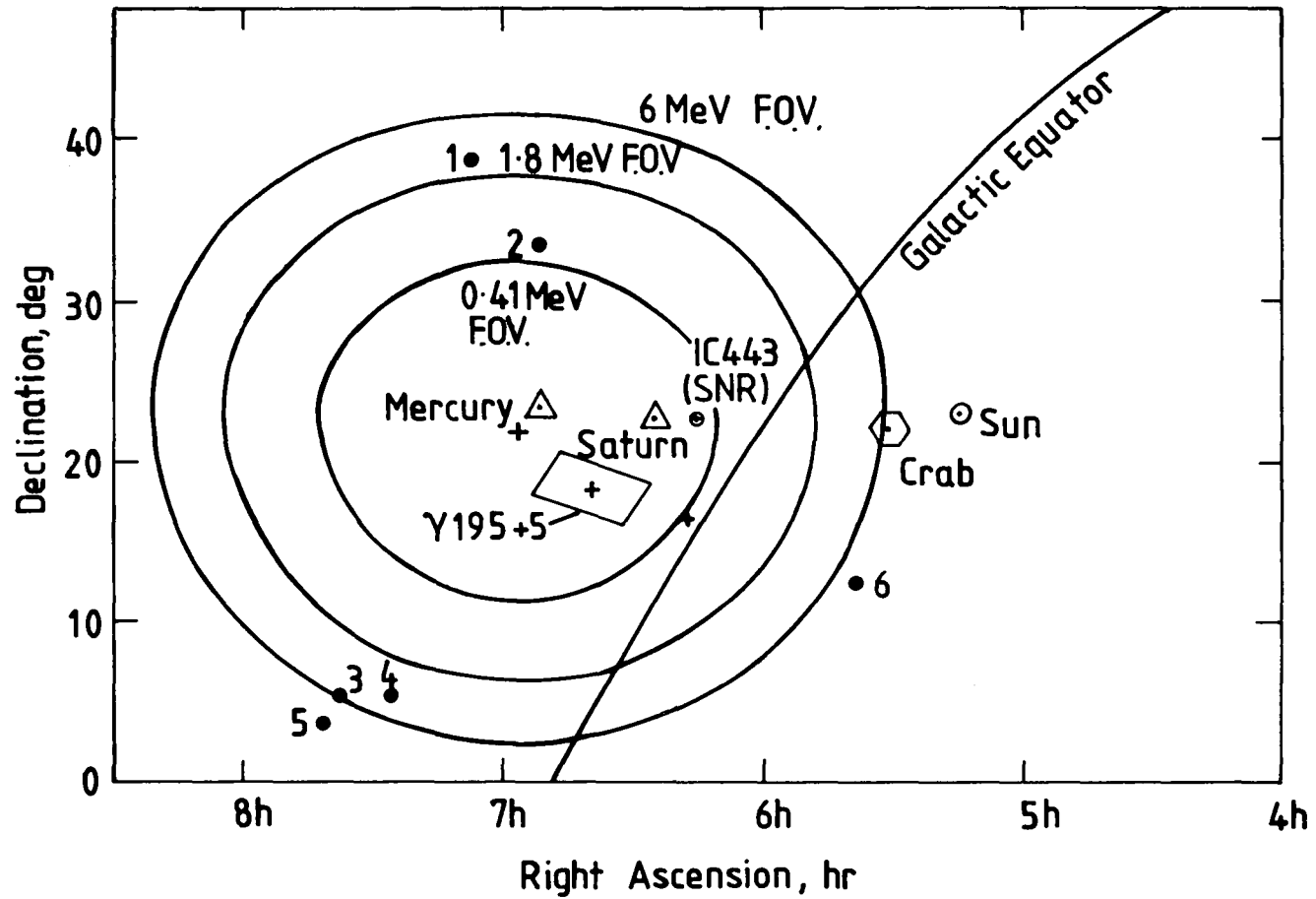
Figure 3·15 The instrument field of view at the mid-time of the transient event of June 10,1974. From Jacobson et al. (1978).

detected because of the large atmospheric and instrumental background at this energy. The 5.95 MeV line is then understood as neutron capture on iron and should be significant only in the redshifted emission from the iron crust of the neutron star.

Since the direction of the source is uncertain, Lingenfelter et al. (1978) and Vedrenne (1979) suggest that the source could be the same as the one producing the 400 keV line reported by Leventhal et al. (1977) while looking in the general direction of the Crab. If this is the case, and the source is transient, then this would explain why other groups looking at the Crab (eg Ling et al., 1977) have failed to detect line emission at 400 keV.

CHAPTER 4

THE DURHAM GAMMA-RAY SPECTROMETER

4.1 DESCRIPTION OF THE TELESCOPE.

Because of the ongoing development of the Durham gamma-ray telescope, the instrument that flew on the first flight will be referred to as the MK1 telescope and that on the second flight as the MK2 telescope. The Durham MK1 gamma-ray telescope is shown schematically in Figure 4.1 and has been described in Ayre et al. (1981a). The telescope has cylindrical symmetry about its axis and is centred around an 86 cm^3 intrinsically pure germanium crystal. Collimation and background rejection for the central detector are provided by a three piece anticoincidence shield; a 12.5 cm thick NaI(Tℓ) annulus (A2), a 12.5 cm thick NaI(Tℓ) plug (A3), and lead scintillator sandwich collimator (A1). Contained within the annulus is a polarimeter. This comprises a section of the shield close to the germanium detector, being optically isolated from the rest of the shield and divided into four quadrants (P1 to P4). The shield is at least two interaction mean free paths thick at all gamma-ray energies and complete 4π protection against data contamination by charged particles is provided by a thin sheet of plastic scintillator that covers the aperture. The geometric aperture defined by the collimator is 4.9° FWHM. The energy range of this instrument is 50 keV-10 MeV.

The telescope is orientated by an alt-azimuth steering system which is described in Appendix A.

Charged Particle Anti-Coincidence A0 (Viewed By One Photomultiplier Not Shown)

Collimator (A1) Viewed By Three Photomultipliers

12cm

Scintillator

Lead

Viewing Window

5cm

Supports To Outer Frame

55·4cm

85·5cm

NaI(Tl) Annulus (A2) Viewed By Four Photomultipliers

12·5cm

30cm

NaI(Tl) Polarimeter (P₁-P₄) Each Viewed By One Photomultiplier

86cm³ Ge

NaI(Tl) Plug (A3) Viewed By Three Photomultipliers

12cm

Scale

10cm

36cm

Figure 4.1 A sectional view of the spectrometer.

4.2 THE GERMANIUM DETECTOR.

The instrument is designed around an 86 cm^3 intrinsically pure germanium crystal (Ge(HP)) in a closed end coaxial configuration (see Figure 4.2). The detector is of conventional design being fabricated from p-type material with a deep p^+ core bottoming out at ~ 1 cm from the forward detector face. The specifications are given in Table 4.1. The difference in specifications for the MK1 and MK2 instruments are due to a cryostat vacuum leak that occurred after the first flight. The crystal is situated at the end of a cold finger 50 cm long attached to a 15L dewar containing liquid nitrogen. Under normal atmospheric pressure the liquid nitrogen consumption is 1.6 liters per day. For flight operation the pressure of the liquid nitrogen is controlled using a relative pressure relief valve set to open at a pressure of 0.4 bar. This ensures that the temperature of the nitrogen remains above - 210^OC and therefore the coolant remains in the liquid state. The bias voltage of the detector was chosen to be 3.8 kV which gave an optimum spectral resolution of 2.26 keV at 1.33 MeV and an efficiency of 23% (relative to a standard 3" NaI(Tℓ) crystal).

4.3 THE ANTICOINCIDENCE SHIELD.

The anticoincidence shield has been described briefly in Section 4.1. In this section a more detailed discussion of each shield piece will be given.
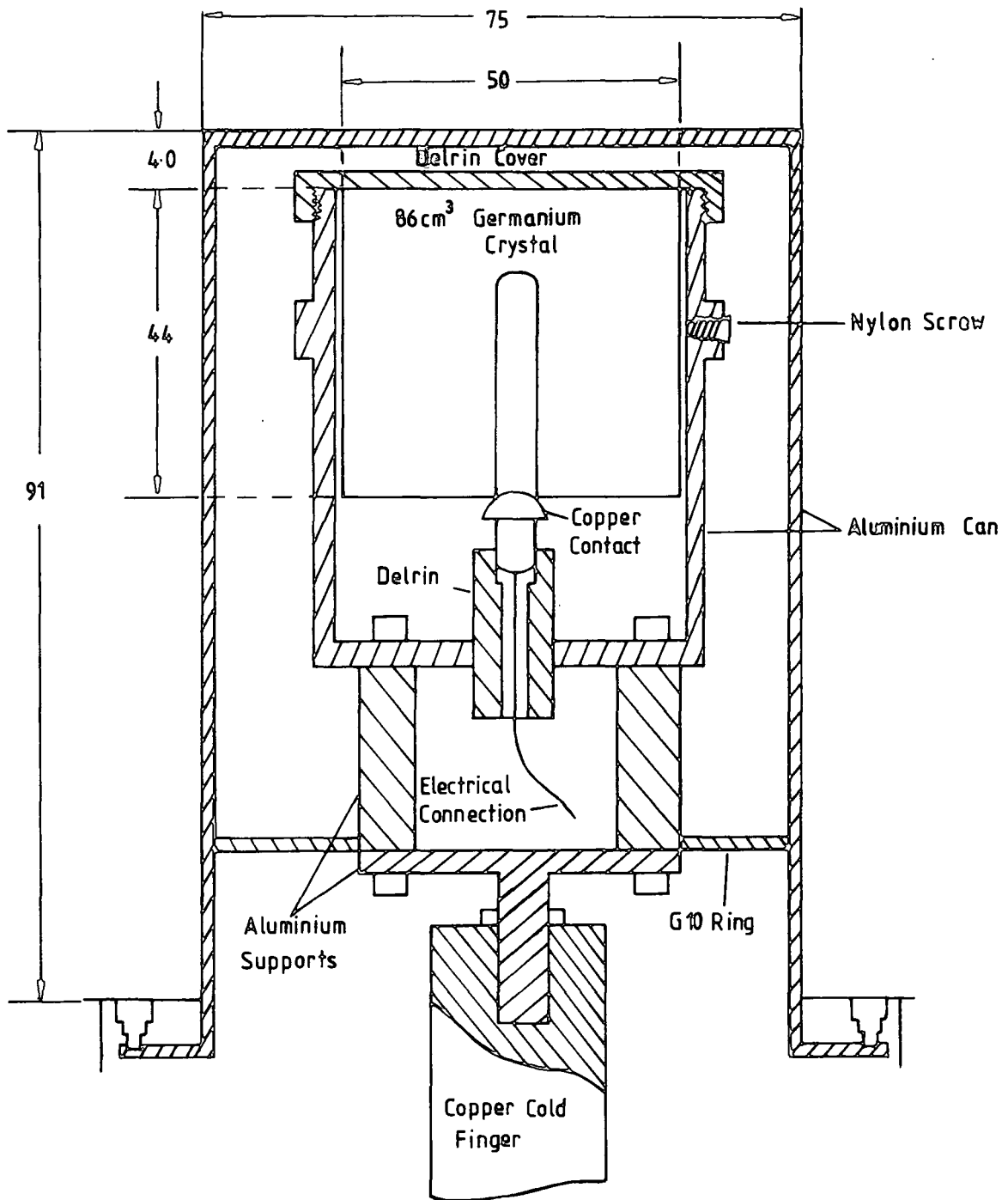
All dimensions in mm.

Figure 4.2 A cross-sectional view of the Germanium detector cryostat.

TABLE 4.1

Ge Detector Characteristics

Diameter (Physical)	50 mm	
Length (Physical)	44 mm	
Core radius	3 mm	
Core depth (from face)	10 mm	
Nominal bias	3800 V	
Leakage current at nominal bias	500 pA	(MK1)
	1500 pA	(Mk2)
Capacitance at nominal bias	20 pF	
Active Volume	61.4 cm^3	(MK1)
	72.2 cm^3	(MK2)
Dead layer thickness	665 ± 9 μm	(MK1)
	1128 ± 20 μm	(MK2)
Efficiency @ 1333 keV	8.2 %	(MK1)
	10.1%	(MK2)
Resolution @ 1333 keV	2.52 keV	

Manufactured by Princeton Gamma Tech (P.G.T.) Limited, Princeton, New Jersey, U.S.A.

4.3.1 THE CHARGED PARTICLE SHIELD.

The charged particle shield (A_o) consists of a 75 mm diameter, 3 mm thick disc of NE 102A plastic scintillator[*] which is viewed by a single 2" photomultiplier tube (EMI type 9757B[†]) through a perspex light pipe. The whole assembly is covered by aluminum foil and wrapped with black adhesive tape to prevent light reaching the photomultiplier from outside the body of the scintillator. The efficiency of the charged particle shield with respect to the detection of charged particles was measured using cosmic ray muons and was in excess of 99%. Using IAEA standard gamma-ray sources the transmission of the scintillator was found to vary from 94% at 50 keV to 96% at 100 keV.

4.3.2 THE ANNULUS AND THE PLUG.

Both the annulus and the plug were made to order by Harshaw Chemie[®] and are shown diagrammatically in Figures 4.3 and 4.4. The annulus is a 30 cm diameter right circular cylinder of NaI(Tℓ) with a 5 cm hole drilled axially through it to define the aperture. The bottom face is rebored to a depth of 11.5 cm to allow the insertion of the germanium cryostat within the shield. The plug is also a 30 cm diameter right circular cylinder of NaI(Tℓ) and has a 14 mm recess bored axially in the top face to accommodate the bottom of the germanium cryostat. NaI(Tℓ) was chosen from the available phosphors as it has a very high luminescent efficiency and exhibits no self absorption of its scintillation light, making it possible to use it in very large volumes. Because NaI(Tℓ) is very hygroscopic, both crystals are

[*] Manufactured by Nuclear Enterprises Ltd., Edinburgh, U.K.
[+] Manufactured by E.M.I Ltd., London, U.K.
[®] Harshaw Chemie BV, Stnijkvientel 67, DeMeeon, Holland.

WINDOW CENTRES on CIRCLE dia. 180

ϕ360
180
ϕ50
ϕ67

WINDOW
OPTICAL INTERFACE

A-B

BODY of ALUMINIUM
300 dia. x 300 hgt
Na(TL) CRYSTAL

REFLECTOR

180 dia. x 92 hgt. Na(TL)
CENTRE CRYSTAL DIVIDED
IN FOUR EQUAL SECTORS

OPTICAL INTERFACE
WINDOW

ϕ310
325
115
20
20
25
ϕ76
ϕ96
145
ϕ360

12 EQ. SPACED M6 TAPPED
THRU HOLES ON 345 P.C.D.
IN TOP AND BOTTOM FLANGES

REFLECTOR
ALUMINIUM PARTITION

ALL DIMENSIONS IN MM

Figure 4.3 The A2 annular crystal assembly.

300 dia x 120 hgt
NaI(TL) CRYSTAL
REFLECTOR
BODY of ALUMINIUM
OPTICAL INTERFACE
WINDOW
OPTICAL COUPLING

ALL DIMENSIONS IN MM

TOP VIEW

12 EQ SPACED M6 TAPPED
THRU HOLES ON 345 P.C.D.

WINDOW CENTRES on
CIRCLE dia. 150
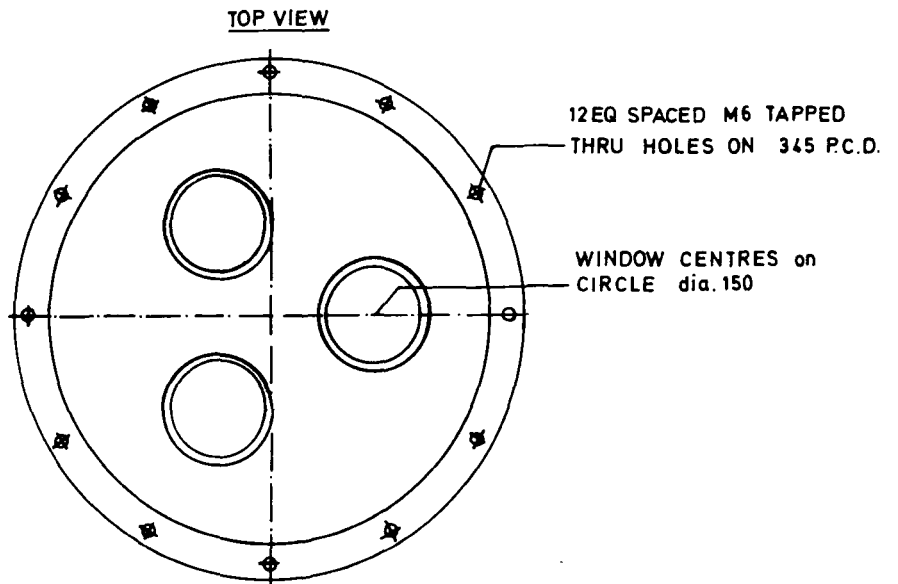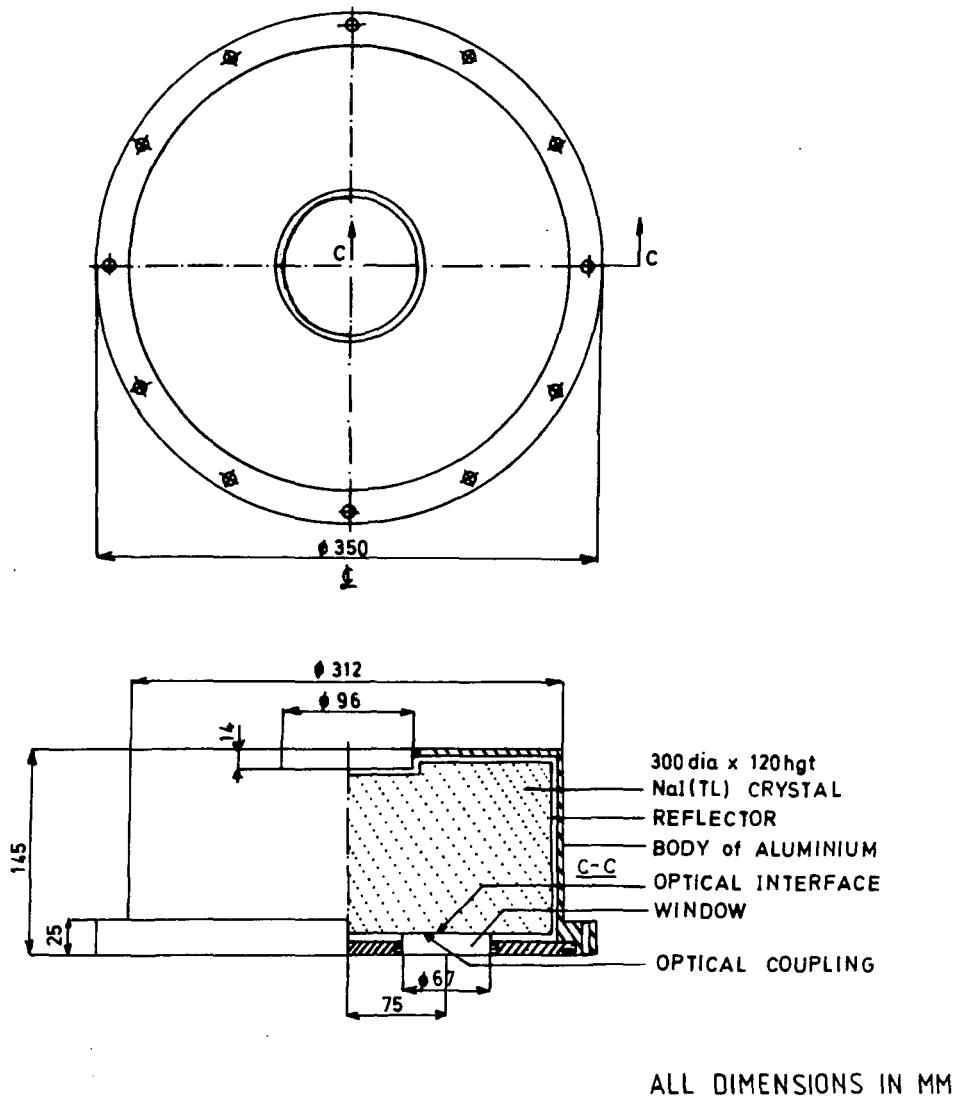
Figure 4.4 The A3 crystal assembly.
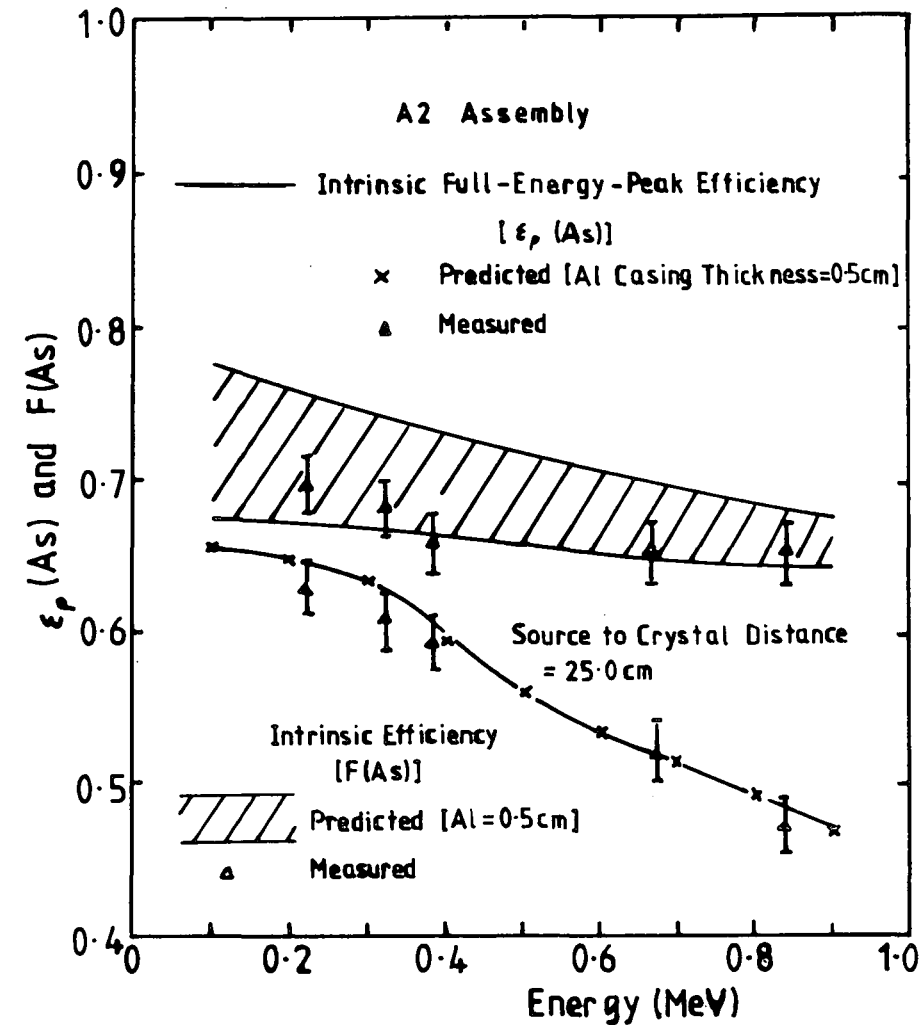
Figure 4.5   Predicted and measured values of
intrinsic efficiency and intrinsic full-
energy-peak efficiency for the A2 shield
assembly as a function of source energy.
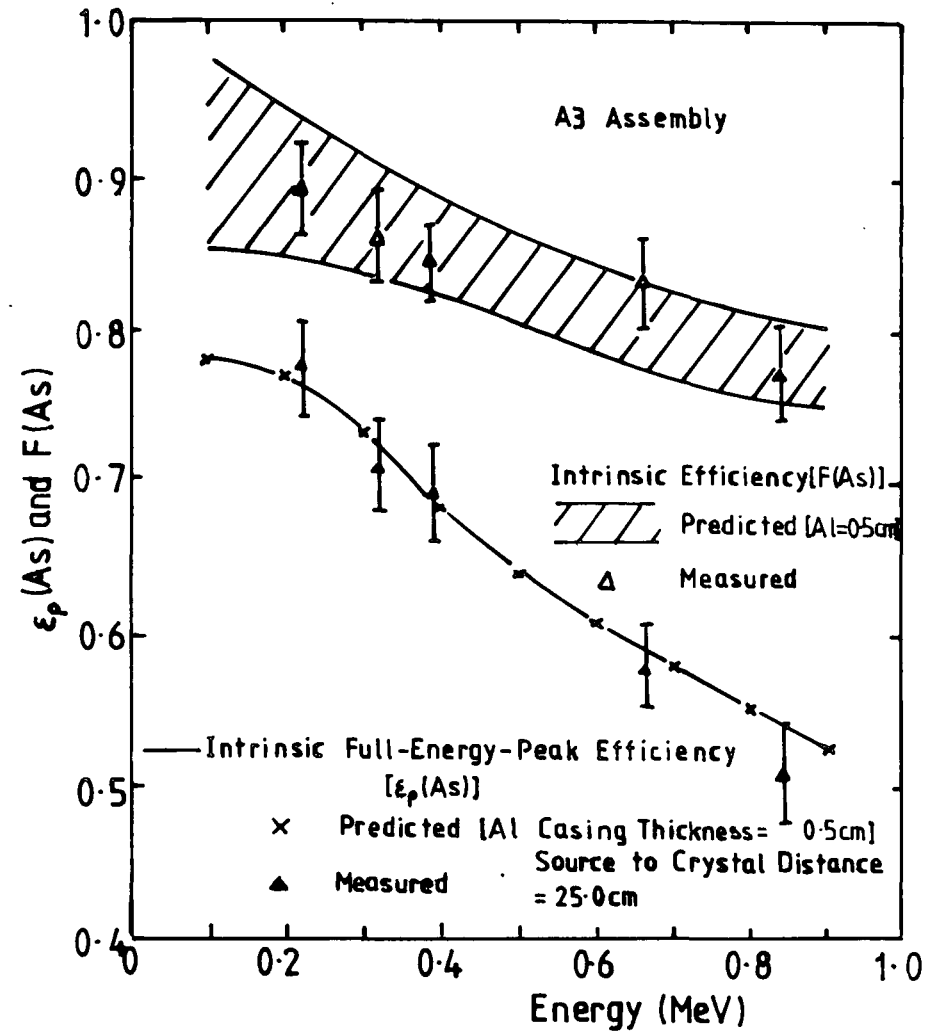
Predicted and measured values of
intrinsic efficiency and intrinsic full-
energy-peak efficiency for the A3 shield
assembly as a function of source energy.

hermetically sealed in spun aluminium housings. Flanges on the top and bottom face of the annulus and the bottom face of the plug allow the crystals to be secured to a cylindrical aluminum frame. The crystals are viewed by 3" photomultiplier tubes through quartz windows; 4 in the top face of the annulus and 3 in the bottom face of the plug. Optical coupling between the windows and the photo- tubes is achieved by using Ne 581 optical cement.[*]

The energy resolution of the plug and annulus have been measured using gamma-ray reference sources and are well represented by the expression,

$$\Delta E(\%) = 12.74 \; E^{-0.33} \qquad\qquad (4.1)$$

The intrinsic detection and full energy peak efficiencies are shown as a function of energy in Figure 4.5. Note that these measurements represent the crystal's response to an isotropic point source. The efficiency of the annulus/plug system in suppressing Compton events scattered from the germanium crystal has been evaluated to be ~90% over the energy range 50 keV to 3 MeV.

4.3.3 THE COLLIMATOR.

The collimator (Al) used in the MK1 telescope was a lead scintillator sandwich. It consisted of alternate circular discs of leads and plastic scintillator each 12.5 mm thick with a central hole of radius 28 mm. A cross sectional view is shown in Figure 4.1. The resolution of this collimator could not be measured as there were no resolvable peaks in its pulse height

---

[*] Nuclear Enterprises Ltd., Edinburgh, U.K.

spectrum of known gamma-ray sources, and therefore the energy range was calibrated using cosmic ray muons. This collimator was extremely efficient, attenuating approximately 100% of gamma-rays in the energy range up to 5 MeV.

The collimator used in the MK2 instrument is an annular NaI(Tℓ) crystal of diameter 22 cm and thickness 15 cm. It is viewed by three photomultiplier tubes. The geometric apertures defined by the collimators used in the MK1 and MK2 instruments are 4.96^O and 3.87^O FWHM respectively.

4.3.4 THE NEUTRON SHIELD.

In an attempt to reduce the detector background due to atmospheric neutrons, the MK2 telescope included a neutron jacket approximately 1 cm thick which surrounded the anticoincidence shield. The jacket contained a mixture of boron, tungsten and lithium compounds, chosen for their high neutron absorption cross sections, set in a wax moderator. The compounds and proportions used were as follows; boric acid (15-20 g/kg), tungsten oxide (20-25 g/kg) and lithium carbonate (20-25 g/kg). The shielding efficiency extends over thermal and epithermal neutron energies.

4.4 THE POLARIMETER.

There is a strong possibility that cosmic gamma-ray production often leads to polarized photons. For this reason a polarimeter is included in the telescope. It comprises a section of the annulus close to the Ge detector being optically isolated from the annulus and divided into four quadrants (P1 to P4). This

is shown in Figures 4.1 and 4.3. Each quadrant has two 2.5 cm diameter quartz viewing windows located in the bottom face of the annulus. Two perspex light pipes transfer the light to a single 2" photomultiplier tube (EMI type 9757B). Optical coupling between the viewing window, perspex and photo-tube window interfaces is achieved by using NE 581 optical cement. The photomultiplier tube assemblies are then held rigidly by an aluminum outer frame. The resolution of each segment of the polarimeter is estimated to be 25% at 662 keV.

4.5 THE ELECTRONICS.

The electronics systems, consisting of power supplies, data processing, telemetry systems, and servo system electronics are for the most part designed around low power military specification CMOS or TTL integrated circuits. Two N.I.M. (Nuclear Instrument Module) bins hold all the analogue and digital electronics associated with the detectors and the housekeeping, and a Cinch plug in card unit holds the electronics for the telemetry interface and the alt-azimuth steering system. Figure 4.6 shows a functional block diagram of the detector electronics, data handling and auxiliary sensor systems.

4.5.1 THE ANALOGUE CIRCUITRY.

The analogue circuitry was largely designed around discrete components as commercially available operational amplifiers do not have the required bandwidth. The main design requirements were low power consumption, fast rise time (<50 ns), good linearity
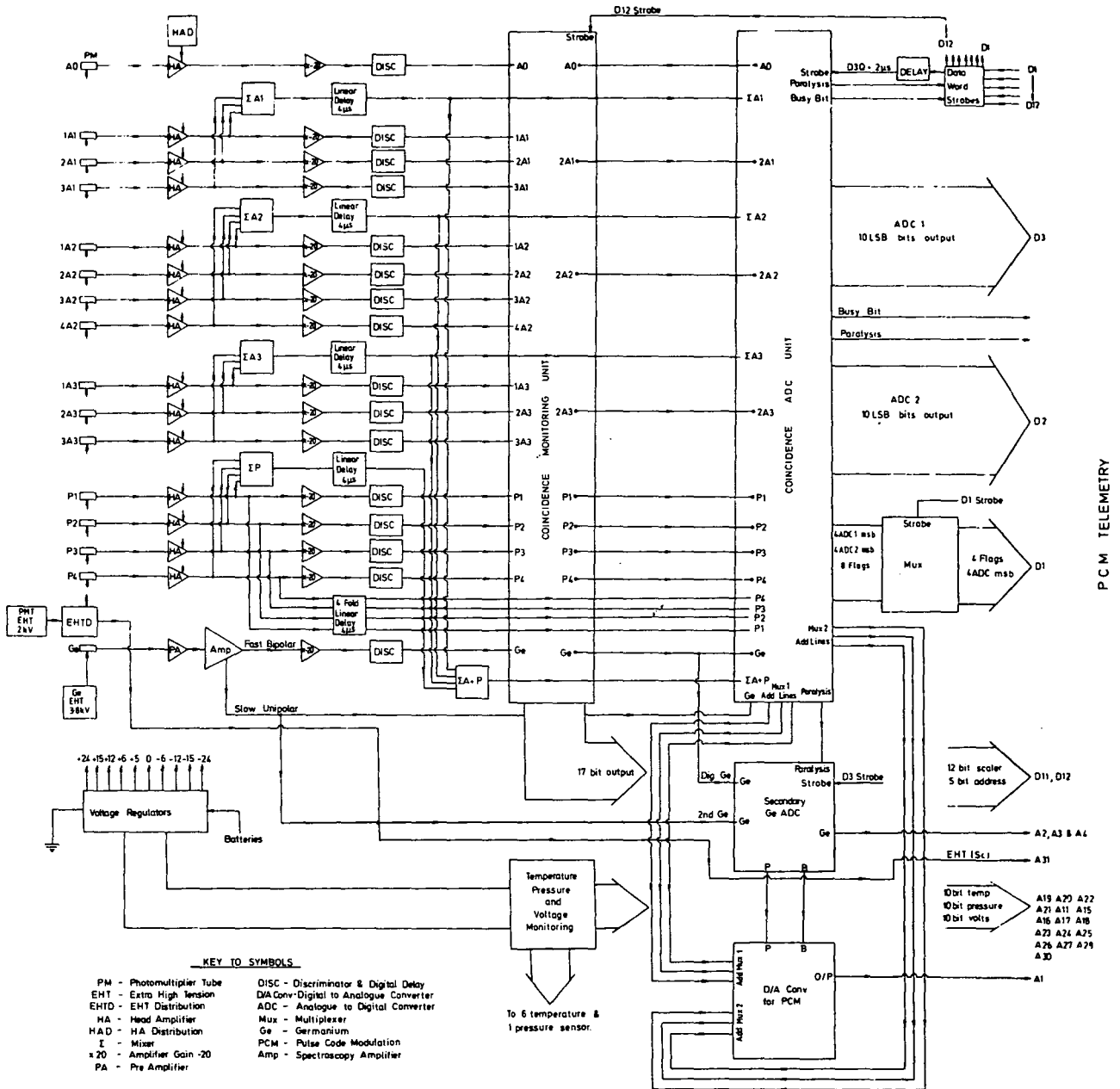
Figure 4.6 The detector electronics, data handling and
auxiliary sensor systems.

(<0.1%), stability (<0.1%), and simplicity (to keep the overall systems bandwidth high).

Pulses from each photomultiplier tube on the shield elements are buffered with a unity gain inverting head amplifier providing a high input impedance (and therefore minimum loading on the photomultiplier anode) and a low output impedance in order to drive 1 m of coaxial cable and the subsequent electronics. The output pulses are then amplified by a high gain inverting amplifier (X-20) so that a reasonable threshold may be set on the discriminators (-1V). This means that the overall threshold is 50 mV or in energy units 50 keV. The discriminator output pulses are standard TTL logic levels and are delayed before being fed to the digital electronics. The analogue head amplifier outputs for each shield element (A1, A2, A3, P) are summed and delayed by 4 µs. These outputs are then available for analysis by the ADC system, along with the germanium analogue output. The analogue and digital delays in the mixers and discriminators respectively are necessary in order that the output pulses arrive at the ADC unit in the correct sequence for analysis.

The overall bandwidth of the analogue stages is 7.5 MHz which is more than adequate to cope with the maximum expected rate from the detectors. The noise voltage at the discriminator inputs is 3 mV r.m.s. at $23^{O}C$ which is much less than the threshold level of 1 volt. The r.m.s. noise voltage at the input of the ADC has been measured to be 0.2 mV at $23^{O}C$ which is less than the accuracy of the ADC, namely 0.3 mV or 1/2 l.s.b.

4.5.2 THE DIGITAL CIRCUITRY.

Logic pulses from the discriminators of each photomultiplier tube in the three elements of the active shield (A1, A2, and A3) are fed into the coincidence monitoring unit which gives an output for each element when pulses from two or more tubes on that element are coincident. Also the unit accepts any input from each element of the polarimeter and gives an output when any input is present. These functions of the coincidence unit may be represented by the following logical statements;

A1 = 1A1.2A1 + 2A1.3A1 + 1A1.3A1

A2 = 1A2.2A2 + 2A2.3A2 + 3A2.4A2 + 4A2.1A2 + 1A2.3A2 + 4A2.2A2

. A3 = 1A3.2A3 + 2A3.3A3 + 1A3.3A3

P = P1 + P2 + P3 + P4   (4.2)

where the prefixes on the shield elements, A1, A2 and A3 donate a particular photomultiplier tube within that element. These output pulses are then considered to signifiy a 'true' event within that particular element.

The coincidence ADC unit then determines which coincidences took place between the eight elements of the total detector system (Ge, A1, A2, A3, P1, P2, P3, P4) and the priority with which they are to be recorded by the ADC. Any of these events is considered an event trigger for the ADC and the system has been designed such that two pulses are analysed for each event trigger. The combinations for the various coincidence and the pulses analyzed are shown in Table 4.2. Ge has the first priority for analysis, a P second and an A third. For the polarimeter the order of

TABLE 4.2

The analogue signals which are recorded for various combinations of detector pulses.

Coincidence'	Use	Analogue Pulses Analysed		Flags	
$G.P.A$	Background	G	P	P_{1-4}	A_{1-3}
$G.P.\bar{A}$	Polarisation	G	P	P_{1-4}	–
$G.\bar{P}.A$	Background	G	A	–	A_{1-3}
$G.\bar{P}.\bar{A}$	Nuclear line	G	$\sum(P + A)$	–	–
$\bar{G}.P.\bar{A}$	Background	A	P	P_{1-4}	A_{1-3}
$\bar{G}.P.A$	Background	–	P	P_{1-4}	–
$\bar{G}.\bar{P}.A$	Background	A	$\sum(P + A)$	–	A_{1-3}
$\bar{G}.\bar{P}.\bar{A}$	None	–	–	–	–

$G \equiv$ Ge Signal

$P \equiv$ Polarimeter Signal   P1,P2,P3,P4   ⎫ in order

$A \equiv$ Anticoincidence Signal   A2,A3,A1   ⎭ of priority

priority is P1, P2, P3 and P4 and for the anticoincidence shield the priority is A2, A3, and finally A1. For example, if G.P.A. were present, then G and A2 would be analyzed if A ≡ A1.A2.A3. Similarly if G.A.P. were present, then A3 and P1 would be analyzed if A ≡ A1.A2.A3, and P ≡ P1.P2.P3.P4. In order to prevent P and A events, i.e. GPA, GPA, GPA, dominating the live time of the ADC, the ADC logic only accepts every 32nd A or P event as a valid event trigger. For the coincidence which could indicate a possible line i.e. G.P.A. as well as recording the Ge detector pulse height, the sum of the pulse heights in the polarization and anticoincidence shields is also recorded. The discriminators are set for a 50 keV energy threshold and so measuring the sum of these individuals pulse heights will increase the sensitivity of the spectrometer.

The conversion gain of the ADC is 14 bits corresponding to an energy resolution of 0.61 keV per channel. The conversion time is 8.4 μs for each pulse. The digital outputs of the ADC are held in flip flops for subsequent telemetry to ground along with flags to signify the coincidence signals in the Ge detector, polarization modules and anticoincidence shields. These flag combinations allow the system to function simultaneously as a total absorption spectrometer, a sum coincidence spectrometer, a pair spectrometer and a polarimeter. The systems dead time at float altitude is ⋎ 30%.

4.5.3 THE HOUSEKEEPING.

As well as pulse height information, 36 analogue and digital housekeeping functions are also recorded. A twelve bit scalar

contained within the coincidence monitoring unit, cyclicly monitors the scalar rates of the fifteen individual photo-multiplier tubes, the germanium detector and the coincidence rates between the individual tubes in each element of the active shield. In all 31 different rates are monitored, each rate being sampled for 250 ms every 8 seconds. The digital outputs of the scalar are held in flip-flops along with 5 address bits for subsequent telemetry to the ground.

The systems monitoring unit monitors the temperatures and pressure within the pressure vessel surrounding the instrument, and also the voltages of each of the main power rails. All outputs are in the form of analogue voltages in the range 0 to 5 volts and are subsequently sent to their respective analogue channels in the telemetry system encoder.

4.5.4 THE POWER SUPPLY.

The power for the detector electronics and data handling systems is provided by a single power pack consisting of 44 three volt Lithium Organic batteries. Lithium Organic[+] batteries were chosen in preference to the Nickel Cadmium rechargeable type because of their high capacity (10 Ah at 200 mA) and small physical size. Each voltage rail in the system was obtained using series and parallel combinations of batteries, earthed at the appropriate point and effectively independent of the other rails. Regulation for the various supply voltages is achieved using monolithic voltage regulators which provides stability of the output voltages to ± 1/4% for temperature variations of ± 20°C and variations of the input voltage of ±15%. The efficiency of these

+ Sulfur Dioxide type, typically 330 W.h/kg.

regulators is typically 75% and the ripple rejection ratio is better than 80 db. The total power consumption for the detector and data handling systems is $\sim$ 50W.

4.5.5 THE TELEMETRY SYSTEM.

The telemetry system used was a Spacetec 2100 Pulse Code Modulation (PCM) telemetry pack supplied as part of the launch facility by the National Center for Atmospheric Research. This was linked to a P.D.P.[*] 11/20 minicomputer in the ground station, that could produce a computer compatible magnetic tape record, and hence greatly reduce the problems of data retrival later.

The telemetry is controlled by a PROM[+] which routes a 32 x 32 ten bit word matrix cyclicly to the ground station at a bit rate of 40.96 k.bits.s^{-1}. Figure 4.7 shows the program that specified each telemetry word. The two 14 bit ADC pulse heights are sampled four times in each telemetry frame and routed to the digital telemetry words D1, D2 and D3 giving a minimum time resolution of 2.44 ms. The germanium analogue pulse is also sampled independantly four times each frame and is routed to the analogue channels A2, A3, and A4. The steering and housekeeping data are distributed throughout the subcommutated words as illustrated in Figure 4.7, and are each sampled every eight seconds.

The main disadvantage of the PCM system is that information is difficult to access in real time because only very minimal display facilities are available in the ground support equipment.

---

* Programable Digital Processor manufactured by the Digital Equipment Corporation Maynard, MA, U.S.A.
+ Programable Read Only Memory.
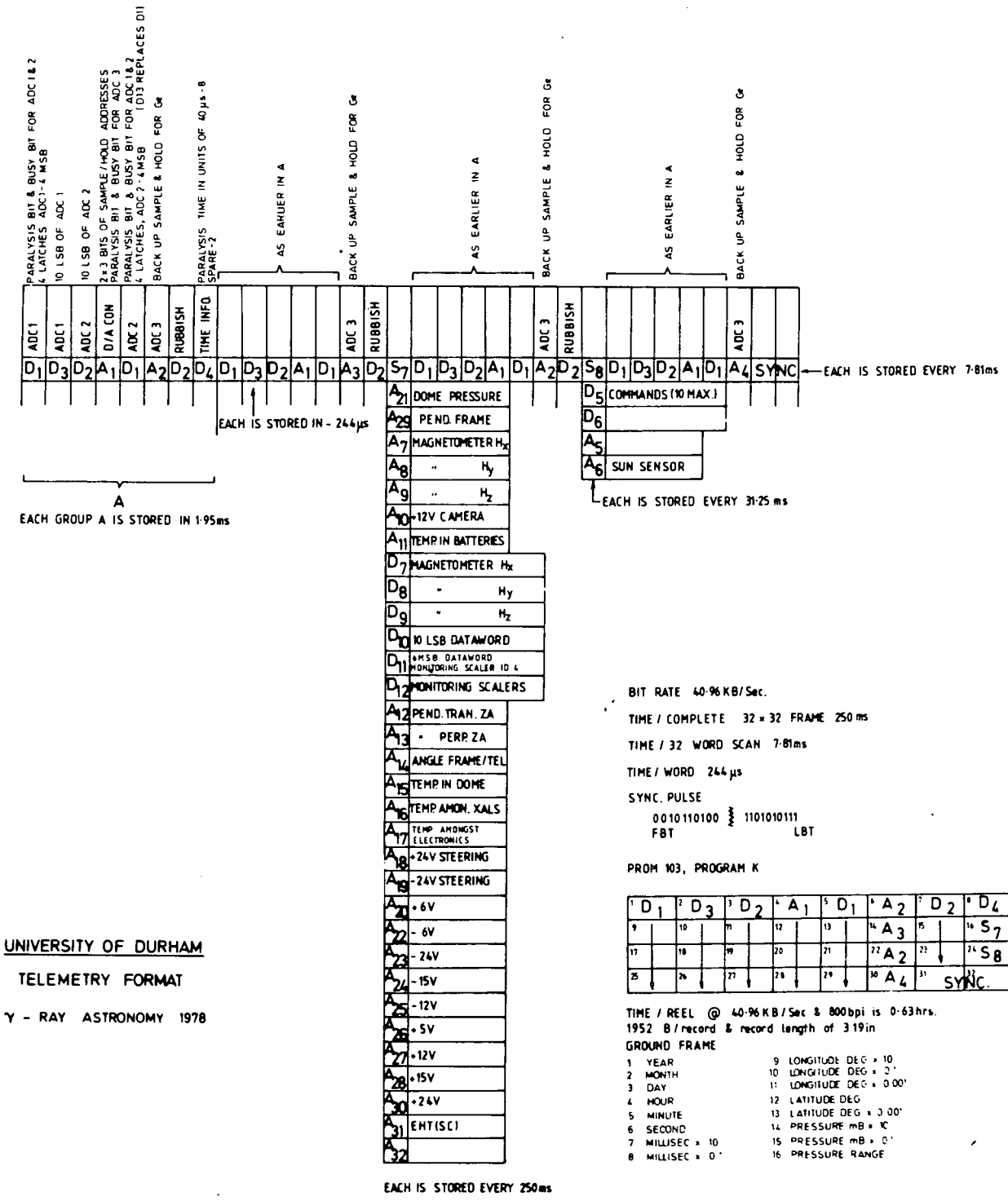
Figure 4.7 The programme that specified the contents of each telemetry word in each telemetry frame.

4.6 INSTRUMENT RESPONSE.

4.6.1 ENERGY RESOLUTION.

Spectral degradation effects in the central germanium detector have been investigated and are described in Appendix B. The measured energy resolution of the Ge crystal at energy E (keV) can be described by the semi-empirical formula,

$$\Delta E(keV) = (a_1 E + a_2 E^2 + a_3)^{1/2} \tag{4.3}$$

where a_1 = 2.16 x 10^{-3} eV, a_2 = 1.82 x 10^{-6} and a_3 = 1.042 eV^2. The coefficients of the quadratic function arise as follows: a_1 corresponds to statistical fluctuations in the number of electron hole pairs, a_2 results from incomplete charge collection and charge trapping within the intrinsic region and a_3 corresponds to energy independent line broadening resulting from electronic noise, detector leakage current, and analyzer channel width.

4.6.2 GAMMA-RAY DETECTION EFFICIENCY.

The measured and calculated efficiencies for vertically incident photons on the Ge detector are shown in Figure 4.8 for the MK2 instrument. The maximum effective area is approximately 14 cm^2 at 100 keV. The MK1 efficiencies were on average 2% larger. The differences are a direct result of a cryostat vacuum leak that occurred after the first flight. The calculations used to produce the theoretical curves are presented in Appendix C.
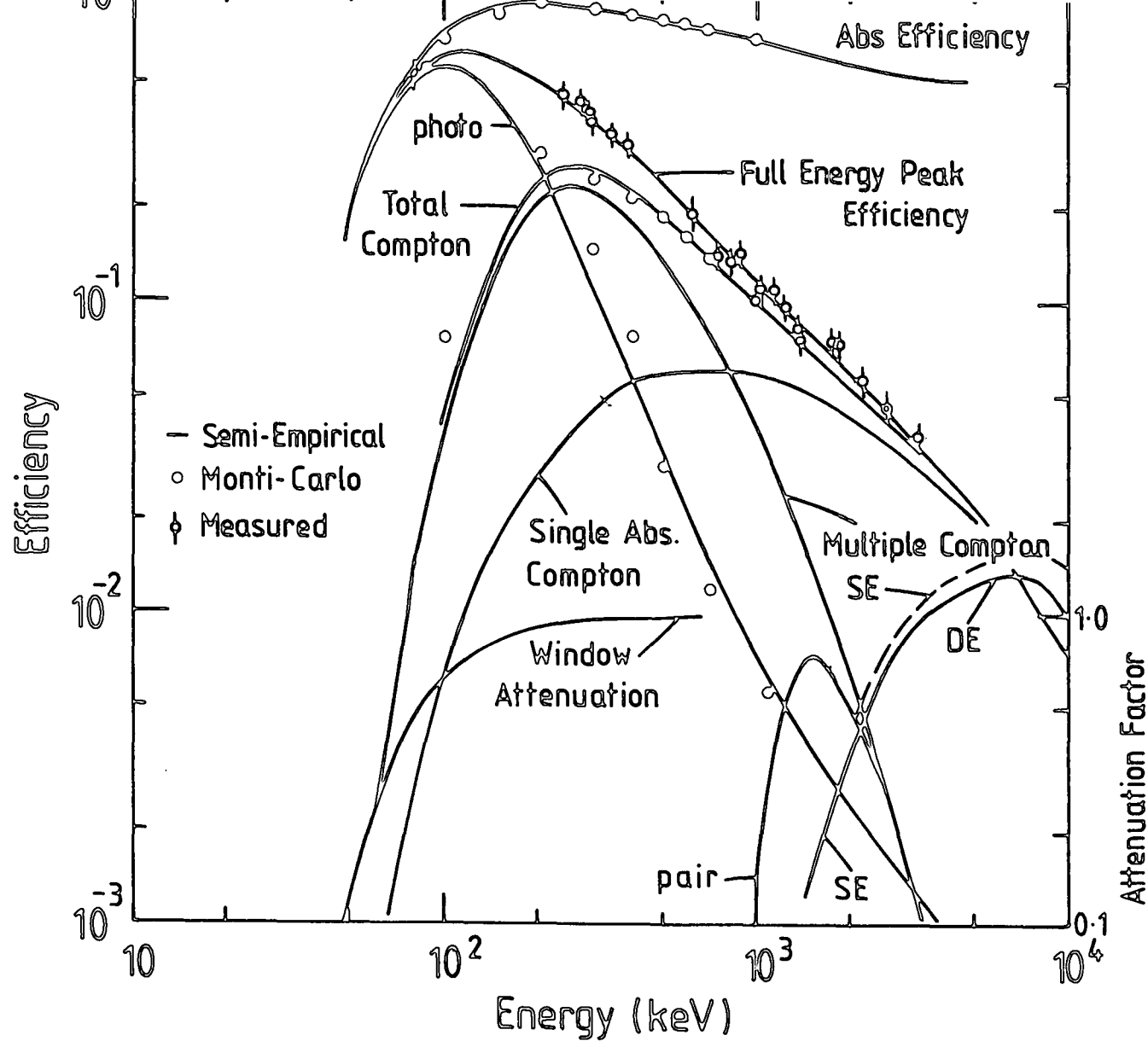
Figure 4.8 The experimental and calculated efficiencies for the MK2 telescope.
Note: Photo, total Compton single absorbtion Compton, multiple Compton
and pair refer to the various contributions to FEPE, SE and DE denote
single and double es... peak efficiencies respectively

4.6.3 SPECTROMETER RESPONSE TO DIFFUSE AND POINT SOURCES.

The sensitive area of the telescope is a function of the angle θ between the photon momentum vector and the collimator axis. At low energies the distant point source[*] response can be approximated by,

$$A(\theta) = \cos\theta \iint_{\text{illuminated area}} dxdy \qquad (4.4)$$

where the integrand represents a differential element of area on the surface of the detector. At energies > 300 keV Equation 4.4 must be modified to account for the increasing penetration of the collimator material with photon energy. Figure 4.9 shows the MK2 detector response as a function of θ for various incident energies. The calculations used to produce these results are described in Appendix D.

For a diffuse source the response of the detector is given by,

$$A(\Omega) = \iint d\Omega(\cos\theta)dA) \qquad (4.5)$$

with the dA integration carried out over the entire detector surface and the $d\Omega$ integration carried out over all solid angles accessible to dA. For low energy photons Equation 4.5 can be approximated by a 'geometric' factor given by,

$$A_o(\Omega) = \frac{\pi^2 r_d r_c}{r_d^2 + r_c^2 + h^2} \qquad (4.6)$$

---

[*] Please note; the term response has been adopted for brevity and is in fact not considered at all. What is being calculated is the effective collimator aperture.
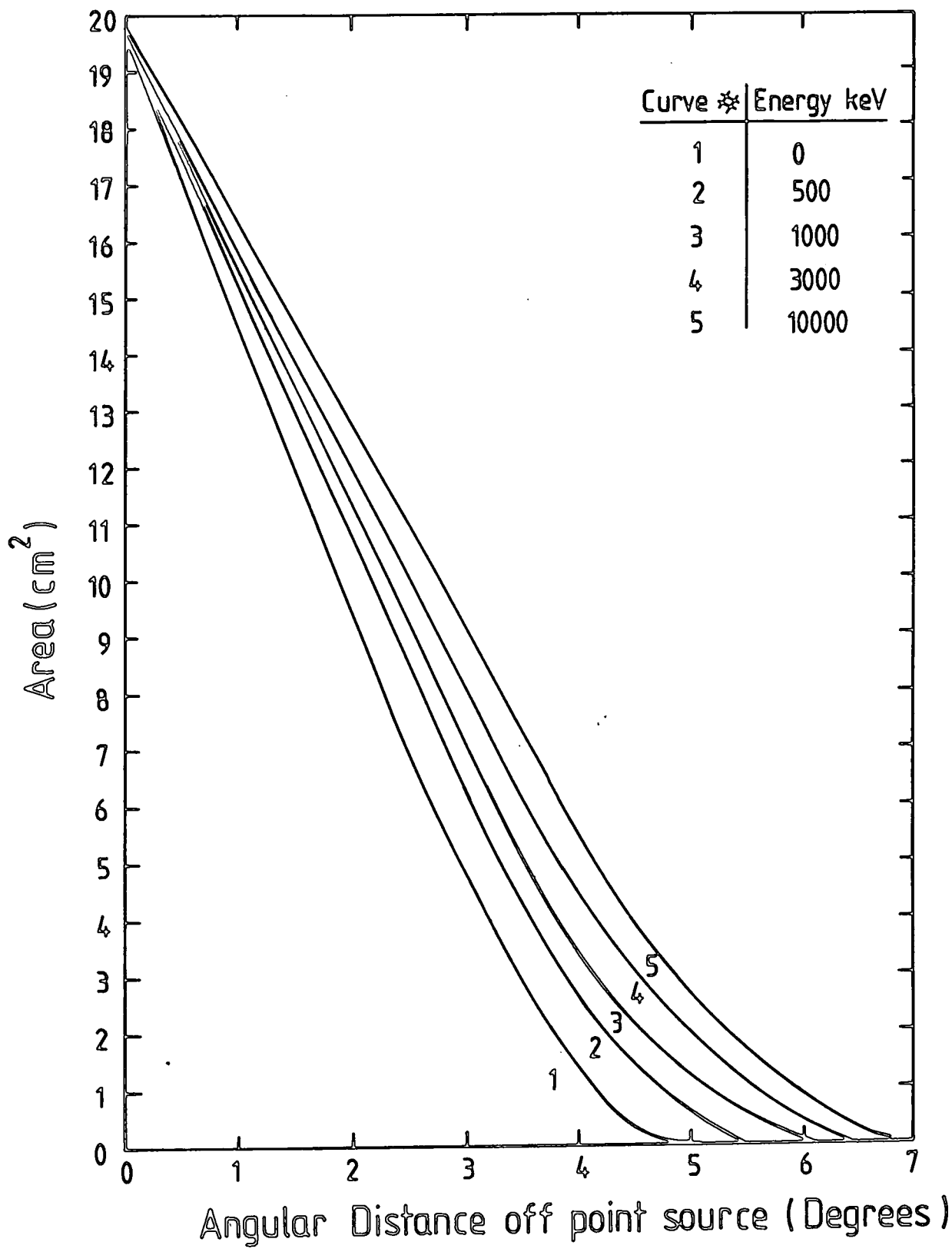
Figure 4.9 The angular response of the MK2 telescope to a distant point source.

where h is distance between the detector and the top of the collimator and r_d and r_c are the radius of the detector and collimator respectively. Alternate forms of $A_o(\Omega)$ may be found in Horstman et al. (1975). For photon energies > 300 keV, the response is given by,

$$A(\Omega) = 2\pi \int_0^\pi A(E,\theta) \sin\theta \, d\theta \qquad (4.7)$$

where $A(E,\theta)$ is the energy dependent detector area at angle θ shown in Figure 4.9. The diffuse source response has been calculated numerically and is shown in Figure 4.10.

4.6.4 POLARIMETRY WITH THE SPECTROMETER.

Monte Carlo calculations have been carried out for the polarimeter arrangement of this experiment (C.A. Ayre, Private Communication). Polarized photons of various energies were allowed to strike the forward face of the Ge(Hp) detector and to be Compton scattered into the quadrants of NaI(Tℓ) surrounding the detector. The results of the calculation are given in Figure 4.11, in which is plotted the ratio of the counts in neighbouring quadrants coincident with a pulse from the Ge(Hp) detector. In the model it is assumed the gamma-rays are 100% polarized with their electric vector normal to one of the quadrants as shown in the Figure inset. The Figure also shows the polarimeter efficiency, ε_p, which is defined as the ratio of the flux of gamma rays which contribute to polarization measurement to the incident gamma-ray flux. Clearly the potential of the spectrometer for
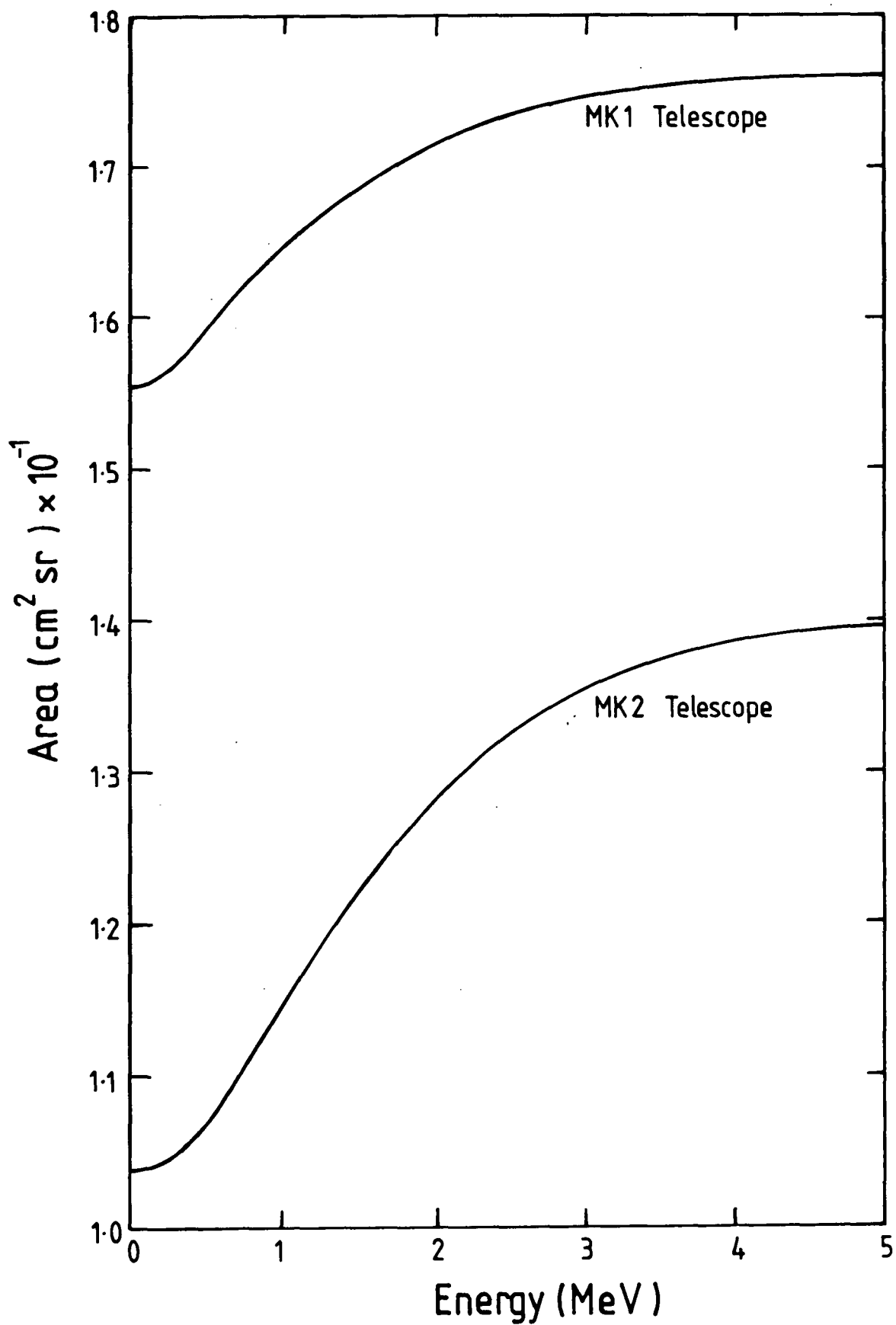
Figure 4.10   The response of the MK1 and MK2 telescopes to a diffuse source.
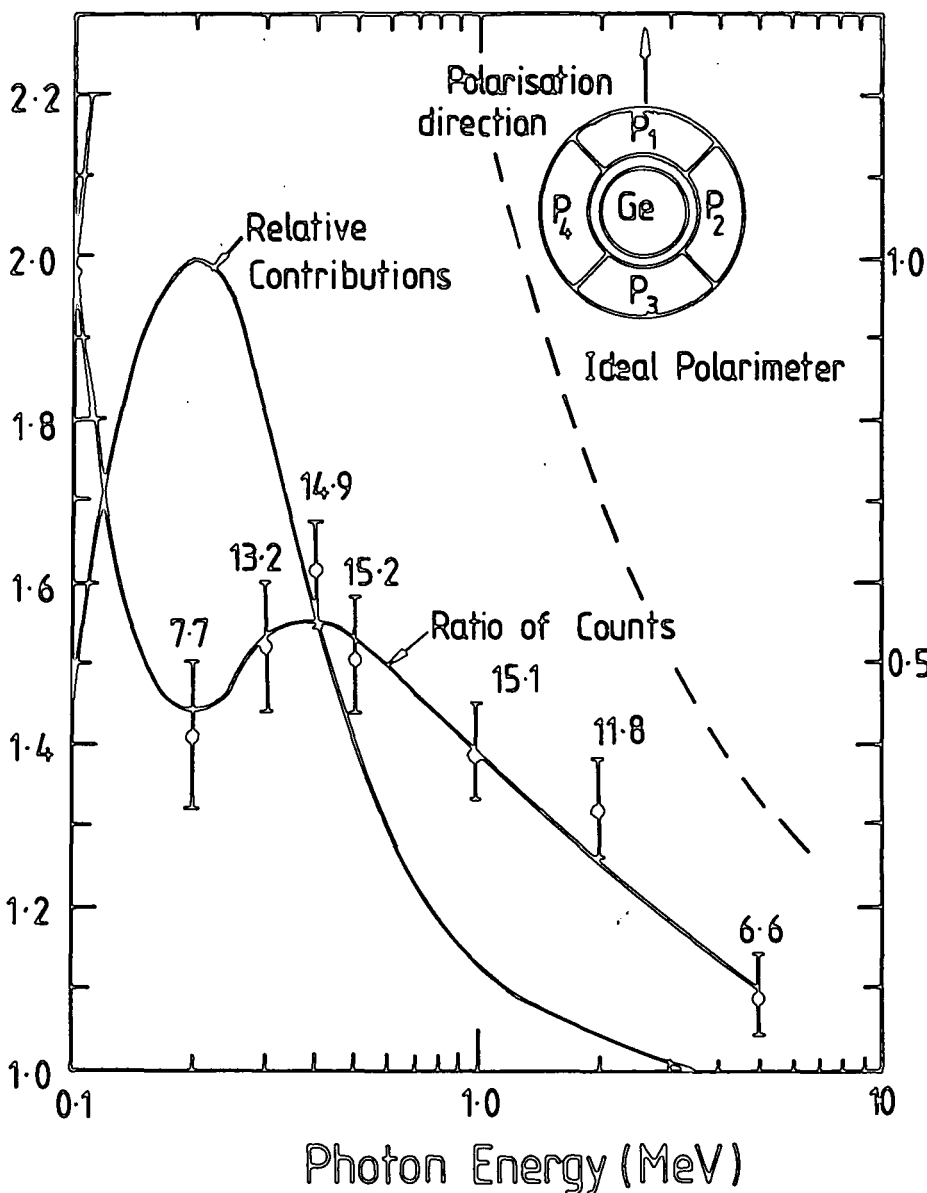
Figure 4.11 The ratio of the counting rates $(P_2 + P_4).Ge / (P_1 + P_3).Ge$ as a function of energy for a 100% polarized incident beam. For comparison the response of an ideal polarimeter is also shown (assuming point scattering and absorbtion). The parameter for each point is the percentage of the incident γ-rays which contribute to the polarisation measurement. For a typical source spectrum $N_\gamma(> E)\propto E_\gamma^{-2}$, the relative contributions of photons to polarisation measurements are shown as a function of energy.

polarization studies is dependent upon the incident gamma-ray flux. For any power law source flux, $\propto E^{-\alpha}$ (where $\alpha > 1.5$) such measurements are most accurately made over a restricted range of energy. Figure 4.11 shows the result of considering a typical gamma-ray source spectrum varying as E^{-2} at the top of the atmosphere. This demonstrates that there is a major contribution to the count rate around 200 keV, and therefore potentially the most precise polarization measurements are made in this region. The polarization detectable at energy E with S standard deviations by the polarimeter is given by,

$$P(E) = \frac{S(2F(E)\epsilon_p(E)f + 2r_b(E)t_s)^{1/2}}{F(E)\epsilon_p(E)fQ(E)} \qquad (4.8)$$

where $r_b(E)$ is the polarimeter background rate at energy E (i.e. $\sum_i G.P_i.A$), F(E) is the source flux incident on the detector, t_s is time spent observing the source, f is the detector exposure to the source in cm^2 s and Q(E) is the polarimeter sensitivity given by,

$$Q(E) = \frac{R(E) - 1}{R(E) + 1} \qquad (4.9)$$

where R(E) is the ratio of counts in segments parallel and perpendicular to the plane of polarization given in Figure 4.11. Equation 4.8 has been evaluated using the observing parameters of the Crab Nebula measurements described in this thesis. For the energy interval 100 keV to 1 MeV it can be written as,

$$P(\Delta E) = \begin{cases} 0.45 \cdot S , & S < 1/0.45 \\ \\ 1 , & S \geq 1/0.45 \end{cases} \quad (4.10)$$

Present measurements of the Crab Nebula extending from the radio through to the low energy x-ray region have indicated a mean polarization of approximately 10% (Apperao, 1973).

4.6.5 INSTRUMENTAL BACKGROUND.

The minimum flux that can be measured by an telescope is ultimately limited by the level of the instrumental background counting rate. The vetoed Ge detector background counting rate has been evaluated semi-empirically and is compared to the experimentally measured energy-loss spectrum in Figure 4.12. These experimental data were obtained during a balloon flight over Palestine Texas, U.S.A. in June 1981 at a mean float altitude of 5.4 g cm^{-2}. The model used in the calculations is similar to that proposed by Dipper (1979). The telescope is approximated by a right-cylindrical Ge detector surrounded by a series of concentric spherical shells representing the anticoincidence shield, neutron jacket and additional absorbing materials. The error in the energy loss spectrum derived from these calculations is estimated to be 50%. The various contributions to the detector counting rate arise as follows:

Aperture Flux: This is due to the atmospheric flux that passes directly through the aperture and will therefore not be vetoed by the shield. This component was calculated using the atmospheric spectrum for vertical gamma-rays given by Schonfelder
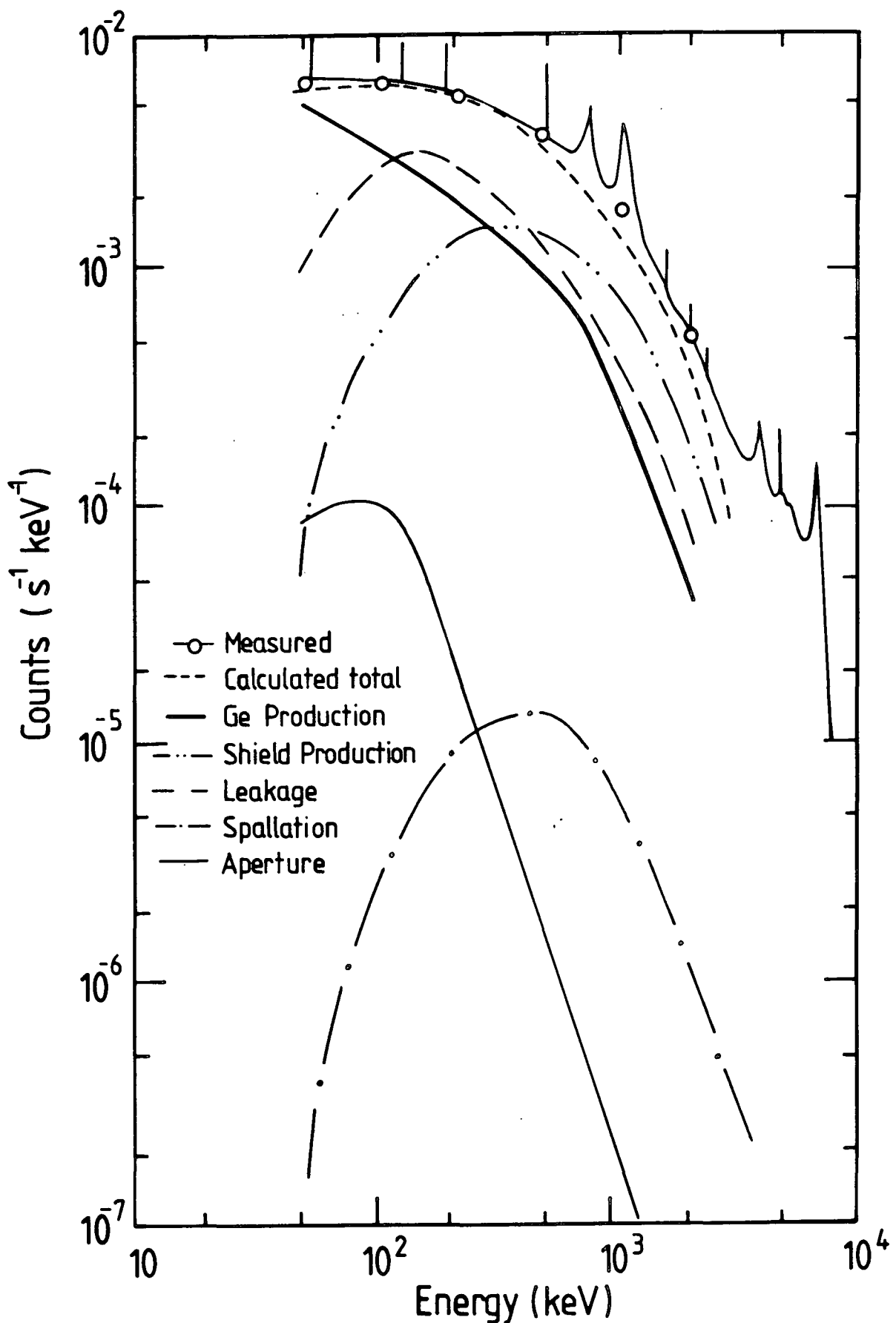
Figure 4.12 The measured and predicted instrumental background (with full vetoe) at a mean atmospheric depth of 5·4 g cm^{-2} over Palestine Texas. The aperture flux, shield leakage, shield production, Ge production and spallation components are shown seperately. The typical uncertainty in the sum of these components (the sum is shown by the short dashed line) is 50%.

et al. (1977).

Shield Leakage: The shield leakage component is due to atmospheric gamma rays that penetrate the shield and deposit energy in the Ge detector. The incident photons or their secondaries can interact in the shield as long as the energy deposited is less than the shield threshold. The flux and angular distribution of the atmospheric gamma rays used in the calculation were taken from the empiric and semi-empiric calculations of Costa et al. (1984).

Shield Production: Neutrons generated in the atmosphere may interact with the shield and produce radioactive nuclei which decay by emitting gamma rays. In order to derive this component the NaI(Tℓ) gamma-ray yields computed by Ling and Gruber (1977) and the experimental data of Shafroth et al. (1958) have been used in the calculation. The atmospheric neutron flux was taken from a best fit to the 'world' data given by Dean and Dipper (1981). The model assumes that the excited nuclei are uniformly distributed throughout the shield.

Neutrons can also be produced within the material surrounding the central detector by high energy cosmic ray interactions. These secondary neutrons can then generate radioactive nuclei in the same way as the atmospheric neutrons. This contribution was calculated by integration over the volume of the payload using the mean number of 'boil off' neutrons per cosmic ray interaction given in Powell et al. (1959). It is assumed that no multiplicity of nuclear interaction particles takes place and the neutrons are likewise unattenuated.

Ge Production: Energetic protons and neutrons produced in the atmosphere or shield may also interact with the nuclei of the

germanium atoms in the central detector producing β^- unstable nuclides. The detector energy loss spectrum is mainly due to the ionization energy loss of the β-decay electrons. This contribution may be estimated from the volume production yields given by Paciesas et al. (1983).

Spallation: Atmospheric charged particles may interact in the shield producing radioactive nuclides which decay in a time longer than the coincidence time of the instrument (1 μs). In sodium iodide, the induced counting rate as a function of energy may be reasonably well described by the empirical formula of Fishman (1972). A proton flux of 0.3 proton $cm^{-2}s^{-1}$ at a rigidity of 4.5 GV (Hayakawa, 1969) was used in the calculations.

4.6.6 THE SENSITIVITY OF THE DURHAM SPECTROMETER.

Using the observed background counting rates given in the previous section the sensitivity of the spectrometer to continuum and narrow line fluxes has been evaluated using the treatment of Jacobson et al. (1975). The results, shown in Figure 4.13, correspond to an exposure time of two hours (1 hour on source, one on background) and a significance of 3σ in the detected flux. The minimum sensitivity to unbroadened lines was found to be 2.2 x 10^{-3} and 9.0 x 10^{-3} photons $cm^{-2}s^{-1}$ for active and passive shielding respectively.

4.7 THE FLIGHT OF THE DURHAM SPECTROMETER

The instrument has flown on two occasions from the National Scientific Balloon Facility in Palestine Texas. The first flight
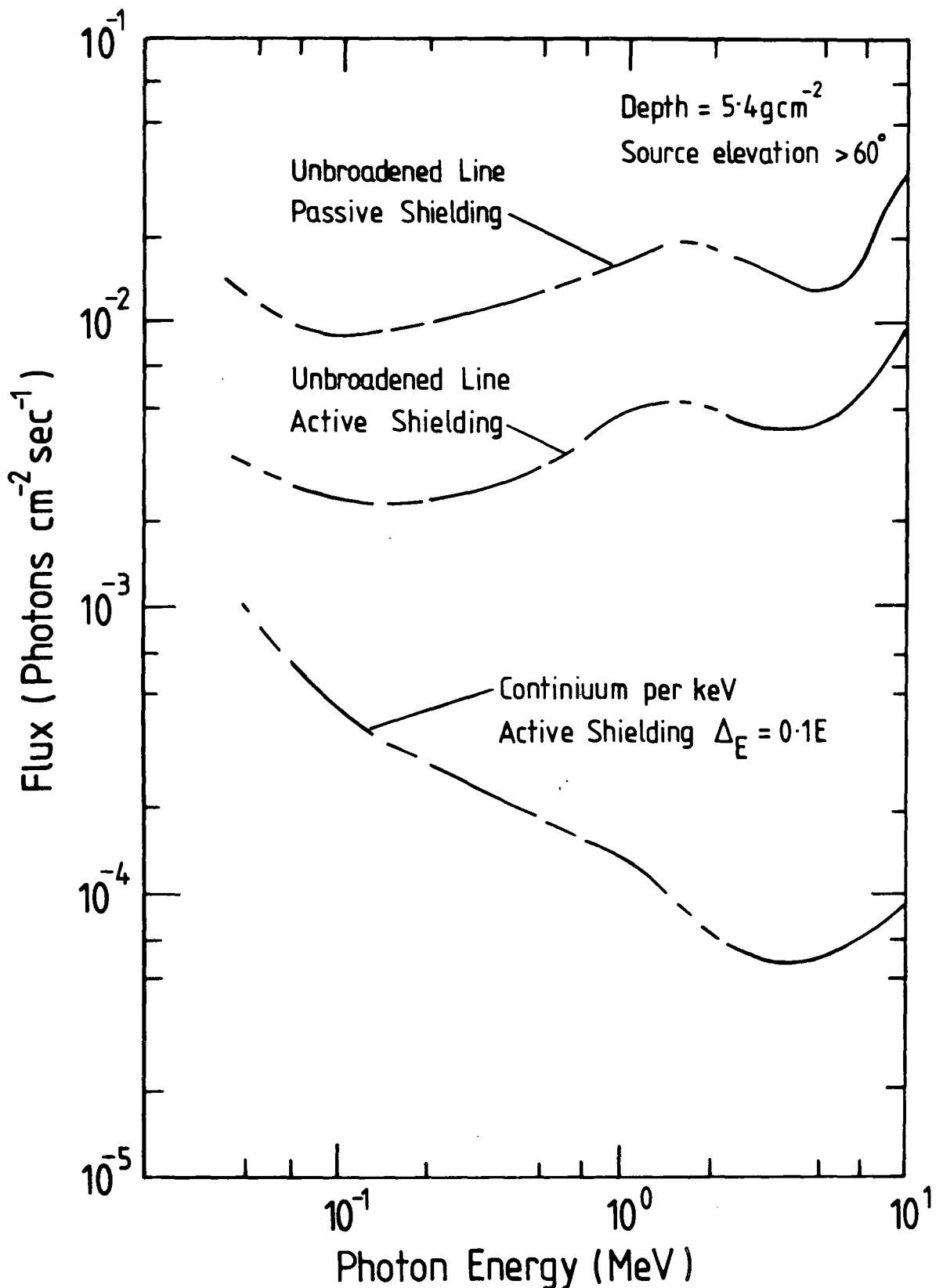
Figure 4.13 The sensitivity of the spectrometer for a 1 hour 'on-source' 1 hour 'off-source' observation and 3σ significance in the detected flux. The gaps in the curves indicate the presence of strong background lines; consequently the sensitivity in these regions will be considerably worse than shown.

of the spectrometer took place on August 28 1979, the balloon reaching a float altitude of 3.9 mb at 16.30 universal time (UT). Unfortunately due to a failure of the steering system, no pointed observations were made. However in every other respect the flight was a success and important background information was obtained (Ayre et al., 1981b, 1981c). A second balloon flight occurred on June 6 1981. The spectrometer was launched at 12.35 UT and remained at a float altitude of 5.4 ± 0.1 mb for approximately 24 hours. The performance of the instrument and the results presented in this thesis are considered in the light of the 1981 balloon flight. During this flight pointed observations were made of the Crab Nebula, NGC1275 and CG195+5 using a raster scan technique. The results are presented in the next chapter.

4.7.1 BACKGROUND LINES.

An analysis of the data obtained for the 511 keV positron annihilation line shows that the system stability was excellent and that the drift in gain of the detector was essentially zero (<< 0.2 keV around 511 keV) during the 24 hour period of the flight. The detector background energy-loss spectrum at float altitude is shown in Figure 4.14 for the energy range 50 to 650 keV. These data represent a total exposure of 5×10^4 seconds obtained at a mean atmospheric depth of 5.4 g cm^{-2}. From this Figure it can be seen that several lines are observable above the background continuum. A total of 62 lines having a significance > 2σ were detected in the energy range 50 to 4000 keV. A complete catalogue of these lines and their properties is given in Ayre et al. (1984). The strongest of these lines, at energies 53, 67,
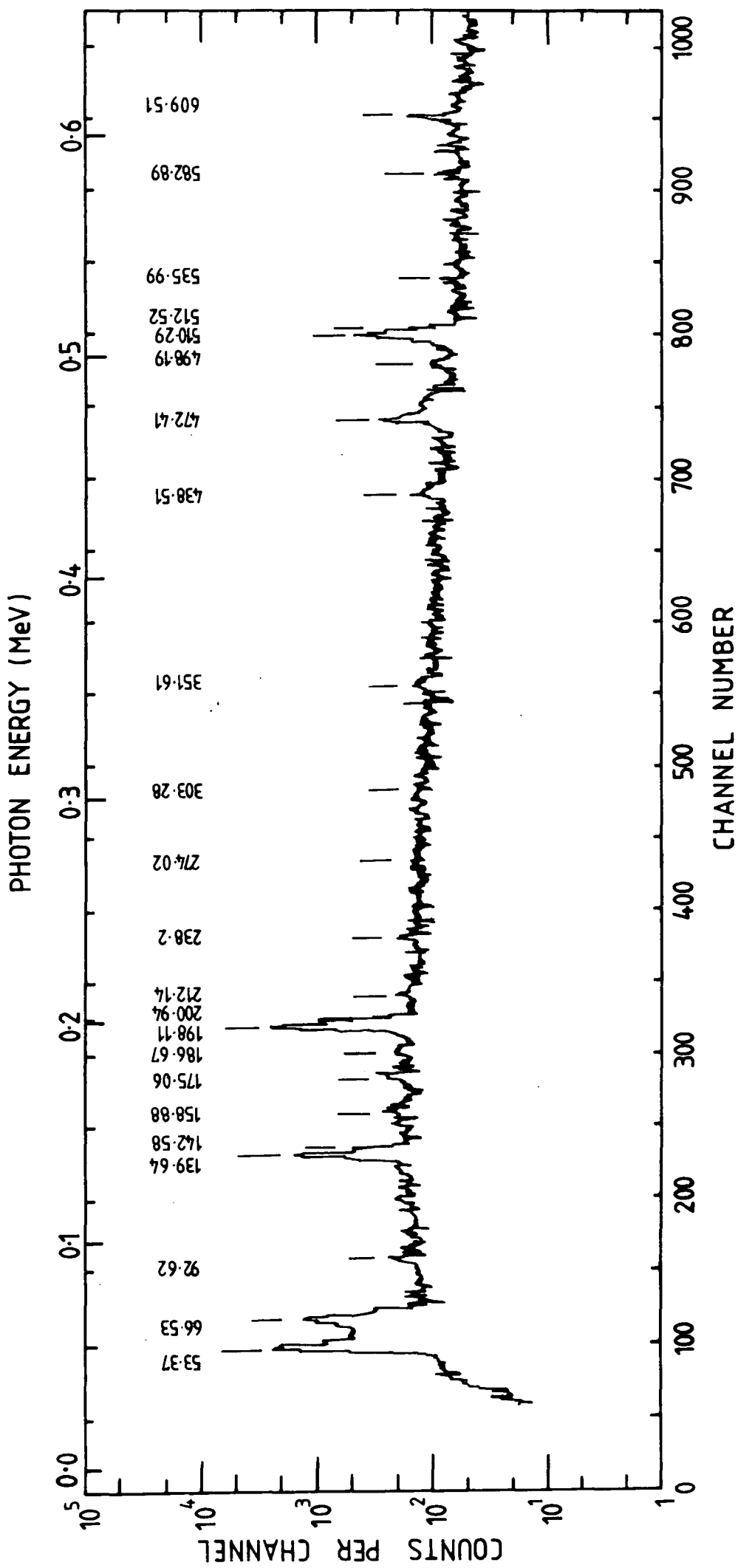
Figure 4·14 The measured background spectrum for an exposure of 5×10^4 secs at 5·4 mb over Palestine, Texas. From Ayre et al. (1984)

139, 198 and 511 keV, are listed in Table 4.3 in which a comparison is given with previous measurements. Their intensity variation as a function of atmospheric depth is shown in Figure 4.15. The depth variation of the 511 keV line differs markedly from each of the other four lines, this reflecting its different origin. The latter lines are principally due to n-Ge interactions and the variation of the intensity is dependant on the neutron flux incident on the detector. The neutron intensity falls with altitude above the Pfotzer maximum and so it might be expected that the intensities of the dependant lines would fall also. This however, is seen not to be the case. This is because neutrons are generated in the anticoincidence shield by high energy cosmic ray interactions. Since the decay times of the isomeric states they produce are generally much longer than the anticoincidence veto time constant, the shield essentially acts as a slab of inert material of thickness 46 g cm^{-2}. To a first approximation the secondary radiation produced in NaI(Tℓ) is the same as that produced in an equivalent thickness of air so even at float the Ge detector is at an equivalent depth of 50 g cm^{-2}, as far as production of these lines is concerned.

4.7.2 EVALUATION OF THE NEUTRON SHIELD.

This section has been included because previous experiments that have flown neutron shields (eg Baker et al., 1979, Leventhal et al., 1980) have failed to give a quantitative description of their effectiveness. The neutron jacket flown on the 1981 flight has been described in section 4.3.4. Calculations have indicated that the neutron jacket will attenuate incident neutrons by a

Energy (keV)	Feature intensity (10^{-3} cm^{-2} s^{-1})		
	Mahoney et al.: area 40 cm^2, length 4 cm	Present results: area 19.6 cm^2, length 4.4 cm	Womack and Overbeck: area 15.3 cm^2, length 1.8 cm
53.44	13.8	9.7 $\pm$ 2.3	10 $\pm$ 2.3
66.73	5.6	6.2 $\pm$ 0.7	5.8 $\pm$ 1.5
139.68	6.1	5.5 $\pm$ 0.7	3.3 $\pm$ 0.1*
198.30	12.0	13.1 $\pm$ 1.1	8.0 $\pm$ 0.4*
511.00	3.1	2.9 $\pm$ 0.3	3.3 $\pm$ 0.3*

Table 4.3   Intensities of some line features from the present experiment at 5.4g cm^{-2} compared with measurements of Mahoney et al (1978) at 3g cm^{-2} and Womack and Overbeck (1970) at 4.7g cm^{-2}. The intensities* are corrected for the large difference between the crystal length of Womack et al., 1.8cm, and that of the other groups, ~ 4cm.
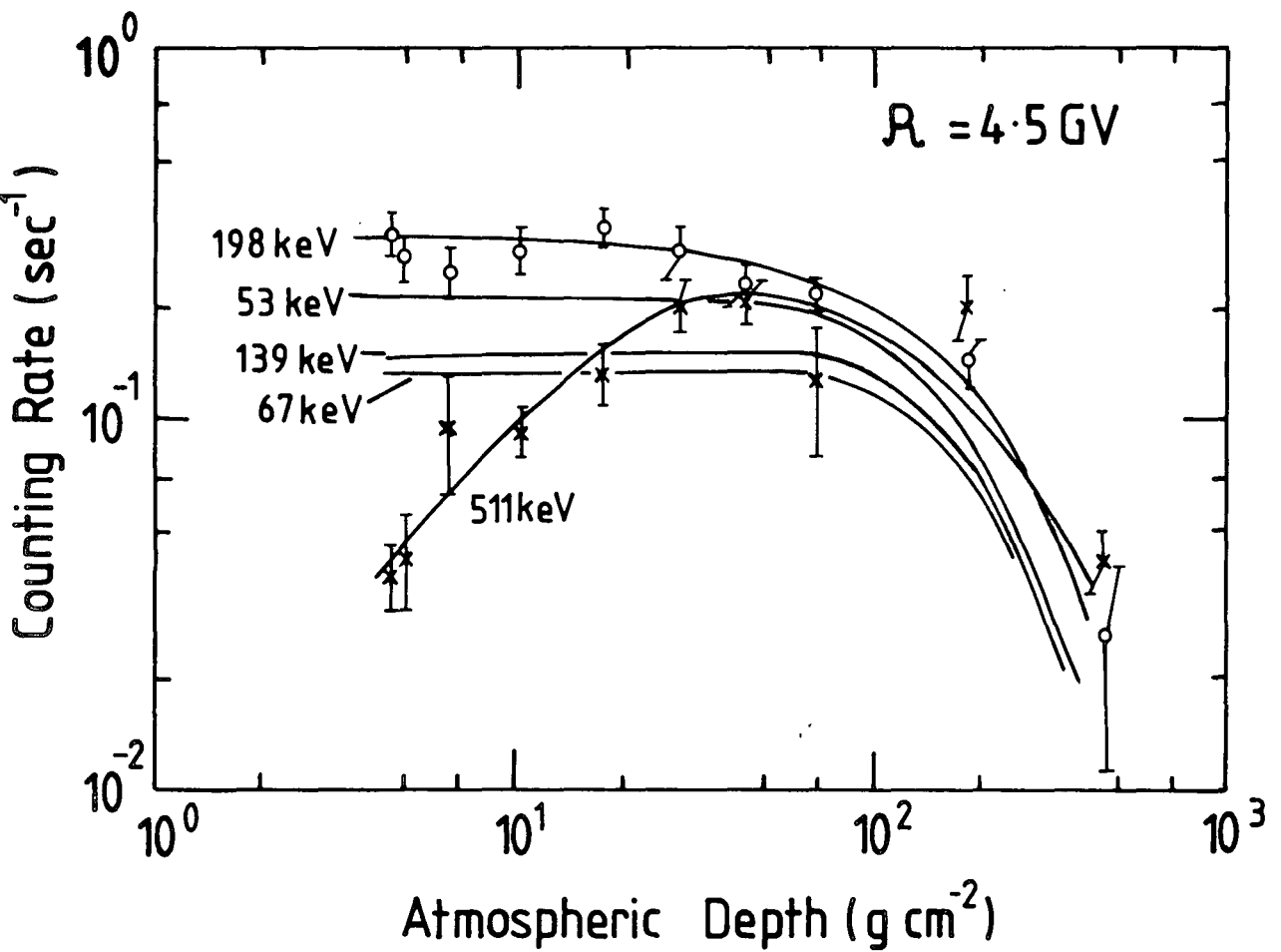
Figure 4·15   The variation of intensities of the 53, 67, 139, 198 and 511 keV lines with atmospheric depth over Palestine Texas. From Ayre et al. (1984)

factor of 10 at 5 MeV and a 100 at 1.8 MeV. This trend continues with decreasing energy and so virtually all thermal and epithermal neutrons are absorbed. Without the neutron jacket it is calculated that the atmospheric neutron fluence incident on the anticoincidence shield is 1974 n s^{-1} at a depth of 5.4 g cm^{-2}. The total number of 'boil off' neutrons, generated by high energy cosmic ray interactions within the anticoincidence shield, is estimated to contribute a further 1983 n s^{-1}. Therefore if the neutron jacket absorbs all the atmospheric neutrons we would expect the total neutron fluence to drop by a factor of approximately two. There is evidence to support this. The background lines at 139 and 198 keV provide a direct measure of the neutron fluence within the spectrometer. The ratio of the fluxes of these lines for the first and second flights were measured to be 2.4 ± 0.6 and 2.7 ± 0.5 respectively, in agreement with our calculations. For comparison the ratio of fluxes for the 511 keV line is 1.4 ± 0.2. Taking into account the absorbtion of 511 keV atmospheric leakage photons by the jacket, the expected ratio is 1.3. This shows that the experimental conditions between the first and the second flights were essentially the same and so the comparison is valid. From Figure 4.12 we see that the detector background counting rate is dominated by neutron effects and therefore we would expect the integral Ge counting rate for the first flight to be approximately a factor of two greater than the second flight. The measured ratio is 2.1, in good agreement.

It should be appreciated that the factor of two reduction in background counting rate is the best that will be achieved, for if we surround the neutron jacket with additional mass in an attempt to absorb the cosmic rays, this mass will in turn act as a

secondary radiator and therefore generate further neutrons. In principle we could electronically veto the resulting decay gamma-rays, however in practice the resulting dead time would be beyond acceptable limits.

CHAPTER 5.

DATA ANALYSIS AND RESULTS.

5.1 CALCULATION OF THE OBSERVED SOURCE FLUX.

The determination of the source flux from the raw data can be considered to be the calculation of the average value of many independant measurements of the 'instantaneous' source flux. This 'instantaneous' source flux may be derived from the difference between two adjacent pointing segments of typically 5 minutes duration; one of high (source) and one of low (background) source exposure. The residual is then divided by the difference in fractional exposure to the source to obtain the net source flux. To negate the effects of a non-constant background during source exposure, each source pointing segment is actually compared to two adjacent background segments. Further, since the intrinsic detector background counting rate varies with atmospheric depth, each accumulation of background counts is normalised to the mean atmospheric depth during the source accumulation. The residual counts C_i in a given PHA channel k are then computed according to;

$$C_{i,k} = S_{i,k} - \frac{t_i}{t_{i-1} + t_{i+1} + 2t_i} \left\{ B_{i-1}\left[\frac{t_{i+1} + t_i}{t_{i-1}}\right] + B_{i+1}\left[\frac{t_{i-1} + t_i}{t_{i+1}}\right] \right\}$$

(5.1)

where,

$S_{i,k}$ = the observed counts in channel k of source pointing segment i.

$B_{i-1,k}, B_{i+1,k}$ = the observed counts in channel k of background pointing segments i-1, i+1.

$t_i, t_{i\pm1}$ = oberving times of segment i,i±1.

The standard deviation associated with the residual counts from channel k in pointing segment i, is then given by,

$$\sigma'_{i,k} = \left[S_{i,k} + \left(\frac{t_i}{t_{i-1} + t_{i+1} + 2t_i} \right)^2 \left\{ B_{i-1} \left[\frac{t_{i+1} + t_i}{t_{i-1}} \right]^2 \right. \right.$$

$$\left. \left. + B_{i+1} \left[\frac{t_{i-1} + t_i}{t_{i+1}} \right]^2 \right\} \right]^{\frac{1}{2}} \tag{5.2}$$

assuming $S_{i,k}$, $B_{i-1,k}$ and $B_{i+1,k}$ are Poisson distributed independant random variables. The use of the above formulation allows for a variety of observation times both on and off source and assumes only that the background is constant or varies linearly during the observation.

The residual counts detected in each channel, $C_{i,k}$, are then corrected for the exposure time and the <u>difference</u> in the normally presented detector area (A_i) during the source and background pointing segments, i.e.,

$$f_{i,k} = \frac{C_{i,k}}{A_i t_i} \tag{5.3}$$

$$\text{and} \quad \sigma_{i,k} = \frac{\sigma'_{i,k}}{A_i t_i} \tag{5.4}$$

To obtain the average observed source flux over the flight it is necessary to sum the individual fluxes $f_{i,k}$. However, in some circumstances, i.e., during steering manoeuvers, telemetry

dropout etc., some data points will be measured to better or worse precision than others. We can express this quantitatively by assigning a different parent population to those data points with the same mean but with a correspondingly smaller or larger standard deviation $\sigma_{i,k}$. The most probable value for the mean is therefore the weighted average of the data points (Bevington 1969),

$$F_k = \frac{\Sigma(f_{i,k} w_{i,k})}{\Sigma w_{i,k}} \tag{5.5}$$

$$\text{where} \quad w_{i,k} = 1/\sigma^2_{i,k} \tag{5.6}$$

Assuming that the fluctuations in $f_{i,k}$ are uncorrelated then the standard deviation of F_k will be given by,

$$\sigma_k = (\Sigma \, w_{i,k})^{-\frac{1}{2}} \tag{5.7}$$

In the Poissonian limit care should be exercised in using equations 5.5 and 5.6 since for a small constant mean rate the summation will generate an incorrect result for the average (no matter how many bins are considered). This is due to the fact that for small $f_{i,k}$ the square root of $f_{i,k}$ is a relatively poor estimator of the true uncertainty. In this case the data is weighted by the expected rather than the observed flux;

$$\sigma^2_{i,k} = \frac{r_k}{t_i A^2} \tag{5.8}$$

where r_k is the detector background rate estimated from,

$$r_k = \frac{\Sigma(B_{i-1,k} + B_{i+1,k})}{\Sigma(t_{i-1} + t_{i+1})} \qquad (5.9)$$

The formal uncertainty in the source flux is·then given by (Maurer 1979).

$$\sigma_k^2 = r_k \left[\frac{1}{\Sigma t_i A_i} + \frac{[\Sigma t_i A_i]^2}{\Sigma(t_{i-1} + t_{i+1})[\Sigma t_i A_i^2]^2} \right] \qquad (5.10)$$

5.2 THE CALCULATION OF THE INCIDENT SOURCE SPECTRUM.

The observed energy loss spectrum derived in the previous section differs from the incident photon spectrum due to instrumental and atmospheric effects. These effects include, attenuation in the inert material above the detector, the detection efficiency, and the finite energy resolution of the detector. The following procedure for deconvolving the incident source spectra is based on the work of Reigler (1969) and Dolan (1972).

The incident photon spectrum on the top of the atmosphere, F_o, and the observed energy loss spectrum, F, are represented by vectors and the various instrumental and atmospheric effects as matrices which attenuate or redistribute the components of the incident spectrum vector. Specifically the observed photon spectrum is given by,

$$F = M F_o \qquad (5.11)$$

where F and F_o are [k x 1] matrices and M is a [k x k] matrix operator representing the combined atmospheric and instrumental response of the detector. Thus,

$$M = M_R \, M_E \, M_B \, M_A \qquad (5.12)$$

where M_A is a [k x k] matrix representing the attenuation of the beam in the residual atmosphere above the detector. If E_j is the centre energy of the j'th energy channel, $\mu(E_j)_a$ is the mass attenuation coefficient of air in g cm^{-2}, x_i is the mean atmospheric depth during pointing segment i in g cm^{-2}, and ϕ_i is the mean telescope zenith angle during segment i, then assuming a flat earth approximation;

$$M_A(j,k) = \delta_{jk} \, \exp[-\mu(E_j)_a \, x_i \, \sec \phi_i] \qquad (5.13)$$

where δ_{ij} is the Kronecker δ (the matrix will be diagonal for all non-distributed processes). The attenuation in the detector window, and additional material above the detector may be treated in a similar manner, i.e.,

$$M_B(j,k) = \delta_{jk} \prod_{\ell=1} \exp[-\mu(E_j)_\ell \, d_\ell \, \sec \theta_i] \qquad (5.14)$$

where θ_i is the mean polar angle with respect to the source during pointing segment i and d_ℓ and $\mu(E_j)_\ell$ are the thickness and mass attenuation coefficient of the ℓ'th material above the detector.

The efficiency of the detector, $\epsilon(E)$, is represented by the

matrix;

$$M_E = \delta_{jk} \, \varepsilon(E_j) \tag{5.15}$$

The full energy peak efficiency (rather than the absolute efficiency) was used in the calculation as partial energy loss events are relatively rare in this detector due to its large photofraction and efficient anticoincidence system. For example, at an incident energy of 100 keV approximately 1% of all non-vetoed events are not in the photopeak. This fraction rises almost linearly with energy to ~15% at 1 MeV. Since both source and background spectra decline with energy it was possible (to within the accuracy of the source flux determination) to neglect the non-photopeak contribution in a given channel. An evaluation of Compton contamination events in this detector is given in Appendix E.

The detector FWHM energy resolution, as discussed in Appendix B, is well represented by the function,

$$FWHM = (a_1 E_j + a_2 E_j^2 + a_3)^{\frac{1}{2}} \tag{5.16}$$

where a_1, a_2 and a_3 are semi-empirical constants. The standard deviation of a Gaussian line shape is related to its FWHM by the formula,

$$\sigma = 0.425 \, FWHM \tag{5.17}$$

The matrix M_R is thus composed of elements,

$$M_R(j,k) = \frac{\Delta E_k}{\sqrt{2\pi}\ \sigma_k} \exp\left[-\frac{(E_k - E_j)^2}{2\sigma^2}\right] \tag{5.18}$$

where ΔE_k is the width of channel k in energy units and σ_k is given by equation 5.17.

The incident photon spectrum is then obtained by solving equation 5.11 for F_o, i.e.,

$$F_o = M^{-1}F \tag{5.19}$$

$$F_o = M_A^{-1} M_B^{-1} M_E^{-1} M_R^{-1} F$$

Since M_A, M_B and M_E are diagonal their inversion is simple,

$$M_A^{-1} = \delta_{jk} \exp[\ \mu(E_j)_a\ xi\ \sec\ \phi_i]$$

$$M_B^{-1} = \delta_{jk} \prod_{\ell=1} \exp[\ \mu(E_j)_\ell\ d_\ell\ \sec\ \theta_i] \tag{5.20}$$

$$M_E^{-1} = \delta_{jk}\ 1/\ \varepsilon(E_j)$$

The resolution matrix M_R is difficult to invert numerically because adjacent rows are nearly equal, making the determinant effectively zero. The matrix is for all practical purposes singular. However, with the exception of line structure studies, M_R may be replaced by the matrix $M_R = \delta_{jk}\ \Delta E_k$ for Ge detectors, since in general, ΔE is much greater than the instrumental energy resolution.

5.3 IMAGING WITH THE DURHAM TELESCOPE.

By exploiting the fine Point Spread Function (PSF) of the Durham Telescope it is possible to image a gamma-ray source with a precision comparable with that of COS-B (typically 1^O). This has several advantages which are discussed below.

1) It allows one to correct for systematic and random uncertainties in the orientation system. It should be remembered that the earth's magnetic field is only known to a precision of 0.5^O and misalignments in the steering platform could also be of the same order. A total error of 1^O in pointing accuracy could underestimate the measured source flux by as much as $\sim$ 26%, depending on energy. The problem is resolved if the source is imaged since the position of maximum intensity can be easily determined.

2) For observations of the Galactic Centre and the Cygnus region, source confusion problems can be greatly reduced. For the specific case of the Crab Nebula measurements described in this thesis, it allows one to rule out flux contamination from the nearby flaring source A0535+26. This source can produce a peak flux $\sim$ 4 times that of the Crab at 100 keV which, even with the narrow PSF of the Durham telescope would increase the measured 'Crab' flux by approximately 40% in the energy range 50 to 100 keV.

3) Low susceptability to spurious effects
Imaging is achieved by searching for statistically significant excesses above the surrounding background having a spatial distribution consistent with the PSF. The general method available for separating signal and background in such a case is

the cross correlation method which has been described in detail by Hermsen (1980).

5.3.1 CROSS CORRELATION TECHNIQUE.

The celestial sphere is subdivided into n small rectangular bins whose coordinates in right ascension and declination are i,j. Each gamma-ray event is characterised by four parameters; 1) the incident energy E, 2) the time of arrival t, 3) the zenith angle ϕ and 4) the azimuth angle θ of the observation. An event is attributed to a particular bin i,j if the projection of the telescope axis (which is a function of θ and ϕ) lies within that bin. The raw counts are then converted into 'on-axis' counting rates, $R_{i,j}$, using the procedures described in section 5.1, in order to obtain a uniform event distribution over the entire sky band within the field of view. The correlation function, C(r), is then defined as the sum of the partial correlation functions, each summed over i,j and E and calculated using the covariance representation of the data for an assumed point source at location r. Let the counting rate per bin be $R_{i,j}$. Then,

$$C(r) = \frac{\Sigma w_{i,j} (R_{i,j} - \bar{R})(G_{i,j}(r) - \bar{G})}{\Sigma w_{i,j}} \qquad (5.21)$$

where $G_{i,j}(r)$ is the response of the telescope for point i,j if there is a source at position r and $\bar{R}$ and $\bar{G}$ are the mean values of $R_{i,j}$ and $G_{i,j}$ over the entire n bins excluding those which lie within 2 x HWHM aperture of r. The weighting factor $w_{i,j}$ takes into account the different uncertainties of the counts $R_{i,j}$ per

bin. A gamma-ray source is thus defined as an excess for which the cross-correlation analysis results in a significant correlation, i.e $C(r)/\sigma > 1$. If the data show only statistical variations (no source present) then $C(r)$ will fluctuate around zero with the standard deviation σ. It should be noted that the function $C(r)/\sigma$ must necessarily take on negative values in some regions within the field of view if there is a source present. This is due to the fact that the source leads to an increase in the mean value of $\overline{R}$.

5.4 OBSERVATIONAL RESULTS.

5.4.1 THE CRAB NEBULA.

The Crab Nebula was observed from 17.01.5 to 21.52.25 UT using a raster scan technique. Events were classified as 'on source' if the alignment of the source and the spectrometer axis was less than 0.5 of the FWHM aperture. The choice of this value is not arbitary and is discussed in detail in Appendix F. Similarly 'off source' events were defined when the alignment was greater than the FWHM aperture. After rejecting corrupted data frames a total source exposure of 52203.7 cm^2 s was obtained, corresponding to total on and off source times of 4413.0 and 3756.25 seconds respectively. The energy-loss spectra for 'on source' (i.e. source plus background) and 'off source' (background) are shown in Figure 5.1. The spectrum of the Crab was obtained by subtracting on a channel by channel basis and correcting to the top of the atmosphere using the techniques described in sections 5.1 and 5.2. The results are shown in
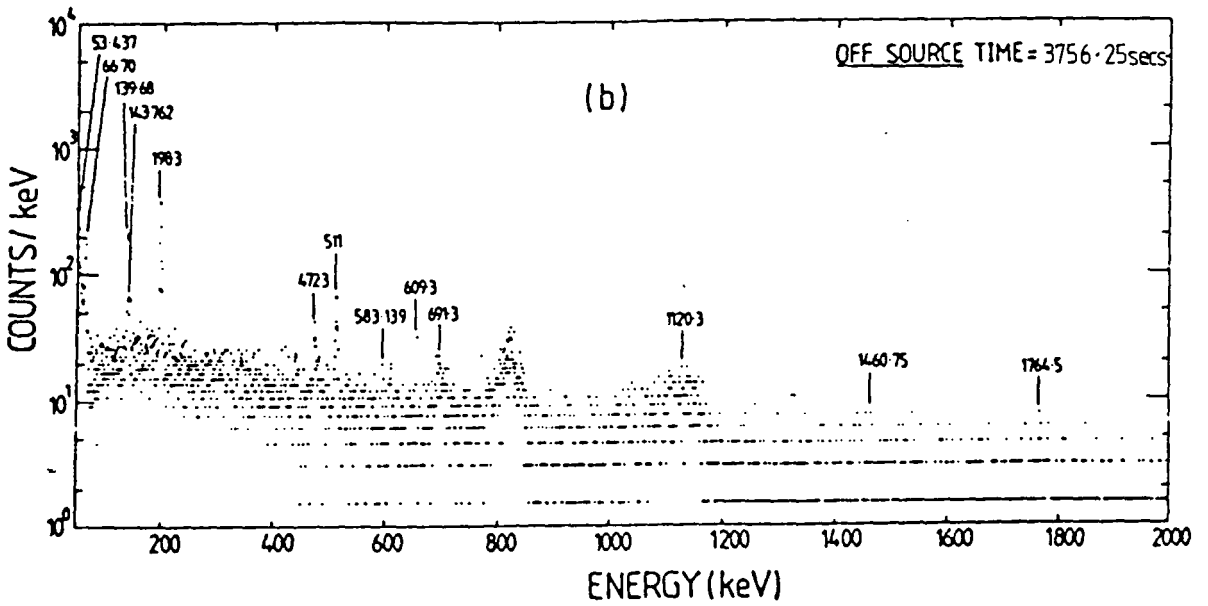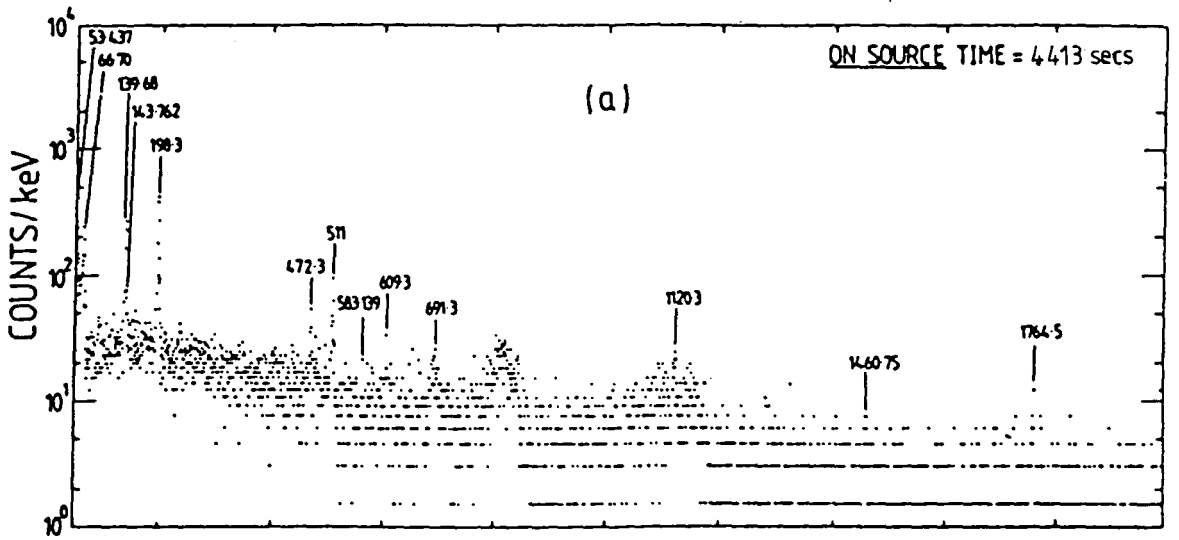
Figure 5.1 (a) The total energy spectrum – on source
measurements,

(b) the energy spectrum for the background
– off source measurements.

Figure 5.2 in which the present measurements in the energy region 50 to 700 keV are compared with previous results. A best fit power law of the form $dN(E)/dE = \beta(E/E_o)^{-\alpha}$ yielded,

$$\frac{dN(E)}{dE} = (8.6 \pm 3.4) \times 10^{-4} \left(\frac{E}{80}\right)^{-2.5 {}^{+2.7}_{-1.2}} \qquad (5.22)$$

compatable with previous measurements. Note E_o is not a free parameter but was chosen to circularise the errors of α and β in two dimensional χ^2 space, thereby enabling these two parameters to be almost statistically independant. The contour shown in Figure 5.2 corresponds to $\chi_{min} + 2.3$ and represents the 68% confidence level for the joint estimation of two parameters (Lampton et al., 1976).

The results of a cross-correlation analysis of the data are shown in Figure 5.3 in which the imaging power of the telescope is clearly demonstrated. For comparison the inset in Figure 5.3 shows the Crab imaged in 3-7 MeV gamma-rays by the MPI Double Compton telescope (Schonfelder, 1979). The contours in the figure mark those regions of the sky where the correlation function has constant positive integer values (1σ levels). The position of the peak of the distribution was determined by fitting the function,

$$C_{i,j} = \begin{cases} a_1[1 - y_{i,j}/\theta_m] , & \text{for } y_{i,j} < \theta_m \\ \\ 0 , & y_{i,j} \geq \theta_m \end{cases} \qquad (5.23)$$

where $y_{i,j} = [(\alpha_i - a_2)^2 + (\beta_j - a_3)^2]^{\frac{1}{2}}$
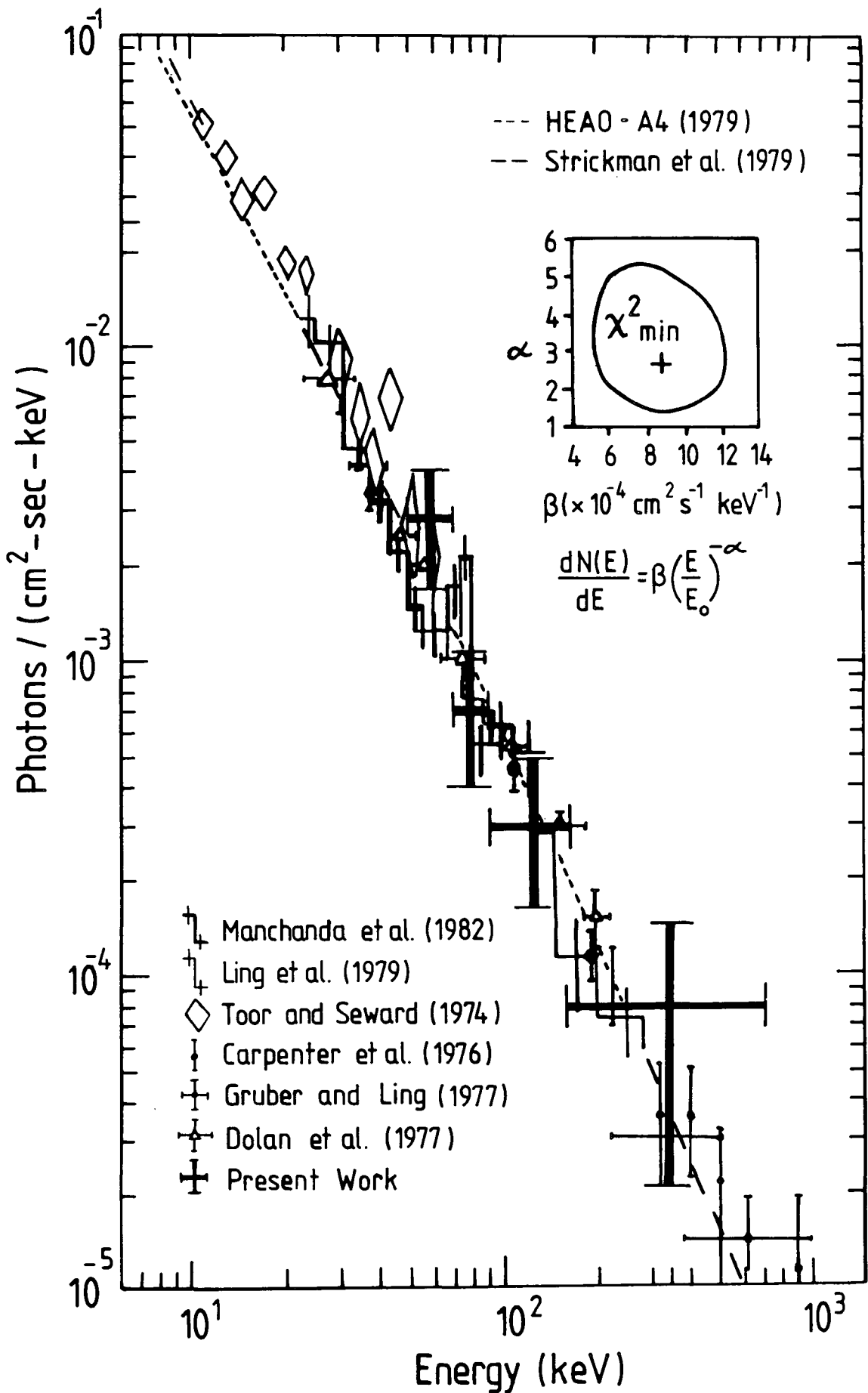
Figure 5·2 The net Crab Nebula photon spectrum measured on June 6 1981. The 68% confidence contour for a single power law fit of the form $dN(E) = \beta(E/80)^{-\alpha}$ is shown in the inset.
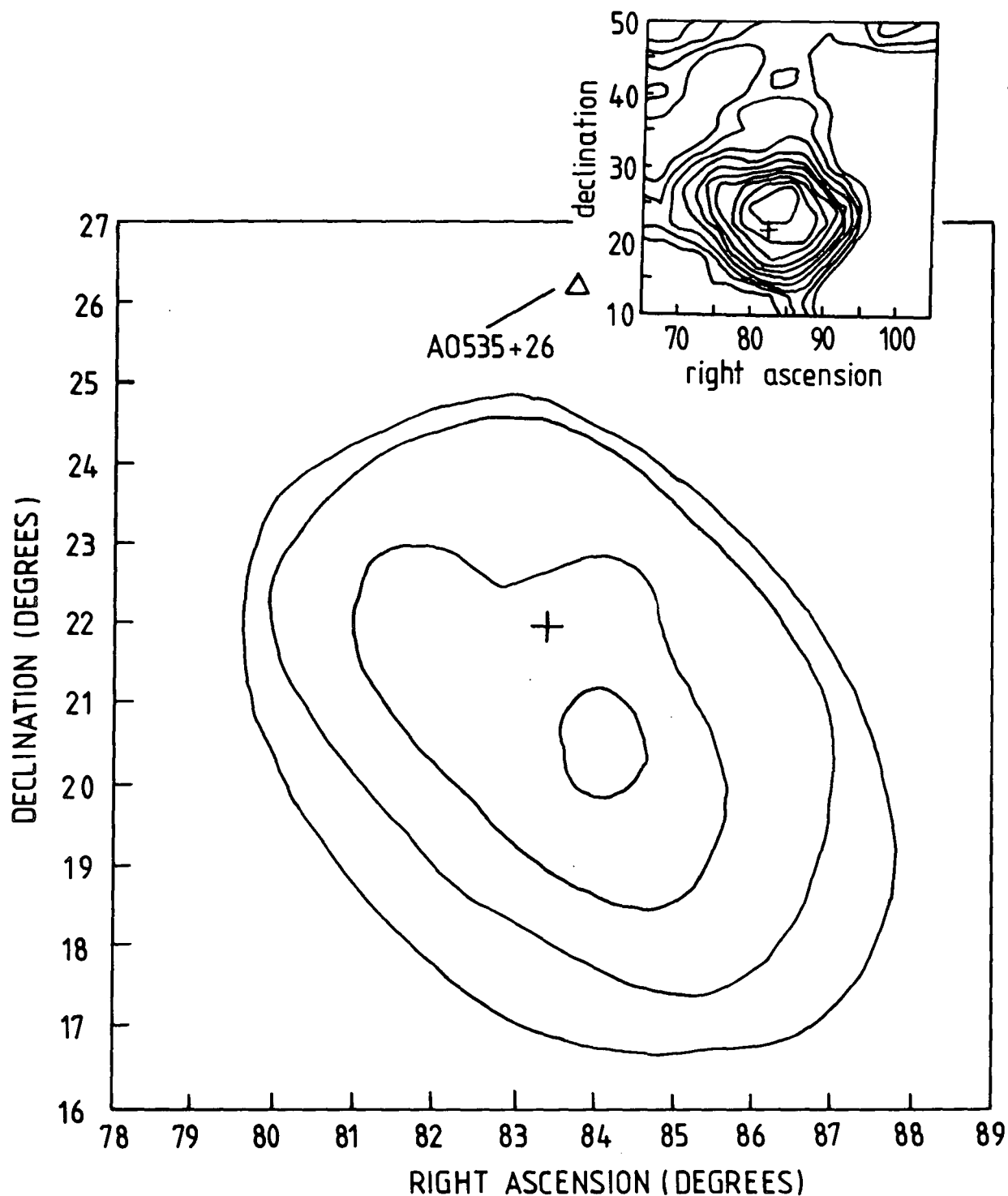
Figure 5·3   Results of a cross-correlation analysis for the field of view containing the Crab. The energy interval of accepted events is 50 to 350 keV. The contours represent positions where the correlation function has constant values at the $n\sigma$ level. The cross denotes the true position of the Crab in 1950 coordinates. From the graph the error in the orientation system is estimated to be 1·4° rms. For comparison the inset shows the Crab imaged in 3-7MeV gamma-rays (Schonfelder, 1979).

to the measured data points $C_{i,j}(r)$, at celestial coordinates α_i, β_j and minimising χ^2 with respect to each of these parameters simultaneously. In the above expression θ_m is the FWHM aperture and a_1, a_2 and a_3 are semi-empirical constants representing the amplitude of the peak and its position in right ascension and declination respectively. A variation of the CURFIT non-linear minimization routine of Bevington (1969) was used to perform the analysis. A minimum χ^2 of 17 for 41 degrees of freedom was recorded at right ascension 83.5° and declination 20.7°. The significance of the peak amplitude was 4.6σ. By perturbing the parameters a_2 and a_3 about their best fit values in χ^2 space the 68% and 90% error radii were determined to be 0.4° and 0.6° respectively.

5.4.2 THE CRAB PULSAR, PSR0531+21

In order to detect pulsed emission from the Crab, the arrival times of events were corrected for the relative motion of the source and telescope and analysed using the epoch folding technique (Yau, 1984). The timing analysis was performed by calculating the phase of the arrival time at the solar centre barycentre of each germanium event. The phase is defined by;

$$\phi = \phi_0 + \nu_0(t - t_0) + \frac{\overset{\circ}{\nu}_0(t - t_0)^2}{2} + \frac{\overset{\circ\circ}{\nu}_0(t - t_0)^3}{6} \qquad (5.24)$$

where ϕ_0, ν_0, $\overset{\circ}{\nu}_0$ and $\overset{\circ\circ}{\nu}_0$ are the pulsar phase, frequency, first time derivative and second time derivative at the reference epoch t_0 respectively and t is the time of the event. The parameters $\overset{\circ}{\nu}_0$

and $\nu_0^{\circ\circ}$ were determined by interpolation from previous observations. The period of the observational epoch was derived from a χ^2 analysis of the resulting light curve. To maximise signal to noise, only data within a geometric acceptance angle of 3.8° (0.95 FWHM) were analysed. Also events whose energies correspond to any of the intrinsic detector background lines were rejected. The maximum recorded χ^2 was 43 for 24 degrees of freedom at a pulsation period of 33.258435 ms. For comparison the expected value of χ^2 is calculated to be 41, assuming a duty cycle for pulsed emission of 60% (Boldt et al., 1971). When the period search is conducted by shifting the light curve over two periods (as recommended by Buccheri et al., 1977) the confidence level that can be associated with the present measurements is 61%. The χ^2 vs period graph shows a fairly narrow peak ~ 20 ns wide which would imply a Q factor $> 10^6$. This essentially rules out the possibility that the pulsations are due to any resonance of the detector or associated electronics. The resulting integrated pulse profile from a superimposed scan of all gamma-ray events in the energy range 50 to 2500 keV is shown in Figure 5.4. This graph represents a total source exposure of 76634.2 cm^2 s. For comparison the predicted response is also shown from which we can see there is good agreement. This curve was obtained by essentially running the analysis techniques described in section 5.2 'backwards' using the magnitude and phase distribution of pulsed emission given in Mahoney et al. (1984). The pulsed and non-pulsed regions of the Crab spectrum were determined using the approach of Helmken (1975). Let N be the total number of phase bins in the light curve of which M are pulsed. The pulsed flux is then calculated from,

0·05 TO 2·5MeV

3·7σ

Measured 243 ± 113 pulsar counts
Predicted 257 ± 96 "   "
Source exposure = 76634 cm^2 s

1·4 σ

Pulsed ——— Non-pulsed

STARTED AT
17·12454
FINISHED AT
21·32252

NO. OF EV=
28813

PERIOD (ns)=
435·00

CHISQ =
1·77982

ORIGIN AT
61200·000

CHANNEL NO.
95 TO
3845

Counts per bin

Phase
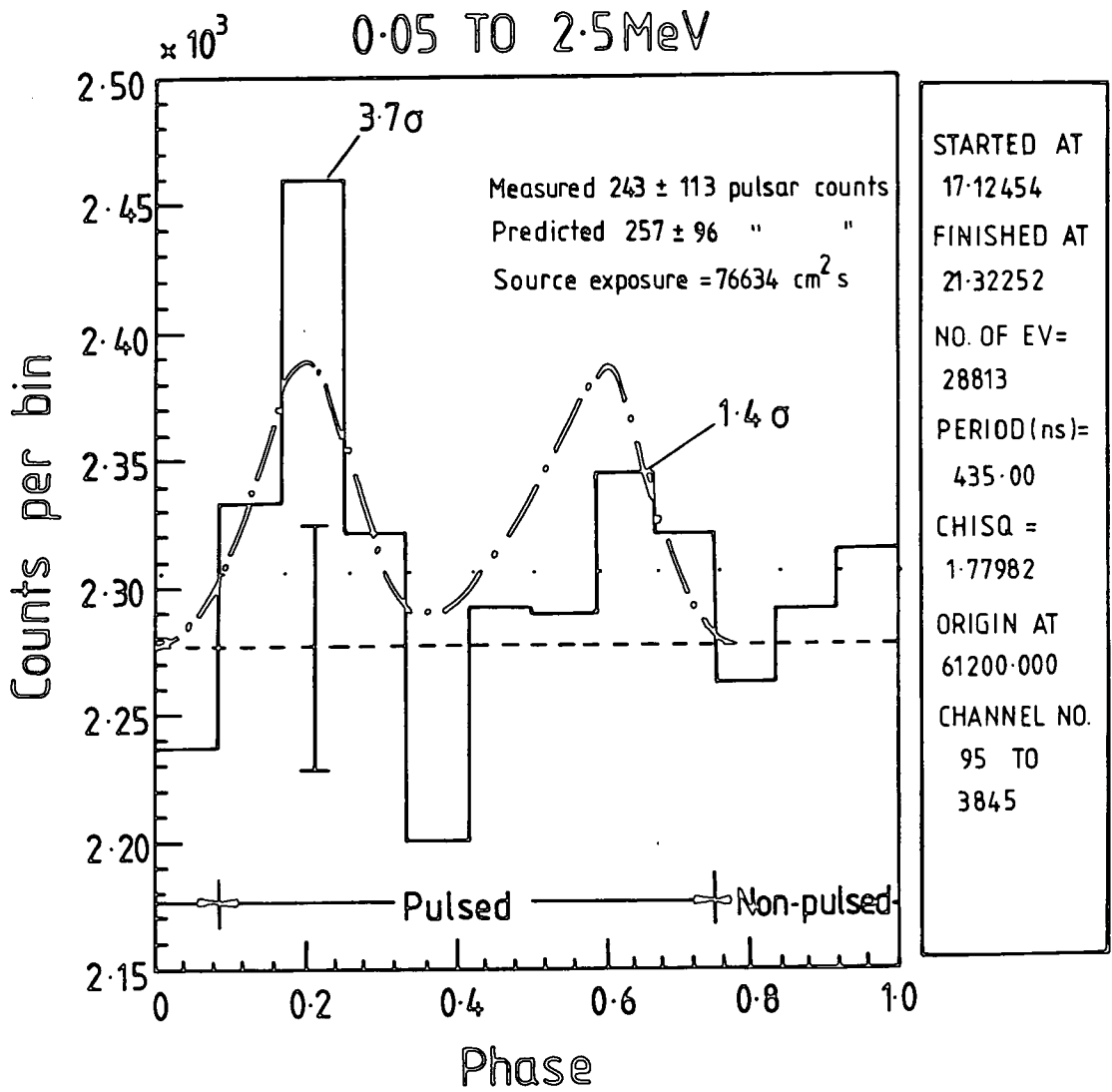
Key :-
· · · · · ·   mean number of counts per bin
— — —   mean background
—·—   predicted response assuming the power law
source flux given in Mahoney et al. (1984)

Figure 5·4   Light curve in the energy range 50keV to 2·5MeV
with 12 bins.

$$F_p = \frac{1}{N} \left[\sum_{i=1}^{M} f(i) - \frac{M}{N-M} \sum_{i=M+1}^{N} f(i) \right] \qquad (5.25)$$

where f(i) is the source flux in phase bin i. The above formula was evaluated for each significant energy interval and corrected to the top of the atmosphere to obtain the spectral distribution of pulsed emission from the Crab. The results shown in Figure 5.5 are in good agreement with previous measurements and are compatable with an $\propto E^{-2}$ power law.

Although marginally significant, it is interesting to note that the present results show a deviation from an extrapolated power law (from either the x-ray or COS B data) at approximately 1 MeV. This is consistent with the measurements of Knight et al. (1982) and Mahoney et al. (1984) which show quite significant deviations ($\sim 2\sigma$) in the MeV region. However it should be noted that the contemporary measurements of Graser and Schonfelder (1982) are consistent with a single power law ($\propto E^{-2.1}$) from the x-ray to the high energy gamma-ray region.

5.4.3 LINES FROM THE CRAB NEBULA.

A computer program scanned the observed Crab energy loss spectrum for statistically significant excesses having a width comparable with the instrumental FWHM energy resolution. A measure of the significance of each detected feature was then obtained using the formulation of Li and Ma (1983) for the hypothesis of zero source counts. Let N_{on} and N_{off} be the number of 'on source' and 'off source' counts accumulated in observing
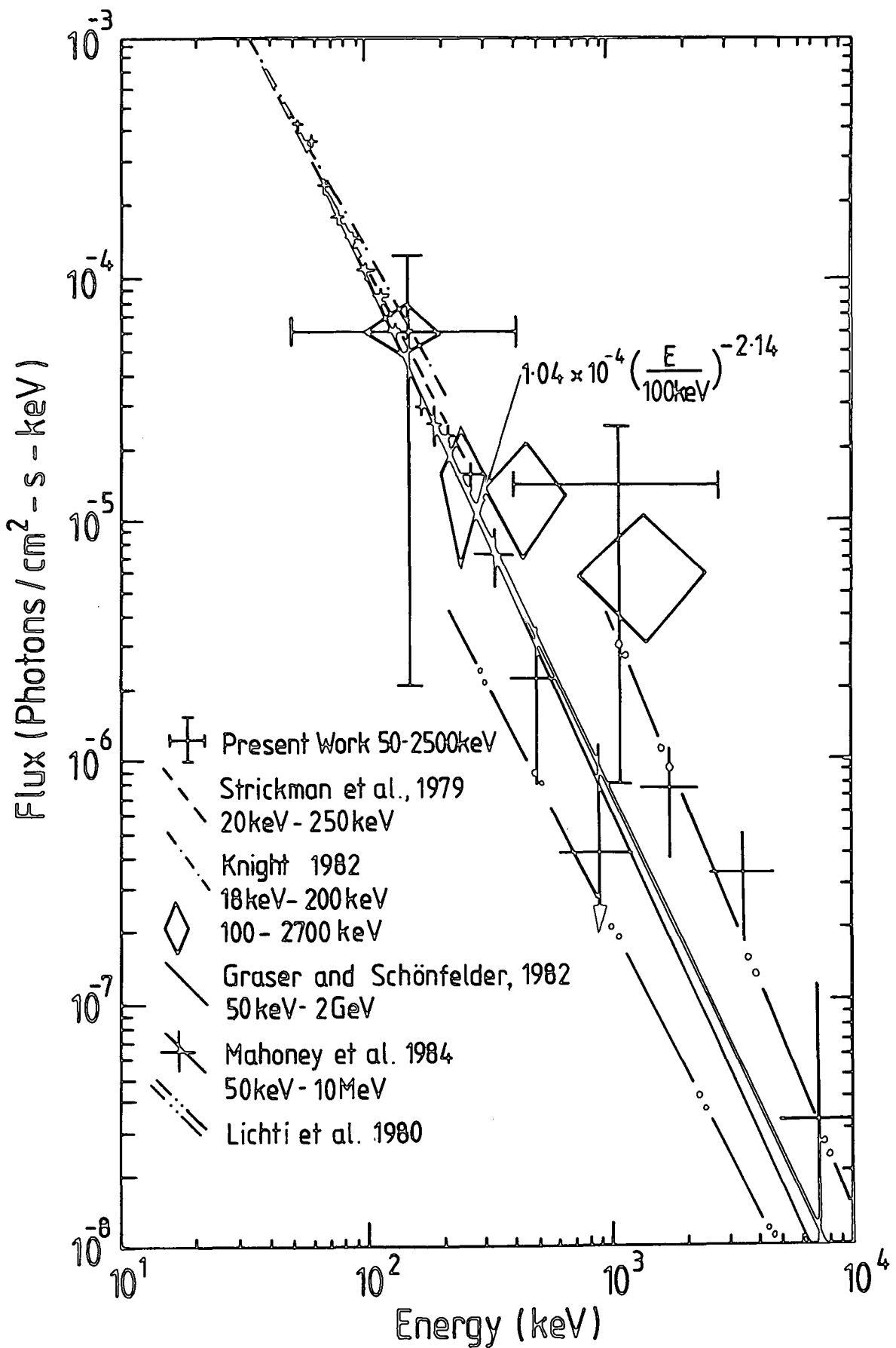
Figure 5·5   The net Crab pulsar spectrum measured on June 6
1981. An extrapolation of the COS-B data (Lichti et al.,
1980) show that the data are consistent with a
single power law from the x-ray to the high energy
gamma-ray region.

times T_{on} and T_{off} respectively. Then the significance, S, of the detected feature will be given by,

$$S = (-2 \ln \lambda) \qquad (5.26)$$

where $\lambda = \left\{ \dfrac{f}{1 + f} \left[1 + \dfrac{N_{off}}{N_{on}} \right] \right\}^{N_{on}} \left\{ \dfrac{1}{1 + f} \left[1 + \dfrac{N_{on}}{N_{off}} \right] \right\}^{N_{off}}$

and $f = T_{on}/T_{off}$. Several features were detected in the energy range 50 to 2000 keV for which S was greater than 3σ. These features centred at energies 330.0, 404.7, 1049.8, 1960 and 1977 keV are listed in Table 5.1 along with their respective calculated significances. In order to estimate the probability of these effects being real the number of degrees of freedom and hence confidence level associated with each candidate line were calculated as follows.

For the 330.0, 1049.8, 1960 and 1977 keV lines, no previous experiments have detected lines around these energy regions. The line search was therefore concentrated in the region between 50 and 2000 keV corresponding to an ADC channel bandwidth of 2985 channels. A peak could have occurred in any of these channels due to random fluctuations of the background. If P_T is the probability that the effect is not due to a random fluctuation in the background at the observed bin, then the probability that the effect is not due to a random fluctuation when M attempts were made to find such an effect is P_T^M. For M, the number of ADC channels corresponding to the energy bandwidth used in the search routine was used. P_T was estimated for each candidate line from the area under the normal distribution for the given value of

Table 5·1   Candidate lines obtained during the total observing period on the Crab. Also listed are the number of degrees of freedom and confidence level associated with each line.

Energy of Feature (keV)	Number of Events		Significance (No. of standard Deviations) at a specific energy	Probability of effect not due to a specific random fluctuation	Predicted range for peak (keV)	Number of degrees of freedom (M)	Confidence level (P_T^M) over M
	Source and Background $(t_{on}=4340.5)$ sec	Background $(t_{off}=3808.25)$ sec					
328.7 – 331.3	73	31	3.5	0.999767	50–2000	2985	0.499
401.8 – 406.4	93	45	3.4	0.999663	395–405	14	0.995
					50–2000 †	2985	0.366
1044.6 – 1053.1	81	26	4.8	0.999999207	50–2000	2985	0.998
1954 – 1965	21	4	3.3	0.999517	50–2000	2985	0.236
1974 – 1980	12	1	3.1	0.999032	50–2000	2985	0.056
77.8 – 79.8*	32	11	4.1	0.9999793	70–80	14 x 3	0.999
					50–2000 †	2985 x 3	0.831

† Predicted range, number of degrees of freedom and confidence level when the line search is allowed to extend over the complete energy range.

* This line was seen only in the last subset of the date with t_{on}= 1571.75 sec and t_{off} = 2019.5 sec.

significance.

For the 404.7 keV line two previous experiments have detected a feature around 400 keV. In the present experiment monitoring of identifiable background lines recorded during the course of the flight indicated that the systematic error associated with any drift of the energy calibration of the spectrometer was < 0.2 keV. Leventhal et al. (1977) reported a feature at (400 ± 1) keV with a 4σ deviation above the continuum and Yoshimori et al. (1979) suggest a 1.4σ effect is present in their data from the Crab at 400 keV. However Ling et al. (1977) reported that they did not observe this line during a balloon flight two years before the balloon flight of Leventhal et al. They concluded that the feature may be variable. The present result would support the two positive experiments. The difference in energy values obtained by Leventhal et al. and the present experiment, which is regarded as significant, cannot be explained by any systematic effect (since monitoring strong background lines enabled both experiments to keep a continuous check on energy calibration). Postulating that the present result confirms that of Leventhal et al. with the difference in energy of the feature being due to source variability, then the number of degrees of freedom can be reduced considerably from the 2985 mentioned previously. The significance of a line is dependant on the number of degrees of freedom, the allocation of which is somewhat subjective. In the present analysis the search for features near to that of Leventhal et al. was reduced to a band of 10 keV centred on 400 keV, corresponding to a range of 14 ADC channels, giving a confidence of 0.995 for the feature centred at 404.7 keV. Taking no account of previous experimental results, the number of

degrees of freedom is increased to 2985 from 14 and the confidence is then reduced to 0.336 (see Table 5.1).

The analysis of the candidate lines suggest that only the 404.7 and 1049.8 keV lines can be regarded as significant. After correcting the fluxes to the top of the atmosphere the incident line fluxes are $(7.2 \pm 2.1) \times 10^{-3}$ photons cm^{-2} s^{-1} at 404.7 keV and $(2.0 \pm 0.5) \times 10^{-2}$ photons cm^{-2} s^{-1} at 1049.8 keV. The corresponding widths (FWHM) are (3.8 ± 1.2) and (6.7 ± 1.5) keV respectively including instrumental resolution. The profiles of the candidate lines are shown in figure 5.6 in which the excess counts (after background subtraction) are plotted as a function of photon energy. The dashed line on each profile represents a best fit non-linear least squares function plus a Gaussian peak of the form;

$$f(E) = a_1 + a_2 E + a_3 E^2 + A \exp\left[-\frac{(E - E_o)^2}{2\sigma^2}\right] \qquad (5.27)$$

The polynomial is included to offset any possible skewness of the peak due to incorrect background subtraction. The fitted widths and peak locations are listed in Table 5.2. After subtracting the instrumental energy resolution, the widths (FWHM) of the 404.7 and 1049.8 keV lines were found to be (3.5 ± 1.4) and (6.3 ± 1.6) keV respectively.

Figure 5.7 shows the results of a cross-correlation analysis of the data for the 405 and 1050 keV lines which are consistent with a point source located at the Crab. In order to determine whether any of the lines given in Table 5.1 were due to spurious effects, the data were reanalysed with the restriction that the
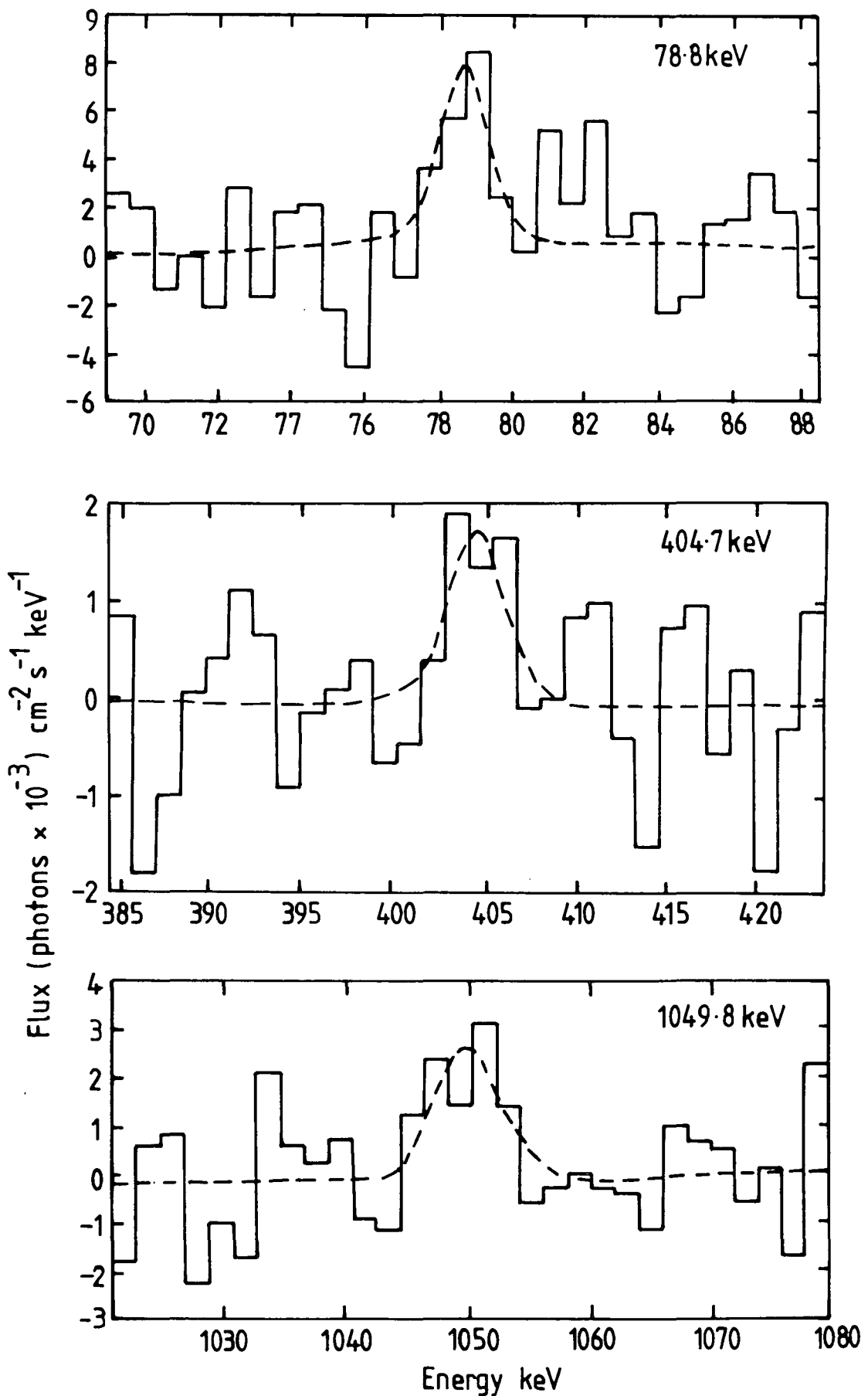
Figure 5·6 Line profiles of the three detected features after correcting to the top of the atmosphere. The dashed line on each profile is a best fit polynomial plus a Guassian peak. The 78·8keV line is discussed in section 5·4·4.

TABLE 5.2   Properies of the significant line features detected on June 6 1981
from the direction of the Crab Nebula. The integral flux in the
energy region 50 to 350 keV is shown for comparison.

Centroid Energy[*]	Position[**]		Error Radius	Flux	Measured	Intrinsic[***]	Luminosity[+]
keV	RA.	Dec.	Degrees	Photons $cm^{-2}s^{-1}$	Width keV	Width keV	erg s^{-1}
50 – 350	83.5	20.7	0.4	$(1.2 \pm 0.3) \times 10^{-1}$	–	–	1.1×10^{37}
78.8 ± 0.2	85.3	20.8	0.4	[+]$(1.1 \pm 0.3) \times 10^{-2}$	1.5 ± 0.4	< 1.5	6.3×10^{35}
404.7 ± 0.7	84.1	21.7	1.0	$(7.2 \pm 2.1) \times 10^{-3}$	3.8 ± 1.2	3.5 ± 1.4	2.1×10^{36}
1049.8 ± 0.8	84.2	21.0	0.5	$(2.0 \pm 0.5) \times 10^{-2}$	6.7 ± 1.4	6.3 ± 1.6	1.5×10^{37}

*   Errors calculated using χ_{min}+ 1, i.e. single parameter determination.

**   Uncorrected for systematic errors in the orientation platform.

*** Instrumental resolution subtracted.

+   Assumed source distance 2 kpc.

†   Peak flux observed in last subset of data with t_{on} = 1572 and t_{off} = 2020 seconds.
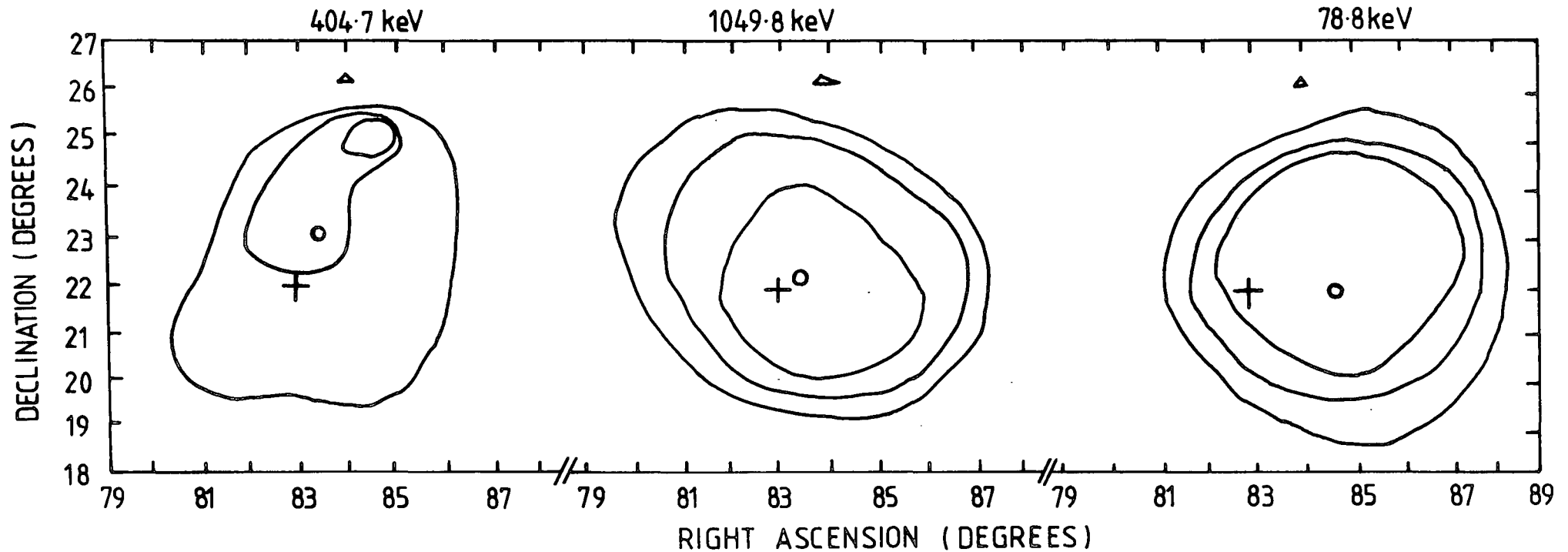
Figure 5·7   Results of a cross-correlation analysis of the significant line features detected on June 6 1981.
The contours represent 1σ levels of the correlation function. The position of the Crab and the
flaring binary x-ray source A0535+26 are shown by the crosses and triangles respectively.
The circles represent the centroids of a best fit aperature response function to the data.
The line feature at 78·8 keV was detected as a transient event and is described in Section 5.4.4.
Note the positions of each of these contours have been corrected for the positional error
in the orientation platform using the gross Crab flux correlation map given in Figure 5·3.
This correction introduces an additional uncertainty in the position of the centroid of about 0·3°.

'on source' polar angle[*]for each celestial bin was $\leq$ 1°. This (at the expense of a statistically degraded data set) prevents any smearing of localised enhancements due to the polar angle distribution. Although the correlation contours for the 303, 1960 and 1977 keV lines are all visibly distorted and do not apparently reflect the PSF, a chi square analysis yielded a reduced χ^2 < 1 for each of these lines primarily due to poor statistics.

The formula of Li and Ma and the search technique are symmetric with respect to both positive and negative deviations. In a search for negative line features it is interesting to note that in the total Crab spectrum only three features were identified with significances greater than 3σ, the largest being 3.87, which when evaluated over 2985 ADC channels corresponded to a confidence level of 0.85.

5.4.4 TEMPORAL BEHAVIOUR.

In order to investigate any possible temporal variation in the intensity of these two lines, the data were divided into three periods having nearly equal source and background observing times for each period. Further subdivision into shorter time periods was not considered worthwhile because of poor statistics. These three subsets were then searched using the same computer line analysis techniques as for the whole data set. The results are shown in Figure 5.8. The dashed region on each graph indicates the mean rate and error over the observation period. The feature of greatest significance (4.1σ) occurs only in the final subset of the data at an energy of (78.8 ± 0.2) keV and a width (FWHM) of (1.5 ± 0.4) keV including instrumental resolution. The properties

---

* See Appendix F for a discussion on the 'on source' polar angle.
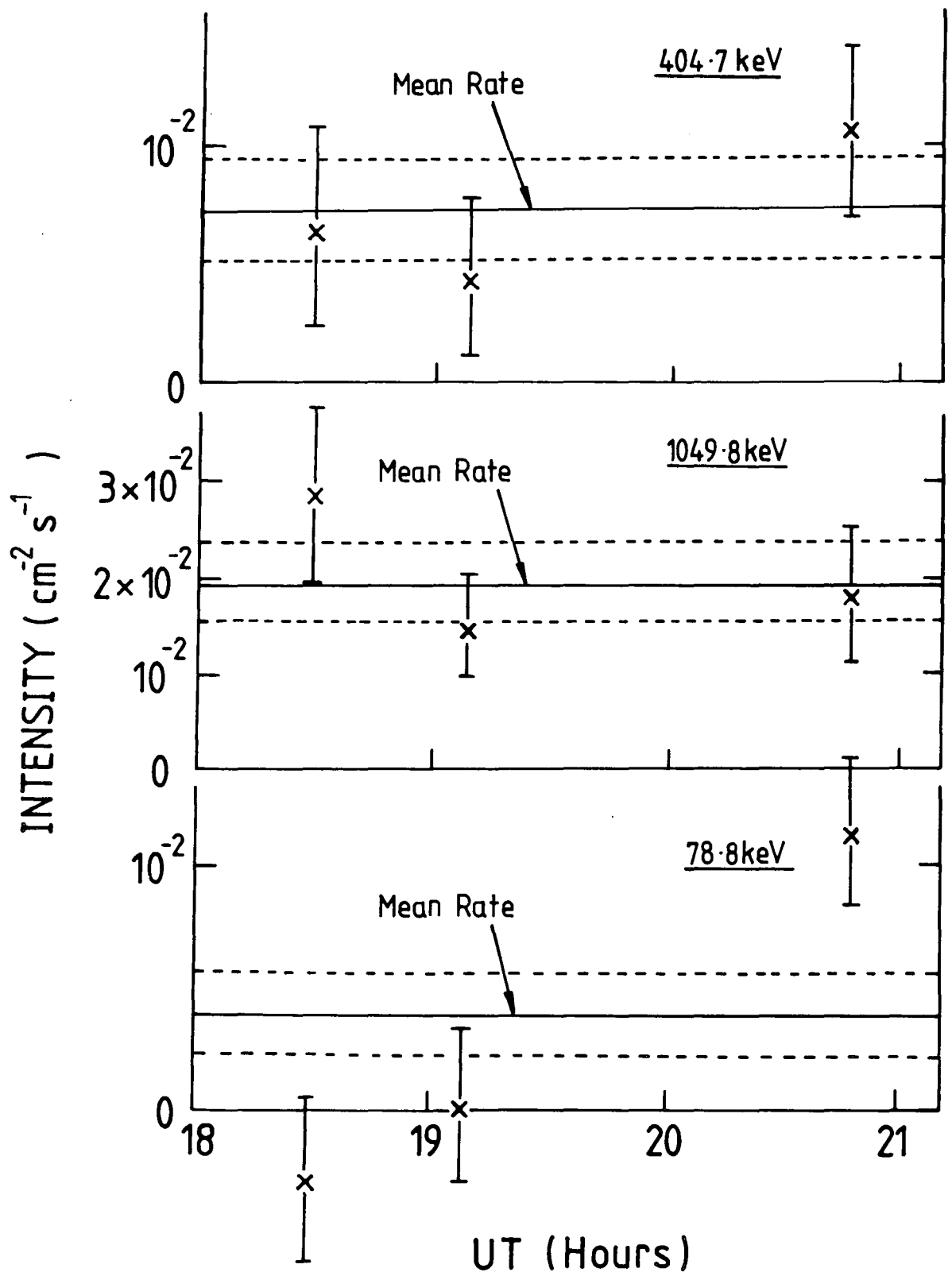
Figure 5·8 Variation in the intensity of the 78·8, 404·7 and 1049·8 keV line features during the observation period.

of this line have been listed at the bottom of Table 5.1 so that a comparison can be made with the other candidate lines. In order to test quantitatively for temporal behaviour a χ^2 test was applied to each of the three lines. The results are shown in Table 5.3. For comparison the 90% upper confidence level for source variability corresponds to a reduced χ^2 of 2.3.

TABLE 5.3

χ^2 Test for Source Variability.

Energy keV	Mean Flux γ cm^{-2}s^{-1}	χ_ν^2 2 dof	$p(>\chi^2)$	Percent Variability
404.7	7.2×10^{-3}	0.89	0.38	< 50
1049.8	2.0×10^{-2}	1.01	0.42	< 35
78.8	3.7×10^{-3}	5.91	0.005	125 ± 39

From the Table it can be seen that both the 405 and 1050 keV lines are consistent with a constant mean rate, or more precisely it is not possible to separate any true source variance from photon noise due to Poisson statistics. However the derived χ^2 for the 79 keV line clearly exceeds the 90% upper limit corresponding to a confidence level of 99.5%.

It is unfortunate that the observation of the Crab finished before any conclusions could be made about the shape of the light curve or when it reached maximum intensity. The present data would indicate a time scale for varibility of approximately 1 hour, mainly limited by bin size. An attempt to determine if any of the detected lines were pulsed at the Crab pulsar frequency was inconclusive due to timing uncertainties and poor statistics.

5.4.5 THE 79 keV LINE.

In the previous section we have shown that there is a high degree of confidence in source variability at 79 keV. However it should be borne in mind that the last data point contributes almost 60% to the resultant χ^2. Therefore perhaps it would be more fitting to rephrase the opening sentence: "we have shown there is a high degree of confidence in the variability of the detector counting rate at 79 keV". The problem we have to address in this section is to determine the degree of confidence we can assign to this last measurement alone. Towards this end we again use the statistics of Li and Ma (1983). As discussed in section 3.2.5 various experiments suggest a line feature in the spectrum of the Crab Nebula in the region 73-77 keV. The measured energy of this feature appears to be variable over an energy range of approximately 5 keV. Consequently for the present analysis a bandwidth of 10 keV centred on 75 keV (i.e. 14 ADC channels) was considered when evaluating the significance of any spectral feature in this energy range. As the effect is only observed in approximately the last third of the data, the number of degrees of freedom is increased to 42 and this gives a confidence level, (P_T^M), of 0.999 for the line. Ignoring previous experimental observations in this energy region, then the number of degrees of freedom associated with the search is increased to 8955 (i.e. 2985 x 3) and the confidence level is reduced to 0.831 (see Table 5.1).

Although it had been previously suggested this line may originate from the nearby binary flaring source A0535+26, a cross correlation analysis shown in Figure 5.7 clearly shows the line emanates from the Crab Nebula region. The parameters for the best

fit to the distribution are given in Table 5.2 and are consistent with a point source. Further, assuming the absence of bulk relativistic motion, we can infer a source size by the usual time of flight argument. This is of the order of 10^{14} cm which strongly implies the emission emanates from the pulsar itself (the Nebula is $> 10^{18}$ cm across).

5.4.6 NGC1275 (3C 84).

The region of the Perseus cluster was observed between 14.55 and 16.55 UT. in an attempt to measure the non-thermal component of its photon spectrum, which most likely originates from the nucleus of the type II Seyfert galaxy NGC1275 (Rothschild et al., 1981). A source exposure of 53836.5 cm^2 s was obtained, corresponding to total on and off source times of 3852.7 and 1150.8 seconds respectively. A spectral analysis yielded mainly 1σ upper limits. The results shown in Figure 5.9 are in agreement with previous measurements. A search for spectral lines detected three features in the energy range 50 to 2000 keV, having a significance in the detected flux of $> 3\sigma$. The properties of these lines, centred at energies 502.1, 621.0, and 911.1 keV, are summarized in Table 5.4. For the 621 and 911 keV features, no previous experiments have detected lines at these energies and therefore in assessing their confidence levels the number of degrees of freedom was taken as 2985. For the 502.1 keV line a bandwith of 10 keV centered on 502.17 keV was used (this being the energy where redshifted annihilation radiation is likely to appear). The analysis of the candidate lines suggests that only the 502 keV feature can be regarded as significant, having a
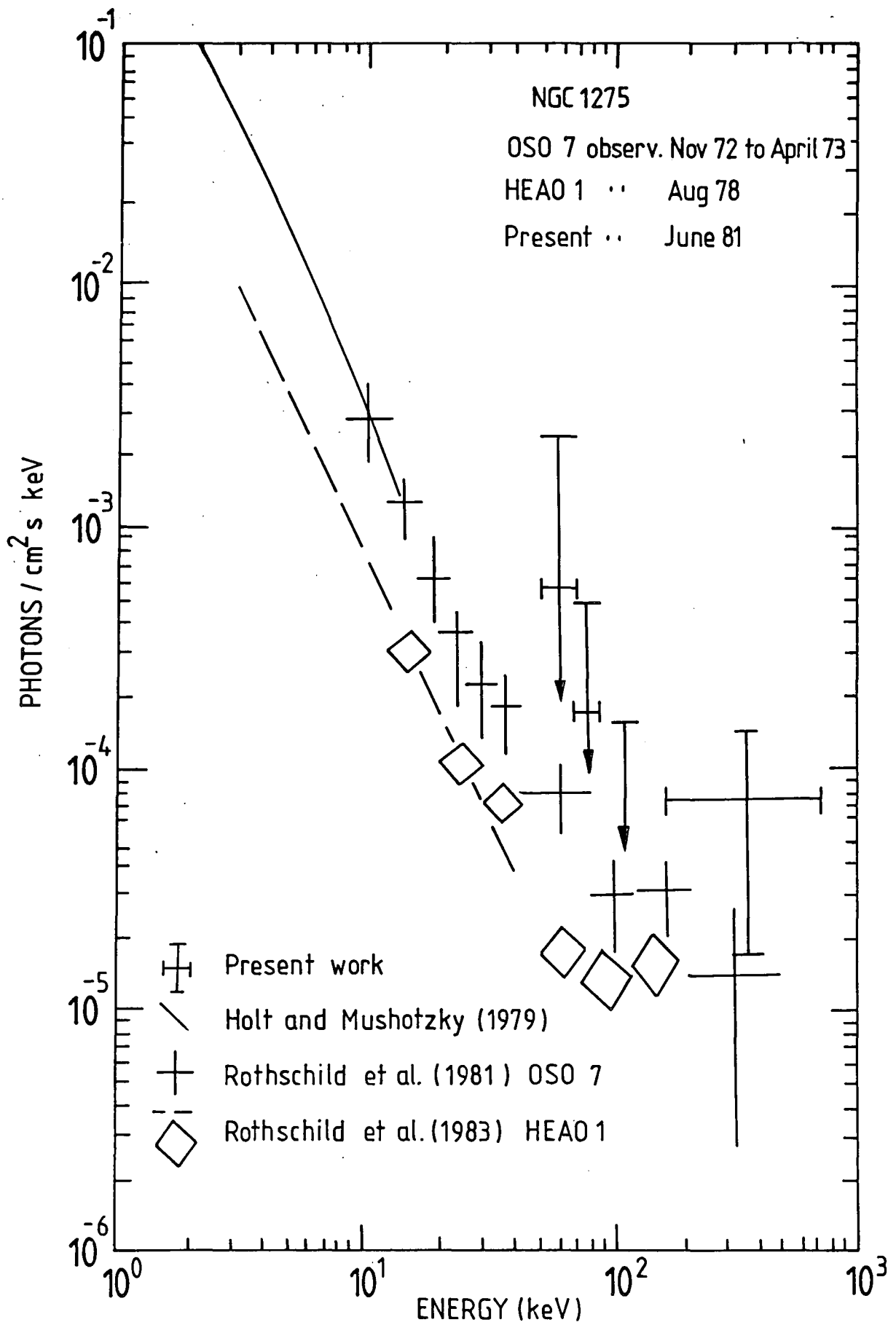
Figure 5·9 Energy spectrum of the Seyfert galaxy NGC1275 in the direction of the Perseus cluster. The upper limits obtained by the present experiment are at the 1σ level. Variability is evident.

TABLE 5.4 Candidate lines obtained during the total observation period on the Seyfert galaxy NGC 1275. Also listed are the number of degrees of freedom and confidence level associated with each line.

Energy of feature (keV)	Number of events		Significance (No. of standard deviations)	Probability of effect not due to a random fluctuation	Range[+] (keV)	No. of Degrees of freedom M	Confidence Level (P_T^M) over M
	Source + Background 3852.8 sec	Background 1150.8 sec					
500.47-503.73	41	2	3.3	0.999517	497-507	14	0.993
					50-2000[*]	2985	0.236
618.05-623.93	56	5	3.1	0.999032	50-2000	2985	0.056
909.41-912.68	32	1	3.3	0.999517	50-2000	2985	0.336

+ Predicted range for peak to occur.

* Predicted range, number of degrees of freedom and confidence level when the line search is allowed to extend over the entire energy range.

confidence level of 0.993. Taking no account of the significance of the energy where the line occurs, then the number of degrees of freedom is increased from 14 to 2985 which reduces the confidence level to 0.24 (see Table 5.4).

The present result is regarded as significant for the following reasons. NGC 1275 appears to contain a scaled up version of the non-thermal radio source at the Galactic Centre (from which annihilation radiation has been detected). Furthermore the non-thermal activity appears to be confined to the central region, implying that energetic particles produced in the nuclei do not escape into the low density regions of interstellar or intergalactic gas (where they would avoid rapid annihilation). The measured flux of this line at the top of the atmosphere is $(7.1 \pm 2.2) \times 10^{-3}$ photons cm^{-2} s^{-1} which suggests that $\sim 10^{51}$ positrons s^{-1} must be annihilating into 511 keV photons at the source, assuming isotropic emission. The line width was determined to be (2.72 ± 1.2) keV. After subtracting the instrumental resolution the intrinsic line width is (2.5 ± 1.3) keV which would imply production in a region of partially ionised gas of temperature $< 2.5 \times 10^4$ K. If the gas were neutral the line width would be larger than that measured due to Doppler broadening; not by the thermal motion of the gas, but by the velocity of the energetic positrons forming positronium in flight by charge exchange with neutral hydrogen (Ramaty and Lingenfelter, 1981). The measured line width would then suggest an ionisation fraction > 10% (Bussard et al., 1979). The present results indicate a luminosity of 8×10^{45} ergs s^{-1}, comparable with the x-ray and infra-red luminosities. Marscher et al. (1984) have proposed that the positron production rate, and therefore the 511

keV flux, should scale roughly as the compact non-thermal radio luminosity. Assuming an averaged Galactic Centre 511 keV line flux of 1.3 x 10^{-3} photons cm^{-2} s^{-1} and an NGC 1275 radio flux density of 4.1 Jy (Haschick et al., 1982), then the expected 511 keV flux is 7.4 x 10^{-3} photons cm^{-2} s^{-1}, which is very close to that measured. However it should be pointed out that Marscher et al. (1984) found no such correlation in a study of 7 mildly active galaxies.

5.4.7 CG195+5

The gamma-ray source γ195+5 was first discovered by the SAS 2 satellite (Thompson et al., 1973) and even though it is the second brightest object in the 2CG catalogue (Swanenburg et al., 1981), it has still not been unambiguously identified at other wavelenghts. Recently Bignami al. (1984) tentatively suggest the weak x-ray source 1E0630+178 as a possible counterpart based on a timing analysis. All previous measurements in the x-ray or low energy gamma-rays have so far yielded upper limits (Coe et al., 1978; Haymes et al., 1979; Hayles, 1981).

The low energy gamma radiation from the direction of CG195+5 was studied between 16.20 and 17.07 UT. yielding a limited source exposure of 1452 cm^2 s. The results shown in Figure 5.10 are consistent with zero flux. The derived 1σ upper limits lie approximately two orders of magnitude above an extrapolation of the COS B measurements. A search for line emission produced a positive result at a centre energy of 511 keV and a significance in the detected flux at the ∿2σ level. The incident flux at the top of the atmosphere was calculated to be (6.9 ± 2.8) x 10^{-2}

photons cm^{-2} s^{-1}. Since there have been no previous reports of 511 keV radiation from the direction of this source, the calculated confidence level for 2985 degrees of freedom is <<1%. However, in spite of the low degree of confidence it is intriguing to note that Haymes et al. (1979) also have a positive detection at approximately 511 keV (see Figure 5.10).
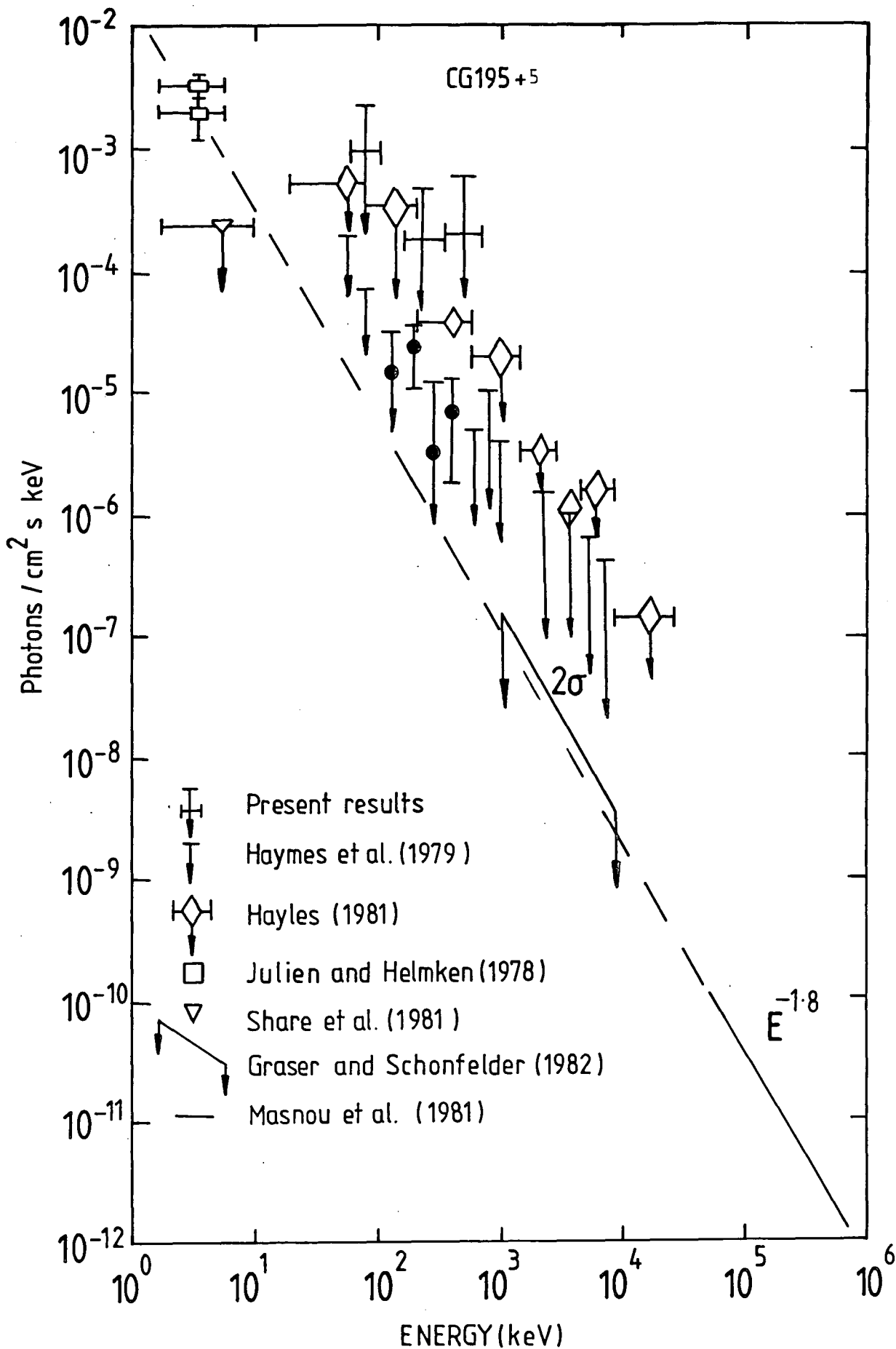
Figure 5·10 Energy spectrum of the Geminga source at the top of the atmosphere. The upper limits obtained by the present experiment are at the 1σ level.

CHAPTER 6.

LINES FROM THE CRAB - A DISCUSSION

6.1 INTRODUCTION.

Of the six significant lines detected by this experiment from the direction of the Crab Nebula, three can be dismissed by confidence arguments. The three remaining lines will be discussed further and, in the absence of self consistent theoretical models, experimental constraints on the emission mechanisms and regions will be given. It should be understood that this thesis is experimental in nature and therefore some of the conclusions reached may be naive.

6.2 THE 404.7 keV LINE.

The physical origin of this feature is uncertain. As there are no known nucleosynthetic lines at or around this energy, it has been previously assumed that this line is due to gravitationally redshifted annihilation radiation (Leventhal et al., 1977). Several mechanisms have been suggested for generating positrons at or near a neutron star. The most widely accepted models generate large positron fluxes in the co-rotating magnetosphere (Sturrock, 1971) or in a polar spark gap (Ruderman and Sutherland, 1975), via various pair production processes (Cheng and Ruderman, 1977). The present experimental data indicates that $\sim 10^{42}$ positrons s^{-1} must be annihilating into 511 keV photons near the stars surface, assuming isotropic emission. Taking into account possible beaming effects, the result is in

good agreement with the $\sim 10^{41}$ positrons s^{-1} predicted in Sturrock's model. Further, the narrow width of this line implies that the annihilation site is one of relatively low density partially ionised gas of temperature less than 10^7 K which would tend to favour an inner gap model. The width of the feature can also be used to place an upper limit on the magnetic field strength in the emission region, even if the line of sight is 0° and the particles annihilate at rest. For this case Daugherty and Bussard (1980) have shown that,

$$\frac{\Delta E_\gamma}{E_\gamma} = \frac{\ell n2}{2} \frac{B}{B_{cr}} \qquad (6.1)$$

where B_{cr} = 4.414 x 10^{13} gauss. The upper limit on the field strength derived using from the present measurements is (1 ± 0.1) x 10^{12} G. The derived redshift of the line is (0.263 ± 0.02) suggesting a pulsar mass of 1.4 to 2.1 $M_\odot$, depending on the equation of state. This value is reasonable (Borner and Cohen, 1973). The apparent variability of the redshift, from 0.28 in 1976 (Leventhal et al., 1977) to 0.26 in 1981 is regarded as significant since systematic errors in the energy calibration of both experiments are negligible. The possible causes of this phenomenon are discussed in a later section.

It has been suggested (Lingenfelter et al. 1978) that the 400 keV feature detected by Leventhal et al. from the general direction of the Crab may also be variable emission from the same source as the June 10 1976 transient event observed by Jacobson et al. (1978). The two observations had overlapping fields of view and the identification of the lines implied essentially the same

neutron star surface redshift. A cross-correlation analysis of the present data shows that the 405 keV line emanates from the Crab, which strongly suggests that the transient event detected by Jacobson et al. does not originate from the same source, since the Crab was essentially out of their field of view (compare Figures 3.15 and 5.7).

6.3 THE 78.8 keV LINE.

Various mechanisms have been proposed for the production of a line near 77 keV; radioactive decay of material produced in a supernova (Ling et al., 1979) and cyclotron emission from electrons moving in the magnetic field around the pulsar (Manchanda et al., 1982; Trumper et al., 1978). Both the pulsed, and the longer term time variability (Strickman et al., 1982) would tend to rule out radioactive decay of debris from the supernova. Cyclotron emission would therefore seem to be the most likely explanation. However the measured width of the present result (< 1.5 keV) would strain even this explanation, placing extremely tight constraints on the emission region.

The exact physics of cyclotron emission around a neutron star are unclear (Basko and Sunyaev, 1975, Meszaros, 1978). A priori it is assumed that the upper Landau levels may be populated which in turn emit resonant radiation at the gyrofrequency. Assuming the 78.8 keV line is due to cyclotron emission, then at the first harmonic,

$$E_\gamma = \frac{heB}{2\pi mc} = \frac{11.6 \ B(gauss)}{10^{12}} \quad (keV) \qquad (6.2)$$

Interpreting the 404.7 keV line as gravitationally redshifted annihilation radiation, the unshifted energy of the 78.8 keV line is 99.5 keV, assuming production in the same region. This would correspond to production in a magnetic field, B, of 8.6 x 10^{12} G assuming the electrons are at rest. A relativistic quantum mechanical treatment might enhance this value by a factor of two (Brecher and Ulmer, 1978). Further, assuming the pulsar energy supply is derived from its rotational kinetic energy, the energy loss rate will be given by,

$$\frac{dE}{dt} = I\Omega\dot{\Omega} = \frac{B^2 R^6 \Omega^4}{c^3} f\left(\frac{R\Omega}{c}\right) \qquad (6.3)$$

where I is the moment of inertia, R is the pulsar radius, Ω is the angular velocity, $\dot{\Omega}$ is the spin down rate and $f(R\Omega/c)$ is a dimensionless quantity approximately equal to one. For the specific case of the Crab pulsar, B $\sim 10^{12}$ to 10^{13} G which is in agreement with our derived value. For a dipolar field this would strongly imply the emission is close to the neutron star surface.

6.3.1 THE EMISSION REGION.

Given the uncertainties in the present theoretical models for cyclotron emission near a neutron star we attempt to use our experimental results to characterise the emission region. The width of the measured line may be due to several mechanisms of which Doppler and magnetic broadening are the most important. Doppler broadening is anisotropic since the thermal agitation of

the electrons in a strong magnetic field is only parallel to the field vector. Let θ be the angle between the photon direction and the magnetic field. Then,

$$\frac{\Delta E_\gamma}{E_\gamma} = \sqrt{8\ell n2 \, \frac{kT}{mc^2}} \quad \cos \theta \qquad (6.4)$$

For a characteristic temperature of 37 keV for the thermal distribution of the electrons (Strickman et al., 1982), θ is greater than 88° which implies that the emission is strongly concentrated in a plane perpendicular to B, i.e. a fan beam. For the case of magnetic broadening we can place limits on the size of the emitting region. Since $\Delta E/E = \Delta B/B$, magnetic inhomogeneities must be less than 1.9% which suggests that the emission cannot not take place over an extended region. Further, for a dipole field (B $\propto$ R^{-3}) it follows that for R = 10 km the radial extent of the emission region is < 63 meters ! A remarkably small quantity to be observed at a distance of 6 x 10^{19} m. It is interesting to note that this small distance would suggest a polar spark gap model (Ruderman and Sutherland, 1975). Production in this region would have little problem in explaining the continuous injection of electrons necessary' to sustain the emission (electrons in excited cyclotron states radiate on time scales considerably shorter than 25 minutes). However as Strickman et al. (1982) point out the acceleration region must be turned off, at least temporarily, for emission to occur.

The apparent shift in the line energy over the last decade has been attributed to movement of the emission region due to magnetic instabilities near the surface. However as we attempt to

show, this may not be entirely correct. Noting that Strickman et
al. (1982) observed the 77 keV line from the Crab within one day
of Leventhal's observation of the 400 keV line, and correcting the
present unshifted line energy for the redshift derived from
Leventhal's result yields a shifted energy of 77.9 ± 1 keV. The
implication is that the apparent energy variability is not due to
a change in field configuration but solely to a variable surface
redshift. If this is true then z has changed from 0.37 in 1974 to
0.26 in 1981. There is no known mechanism that would explain this
since the redshift at a particular point depends only on the
pulsar's mass. Either the mass has decreased by ~ 0.05 $M_\odot$ or the
emission regions of <u>both</u> the 400 keV and the 77 keV lines have
moved radially outwards by approximately 850 m. This latter
explanation would suggest an outer gap model and a common emission
region which in turn suggests production from the same population
of particles. With respect to a common emission region, the
magnetic broadening of each line implies that the emission region
of the 405 keV line is located approximately twice the distance
from the neutron star's surface than that of the 79 keV line.
However there is some tenuous (very) evidence to support either a
common emission region or production mechanism. From inspection
of the world data given in Figure 6.1 we can see that with one
exception the data are consistent with coincident emission of both
lines (at least within 1 day). The present results would also
support this conclusion.

At this juncture it may be worthwhile to try and determine
the observational prospects for the 79 keV feature. A frequency
analysis was performed on the world data given in Figure 6.1
assuming that the light curve is a delta function of duration < 1
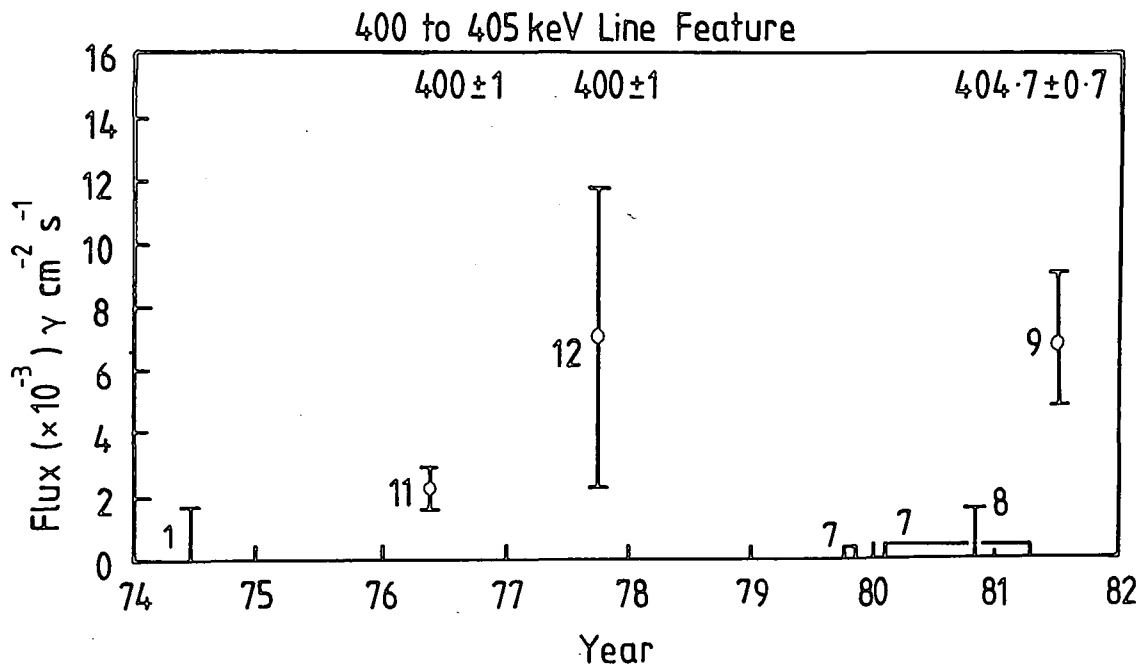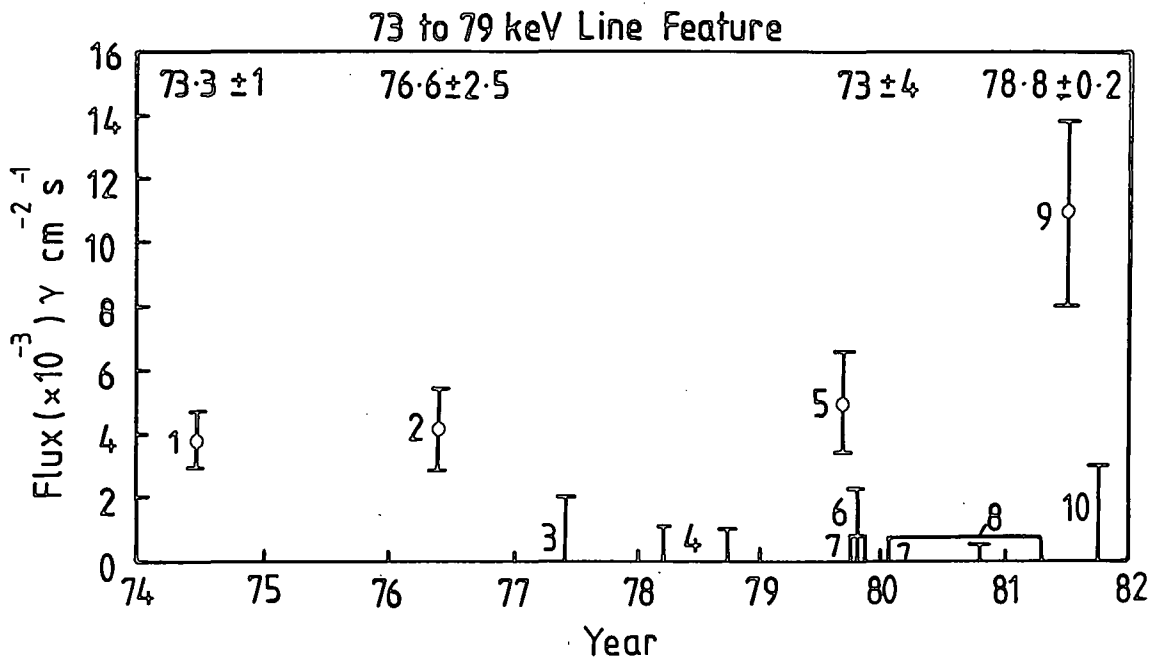
Figure 6·1   Presentation of the observational status of the 77 and
400 keV line features. Upper limits are given at the 3σ
level. Above each significant measurement is given the
centroid of the peak. The reference numbers are ;
1 Ling et al.(1979), 2 Strickman et al.(1982), 3 Dipper (1979),
4 Knight (1982), 5 Manchanda et al.(1982), 6 Schwartz et al.
(1980), 7 Mahoney et al.(1984), 8 Hameury et al.(1983),
9 Present work, 10 Hasinger et al.(1982), 11 Leventhal et al.
(1977), 12 Yoshimori et al.(1979).

day. Also the HEAO C data were ignored since the data correspond to 2 day integrations and as Mahoney et al. (1984) point out a flare of duration 25 minutes would not have been detected. A surprisingly good fit was found at a period of 12.5 days and a maximum width of 33 minutes. At half this period the results are at variance with the upper limit of Knight (1982). However it should be noted that Knight searched the data for a line at 73 keV and may therefore have missed a feature around 77 keV. If the result of Knight is ignored, then a statistical analysis of the world data would indicate a fundamental period for flaring of 3.1 days. This last result should be interpreted with caution since periodic behaviour on this time scale cannot be satisfactorily explained for an isolated neutron star.

6.4 THE 1049.8 keV LINE.

The 1049.8 keV line has not been seen before and there is no obvious mechanism for producing a line at this energy. If the effect is real then the narrow width and high luminosity ($\sim 10^{37}$ ergs s^{-1}) would suggest production at the pulsar itself. In this case the line represents almost 20% of the total electromagnetic luminosity. Although a search for pulsed emission was inconclusive because of timing uncertainties, it is interesting to note that the excess in the MeV region of the derived pulsar spectrum (Figure 5.5) can be accounted for by this line. This would therefore imply pulsed emission, and add further weight to a pulsar origin. The measured width of the feature places upper limits on the temperature and magnetic field strength within the emission region. These are 10^7 K and 7×10^{11} G respectively

which would suggest a common emission region with the 405 keV line and therefore production from the same population of particles. One might, at first thought, invoke single photon annihilation (Daugherty and Bussard, 1980), but the width of the line and the relative intensity of the 405 keV line rule out this possibility.

As mentioned previously the 1049.8 keV line has not been seen before, however in an analysis of a balloon flight in September 1972, Baker et al. (1973) have suggested that the continuum flux in the MeV region is higher than that expected from an extrapolation of low energy data. Similar results were found by Gruber and Ling (1977) from data obtained from a balloon flight on August 8 1971. The measured excess over a power law spectrum represented almost 50% of the total energy output of the Crab. Gruber and Ling speculate that the excess may be due to either the flaring source A0535+26 or a pulsar timing 'glitch'. Assuming this excess was due to an emission feature at 1050 keV the former explanation can be ruled out from a cross correlation analysis of the present data which is consistent with a point source located at the Crab (see Figure 5.7). With regard to the latter explanation, Fazio et al. (1972) reported observable levels of 10^{11} eV flux following (within a 60 day delay) 'glitches' on September 29 1969, August 1 1971 and October 20 1971. However the present pulsar timing analysis rules out any glitch. Also it should be pointed out that the contemporary measurements of Schonfelder et al. (1975) and Carpenter et al. (1976) are consistent with a single power law.

It is clear therefore that confirmation of this line is required by a separate experiment.

6.5 CODA.

The advent of cooled semi-conductor detectors into gamma-ray astronomy can be likened to the introduction of the modulation collimator or coded aperture masks into soft x-ray astronomy. In contrast though, the present results clearly demonstrate that high resolution astronomy is still in the discovery phase. It is hoped that the analysis techniques and interpretation of data described in this thesis have been clearly presented and an overall impression of caution has been given. Unlike earlier gamma-ray line experiments, we claim positive detection on purely confidence grounds and not on positional or theoretical coincidences. In the absence of suitable theoretical models, it is perhaps not so surprising that the present results seem not only at variance with other measurements but also with themselves. Therefore further work, both observational and theoretical, is necessary to understand the processes taking place within the Crab Nebula. In view of the fact that the present measurements have raised many more questions than they have answered, these processes would appear to be at the most basic level.

APPENDIX A

THE PLATFORM AND STEERING SYSTEMS

A.1 DESIGN CRITERIA.

To utilize the high sensitivity of the Durham spectrometer to point sources, a stable platform that could be steered accurately was required. In this context, an alt-azimuth steering system was chosen to orientate the telescope. The chief constraint on its simplicity was set by the sharply peaked angular response function of the collimator (5° FWHM), which suggested an absolute steering accuracy in both azimuth and zenith of about $\pm$ 1^O.

The extra steering problems encountered by using a balloon borne telescope over those of a ground based instrument are related to balloon drift, rotation, and balloon-payload pendulation. Balloon drift in the prevailing winds causes changes in latitude and longitude, which during a typical flight of $\sim$ 10 hrs might be as much as 6° away from the launch site. Rotation is believed to be caused by wind shears and small vertical oscillations, and though erratic can produce angular velocities as great as 1^O s^{-1} (O. Mace, private communication). The causes of compound pendulation between the balloon and payload are closely related to those of rotation but little is known about its magnitude as few practical guides are available. The natural period of a typical balloon and payload would be $\sim$8 minutes and an amplitude no greater than 1^O would seem reasonable (T. Jenkins, private communication).

Additionally, the platform would have to operate over a wide

temperature range, from ∿20°C during daylight to ∿-40°C at night at float altitude, and be capable of withstanding temperatures as low as -80°C during ascent through the tropopause.

Finally the platform would have to be mechanically strong to endure the rigours of launch and landing and yet light enough so that a maximum ceiling altitude < 5 g cm^{-2} may be achieved.

A.2. MECHANICAL CONSTRUCTION OF THE GONDOLA.

With such a large payload working within strict weight limitations, it was imperative that the gondola was as light as possible and that there were no redundant parts remembering that stiffness was vital if a systematic position accuracy < 0.5° on each axis was to be obtained. The construction of the gondola was also restricted to non-magnetic materials as the payload was to be orientated using the earth's magnetic field and the proximity of moving ferro-magnetic components would produce erroneous results from the magnetometers. For these reasons HE 30TF aluminum alloy was chosen for the construction material because of its adequate tensile strength, good welding characteristics, and ready availability.

Figure A.1 shows the completed gondola with the telescope integrated. The telescope is supported in an inner aluminum structure which is bolted to a 1/2" thick dural plate welded into an outer 4ft. diameter ring. The telescope is then enclosed by two 1/16" thick aluminum pressure domes maintaining the instrument at ground level atmospheric pressure. This removed the possibility of corona discharge occurring with the EHT power supplies, and also put less strain on the venting system for the
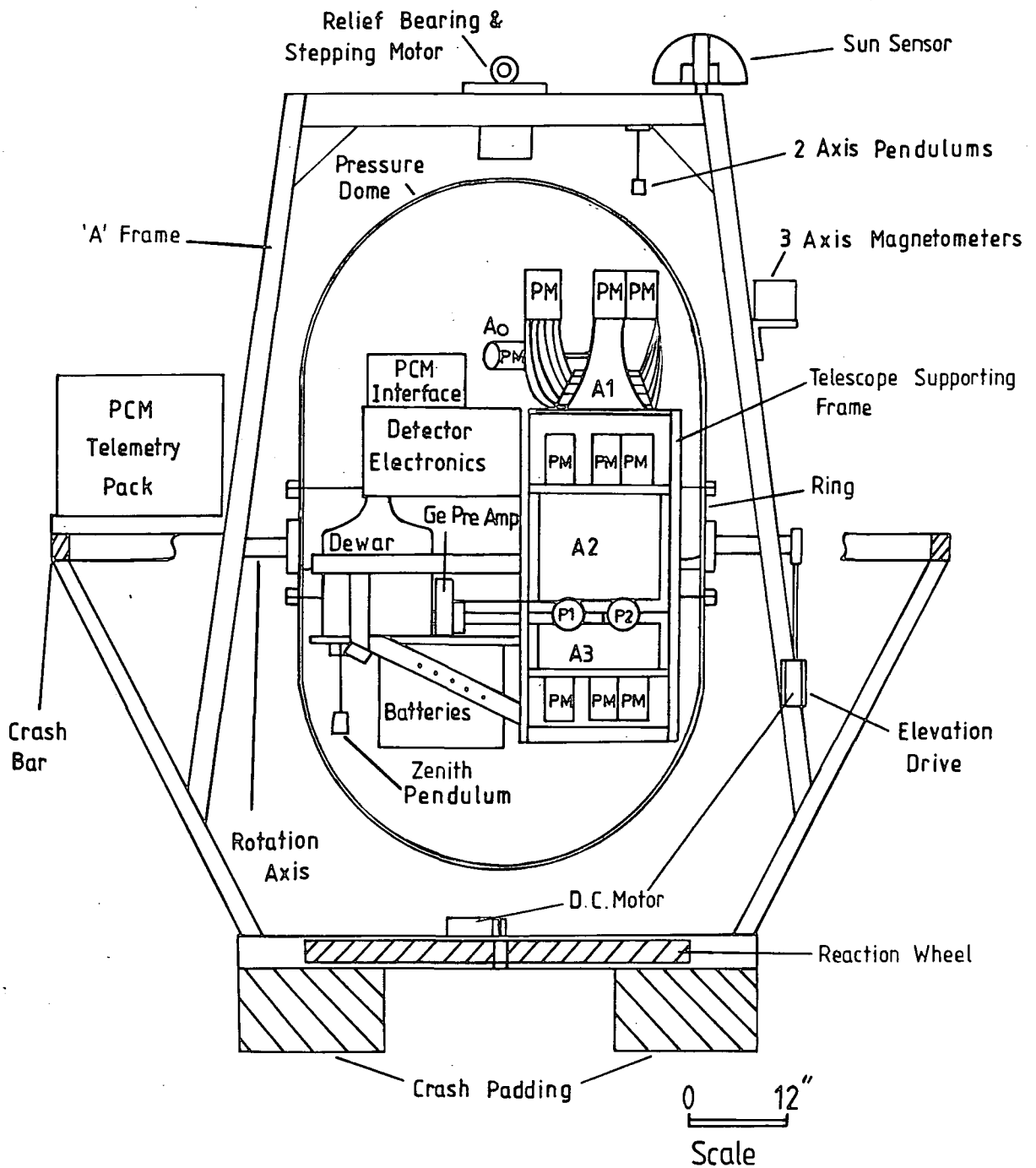
Figure A.1   The Gondola. (Some struts and ties
have been omitted for clarity.)

liquid nitrogen dewar. Electrical connections between the instrument, the steering system, and the telemetry pack were made through Varelco and Cinch connectors located in the centre ring. Two 1-1/2" diameter bars, welded either side of the centre ring on its central axis, serve as the rotation axis of the telescope. The battery box is bolted into one of several positions under the telescope. The final position is chosen so as to align the centre of gravity of the telescope with its rotation axis. The ring and telescope are then supported in an inner 'A' frame which in turn is supported and surrounded by an outer octagonal frame. The outer frame serves as a crash barrier to protect the instrument on landing.

Thermal insulation for the instrument is provided by 10 cm of polystyrene foam with an aluminum foil outer surface. To avoid excessive solar heating the surface is painted white. Extensive calculations have been carried out using a modified version[*] of the thermal simulation program PKTHERMAL (Carlson and Morgan, 1973). This program is capable of predicting the thermal history of the payload during the flight to within a few degrees. The results agree well with the measured temperatures throughout the payload and indicate that the payload is thermally optimally designed, maintaining the temperatures of the NaI(Tℓ) crystal's and electronics at $\sim 20^{\circ}$ C.

Triangular wooden stabilizers, fitted to the apexes of the base with crash padding, are designed to withstand a '3g' landing. The outer frame is designed to collapse in the event of a heavier impact thus absorbing the shock.

---

* A copy of this program may be obtained upon request. All enquiries should be sent to the author, Physics Dept., Case Western Reserve University, Cleveland, Ohio 44106, U.S.A.

A.3   THE STEERING SYSTEM.

The design criteria for the steering system were:

(a)   a pointing accuracy in zenith to $< \pm 0.5^O$ over the range 0° to 50°.

(b)   a pointing accuracy in azimuth to $< \pm 1^O$ over the range 0° to 360°.

(c)   a slew rate of $2^O s^{-1}$ in azimuth which would be ample to deal with the maximum expected balloon rotation rate of $1^O s^{-1}$.

(d)   a settling time to a step input of less than 10s, as frequently stepping off the source by 10° would be necessary for background estimation.

(e)   the ability to offset the azimuth by $\pm 10^O$ to the source pointing direction for background measurements.

(f)   the ability to reference the azimuthal angle with respect to true north rather than magnetic north.

The   system   constructed   to meet these requirements will be discussed in the following sections.

A.3.1   THE ZENITH SYSTEM.

Elevation in zenith is achieved by turning a threaded 1/2" diameter rod through a lever attached to the central rotation axis of the telescope.   Figure A.2 shows this diagrammatically. A permanent magnet d.c. motor is used to drive the rod and is pivoted to allow for lateral movement. The rod drives through a threaded block, again pivoted to allow for lateral movement, attached to the lever. A stop is located on the free end of the

Pointing
Direction

Lever

End Stop

Threaded
Block

Pivot

$\frac{1}{2}''$ ⌀ Threaded Rod

'A' Frame

Centre
Ring

Pivot

D.C. Motor and
Gearbox
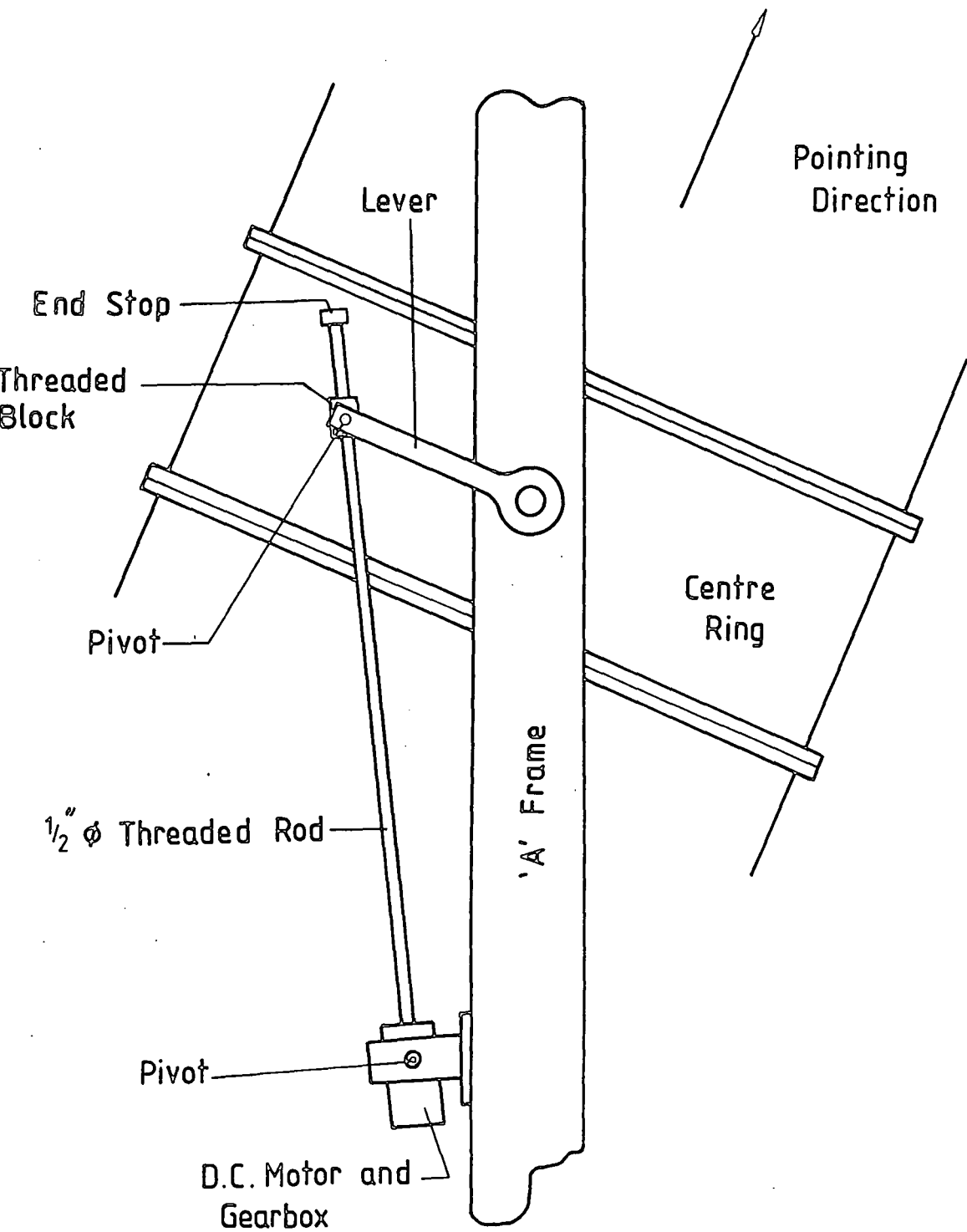
Figure A.2 The Zenith Drive.

rod to prevent it winding off the threaded block.

The zenith position is given by a pendulum connected to a linear potentiometer located within the telescope itself (see Figure A.1). To provide some degree of redundancy a linear potentiometer connected to the rotation axis also measures the angle of the telescope with respect to the frame. This may not be the same as the true zenith angle; the difference being due to the tilt of the frame with respect to the vertical.

The zenith drive electronics are shown in Figure A.3. Zenith drive may be chosen in one of two modes by the Auto or Manual telemetry commands. These are used to address an analogue switch which routes either the manual or auto directional information to the zenith motor power amplifier. In the manual mode the zenith increase and decrease commands are used to set flip-flops structured in such a way that both cannot be active simultaneously. The outputs are then sent to the differential inputs of an operational amplifier that provides the directional analogue voltage which drives the zenith motor.

In the auto mode a 12 bit digital word representing the desired pointing angle is telemetered up from the ground and held in one of two registers, depending on whether the information is required by the zenith or azimuth auto system. In the zenith system this word is converted to an analogue voltage by a 12 bit D.A.C.[*] and compared with the pendulum analogue voltage by an operational amplifier. The output then represents an error signal which is used to drive the zenith motor until a null condition is reached.

The drive rate in zenith is approximately 0.25°/sec and the error in the manual mode is estimated to be $\pm 0.2^{\circ}$, mainly due to

---

[*] Digital to Analogue Converter
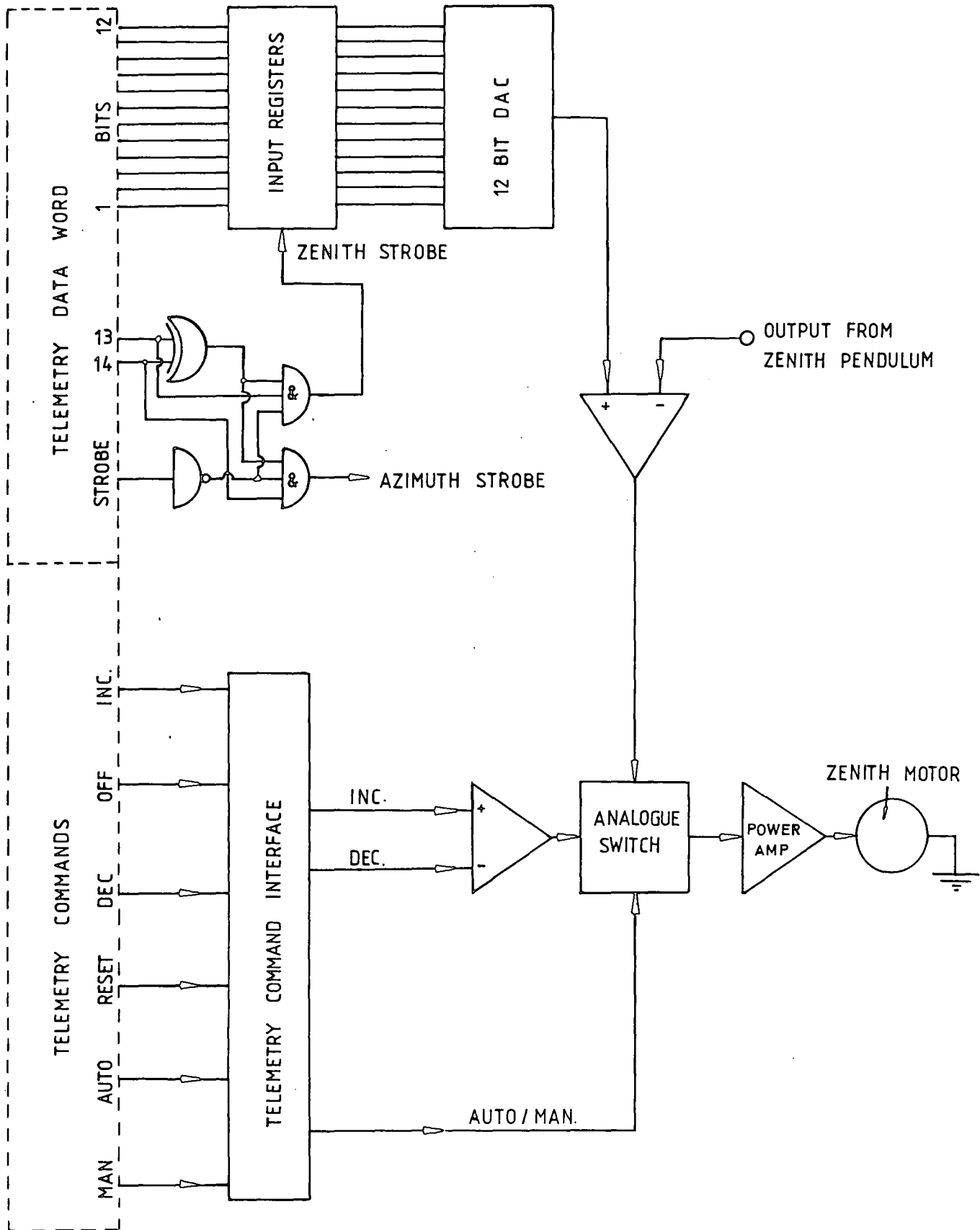
Figure A.3 The Zenith Drive Electronics.

the hysteresis of the pendulum.

A.3.2   THE AZIMUTH SYSTEM.

The orientation of the platform in the azimuthal plane is based on sensing the earth's magnetic field using a 3 axis fluxgate magnetometer, the operation of which has been discussed in detail by Sanderson (1972). The output of each element ranges from 0 volts in a field of -50,000 γ (-0.5 gauss) to 5 volts in a field of +50,000 γ and is digitized such that $10^5\gamma$ = 10 bits, giving a sensitivity of 100 γ per bit. It follows from this that the upper limit to the accuracy of the measurement due to digitization of the horizontal field component of 30,000 γ is 0.2°. Generally, the absolute direction of the earth's magnetic field is not known to better than $\sim 1/2^{\circ}$ and so the overall error in azimuth is expected to be around 1°.

The two magnetometers in the horizontal plane produce signals proportional to the component of the earth's magnetic field in the direction of the probes. If the probes mounted in this plane (say the $\hat{x}$ and $\hat{y}$ axis) are rotated about a vertical $\hat{z}$ axis they will produce outputs such that the function $\tan^{-1} x/y$ represents the azimuth of the payload. The individual analogue outputs of two magnetometers are given by,

$$V_x = k \sin\theta \; \sin\phi \qquad\qquad (A.1)$$
$$V_y = k \sin\theta \; \cos\phi$$

where ϕ is the azimuthal angle referenced to magnetic north, k is a constant proportional to the resultant magnetic field strength,

and θ is the angle between the vertical and the resultant field direction. Figure A.4 shows a functional block diagram of the azimuth steering system electronics. In the auto mode a 12 bit digital word representing the desired pointing angle, α, is telemetered up from the ground and stored in registers. It subsequently passes to a digital adder where an 11.25° offset may be added or subtracted for background measurements. The digital magnetometer information and the digital word representing α are then fed into a resolver which multiplies V_x and V_y by the sine and cosine of α using two multiplying D.A.C.'s. The two analogue outputs voltages,

$$V_1 = k \sin\theta \cos\phi \sin\alpha \qquad (A.2)$$
$$V_2 = k \sin\theta \sin\phi \cos\alpha$$

are fed to the differential inputs of an operational amplifier whose output is given by:

$$V_e = k \sin\theta \sin(\phi - \alpha) \qquad (A.3)$$

This voltage can then be used as an error signal with which to control the azimuth of the payload. Rotation of the payload beneath the balloon is achieved using a reaction wheel to provide a good dynamic response. The reaction wheel is housed in the platforms understructure and consists of 8 spokes each carrying a lead block whose weight can be adjusted for final fine tuning. A torsion relief drive is provided above the payload to prevent the suspension cables twisting and to provide a steady torque for continuous rotations.
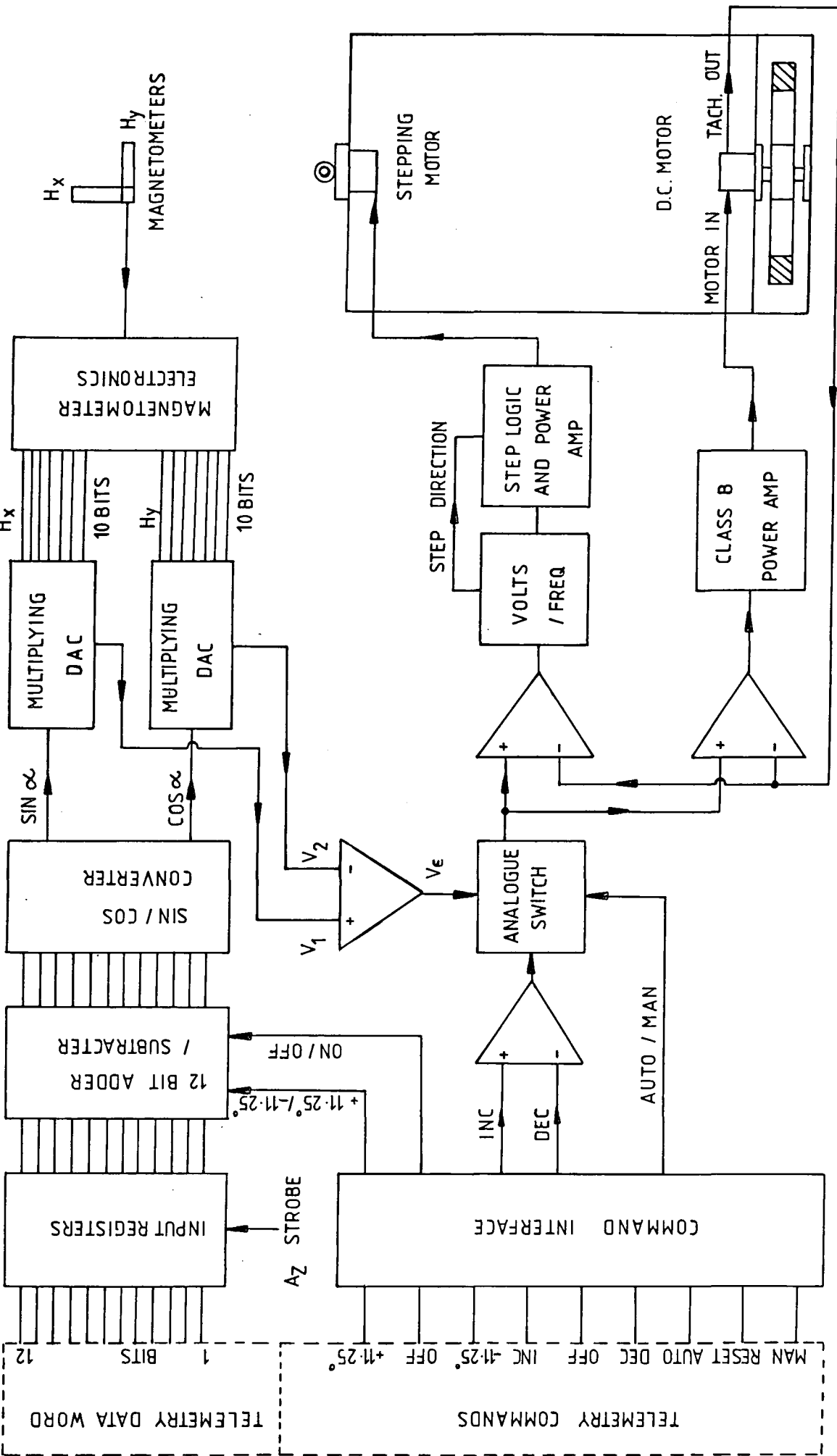
Figure A.4 The Azimuth Steering Electronics.

The error signal passes through an analogue switch and is used to drive a class B power amplifier for the reaction wheel motor and voltage to frequency converter for the upper torsion relief stepping motor. A velocity signal derived from a tachometer attached to the reaction wheel motor, is summed with the position error signal at the shaping amplifiers in order to provide a stabilization term.

In the manual mode the azimuth increase and decrease commands operate directly on the main reaction and torsion relief motors in a similar way as has already been described for the zenith manual system.

A.4 THE AUXILIARY POSITION SENSORS.

A.4.1 THE SOLAR SENSOR.

The solar sensor is an electro-mechanical device which is used to track the sun with respect to the gondola and so supply extra azimuthal information that can be used to verify the operation of the magnetometers. It is positioned as shown in Figure A.1 on top of the 'A' frame. Essentially it consists of a vane that partially obscures the fields of view of two solar cells attached to it, one either side (Figure A.5). The vane is driven by a servo-positioning motor until the signals from each of the cells are equalized, which occurs when the vane is centered on the sun. The vane direction is sensed by a linear potentiometer.

Since the time of the measurement is recorded in the telemetry ground frame along with latitude and longitude information, the sun's bearing β (angle between true north and the

SIDE VIEW

Vane

Solar cell

Electronics

D.C. motor

Slip rings

Drive shaft

Flexible coupling

Linear potentiometer

0"   1"
Scale

PLAN VIEW

Apparent size of
the sun
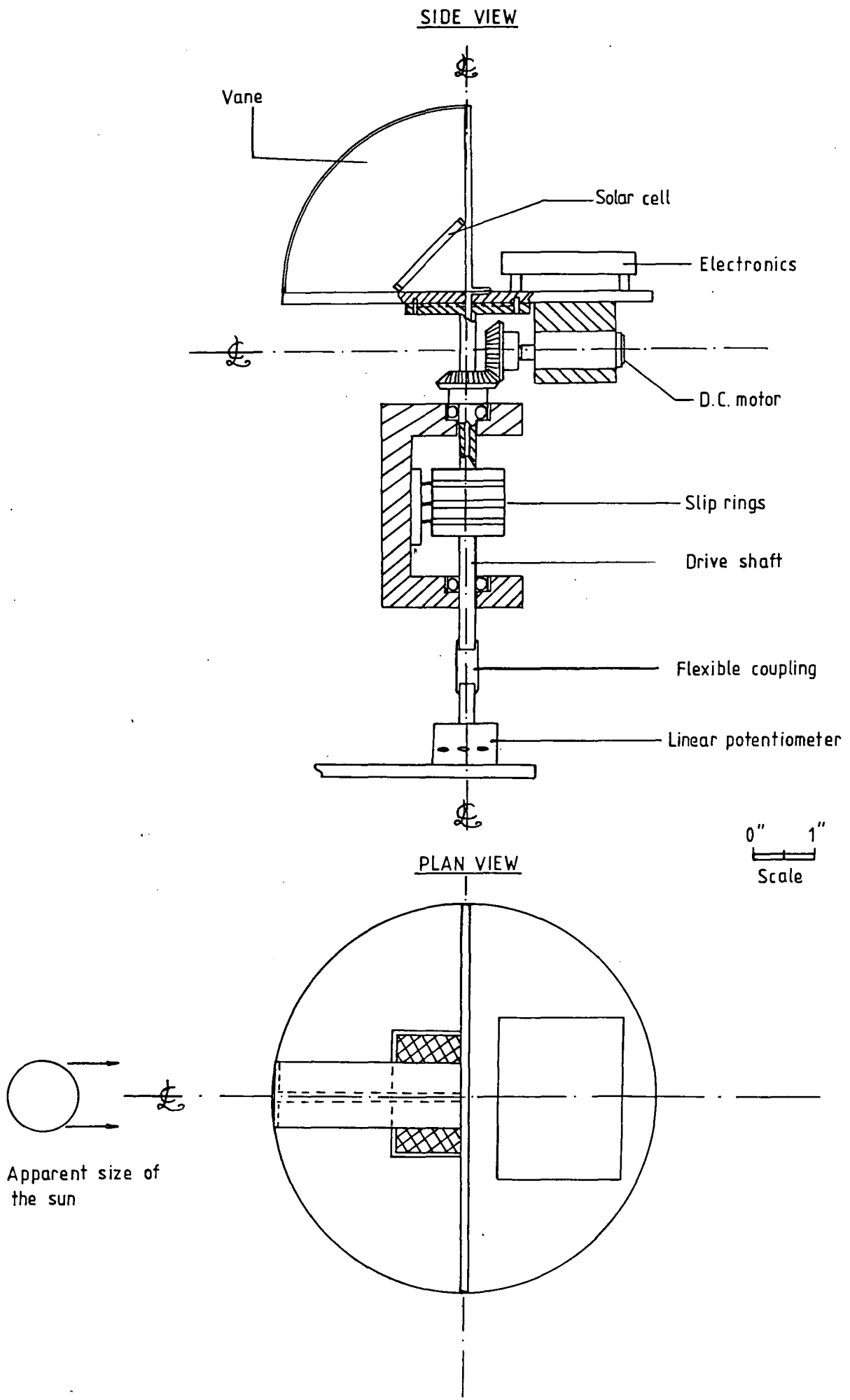
Figure A.5   The Solar Sensor

vane) can be calculated from,

$$\beta = \tan^{-1} \left(\frac{\sin(lat)\cos(long) - \tan(\delta)\cos(lat)}{\sin(long)} \right) \qquad (A.4)$$

where δ is the sun's declination. Thus knowing the sun's bearing and the angle between the vane direction and the magnetometer x-axis, the magnetometer information could be verified.

The intrinsic accuracy of the sensor is set by the distance between the solar cells and the vane and by the degree of digitization of its analogue output. this was estimated to be $1/3^{\circ}$. However, in ground tests the measured error was $\sim 1^{\circ}$, primarily due to the hysteresis in the potentiometer.

A.4.2   THE PENDULUMS.

A pendulum internal to the pressure dome measures the angle in a plane perpendicular to the rotation axis of the telescope, and a potentiometer on the rotation axis of the telescope measures the angle between the telescope and the frame. If however, the frame is tilted with respect to the vertical then these devices will not measure the true zenith of the telescope. The magnetometer can in principle give the zenith axis of the frame. Thus knowing the zenith and azimuthal coordinates of the frame from the magnetometers and the angle between the frame and telescope from the internal pendulum, the true zenith of the telescope could be calculated. However, this would be difficult to calculate in real time during the flight and so a 2 axis pendulum is fitted to the top of the "A' frame (see Figure A.1)

which measures inclinations both parallel and perpendicular to the frame. The true zenith angle of the telescope θ_T is then given by,

$$\theta_T = \arctan \, (\tan^2(\theta_\perp + \theta_p) + \tan^2\theta")^{1/2} \qquad (A.5)$$

$$\text{for } \theta_\perp + \theta_p < 90^o, \text{ and } \theta" < 90^o$$

where θ_p is the angle between the frame and telescope measured by the internal pendulum $\theta_\perp$ is the angle measured by the pendulum perpendicular to the frame, and $\theta"$ is the angle measured by the pendulum parallel to the frame.

The pendulums are 11" long and are attached to linear potentiometers by a 1:2 pulley arrangement. The natural period is 1 sec which is more than adequate to deal with the expected balloon payload pendulation period of 8 minutes. Due to friction in the system there was a hysteresis error of about $\pm 0.2^o$ in each pendulum, giving a total error in the zenith measurement of about $\pm 0.5^o$.

APPENDIX B

SPECTRAL DEGRADATION EFFECTS IN AN 86 cm^3 Ge(HP) DETECTOR

B.1 INTRODUCTION

In determining the continuum and line fluxes for cosmic point sources, Jacobson et al. (1978) have shown that the threshold sensitivity of a detection system is proportional to $\Delta E^{\frac{1}{2}}$ /A, where ΔE is the detectors FWHM energy resolution and A is the normally presented detector area. It is apparent, therefore, that a good understanding of the detector resolution is essential especially when one considers that many of the lines predicted to occur at astrophysical sites are expected to exhibit broadening (Ramaty and Lingenfelter, 1979). The width of these lines, which generally range up to a few tens of keV, are due to several mechanisms of which Doppler broadening and magnetic broadening are the most important. In the case of Doppler broadening, an accurate measurement of the line width can provide information not only on the temperature of the source but also on the density of particles within the production region. Similarly for magnetic broadening a measurement of the line width allows one to place limits on the magnetic field strength and also the size of the emission region.

In this appendix we will review spectral distortion effects in the light of previous work and develop a simple semi-empirical formula which relates the FWHM energy resolution to the incident gamma-ray energy. By considering the various contributions to the FWHM for the Durham 86 cm^3 HPGe detector it will be shown that the data are consistent with a Fano factor of 0.06 (in agreement with

that obtained by other workers (eg Strokan et al., 1971; and Pehl and Goulding, 1970) and a linear variation of charge trapping on energy. Also it will be shown that non-linearity and instability effects may be neglected for this detector.

B.2 SPECTRAL DEGRADATION EFFECTS

All detectors of electromagnetic radiation suffer from spectral degradation as a result of the departure of one or more properties of the detector from the idealized model. In semiconductor detectors these effects (linearity, stability and energy resolution) ultimately stem from the properties of the detector material itself which alter the electric field within the intrinsic region and introduce allowed energy states or traps. Non-linearity and instability are usually very small over large energy ranges and can generally be neglected or easily corrected for. Energy resolution however, is more intimately dependent, not only on the detector properties and operating conditions, but also on the external acquisition electronics. Indeed it will be shown that electronic noise comprises an appreciable fraction of the energy resolution FWHM for energies up to ∿1000 keV.

B.3 CONTRIBUTIONS TO THE FWHM

Due to noise in a spectrometer system, an infinitely sharp line $n(E) = n_o \delta(E - E_o)$ at $E = E_o$ is broadened to $\overline{n}(E)$ given by the convolution,

$$\overline{n}(E) = n_o \{ p_1(E) \star p_2(E) \star \ldots \ldots \star p_n(E) \} \qquad (B.1)$$

where $p_n(E)$ is the probability density distribution of the nth noise contribution. In general one need only consider four major conponents of noise:

a) Noise resulting from the statistical nature of the charge generation whose mean $\mu = E_o$ and variance given by,

$$\sigma_g^2 = F\varepsilon E_o \qquad (keV)^2 \qquad (B.2)$$

where F is the Fano (Fano, 1947) factor which describes the fluctuations in ionization and ε is the energy required to liberate an electron-hole pair.

b) Shot noise of the detector leakage current which is normally distributed with mean $\mu = 0$ and variance,

$$\sigma_s^2 = \frac{2\varepsilon^2 I_d \tau}{e} \qquad (keV)^2 \qquad (B.3)$$

where I_d is the detector leakage current, e is the electronic charge and τ is the amplifier time constant.

c) Amplifier shot noise referred to the input, likewise normally distributed with $\mu = 0$ and variance σ_a^2 which depends on the actual design.

d) Noise due to the incomplete charge conversion, characterized by a FWHM Δ_c.

Other sources of noise, for example grid current noise, flicker noise, Johnson noise etc., were shown by Hansen and Goulding (1968) to be negligible. Assuming each of these components are normally distributed, Equation B.1 becomes;

$$\bar{n}(E) = \frac{n_o}{\sqrt{2\pi}\,\sigma} \exp\left[-\frac{(E - Eo)^2}{2\sigma^2}\right] \tag{B.4}$$

where

$$\sigma^2 = \sigma_g^2 + \sigma_s^2 + \sigma_a^2 + \sigma_c^2 \qquad (keV)^2 \tag{B.5}$$

Bilger (1967) made use of this assumption to determine the Fano factor for Ge. Analyzed in this way, Bilger's data gave inconsistent values for σ_c and a value for F of 0.129. The same assumptions were applied to the data of Sher and Pate (1969) yielding similar results. However, it has been shown (Trammell and Walter, 1967) that the local difference in the collection of charge carriers lead to peak asymmetries which can, under certain conditions (Strokan and Tisnek, 1969), cause a higher value of FWHM than that given by Equation B.5. These erroneous predictions can therefore be attributed to the assumption that the noise due to charge loss is normally distributed, and the subsequent conversion of σ to Δ (in determining the FWHM resolution Δ, the shape of the peak is irrelevant by definition).

B.4 CHARGE COLLECTION EFFECTS

Trammell and Walter (1967) approached the problem by considering the relative pulse height expected from a gamma-ray interaction taking place in an infinitesimal layer of thickness dx parallel to the junction. The spectrum produced by the summation of the spectra from the individual slices over the detector thickness d is then given by,

$$\overline{dn}(E) = \frac{1}{\sqrt{2\pi}} \int_0^d \frac{1}{\sigma(x)} F(x) \exp\left[-\frac{(E - \eta(x)E_o)^2}{2\sigma^2(x)}\right] dx \, dE \qquad (B.6)$$

where $F(x)$ is a geometrical weighting factor, $\eta(x)$ is the charge collection efficiency (which is a function of the detector material and field configuration) and $\sigma(x)$ is the resulting spread in amplitude for interactions at point x:

$$\sigma^2(x) = \sigma_g^2 + \sigma_a^2 + \sigma_s^2 + \sigma_c^2(x) \qquad (B.7)$$

The important point which Trammell and Walter's presented is that the spread in pulse amplitudes produced at various points of interaction within the intrinsic region may be different. Consequently the symmetry of resulting pulse height distribution is not assured and therefore σ may not be simply related to Δ. McMath and Martini (1970) have calculated the charge collection efficiency for a perfectly compensated planar detector using a modified form of Equation B.6 in which the spread in amplitudes, $\sigma(x)$, was related to the crystal trapping parameters. The model assumed uniform trapping and that the trapped carriers remain trapped for a long time relative to the amplifier time constant. Good agreement was found between the shapes of the calculated peaks and those determined experimentally from collimated beam measurements. Armantrout and Thompson (1970) followed a different approach. Although their model assumes σ is constant throughout the detector it includes provisions for treating the effects of a non-uniform field and incomplete charge compensation in the detector. Henck et al. (1970) derived a semi-empirical expression relating the charge collection efficiency to Δ_c for planar

detectors;

$$\Delta_c = 0.46 \ (1 - \overline{\eta}) E_o^{\frac{1}{2}} \tag{B.8}$$

where $\overline{\eta}$ is the average charge collection efficiency. However, their original theoretical treatment based on Armantrout and Thompson's model yielded a linear dependence on E_o. Unfortunately there does not seem to be a simple way to approximate Δ_c for the general case, however for coaxial detectors a linear dependence on E_o would seem to be indicated (Strokan et al., 1971; Zullinger et al., 1969; Makovskii et al., 1968)

It is interesting to note that the factor $(1 - \eta)$ in Equation B.6 is in effect, a pulse height defect. Therefore the variation of the charge collection efficiency with energy and bias will lead directly to the determination of the linearity and stability respectively of the detector.

B.5 EVALUATION OF THE RESOLUTION FUNCTION

In practice the FWHM due to electronic noise, Δ_n, can be determined quite simply by injecting additional noise into the preamplifier input. After subtracting this component quadratically, the FWHM contribution due to carrier generation can be obtained by measuring ΔE as a function of bias voltage and extrapolating to infinite field. It is assumed that at this value all charge will be collected and so the remaining distribution must be due to carrier generation statistics. Using this method it has been found that the intrinsic Fano factor for Ge is 0.05 (Strokan et al., 1971; Pehl and Goulding, 1970). This value is in

agreement with theory (Zullinger, 1970).

B.6 APPLICATION TO THE DURHAM GAMMA-RAY TELESCOPE

This instrument (Ayre et al., 1981) is centered around an 86 cm^3 intrinsically pure germanium crystal in a closed end coaxial configuration (see Figure 4.2). The detector is of conventional design being fabricated from p-type material with a deep p^+ core bottoming out at $\sim$ lcm from the detector face. The specifications are given in Table 4.1. The detector was manufactured by Princeton Gamma Tech Ltd. (PGT) and was used in conjunction with a PGT model RG-11A preamplifier and a Tennelec TC-205A amplifier. Integration and differentiation time constants of 4 μs were chosen so as to optimize both energy resolution and linearity.

B.7 STABILITY AND LINEARITY

Gamma ray spectra at energies ranging from 81 keV to 1333 keV were obtained at several values of the applied field using uniform irradiation. The difference in the channel number corresponding to the maximum value of the pulse height distribution (PH) to the value obtained at the nominal bias (PH_n) is shown in Figure B.1. For changes in bias of $\sim$ 2000 volts the variation in channel number was found to be < 2% at all energies. Using the manufacturer's figure for the regulation of the HT supply, the stability of the detector is calculated to be better than 1 part in 10^4. Long term measurements under flight conditions have indicated a value of << 4 parts in 10^4. By extrapolating the curves in Figure B.1 to infinite field, the

Energy keV	Intercept ch
81	−2·32
303	−8·10
356	−9·51
511	−14·14
662	−17·74
1 173	−31·86
1 275	−35·34
1 333	−35·86

1ch = 0·66406 keV @   3800 Volts
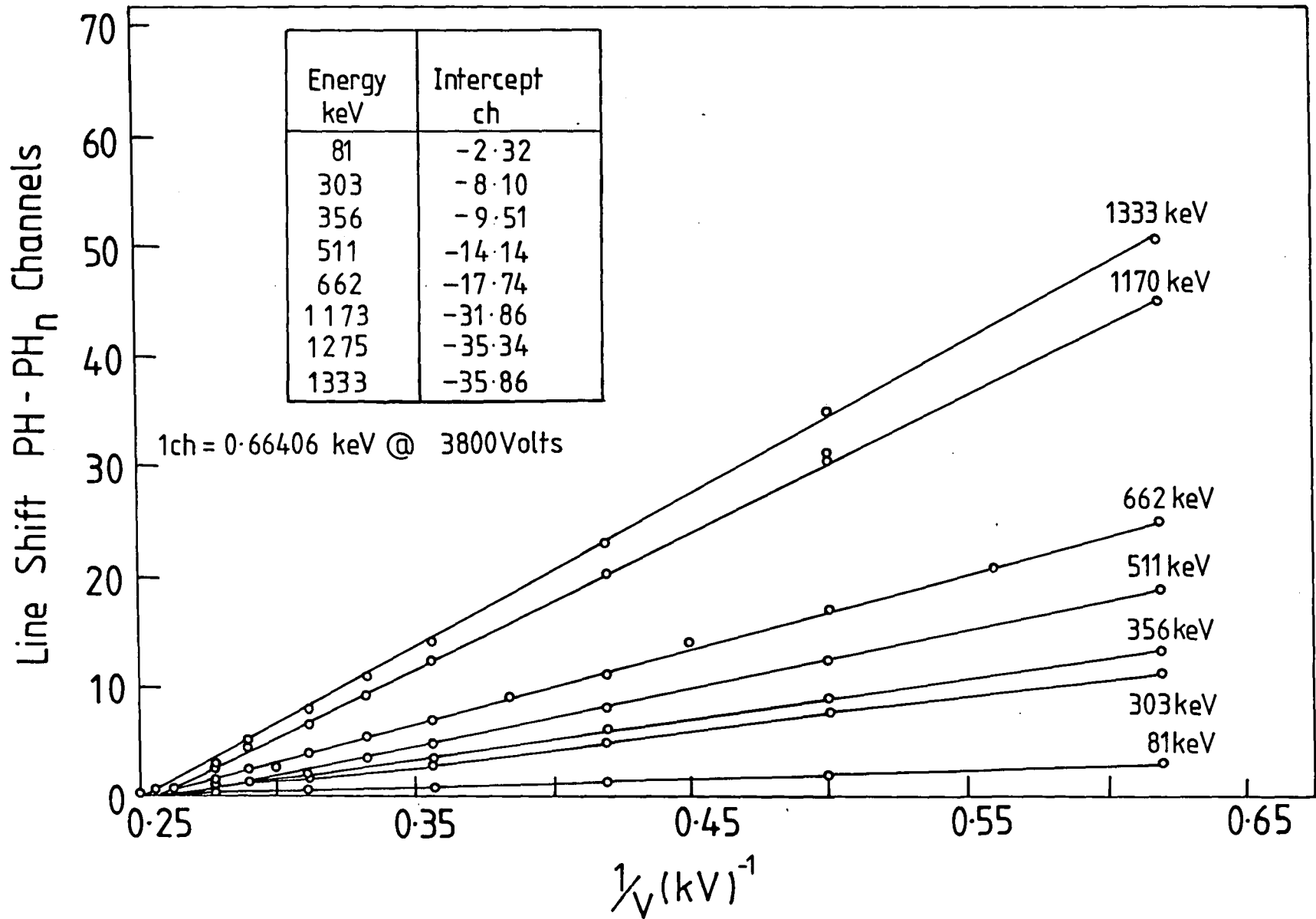
Figure B.1   Full energy peak shift as a function of detector bias.

charge collection efficiency as a function of bias can be determined from the relationship

$$\eta(V) = \frac{PH}{PH_{max}}$$
(B.9)

where PH_{max} is the channel number corresponding to $1/V = 0$. At the nominal bias voltage (3800V) the charge collection efficiency was found to be 98.2 ± 0.1%. This figure agrees well with the calculated value of 98.3% (Sakai, 1968). This value shows no systematic trend with energy indicating the uniformity of traps throughout the depth of the detector. The charge loss inhomogeneity was measured to be $\leq$ 0.1%. Note that since each of these measurements take place over a relatively small number of energy channels, the non-linearity in the associated electronics can be neglected and therefore what is really being measured is the non-linearity of the crystal itself. For comparison a best fit line through the peak channel versus energy data yielded a systems non-linearity of 0.2%. The last measurement is useful in that it shows ballistic deficiency effects constitute < 0.2% non-linearity in this energy range.

B.8 ENERGY RESOLUTION

Because of the high bias used with this detector Δ_c is expected to be small. Furthermore, it has been shown experimentally that trapping effects in coaxial detectors made from a crystal exhibiting preferential trapping of one carrier (which is generally true) are reduced if the trapped carrier moves

radially outward from the central high field region (Sakai et al., 1969). The measured ratio of the hole to electron lifetimes, τ_p/τ_e is $\sim$ 5. This is most consistent with the ratio of carrier capture cross sections of the lithium defect trap (Armantrout and Thompson, 1970) thereby strongly indicated preferential electron trapping. The shape of the full energy peak will therefore be very nearly Gaussian (McMath and Martini, 1970) which is borne out by observation. Indeed low energy tailing only became serious at biases < 1500 Volts. Therefore, we feel justified in using the central limit theorem to derive the various contributions to the FWHM.

Using the procedures outlined in the previous section, the FWHM due to carrier generation statistics, Δ_g, was determined as a function of energy from which the Fano factor was derived. The results listed in Table B.1 show that F is essentially constant over the energy range 81 to 1333 keV, in agreement with the results of Pehl and Goulding (1970) and Strokan et al. (1971). The data point at 511 keV as determined by first correcting for the line width due to Doppler broadening of the positron annihilation line (Jackman et al., 1974; Ljubicic et al., 1974). By subtracting quadratically Δ_n and Δ_g from the measured FWHM, ΔE, the FWHM due to charge collection Δ_c was determined as a function of energy at the nominal bias of 3800V. The results are shown in Figure B.2 from which it can be seen that Δ_c is a linear function of energy. A best fit to the data yielded;

$$\Delta_c = 1.09 + 5.8 \times 10^{-4} E_o \qquad (keV) \qquad (B.10)$$

Since Δ_c is finite at zero energy we must conclude that there is

TABLE B.1

The experimentally determined Fano factor as a function of energy.

E (keV)	Fano factor
81	0.057 ± 0.017
303	0.045 ± 0.023
356	0.035 ± 0.023
511	0.047 ± 0.019
662	0.048 ± 0.018
1173	0.071 ± 0.018
1275	0.103 ± 0.020
1333	0.091 ± 0.026

TABLE B.2

Coefficients derived from Equation B.13.

Coeff.	Units	Present work measured	*Mahoney et al. (1981)	Semi-empirical fit of previous data (see text)
a_1	keV	2.28×10^{-3}	2.19×10^{-3}	2.16×10^{-3}
a_2	-	3.39×10^{-7}	1.71×10^{-7}	1.82×10^{-6}
a_3	keV^2	2.63	6.43	1.042

* Four detector average.
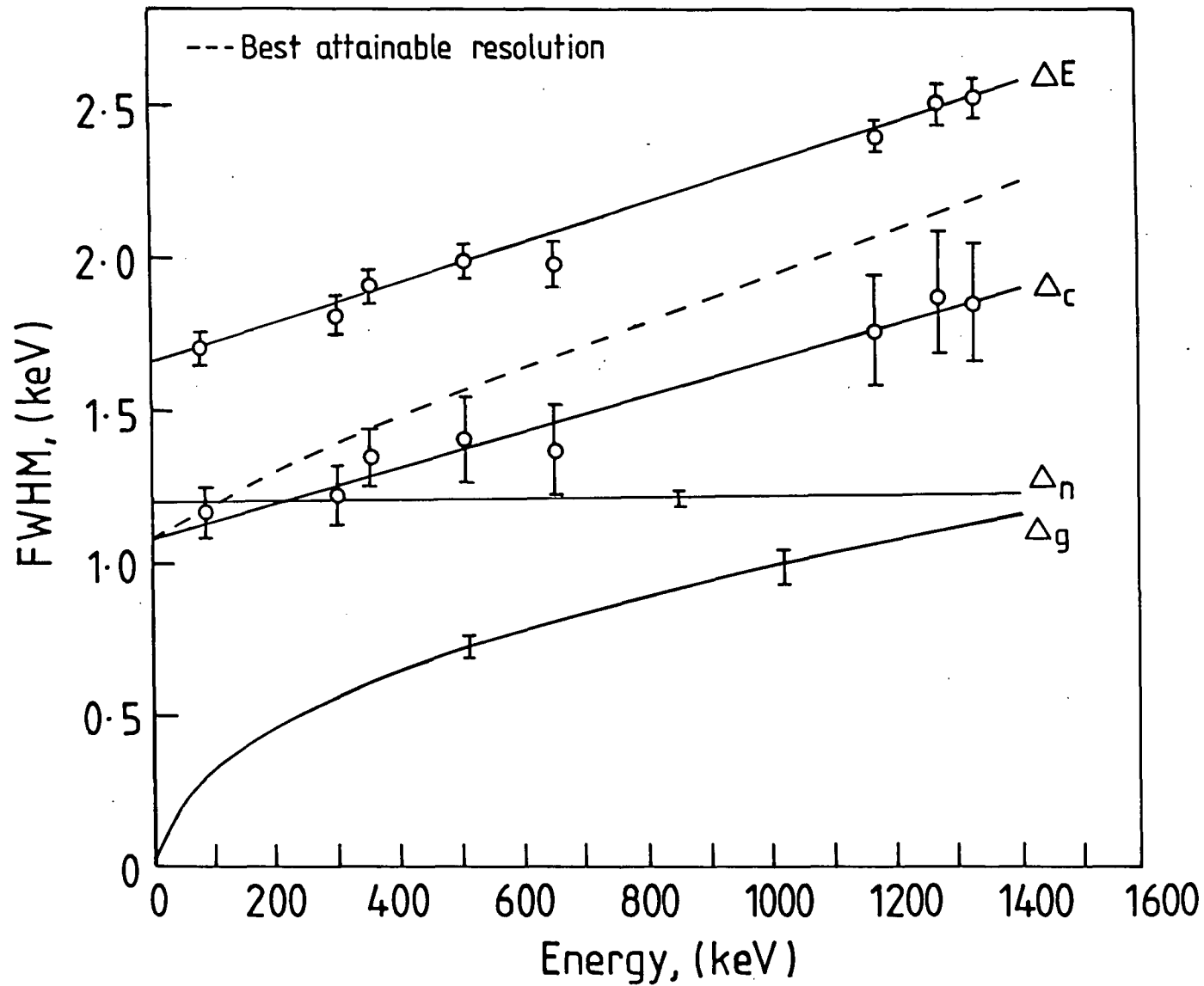
Figure B.2   The detector Energy Resolution FWHM as a function of energy at the nominal Bias. The various contributions to the FWHM are shown seperately.

another source of field dependent noise. The FWHM resolution is then given by,

$$\Delta E = 8 \ell n 2 \ [F \epsilon E_o + (\alpha + \beta E_o)^2 + \sigma_n^2]^{\frac{1}{2}} \quad (keV) \qquad (B.11)$$

where α and β are constants and σ_n is the standard deviation of the electronic noise. The various contributions to the FWHM derived from the measurements are shown in Figure B.2.

Equation B.11 can be simplified further to:

$$\Delta E = (a_1 E_o + a_2 E_o^2 + a_3)^{\frac{1}{2}} \qquad (keV) \qquad (B.12)$$

where a_1, a_2 and a_3 can now be treated as semi-empirical constants. Note Equation B.12 is of the same form as the resolution function used by Mahoney et al. (1981) who found a good fit up to energies of 10 MeV using similar detectors. Coefficients a_1, a_2, and a_3 are compared to the empirically determined values of Mahoney et al. in Table B.2 from which it can be seen there is good agreement. The detector used in the present measurements had recently been repaired thus changing its resolution properties. Using existing FWHM data for the MK1 detector, Equation B.12 was fitted using a non-linear minimization routine assuming a_1, a_2 and a_3 are semi-empirical constants. A best fit yielded a χ^2 of 20.02 for 29 degrees of freedom. The coefficients a_1, a_2 and a_3 are listed in Table B.2 and the calculated and measured resolution data are shown graphically in Figure B.3 for energies up to $\sim$3.5 MeV. By comparing columns 1 and 3 of Table B.2 and Equations B.11 and B.12 we can conclude that since the repair of the detector the contribution to the FWHM
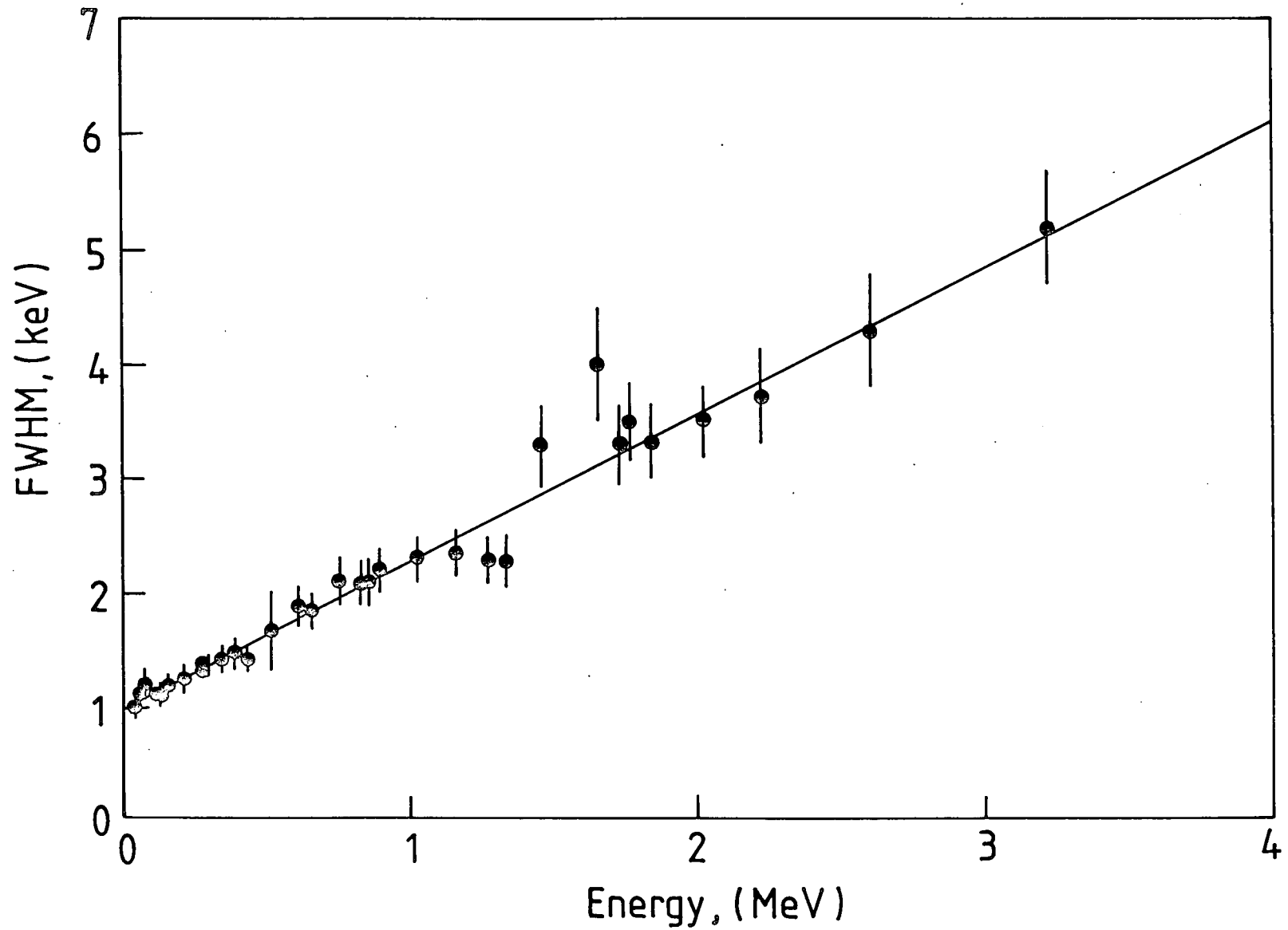
Figure B.3   The detector Energy Resolution FWHM as a function of energy at the nominal
bias (see text).

due to incomplete charge collection has decreased by a factor of 2 while the energy independant noise has increased by approximately the same factor. The overall effect is a degradation of the low energy performance of the detector.

B.9 DISCUSSION

From Figure B.2 we can see that the FWHM resolution due to charge collection effects represents the dominant noise component for energies > 200 keV. Below this value, electronic noise dominates although it comprises an appreciable fraction of the FWHM for energies up to $\sim$1000 keV. It is unfortunate that for a given detector this is the only component that can be improved upon. Using a 'state of the art' preamplifier employing pulsed light feedback techniques should improve the electronic noise contribution by a factor of $\sim$ 2. The best attainable resolution using this detector is shown by the broken line in Figure B.2 assuming $\Delta_n << \Delta E$.

APPENDIX C

SEMI-EMPIRICAL EFFICIENCY CALCULATIONS FOR GE DETECTORS

C.1   INTRODUCTION.

For a precise measurement of the intensities of γ-ray lines or spectra, an accurate knowledge of the Full Energy Peak Efficiency (FEPE) is required. Various approaches have been employed including experimental measurement with absolutely calibrated standards or with "relative intensity standards", empirical calculations based upon various detector parameters, and Monte-Carlo computations. The precision of the efficiency calibration claimed depends upon the specific energy interval under study and upon whether relative or absolute efficiency is required. Mowatt (1969) has shown that with the use of a set of IAEA gamma-ray standards it is possible to determine the absolute efficiency of a small planar detector to less than 1% over the energy range 120-1400 keV. These measurements, although simple to undertake, involve tedious procedures, and often necessitate the use of functional fits especially when analysing continuum spectral data. Monte Carlo calculations, on the other hand, do not give sufficiently accurate results without the introduction of 'arbitary factors'. This is because of the imprecise definition of active detector boundaries, composition and operating conditions. Semi-empirical calculations provide the simplest and potentially the most accurate approach second only to direct measurement, because the results are based on ensemble averages, and all geometry and normalisation factors are treated as empirically determined parameters. In this appendix we will examine the

various approaches to calculating the FEPE empirically and semi-empirically and will derive values for the Durham MK1 and MK2 $86cm^3$ HPGe detector following the approach of Hajnal and Klusek (1979). These data will be compared to existing measurements and Monte Carlo calculations.

C.2 MEASUREMENTS.

The absolute FEPE was measured for both the MK1 and MK2 detectors using a set of IAEA standard sources. The original source strengths were 10 μCu and the source to detector distance was 25 cm. Although the background spectrum was subtracted for each set of measurements, the corrections never exceeded 2%. Also because of the strengths and sizes of our sources, dead time and self absorption corrections were estimated to be < 2% and were therefore neglected. Based on the work of Meyer et al. (1976), we further conclude that sum-coincidence effects may be neglected for the present source/detector geometry. Each source was placed coaxially on the central axis of the detector and the FEPE determined using the relationship,

$$\epsilon = \frac{\Sigma N_p - \Sigma B_p}{A_t G t_s f} \qquad (C.1)$$

where ΣN_p is the number of counts in the photopeak, ΣB_p is the corresponding number of background counts, t_s is the exposure time, f is the branching ratio of the particular line under study, G is the geometric factor (given by $\pi r^2/4_\pi d^2$ where r is the detector radius and d is the source to detector distance), and

finally A_t is the activity of the source at time t_s given by,

$$A_t = A_o \exp (-t_s/0.693 \ T_{1/2}) \qquad (C.2)$$

where A_o is the activity at $t_s = 0$ and $T_{1/2}$ is the source half life. The error in the measurement is given by,

$$\sigma_\varepsilon = \frac{\left[\sigma_{Np}^2 + \sigma_{Bp}^2 \right]^{1/2}}{A_t G t_s f} \qquad (C.3)$$

and was estimated to be < 4% and 8% on average for the MK1 and MK2 detectors respectively. The measured efficiencies are given in Table C2 for energies ranging from 59.5 to 3254 keV.

C.3   FUNCTIONAL FITS TO EFFICIENCY CURVES.

Perhaps the simplest approach involves fitting a polynomial to the experimentally measured data points (Euler and Kaplan, 1970). However, this method suffers from the disadvantage that the function is usually only well behaved within specific bounds because of the complex shape of the efficiency function. Also, within these bounds spurious maxima and/or minima may be introduced. For instance a third order fit to the MK1 experimental data yielded a reduced χ^2 of 1140 over the energy range 81 keV to 3254 keV with spurious maxima exident at ~ 800 keV (54% deviant) and minima at ~ 2000 keV (96% deviant). No improvement was found using higher order polynomials.

Kane and Mariscotti (1967) proposed the following analytic form which relates the detector FEPE, ε, at energy E by,

$$\ln \varepsilon = a_1 x + a_2 x^2 \qquad (C.4)$$

where $x = \ln (1.022/E)$, and $a_1, \ldots, a_n$ are empirical constants. East (1971) proposed a similar expression,

$$\varepsilon = a_1 \exp (-a_2 E) + a_3 \exp (-a_4 E) \qquad (C.5)$$

McNelles and Campbell (1973) fitted the above expressions to the experimental data obtained from a 25 cm^3 coaxial Ge detector. For energies between 122 to 1332 keV they found Equation C.4 gave a poor fit to the data at low energies (~ 100 keV) while Equation C.5 fits well over the entire energy range with a mean deviation of 1.2%. Both expressions C.4[*] and C.5 gave good fits to the experimental data obtained for the Durham MK1 detector over the energy range 356-1770 keV, with a mean deviation of 1.7% in both cases. At energies less than 356 keV both equations gave poor fits unless account was taken of absorption effects.

McNelles and Campbell (1973) considered various combinations of functions and eventually arrived at the eight parameter fit given below:

$$\varepsilon = \left[\frac{a_1}{E} \right]^{a_2} + a_3 \exp(-a_4 E) + a_5 \exp(-a_6 E) + a_7 \exp(-a_8 E) \qquad (C.6)$$

Mean deviations of 1 or 2 percent have been claimed by McNelles and Campbell (1973) and Singh (1976) over the energy range 120 to 2589 keV. Singh has pointed out however, that the last term in Equation C.6 appears to be redundant.

Various other functional forms have been suggested, Harvey

---

[*] Note; the factor 1.022 was replaced by an empiric constant a_3.

(1970) and Johnson and Mann (1973), and Willet (1971).

Finally a novel form is given by Vano et al (1975) in which the slope of the efficiency curve S (viz the slope of $\varepsilon=f(\log(E))$ is related to the _active_ detector volume V_a,

$$S = a \log (V_a) + b \qquad\qquad (C.7)$$

where a = 0.629 and b = 2.14. The authors claim an accuracy of 3% over the energy range 200 to 6000 keV. Somorjai (1975) has shown that Vano et al's empirical equation is not valid for the gamma-ray energies greater than 3 to 4 MeV. Allowing the active volume to be a free parameter, Equation C.7 was fit to the measured efficiency curves for the Durham MK1 and MK2 detectors. Mean deviations of 4% were obtained over the energy range 356 to 1770 keV for active volumes of 60.6 cm^3 (MK1) and 72.2 cm^3 (MK2). For comparison the estimated active volume of the detector (found by subtracting the estimated volume of the p^+ core and n^+ contact from the physical volume) is (68 ± 4) cm^3.

C.4 SEMI EMPIRICAL FITS TO EFFICIENCY CURVES.

Freeman and Jenkins (1966) related the relative FEPE to the gamma ray energy and detector thickness x by the following expression:

$$\varepsilon \sim [1 - \exp(-\tau x) + a_1\sigma \exp (-a_2 E)] \qquad (C.8)$$

where τ and σ are the photoelectric and Compton absorption cross sections at energy E. Equation C.8 can be approximated by,

$$\varepsilon \sim [\tau x + a_1 \sigma \exp (-a_2 E)] \qquad\qquad (C.9)$$

for energies above 500 keV. An accuracy of $\sim 1\%$ is claimed for energies up to 1500 keV. For the Durham MK1 detector Equation C.9 fitted the experimentally measured data to approximately 3% over the energy range 400 to 1400 keV. Beyond this energy range the calculated values become increasingly deviant from the measured values due to the increasing importance of pair production and attenuation in the detector window and dead layers. By including a factor which accounts for attenuation in the materials present between the source and the intrinsic region of the detector, Mowatt (1969) extended the low energy threshold down to 50 keV,

$$\varepsilon = a_1 \left[\frac{\tau + \sigma a_2 \exp(-a_3 E)}{\tau + \sigma} (1-\exp[-a_4 (\tau+\sigma)]) \right] \prod_{i=1} T_i \qquad (C.10)$$

where $T_i = \exp (-\mu_i x_i)$ and μ_i is the attenuation coefficient for material i of thickness x_i. It should be noted that the constant a_4 in effect represents an "effective depletion depth". Although accuracies of $< 3\%$ have been found for planar detectors (Singh, 1976, Mowatt, 1969) Equation C.10 could not be fitted to the Durham 86 cm^3 coaxial detector. This was because the matrices describing the function used in the minimization routines (Bevington, 1969) turn out to be singular thereby indicating that the function does not have a unique solution. In order to fit this function, a procedure analogous to the backward reduction technique (eg, see Gorenstein et al., 1968) would be required.

Hajnal and Klusek (1974) extended the previous analysis by

including terms to account for the multiple Compton scattering process and for pair production. The approach will be described in the next section. The authors claim an average accuracy of 2% over the energy range 12 keV to 11 MeV. For comparison a best fit to both the MK1 and MK2 data yielded an average accuracy of 1.7% and 3.8% for the MK1 and MK2 detectors respectively over the range 59.5 keV to 3259 keV. It should be noted that the latter result reflects the quality of the measured data and therefore is not a true indication of the deviation of the fit from 'reality'. Also by fitting to the efficiency data of Mahoney et al. (1980) good agreement was found up to 10 MeV. Thus the above approach was adopted because not only did it fit well over the entire energy range, but it also offered the possibility that the various contributions to the efficiency could be extracted and compared to the existing Monte Carlo calculations of Summers (1983).

Finally, a compilation of functional and semi-empirical fits is given in Table C.1.

C.5 METHODOLOGY.

In this section we will describe the approach of Hajnal and Klusek. Note this is similar in many respects to the 'Dirac cord' method employed by Euler and Kaplan (1970) to calculate escape peak efficiencies.

Total energy absorption of an incoming photon occurs in a detector when there is either:

a) a photoelectric collision of the incoming photon with an electron,

b) a sequence of Compton collisions terminated by a photo-

TABLE C.1

Comparison of Functional and Semi-Empirical Formulas.

Function/Formula Reference	Energy Range keV	Mean Deviation Percent	References
Polynomial	81-3254	37	Present work (MK1)
Kane and Mariscotti	279-1332	3.3	McNelles and Campbell (1973)
	319-2599	good*	Singh (1976)
	356-1770	1.7	Pesent work (MK1)
East (1971)	122-1332	1.2	McNelles and Campbell (1973)
	319-2599	good*	Singh (1976)
	356-1770	1.7	Present work (MK1)
McNelles and	122-1332	0.5	McNelles and Campbell (1973)
Campbell (1973)	100-1770	4	Roney and Searle (1978)
	319-2599	excellent*	Singh (1976)
Harvey (1970)	400-1500	10	Harvey (1970)
Johnson and Mann (1973)	500-2700	not given	Johnson and Mann (1973)
Willet (1971)	392-1332	4.8	McNelles and Campbell (1973)
Vano et al. (1975)	200-6000	3	Vano et al. (1975)
	< 4000	3	Somorjai (1975)
	356-1770	4	Present work (MK1,MK2)
Paradellis and	300-1200	3	Paradellis and Hontzeas (1969)
Hontzeas (1969)	59-1836	54% worst*	Singh (1976)
Freeman and Jenkins	511-1330	1	Freeman and Jenkins (1966)
	100-1770	8	Roney and Searle (1978)
	511-1332	25% worst*	Singh (1976)
	150-1500	3	Tokan and Cothern (1969)
	356-1900	3	Present work (MK1)
Mowatt[+] (1969)	120-1332	1	Mowatt (1969)
	59-1836	Good*	Singh (1976)
Hajnal and Klusek (1974)	12-11000	2-5	Hajnal and Klusek (1974)
	59-3254	1.7	Pesent work (MK1)
	81-3254	3.8	Present work (MK2)

* Mean deviation not given.

+ May not be applicable for coaxial detectors (see McNelles and Campbell (1973)).

electric collision or,

c) pair production followed by absorption of the secondary

photons through mechanisms a or b.

The probability that a gamma ray of energy E_o will lose some or all of its energy within the detector will be given by,

$$P = (1 - e^{-\mu_o d})$$ (C.11)

where μ_o is the mass attenuation coefficient at energy E_o and the d is the thickness of the intrinsic region in gm/cm^2. The probability of occurrence of the three primary interactions will be given by weighting Equation C.11 by the relevant attenuation coefficient. Thus the probabilities for a photoelectric and Compton interaction are;

$$P_o = \frac{\tau_o}{\mu_o}(1 - e^{-\mu_o d})$$ (C.12)

and

$$C_o = \frac{\tau_o}{\mu_o}(1 - e^{-\mu_o d})$$ (C.13)

respectively. For Compton interactions, the average energy of single and multiply scattered photons will be given by,

$$E_1 = E_o \frac{\sigma_{so}}{\sigma_o} \quad \text{and } E_2 = E_1 \frac{\sigma_{s1}}{\sigma_1} ,\ldots \text{ etc}$$ (C.14)

and the corresponding energy of the Compton electrons,

$$T_1 = E_o \frac{\sigma_{ao}}{\sigma_o} \qquad , \quad T_2 = E_1 \frac{\sigma_{al}}{\sigma_1} \quad , \ldots \text{ etc} \qquad \text{(C.15)}$$

where σ, σ_s and σ_a are the average Compton collision, scattering and absorption coefficients respectively. Therefore, on average, a fraction σ_{ao}/σ_o of the gamma ray energy is absorbed during the first Compton scattering and the remaining σ_{so}/σ_o fraction is available for multiple scattering processes. The number of single-scattered gamma rays is also proportional to σ_s/μ_o. The relative probability that the scattered photon will again interact within the intrinsic region of the detector will now be given by,

$$\frac{\tau_1}{\mu_1} \quad , \quad \frac{\sigma_1}{\mu_1} \quad \text{and} \quad \frac{\kappa_1}{\mu_1} \qquad \text{(C.16)}$$

where κ is the pair production attentuation coefficient and where μ_1 is the new linear attenuation coefficient corresponding to the scattered photon energy E_1. By describing primary and secondary interactions in a 'chain of events' fashion the probability that a Compton-scattered gamma ray will lose all its energy within the intrinsic region is given by,

$$P_c = C_o P_o + C_o C_1 P'_o + \ldots + C_o C_1 C_2 \ldots \qquad \text{(C.17)}$$

where the subscript, $0,1,\ldots n$ denote the $1,2,\ldots n$th interaction. Considering only two scatters, then;

$$P_c = \frac{(1 - e^{-\mu_o d})}{\mu_o} \left[a_1 \sigma_a + a_2 \sigma_s \left(\frac{1 - e^{-\mu_1 d'}}{\mu_o} \right) (\tau_1 + a_3 \sigma_1 f_2') \right] f_1 \qquad \text{(C.18)}$$

where d′ is the active depth of the detector for Compton scattered photons and $f_1(E_1)$ and $f_2(E_2)$ are exponential functions* of the scattered gamma ray energies E_1 and E_2.

A fraction of the incident gamma-rays will interact via pair production. This probability will be proportional to,

$$P_{\pm} = \frac{\kappa_o}{\mu_o}(1 - e^{-\mu_o d}) \tag{C.19}$$

where f_3 is an exponential function of the energy of the electron-positron pair,

$$f_3 = \exp(-aT) \tag{C.20}$$

and $T = (\dot{E}_o - 1.022)$. By accounting for absorption in the cryostat and detector dead layers, we can now construct the efficiency function.

$$\varepsilon = \Sigma P = \overset{1}{e^{-\mu_w W}} \overset{2}{e^{-\mu_o a_1}} \overset{3}{\left(\frac{1 - e^{-\mu_o a_2}}{\mu_o}\right)} \left\{ \overset{4}{a_3\tau_o} + \left[a_4\sigma_{ao} + \right. \right. \tag{C.21}$$

$$\overset{5}{a_5\sigma_{so}}\overset{6}{\left(\frac{1 - e^{-\mu_1 a_6}}{\mu_1}\right)} \overset{7}{(\tau_1 + a_7\sigma_1 e^{-E_2 a_7})} \right] e^{-a_9 E_1} + \overset{8}{a_{10}\kappa_o e^{-a_{11} T_1}} \left. \right\}$$

where the various terms arise as follows.

1) Attenuation in the cryostat window of thickness W and attenuation coefficient μ_w.

2) Attenuation in the detector dead layers.

---

* Note; other energy dependences are possible.

3) Probability of an interaction taking place.

4) Direct photoelectric absorption.

5) Single Compton scattering,...

6) Followed by photoelectric absorption or, ...

7) Another scatter. The exponential term corresponds to further scatters.

8) Pair productions.

It sould be borne in mind that the following assumptions have been made in the previous analysis.

a) All photoelectrons and K and L x-rays are totally absorbed in the detector volume.

b) Bremsstrahlung has been ignored (although first order effects are included in the absorption factors, f_1, f_2 and f_3). Since energy loss dE_{Brem}/dx, is proportional to E, the inclusion of a term $a_n E$ should account for this contribution.

c) Secondary pair productions and third and higher Compton scattering are neglected. A third order scattering term was originally included in Equation C21, but made no statistically significant change to the results.

The absolute detector efficiency, ε_a, is given by the first three terms of Equation C.21, ie,

$$\varepsilon_a = e^{-\mu_w W} e^{-\mu_o a_1} (1 - e^{-\mu_o a_2}) \tag{C.22}$$

C.6 RESULTS.

Equation C.21 was fitted to the experimentally determined data of the MK1 and MK2 detectors. The results are listed in Table C.2

Table C.2 A comparison of the measured and calculated Full Energy Peak Efficiences for the MK1 and MK2 detectors.

MK1 Detector

REDUCED CHI SQUARED= 0.4037558

A COEFFICIENTS (A1, ..., Al)

0.3544243	0.9865803	0.3179638	4.4996478E-02	23.06847
71.79338	8.137260	0.5442259	15.21282	8.902893

FITTED VALUES

ENERGY	MEASURED	FITTED	ERROR PERCENT
5.9500001E-02	0.4500000	0.4541715	0.9270046
8.1000000E-02	0.6400000	0.6311179	-1.387848
0.1600000	0.6270000	0.6417187	2.347482
0.2230000	0.5750000	0.5645466	-1.817973
0.2420000	0.5370000	0.5382762	0.2376527
0.2760000	0.5040000	0.4910931	-2.560889
0.2950000	0.4600000	0.4655432	1.205050
0.3050000	0.4600000	0.4524947	-1.631593
0.3520000	0.3920000	0.3957972	0.9688819
0.3560000	0.3930000	0.3913532	-0.4190449
0.3840000	0.3625000	0.3619559	-0.1501133
0.6620000	0.1915000	0.1922302	0.3812830
0.7690000	0.1580000	0.1612242	2.040629
0.8970000	0.1445000	0.1358456	-5.989205
1.038000	0.1200000	0.1186245	-1.146253
1.173000	0.1108000	0.1090445	-1.588419
1.238000	0.1059000	0.1057654	-0.1270679
1.275000	0.1090000	0.1040668	-4.525831
1.333000	9.9200003E-02	0.1014899	2.308403
1.360000	9.7999997E-02	0.1002902	2.336966
1.764000	7.9000004E-02	8.0503903E-02	1.903670
1.771000	8.3099999E-02	8.0163896E-02	-3.533216
2.204000	6.1000001E-02	6.2998533E-02	3.276283
2.599000	5.3300001E-02	5.3295825E-02	-7.8349914E-03
3.254000	4.3249998E-02	4.3009937E-02	-0.5550554

ERROR SUM= 1.2591010E-02 ABS SUM (PERCENT)= 43.36945
CHI SQUARE= 0.4037558

$

MK2 Detector

REDUCED CHI SQUARED= 0.8183690

A COEFFICIENTS (A1, ..., Al)

0.6015930	1.059277	0.2552169	3.9437003E-02	73.88098
55.55178	7.418661	0.5558146	6.402564	6.733731

FITTED VALUES

ENERGY	MEASURED	FITTED	ERROR PERCENT
8.1000000E-02	0.5429100	0.5423935	-3.0411095E-03
0.2420000	0.4553800	0.4586422	0.7163801
0.2760000	0.4273900	0.4153268	-2.822536
0.2950000	0.3897800	0.3933361	0.9123282
0.3030000	0.3758100	0.3845280	2.319785
0.3520000	0.3324300	0.3359922	1.071550
0.3560000	0.3327800	0.3324147	-0.1097773
0.3840000	0.3094300	0.3088518	-0.1868580
0.6090000	0.1890800	0.1876197	-0.7723023
0.7690000	0.1342000	0.1437610	7.124432
0.8470000	0.1296000	0.1289407	-0.5086861
0.8980000	0.1383700	0.1208819	-12.63864
1.035000	0.1057000	0.1044651	-1.168282
1.120000	0.1058200	9.7286977E-02	-8.063715
1.238000	9.2699997E-02	9.0024494E-02	-2.886196
1.360000	8.0399998E-02	8.4440447E-02	5.025435
1.378000	7.3760003E-02	8.3702318E-02	13.47923
1.764000	6.7220002E-02	6.8806991E-02	2.360888
1.770000	7.2499998E-02	6.8579592E-02	-5.407457
1.836000	7.1837001E-02	6.6104077E-02	-7.980461
2.204000	5.1430002E-02	5.3893190E-02	4.789399
2.600000	4.4500001E-02	4.4507049E-02	1.5838761E-02
3.254000	3.7900001E-02	3.4807559E-02	-8.159476

ERROR SUM= 9.2083809E-04 ABS SUM (PERCENT)= 68.52274
CHI SQUARE= 0.8183690

$

and shown graphically in Figures C.1 and 4.8. The window thickness, W, and detector depth, a_2, were known from the manufacturer's data and were therefore assigned the constant values of 0.162 and 23.452 gcm^{-2} respectively. A best fit yielded a χ^2 of 6.0 (15 dof) and 10.6 (13 dof) for the MK1 and MK2 detectors respectively, corresponding to mean deviations 1.7% and 3.8%. The fractional deviations between the experimental and fitted results are shown in Figure C.2 from which it may be seen that there are no systematic trends with energy thus illustrating the quality of the fit. From inspection the errors appear to be overestimated which would account for the rather low values of χ^2.

From the fitted parameters we can derive a value for detector dead layer. This is given by the parameter a_1. By varying this parameter in χ^2 space we obtain the values (665 ± 9) μm and (1128 ± 20) μm for the MK1 and MK2 detectors respectively. These values seem reasonable. It is interesting to note however, that as a result of a vacuum leak, the dead layer has increased by a factor of two.

C.7 COMPARISON WITH MONTE CARLO RESULTS.

Monte-Carlo calculations have been carried out for the MK2 detector (Summers, 1983). These calculations take into account all processes except pair production and are therefore only valid for gamma-ray energies $\leq$ 1 Mev. The calculated FEPE fits the measured data well for energies > 500 keV but is consistently greater than the experimental values for energies < 400 keV. Summers speculates that the discrepancy at low energies must be due to an extra .8 gcm^{-2} of delrin between the detector face and
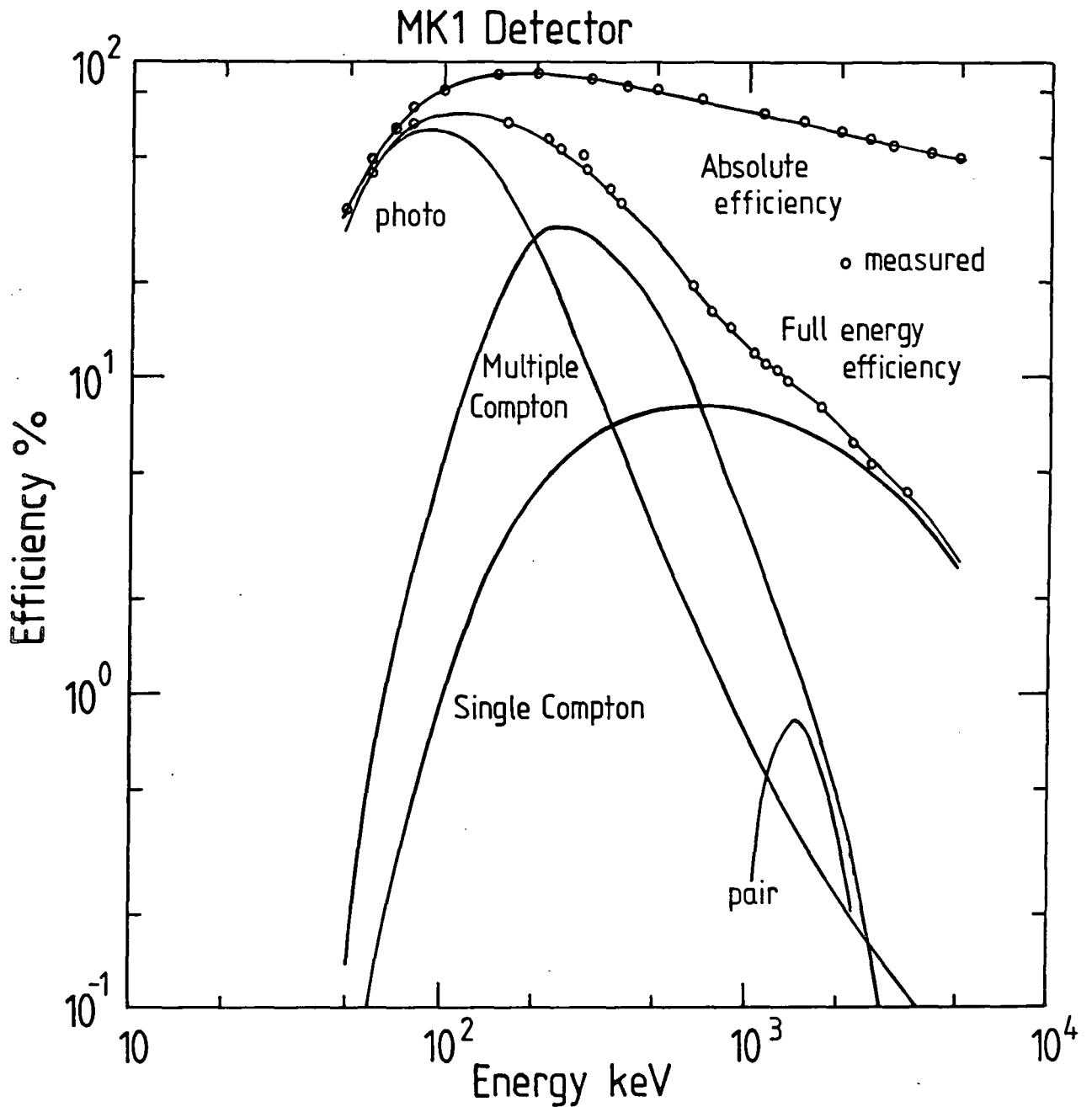
Figure C.1 The experimental and calculated efficiencies for the MK1 detector. Also shown are the individual contributions to the FEPE.
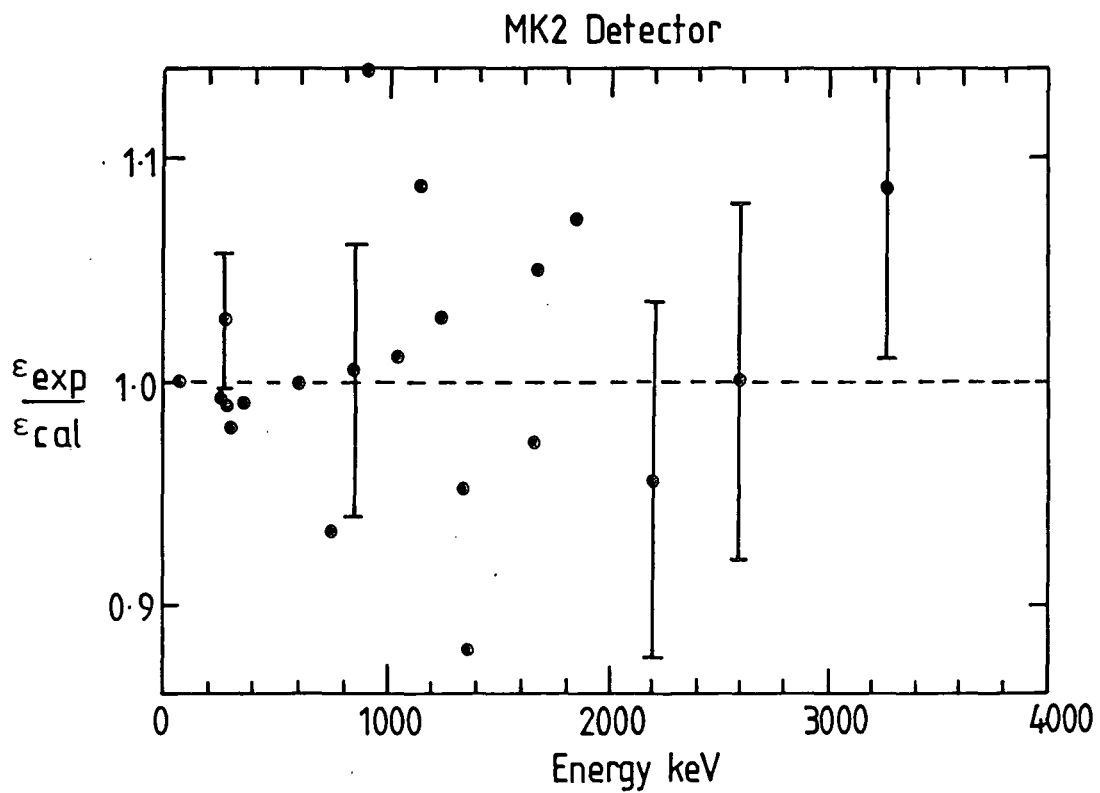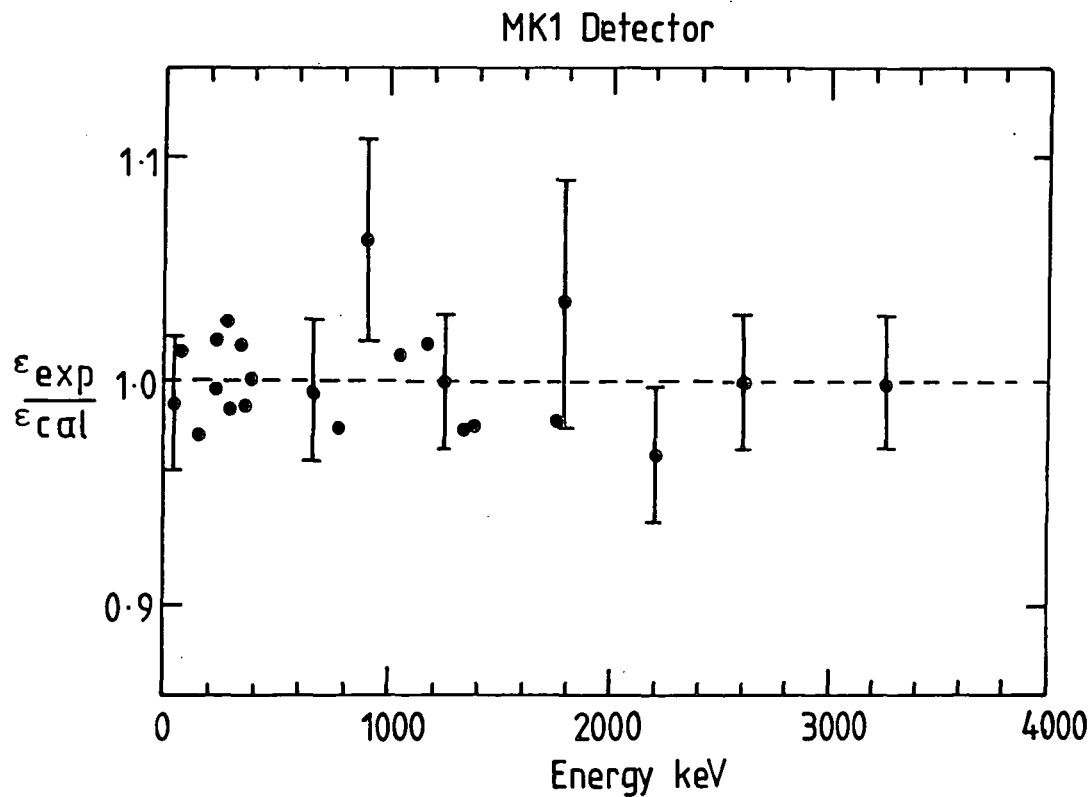
Figure C.2   The ratio of the experimental to calculated
FEPE as a function of energy for the MK1
and MK2 detectors.

cryostat. This discrepancy is almost certainly due to failure to include the dead layer in the detector model. The dead layer thickness is ~ 0.6 gcm^{-2} which corresponds to a transmission of 0.91 at 200 keV. For comparison the transmission of .8 gcm^{-2} of delrin is also 0.91 at 200 keV.

The relative contributions to the FEPE (ie, photoelectric and Compton) were extracted from Equation C.21) and are compared to the Monte Carlo calculated values in Figure 4.8. The Monte Carlo values were corrected for the dead layer thickness by expressing each quantity as a fraction of the associated value of the FEPE and multiplying by the measured efficiency. The corrections for the absolute efficiency were somewhat simpler.

$$\varepsilon_a = \varepsilon_a^* \exp(-\mu a_1) \qquad (C.23)$$

where ε_a^* is the Monte Carlo derived value. The agreement between the Monte Carlo and semi-empirical models for the absolute efficiency, photoelectric and total Compton contributions to the FEPE is excellent. However, it should be noted that the models do not agree on the relative amounts of indirect photoelectric and plural Compton contributions. This is probably due to the similarity of functions in terms 4 and 5 of Equation C.21, thereby indicating that there may not be unique solutions for a_3, a_4, and a_5.

C.8 CONCLUSION.

We have shown that provided all dominant physical processes are accounted for (and the parameters are constrained accordingly)

semi-empirical calculations can provide an excellent and accurate
description of a physical system.

APPENDIX D

CALCULATION OF THE POINT SOURCE EFFECTIVE COLLIMATOR
APERTURE FOR COLLIMATED X-RAY AND γ-RAY TELESCOPES

D.1 INTRODUCTION

In determining the absolute fluxes and spectral characteristics of diffuse and cosmic point sources with conventional collimated x-ray and γ-ray telescopes, an accurate knowledge of the effective collimator aperture is imperative. For a perfectly opaque collimator the determination of the incident photon spectrum is relatively straightforward since the area of the detector presented to the source can be derived from simple geometrical arguments. Unfortunately for practical telescopes photon leakage through the body of the collimator and the edges of the aperture result in an increase in the effective area of the detector. The response of the collimator can then be understood as the sum of two functions; a geometric component plus a leakage or penetration component. For the collimators typical of gamma-ray astronomy ($\gtrsim$ 20 cm of NaI(Tℓ)) the leakage flux can increase the effective detector area (and therefore the measured flux) by as much as 30% in the MeV range. In this appendix a procedure for calculating the energy dependent point source response (or effective collimator aperture) for a right-cylindrical collimator will be derived. It is assumed that interactions only take place on the forward face of the detector, although in principle the depth of the detector can be taken into account. Although we consider point sources, the method is quite general and can easily be applied to line, plane or extended sources. The results will

be compared to the experimental data of the Durham MK1 γ-ray telescope.

D.2 POINT SOURCE RESPONSE

The sensitive area of a collimated detector is a function of the angle between the photon momentum and collimator axis. At low energies (say < 300 keV) the collimator material is almost completely opaque to gamma-rays. For a distant point source (which we define to be located at an infinite distance) the sensitive area can be approximated by a 'geometric' response given by:

$$
A(\theta) = \begin{cases} \pi r_c^2, & \text{for } \theta = 0 \\ 2r_c^2 \cos\theta \left\{ \cos^{-1}\left(\dfrac{\tan\theta}{\tan\alpha}\right) - \dfrac{\tan\theta}{\tan\alpha}\left[1 - \dfrac{\tan^2\theta}{\tan^2\alpha}\right]^{\frac{1}{2}} \right\}, & 0 < \theta < \alpha \\ 0, & \text{for } \theta \geq \alpha \end{cases}
\tag{D.1}
$$

for $r_c \leq r_d$. Here θ is the polar angle between the source and the telescope axis, and α is the maximum geometric opening angle of the telescope i.e.,

$$
\alpha = \tan^{-1}\left(\frac{2r_c}{h}\right)
\tag{D.2}
$$

where h is the height of the collimator and r_c and r_d are the radii of the collimator and detector respectively. Note this formula is only valid for the case where the radius of the

collimator is less than or equal to that of the detector. For r_c > r_d, $A(\theta)$ for a distant point source is given by;

$$A(\theta) = \cos\theta \left(r_c^2 \cos^{-1} \left[\frac{1}{2r_c} \left\{ h\tan\theta + (r_c - r_d) \frac{\tan\alpha}{\tan\theta} \right\} \right] \right.$$

$$+ r_d^2 \cos^{-1} \left\{ \frac{1}{2r_d} \left[h\tan\theta - (r_c - r_d) \frac{\tan\alpha}{\tan\theta} \right] \right\}$$

$$\left. - \frac{1}{2} \left[4r_d^2 r_c^2 - (h^2\tan^2\theta - r_d^2 - r_c^2)^2 \right]^{\frac{1}{2}} \right) \qquad (D.3)$$

for $\theta_o < \theta < \alpha$ and,

$$A(\theta) = \begin{cases} \pi r_d^2, & \theta \leq \theta_o \\ \\ 0, & \theta \geq \alpha \end{cases}$$

where $\alpha = \tan^{-1} \left(\frac{r_c + r_d}{h} \right)$ and $\theta_o = \tan^{-1} \left(\frac{r_c - r_d}{h} \right)$

For the case of a near point source (i.e one located at a finite distance above the collimator) Steyn et al. (1969) have given analytical relationships for determining the geometrical response to point, line and plane sources, under the restrictions $r_c < r_d$ and $r_c << h$. Their analysis includes provisions for the treatment of cylindrical and conical collimators with any orientation of the source plane.

At energies greater than 300 keV simple geometric arguments begin to break down due to increasing penetration of the collimator material with photon energy. The resulting effect is that at a given angle the sensitive area is increased. Mather (1957) approached the problem by assuming the effective point source aperture response is the sum of three functions; a geometric aperture G_O given by Equation D.1, a penetration aperture P, and a scattering aperture S which takes into account scattered radiation from the walls of the aperture. The penetration aperture (which is due to radiation leakage through the edges of the aperture) can be expressed simply by,

$$ P = \int_a^1 e^{-\mu(E)\lambda} \left(\frac{dA(\lambda)}{d\lambda} \right) d\lambda \qquad (D.4) $$

where
$$ a = \begin{cases} 0, & \theta \leq \alpha \\ 1 - \dfrac{\tan\theta}{\tan\alpha}, & \theta > \alpha \end{cases} $$

and μ is the linear attenuation coefficient for the collimator material at energy E and λ is the path length.

The problem with Mather's approach is three fold in that it assumes, a) an infinite detector, b) a small angle approximation and, c) homogeneous collimator material. Also the approximations given by Mather for performing the integration consist of two empirical fits which fail as $\tan\theta/\tan\alpha$ approaches unity.

Lee (1982) has considered edge penetration for the specific

case when the collimator is located a distance ℓ above the detector, such that $\ell \gg h$, where h is the height of the collimator. As with Mather's aproach, Lee also assumes a small angle approximation and an infinite detection plane.

In the procedure outlined below we consider the general case for any source to detector distance, and size of detector or collimator aperture. It is assumed that since one only considers detected events in the photopeak, scattering effects can be neglected. This is certainly true for processes which redistribute the photon energy, such as Compton scattering. Rayleigh scattering might at first thought contribute to the aperture response, but a perusal of the relevant cross-sections for commonly used collimator materials show that only photons with energies up to ~400 keV would contribute. Furthermore, the calculations of Mather would indicate that the effect is negligible, being approximately equal to that of Compton scattering effects and at worse a factor of approximately 40 below that of the geometric aperture at low energies.

These calculations are most easily carried out by means of a computer program and where necessary comments on computer implementation will be given.

D.3 METHODOLOGY

The foregoing analysis is based on the simpler case of $r_c \geq r_d$, however we will point out where changes in formulae are required for $r_d > r_c$. Consider the point source located at (x_s, o, z_s) in Figure D.1. We introduce a Cartesian coordinate system with the z axis along the aperture axis and origin at the centre
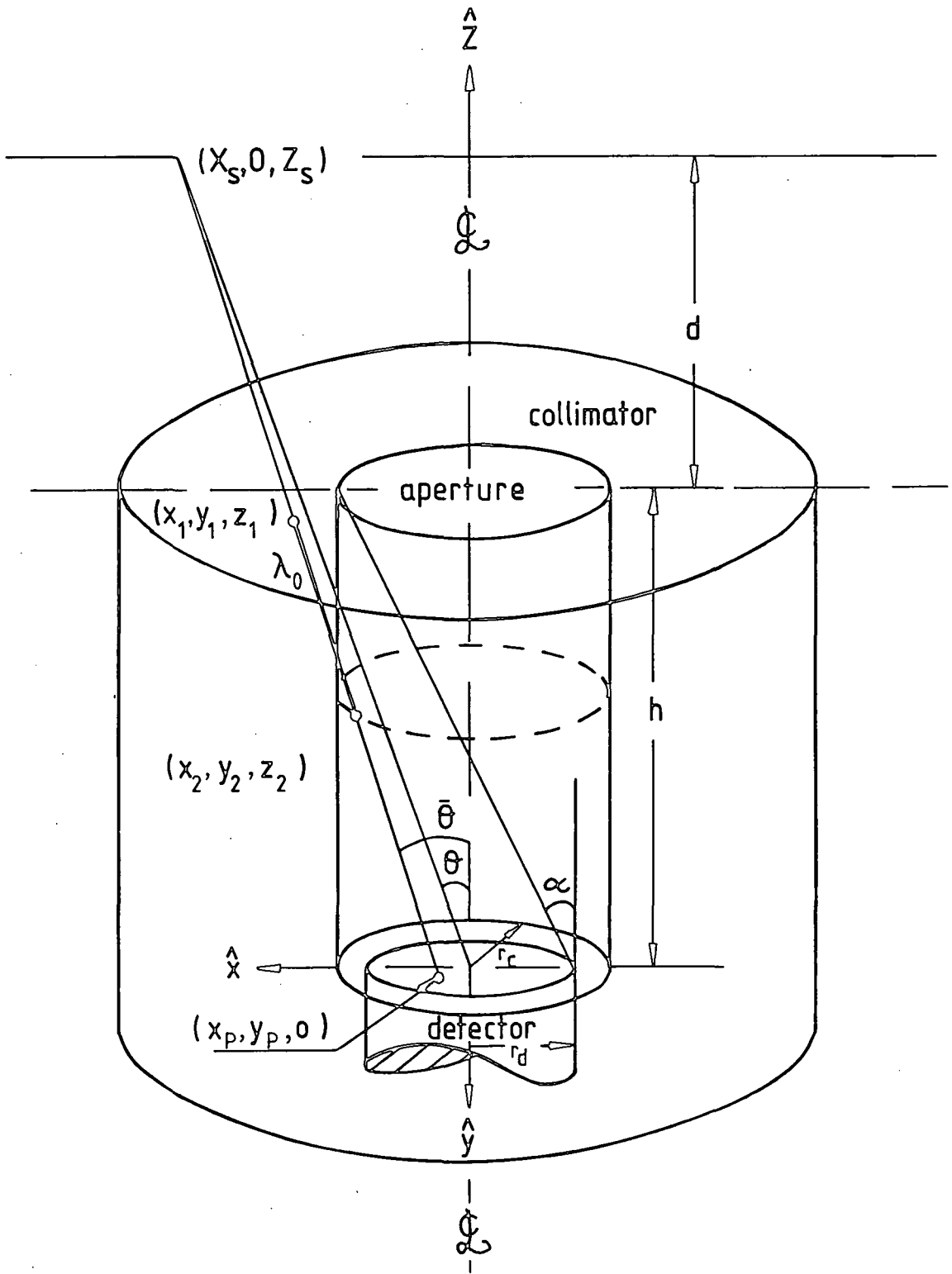
Figure D.1 Model of a collimated detector system. The geometry here is for the specific case where the radius of the collimator is greater than the radius of the detector. Refer to the text for a definition of the symbols.

of the detector (which lies in the $\hat{x},\hat{y}$ plane). For any point on the detector plane we can define a set of parametric equations for the line from the source to this point,

$$x = a_x t + b_x$$
$$y = a_y t + b_y \qquad (D.5)$$
$$z = a_z t + b_z$$

We define $t = 0$ at the source plane and 1 at the detector plane. Therefore at the source (x_s, o, z_s): $b_x = x_s$, $b_y = 0$, $b_z = z_s$, and at the detector $(x_p, y_p, 0)$: $a_x = x_p - x_s$, $a_y = y_p$ and $a_z = -z_s$ Substituting, the line equations now become,

$$x = (x_p - x_s)t + x_s$$
$$y = y_p t \qquad (D.6)$$
$$z = z_s(1 - t)$$

At the first interaction point on top of the collimator (x_1, y_1, z_1),

$$t_1 = 1 - h/z_s$$
$$x_1 = (x_p - x_s)t_1 + x_s \qquad (D.7)$$
$$y_1 = y_p t_1$$
$$z_1 = h$$

For cases when $x_s > r_c$ we can determine the coordinates (x_2, y_2, z_2) for the point where the photon exits the collimator into the aperture using,

$$x_2^2 + y_2^2 = r_c^2 \tag{D.8}$$

and solving the quadratic in t_2,

$$((x_p - x_s)^2 + y_p^2)t_2^2 + 2(x_p x_s - x_s^2)t_2 + x_s^2 = r_c^2 \tag{D.9}$$

The photon pathlength through the collimator is then given by,

$$\lambda_o(x_p, y_p) = ((x_1 - x_2)^2 + (y_1 - y_2)^2 + (z_1 - z_2)^2)^{\frac{1}{2}} \tag{D.10}$$

for $x_p^2 + y_p^2 \leq r_c^2$. For $x_p^2 + y_p^2 > r_c^2$ the photon pathlength is determined from geometric arguments based on sign of the roots of Equation D.9. The sensitive area will then be given by integrating dx_p, dy_p ($= rd\theta dr$) over the detector plane and weighting by $\exp(-\mu(E)\lambda_o(x_p, y_p))$;

$$A(\theta, E) = \int_{-r_d}^{+r_d} dx_p \int_{-\sqrt{r_d^2 - x_p^2}}^{+\sqrt{r_d^2 - x_p^2}} dy_p \cos \bar{\theta} \exp(-\mu(E)\lambda_o(x_p, y_p)) \tag{D.11}$$

$$\text{for} \quad x_s > \begin{cases} (r_c + r_d)z_s/h - r_d, & \text{for} \quad r_c \geq r_d \\ \\ 2r_c z_s/h - r_c, & r_d > r_c \end{cases}$$

For x_s less than or equal to the above limits there is also a direct contribution, i.e. photons passing straight down the aperture. This latter condition is achieved simply in a program

sense, by setting $\lambda_o = 0$ whenever $z_2 \geq h$. For $x_s \leq r_c$, $A = A_o$ the geometric area. For the telescope described in this thesis corrections must be made to λ_o for the gap between the collimator and annulus and the various materials used in both. Specifically, Equation D.11 may now be written:

$$A(\theta,E) = \int_{-r_d}^{+rd} dx_p \int_{-\sqrt{r_d^2 - x_p^2}}^{+\sqrt{r_d^2 - x_p^2}} dy_p \cos\overline{\theta} \prod_{i=1} \exp(-\mu_i(E)\lambda_i) \qquad (D.12)$$

where $\Sigma\lambda_i = \lambda_o(x_p, y_p)$. Note Equation D.12 is quite general and applies to both near and distant point sources and also to any size of detector and collimator. In practice the line equations (Equations D.8 - D.10) break down for $z_s > 50h$ due to finite precision resulting in an inability to separate the roots of Equation D.9. It should be noted however that at source distances $> 20h$ the near and distant point source responses concur within a few percent for any collimator geometry such that $r_c \ll h$.

If one need only consider a distant point source (as is generally the case in gamma-ray astronomy) then Equations D.5 to D.10 can be simplified considerably. The line equations now become:

$$y = y_p \qquad (D.13)$$
$$z = (x - x_p)\cot n\theta$$

where θ is the polar angle between the source and the telescope

axis.   The photon coordinates at the top of the collimator are,

$$x_1 = h\tan\theta + x_p$$
$$y_1 = y_p \tag{D.14}$$
$$z_1 = h$$

and at the collimator/aperture interface:

$$x_2 = (r_c^2 - y_p^2)^{\frac{1}{2}}$$
$$y_2 = y_p \tag{D.15}$$
$$z_2 = (x_2 - x_p)\cot n\theta$$

therefore,

$$\lambda_o(x_p, y_p) = ((x_1 - x_2)^2 + (z_1 - z_2)^2)^{\frac{1}{2}} \tag{D.16}$$

for $x_p^2 + y_p^2 \le r_c^2$. Again for $x_p^2 + y_p^2 > r_c^2$ the photon pathlength is determined from geometric arguments based on the values of x and y.   For ease of computation a useful approximation can be made as follows. Using Equation D.12 to   calculate   where   the   sensitive area   falls   to   0.5 A_o the energy dependent FWHM of the aperture ($\theta(E)_{\frac{1}{2}}$) can be   determined.[*]   We   can   then   apply   a   trapezoidal approximation   of   the   sensitive   area   as a function of the FWHM i.e.,

$$A(\theta,E) = A_o \cos\theta \begin{cases} 1, & 0 \le \theta \le \theta_o \\ 1 - \dfrac{(\theta - \theta_o)}{\theta_m}, & \theta_o < \theta < \alpha \\ 0, & \theta \ge \alpha \end{cases} \tag{D.17}$$

Note: omit the factor `$\cos\bar{\theta}$´ in equation D.12 when evaluating $\theta(E)_{\frac{1}{2}}$

where $\qquad \theta_m = \theta(E)_{\frac{1}{2}} - 2\theta_o$

$$\theta_o = \begin{cases} \tan^{-1}\left(\dfrac{r_c - r_d}{h}\right), & r_c > r_d \\[2em] 0, & r_d \geq r_c \end{cases}$$

and

Values of sensitive area were calculated for energies ranging from 50 keV to 10 MeV using Equation D.12 and compared with those calculated using the trapezoidal approximation for the Durham telescope described in Chapter 4. For $\theta \leq 0.75 \, \theta(E)_{\frac{1}{2}}$ the average error is $\leq$ 1% at all energies. For $\theta > 0.75 \, \theta(E)_{\frac{1}{2}}$ the error rises rapidly up to 100% at $\theta = \theta(E)_{\frac{1}{2}}$.

D.4 RESULTS

Calculations were originally carried out for the detector geometry described in Tomnovec and Mather (1957) and are compared to the experimentally measured data in Figure D.2. The pertinent specifications of this detector are given in Table D.1. The agreement is good for both near (source to detector distance = 147.3 cm) and distant point sources.

The energy dependent transmission of the Durham spectrometer collimator was measured using IAEA standard γ-ray sources. Table D.1 lists the relevant details of the detector and collimator. Each radioactive source was placed 88.9 cm above the detector plane and moved in one centimeter steps along a diametrical line. At each position a pulse height spectrum was obtained and the area
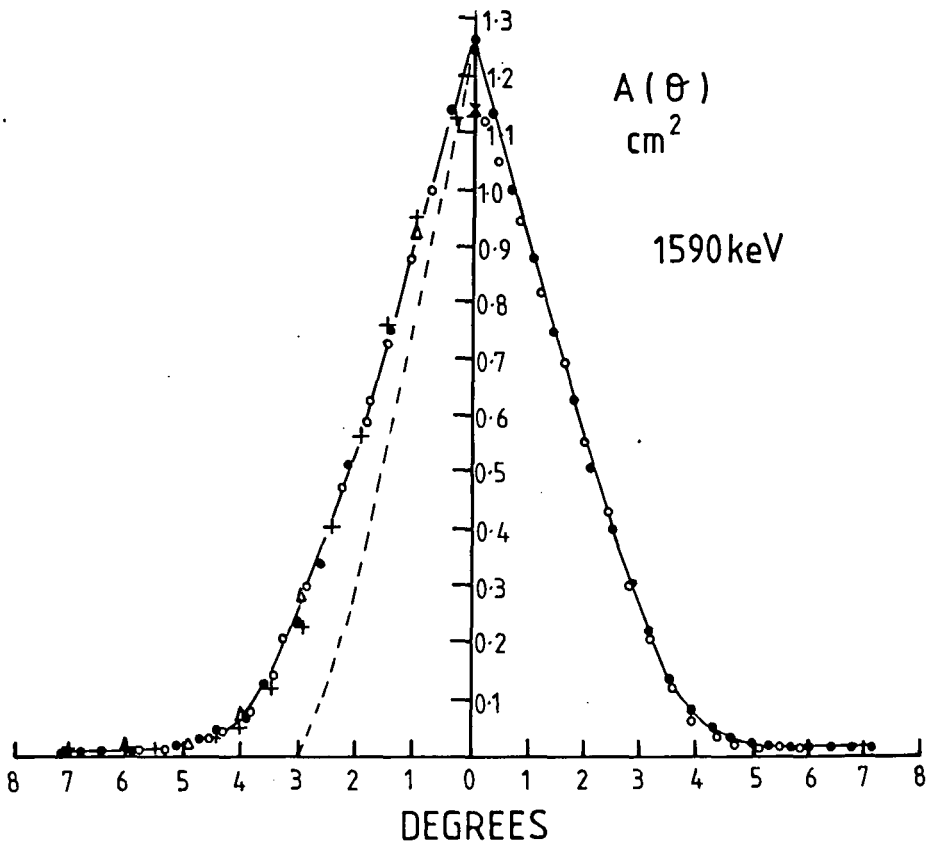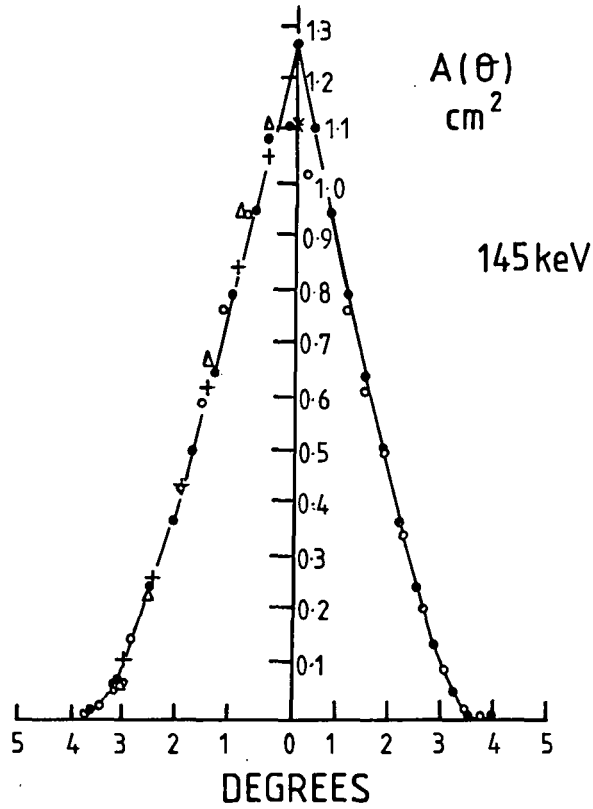
Figure D.2 A comparison of the present calculations, +(∞ distant source),
Δ (147cm distant), with the experimental and theoretical data
of Tomnovec and Mather (1957) : o - experimental-, • - theoretical
(∞ distant source), × - theoretical (147cm distant), --- geometric
aperture (147 cm distant). Adapted from Figures 3 and 5 of
Tomnovec and Mather (1957)

TABLE D.1

Collimated detector parameters used in the calculations.
All dimensions are in cm.

Telescope Reference	Mather and Tomnovec (1957)	Ayre et al. (1981)
Detector Radius	5.1	2.50
Collimator Radius	0.6	2.78
Collimator Thickness	20.3	55.4
Collimator Material	Pb (20.3)	Pb (7.5), Ne102 (7.5)
		NaI (20.3), Air (18.1)

under the peak (background subtracted) was recorded. The areas in the peak were plotted as a function of position and the FWHM was taken as the angular aperture at that energy. Using Equation D.12 the FWHM aperture was calculated as a function of energy and compared to the experimental values. The integrals were performed numerically using Gaussian Quadrature techniques; typical integration errors were $\leq 1\%$. The detector model takes into account the multi-layered structure of the collimator and the annulus. The results are shown in Figure D.3 from which it may be seen that there is good agreement. A χ^2 test of the theoretical data points yielded a reduced χ^2 of 0.8. For comparison, the predicted distant point source response is also shown in Figure D.3. Finally the predicted energy dependant distant point source response for the MK2 telescope is shown in Figure 4.9. This curve was used to produce the final source spectra given in this thesis.
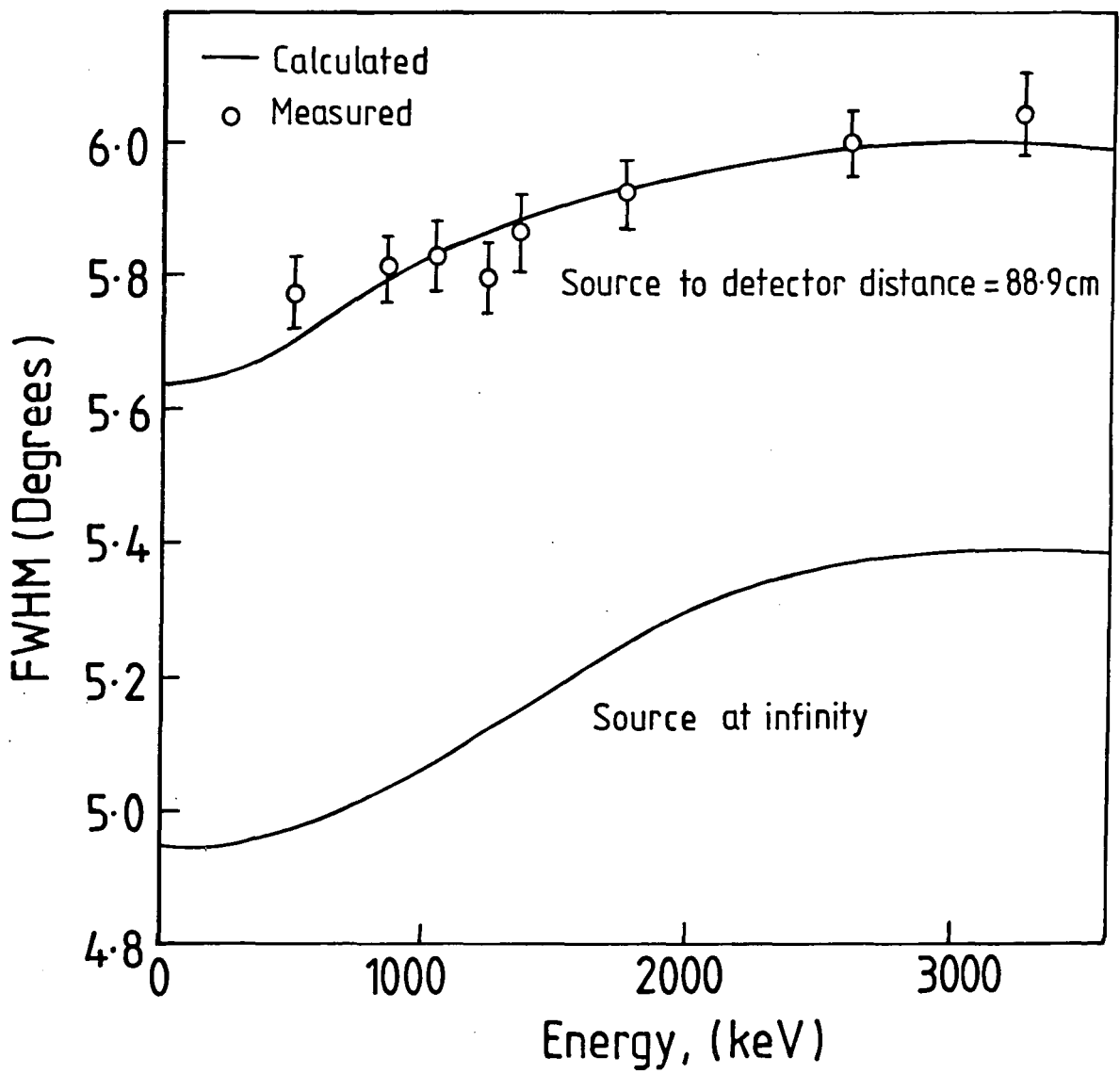
Figure D.3   The FWHM aperture of the Durham MK1 telescope as a
function of energy.

APPENDIX E.

AN EVALUATION OF COMPTON CONTAMINATION EVENTS IN AN ACTIVELY SHIELDED GE GAMMA-RAY DETECTOR.

E.1 INTRODUCTION.

In determining the source flux from a set of gamma-ray observations it is usual to employ matrix techniques (Dolan, 1972) to deconvolve the various atmospheric and instrumental responses from the observed energy loss spectrum. Specifically the observed energy loss spectrum is given by,

$$F = M F_o \qquad (E.1)$$

where F_o is a column matrix representing the incident source flux and M is a square matrix representing the combined atmospheric and instrumental responses of the detector. If we assume an ideal anticoincidence system the various components of M can be directly measured or calculated. However, in practice account must be taken of unvetoed Compton interactions due to the finite shielding efficiency. The determination of this component is generally not straightforward, requiring lengthy Monte-Carlo calculations. In this appendix we will evaluate the photopeak and unvetoed Compton components for the Crab Nebula flux mesurements described in this thesis.

E.2 METHODOLOGY.

Consider the observation of a celestial point source using a

conventional collimated gamma-ray telescope at polar angle θ with respect to the central axis of the telescope, atmospheric depth x g cm^{-2}, and zenith angle $\phi > |\lambda-\delta|$ where λ is the latitude of the observation and δ is the declination of the source.

For the ideal case the vetoed counting rate due to the source in energy interval $\Delta E = E_n - E_{n-1}$ will be due purely to the photopeak contribution and will be given by:

$$r_p = \delta t \cos \theta \, (1-2\Sigma r_{ai}\tau) \int_{E_{n-1}}^{E_n} \int_0^\infty I(E)A(E,\theta)\varepsilon_p(E)G(E,E')B(E,\theta,\phi)dE \, dE'$$

where

$$G(E,E') = \frac{1}{\sqrt{2\pi}\,\sigma_R(E)} \exp\left(-\frac{(E-E')^2}{2\sigma_R^2(E)}\right) \qquad (E.2)$$

and

$$B(E,\theta,\phi) = \exp\left(-\left[\frac{\mu_a(E)x}{\cos\phi} + \sum_{j=1}\frac{\mu_j(E)d_j}{\cos\theta}\right]\right)$$

$I(E)$ is the differential source intensity (photons cm^{-2}s^{-1}keV^{-1}), $\varepsilon_p(E)$ is the detector full energy peak efficiency at energy E, $A(E,\theta)$ is the detector sensitive area at angle θ, τ is the resolving time of the anticoincidence circuitry, r_{ai} is the rate of the ith anticoincidence element, δt is the fractional live time of the data aquisition system and μ_a and μ_j represent the mass attenuation coefficients for air and additional absorbing materials above the detector corresponding to equivalent thicknesses x and d_j g cm^{-2}. The detector energy resolution $\sigma_R(E)$, is given by:

$$\sigma_R(E) = \begin{cases} (hE)^{0.5}, & \text{for NaI detectors} \\ \\ (p + qE + sE^2)^{0.5}, & \text{for Ge detectors} \end{cases} \quad \text{(E.3)}$$

where h,p,q and s are constants.

The corresponding background rate is well approximated by two functions representing the continuum spectrum and the contribution due to line components,

$$r_b = \int_{E_{n-1}}^{E_n} a \exp[-bE]dE + \int_{E_{n-1}}^{E_n} \sum_{k=1}^{E_n} \ell(E_k)G(E_k,E)dE \quad \text{(E.4)}$$

where a and b are semi-empirical constants and $\ell(E_k)$ is the <u>measured</u> intensity of the kth line component at energy E_k. Depending on the detector geometry, it should be noted that other energy dependences are possible for the first term in Equation E.4.

The effect of a finite shielding efficiency will be to increase our measured source rate due to continuum events caused by unvetoed Compton interactions. Specifically our measurement will now yield:

$$r_s \pm \sigma_s = (r_p + r_c) \pm \left[r_b \left(\frac{1}{t_s} + \frac{1}{t_b} \right) \right]^{\frac{1}{2}} \text{sec}^{-1} \quad \text{(E.5)}$$

assuming $r_b \gg r_s$. In the above equation σ_s represents the error in the source flux determination, r_c is the counting rate of unvetoed Compton events, and t_s and t_b are the source and

background observing times respectively.

We define $S(E,\overline{E})$ to be the probability that a gamma-ray of energy E will be scattered producing a continuum event at energy $\overline{E}$. Therefore the counting rate in interval ΔE due to unvetoed Compton events will be given by,

$$r_c = \int_{E_{n-1}}^{E_n} \int_0^\infty \int_0^\infty r(E)(1 - \varepsilon_a(E-\overline{E}))S(E,\overline{E})G(\overline{E},E')\ dE\ d\overline{E}\ dE' \quad (E.6)$$

where $\quad r(E) = \delta t \cos\theta\ (1 - 2\Sigma r_{ai}\tau)I(E)A(E,\theta)B(E,\theta,\phi) \quad (E.7)$

and $\varepsilon_a(E-\overline{E})$ repesents the efficiency of the anticoincidence system for detecting the scattered photon.

Although $S(E,\overline{E})$ will reflect the Compton electron distribution, a useful approximation can be made by assuming that the detected non-photopeak events for incident monoenergetic gamma-rays are uniformly distributed in the interval 0 to E_c (where E_c is the energy of the Compton edge). In this case:

$$S(E,\overline{E}) = \begin{cases} (\varepsilon(E) - \varepsilon_p(E))/E_c & 0 \leq \overline{E} \leq E_c \\ \\ 0 & \overline{E} > E_c \end{cases} \quad (E.8)$$

where $\varepsilon(E)$ is the intrinsic detector efficiency and;

$$E_c = \frac{2E^2}{2E + m_o c^2} \quad (E.9)$$

By comparison with experimental data, the average error in $S(E,\overline{E})$ is estimated to be $< 10\%$ using the approximation given in Equation E.8.

E.3 APPLICATION TO GE DETECTORS.

With regard to germanium detectors several further simplifications may be made to Equation E.6.

1) The resolution function $G(E',\overline{E})$ may be neglected since in general $\Delta E >> \sigma_R(E)$.

2) The second integral involving $\overline{E}$ may also be removed, as the 'veto' efficiency, $\epsilon_v = (1 - \epsilon_a(E-\overline{E}))$, is seen from experimental data to be very nearly independant of energy (Brauer et al. 1972, Ayre et al. 1981).

Under these conditions Equation E.6 can be written,

$$
r_c = \int_{\xi_1}^{\xi_2} r(E)(\epsilon(E) - \epsilon_p(E))\epsilon_v \left(1 - \frac{E_{n-1}}{E_c} \right) dE
$$
$$
+ \int_{\xi_2}^{\infty} r(E)(\epsilon(E) - \epsilon_p(E))\epsilon_v \frac{\Delta E}{E_c} dE \qquad (E.10)
$$

Note that the integration has been split into two parts to ensure that the function is analytic. The integration limits are determined by the fact that a gamma-ray with a Compton edge $E_c < E_{n-1}$ cannot contribute directly to r_c. Rearranging Equation E.9 gives:

$$
\xi_1 = 0.5 \ [E_{n-1} + (E_{n-1}^2 + 2E_{n-1}m_oc^2)]^{\frac{1}{2}} \qquad (E.11)
$$

and
$$\xi_2 = 0.5 \, [E_n + (E_n^2 + 2E_n m_o c^2)]^{\frac{1}{2}} \qquad (E.12)$$

E.4 RESULTS AND DISCUSSION.

The various components of the detector energy loss spectrum have been calculated numerically using the observational parameters listed in Table E.1 for the Crab Nebula observations described in Ayre et al. (1983). The functional forms of ϵ_p and ϵ were determined from semi-empirical calculations (Hajnal and Klusek, 1974) and the principle background line intensities were determined from experimental data and are listed in Table E.2. We assume a differential source flux given by (Jacobson et al. 1978),

$$dI(E) = 9.7E^{-2.1} \, dE \quad \text{photons cm}^{-2}\text{s}^{-1} \text{ keV}^{-1} \qquad (E.13)$$

The results are shown in Figure E.1 from which one can see there is good agreement between the predicted and experimentally determined energy loss spectrum. The shaded area in the figure represents the predicted uncertainty of the measured data points assuming that both source and background counting rates are Poisson distributed independant random variables. For comparison the predicted energy loss spectrum for unvetoed Compton events is also shown. The error in this component is estimated to be no more than 40%. From the figure it can be seen that unvetoed Compton events comprise less than 10% of the total flux r_s at energies < 500 keV, but because of the softer power law energy dependance ($\sim E^{-2}$ as opposed to $\sim E^{-3}$) becomes comparible to r_s at energies > 2 MeV.

TABLE E.1

Crab Nebula Observing Parameters.

Parameter	Value	Units
t_s	4413.00	s
t_b	3756.25	s
$\int \cos\theta A(\theta)dt$	52203.70	$cm^2 s$
a	6.78×10^{-3}	s^{-1}
b	1.34×10^{-3}	keV^{-1}
$\langle\phi\rangle$	17.509	degrees
$\langle\theta\rangle$	2.39	degrees
$\langle x\rangle$	5.785	$g\ cm^{-2}$
δt	0.747	–
r_{ai}	28233.0	s^{-1}
τ	1.0	μs
ϵ_v	0.1	–

TABLE E.2

Principle background lines observed during the Crab Nebula observation. The intensities have been normalised according to the detection area (19.63 cm^2) and corrected for dead time and accidental coincidences.

Energy keV	Intensity $\gamma \text{ cm}^{-2}\text{s}^{-1}$	Parent Nucleus	Possible Origin
53.44	9.7×10^{-3}	Ge^{73m}	$Ge^{72}(n,\gamma)Ge^{73m}, Ge^{74}(p,d)Ge^{73m}, Ge^{73}(p,p')Ge^{73m}$
66.73	6.2×10^{-3}	Ge^{73m}	.. .. ..
139.68	5.5×10^{-3}	Ge^{75m}	$Ge^{74}(n,\gamma)Ge^{75m}, Ge^{76}(n,2n)Ge^{75m}$
198.30	1.3×10^{-2}	Ge^{71}	$Ge^{70}(n,\gamma)Ge^{71}, Ge^{72}(p,d)Ge^{71}$
511.00	2.9×10^{-3}	$e^{+}/e^{-}, Tl^{208}$	Positron Annihilation

TABLE E.3

Measured and Calculated Total Crab Nebula Counting Rates.

Energy Interval keV	Measured Rate $s^{-1} \times 10^{-2}$	Calculated Rate $s^{-1} \times 10^{-2}$	Photopeak Component $s^{-1} \times 10^{-2}$	Compton Component $s^{-1} \times 10^{-2}$
50 – 70	2.44 ± 1.70	2.22 ± 1.37	2.153	0.0657
70 – 90	1.97 ± 0.79	2.53 ± 0.81	2.486	0.0485
90 – 150	3.70 ± 1.60	4.75 ± 1.56	4.659	0.0929
150 – 700	5.44 ± 3.76	4.61 ± 3.74	4.417	0.1930
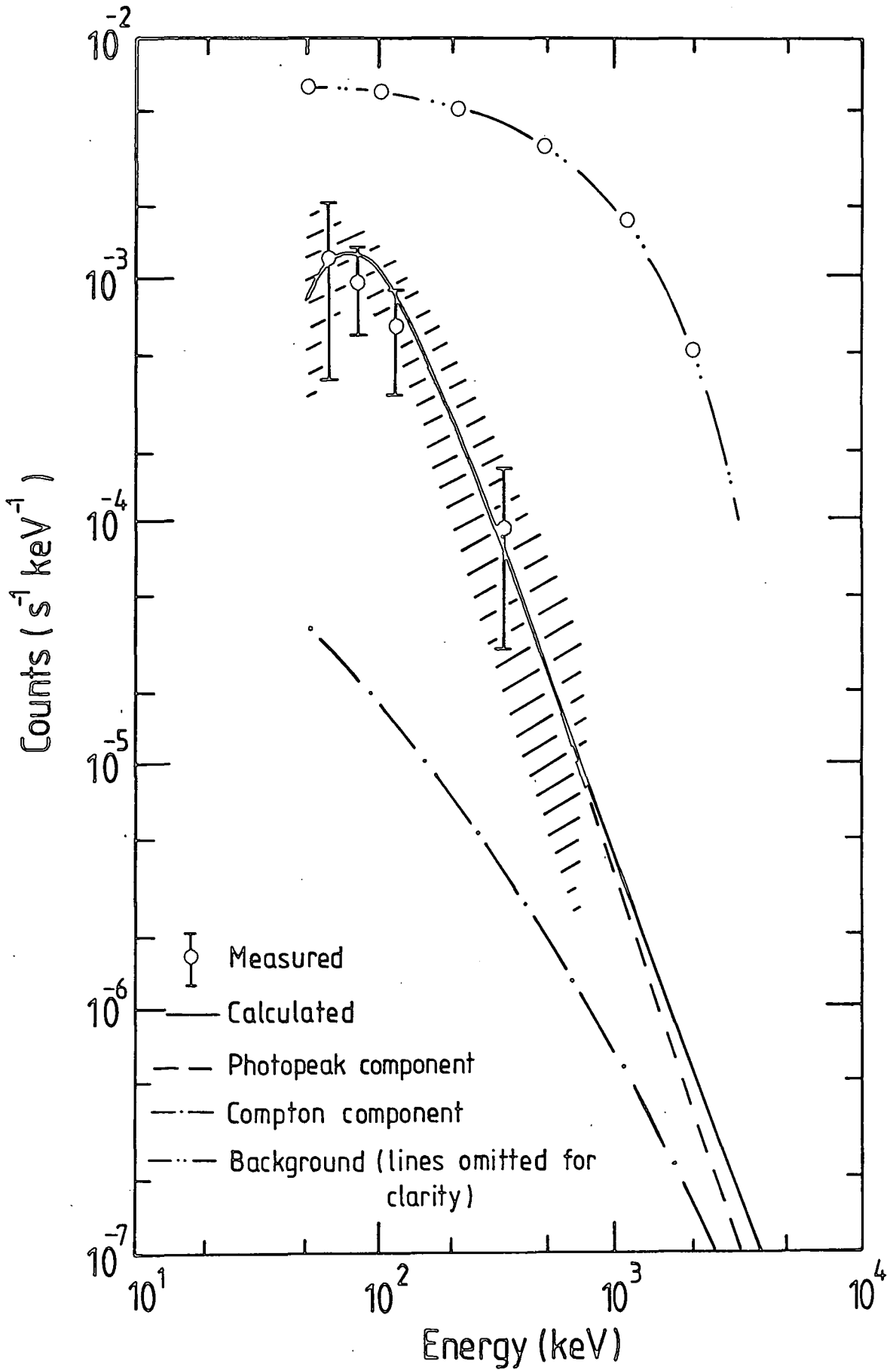
Figure E1. The measured and predicted loss spectra for the total data from the Crab Nebula.

It should be noted however that because of the statistical inprecision of the present experimental data, it is more meaningful to compare r_c with the error in the source flux, σ_s. This provides a more sensitive comparison since σ_s is always less than r_s (otherwise the result is statistically insignificant). Also if $\sigma_s \gg r_c$ this would imply that Compton contamination events can be ignored when deconvolving the final spectrum. In Figure E.2 the ratio of r_c to σ_s is shown as a function of $\Delta E/E_o$ for various energies (E_o is the centre energy of interval ΔE). We note that r_c/σ_s rises almost linearly at small ΔE and saturates at $\Delta E/E_o \simeq 1$. The reason for the 'bumps' in the graph at low energies is due to the gradual inclusion of background lines into ΔE thus increasing σ_s. Figure E.3 shows the maximum value of r_c/σ_s plotted as a function of energy. From the Figure it can be seen that at worse r_c is $\sim 10\%$ of the total error at low energies and (even though r_c is comparable to r_s at high energies) comprises less than 3% of the total error at energies > 1 MeV. For the sake of completeness Table E.3 lists the measured and calculated counting rates for the 4 data points used to produce the final spectrum given in this thesis (Figure 5.2). From the table we conclude that the non-photopeak component can be neglected, being approximately a factor of 20 smaller than either the total flux or the error in our measurement.

E.5 CONCLUSION.

For the exposures typical of balloon borne observations, and a reasonably efficient anticoincidence efficiency ($>50\%$) it has been shown the non-photopeak component of the detected source
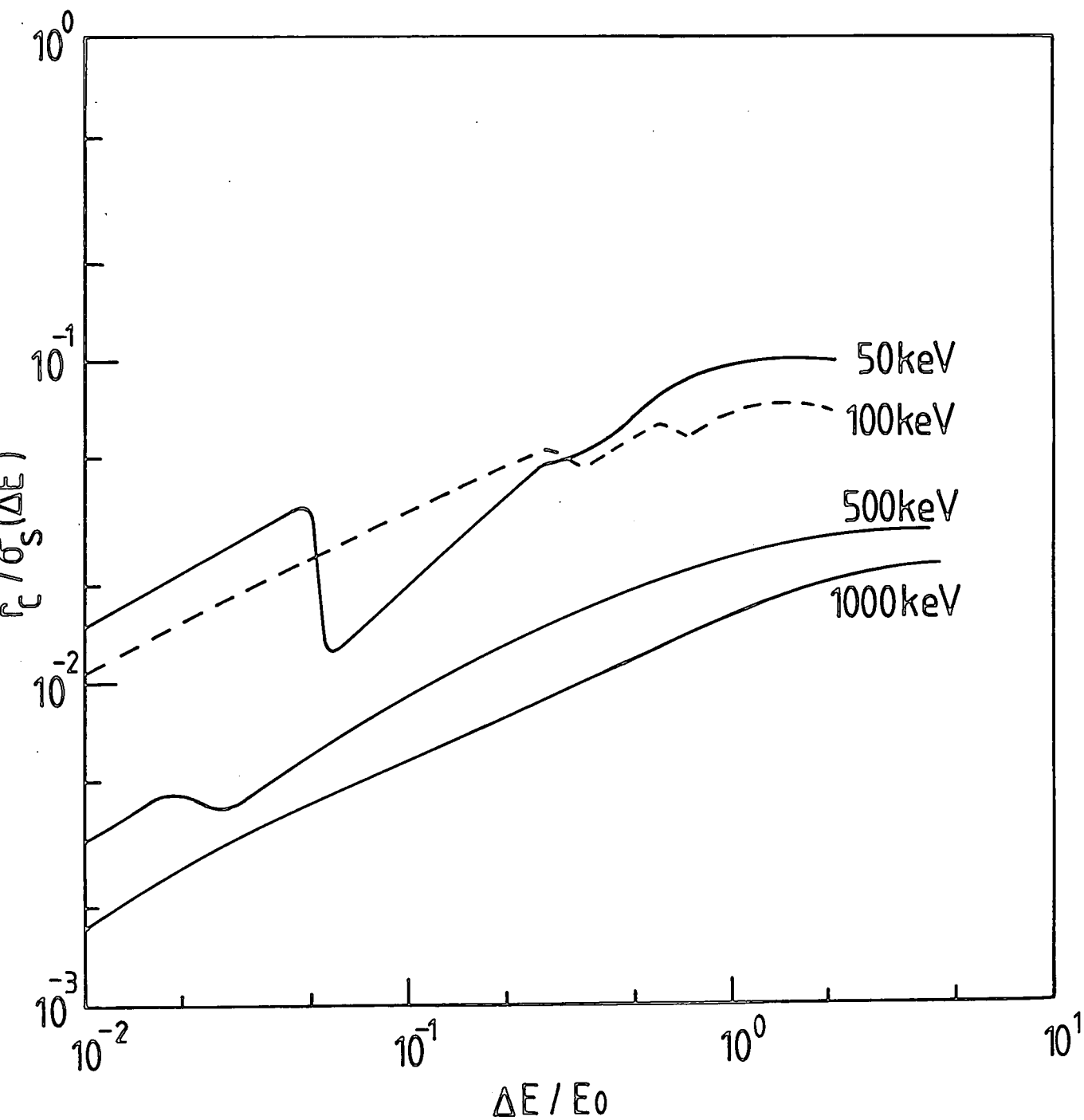
Figure E2. The ratio of the unvetoed Compton component R_C to the error in the source flux determination, σ_S, as a function of bin width ΔE.
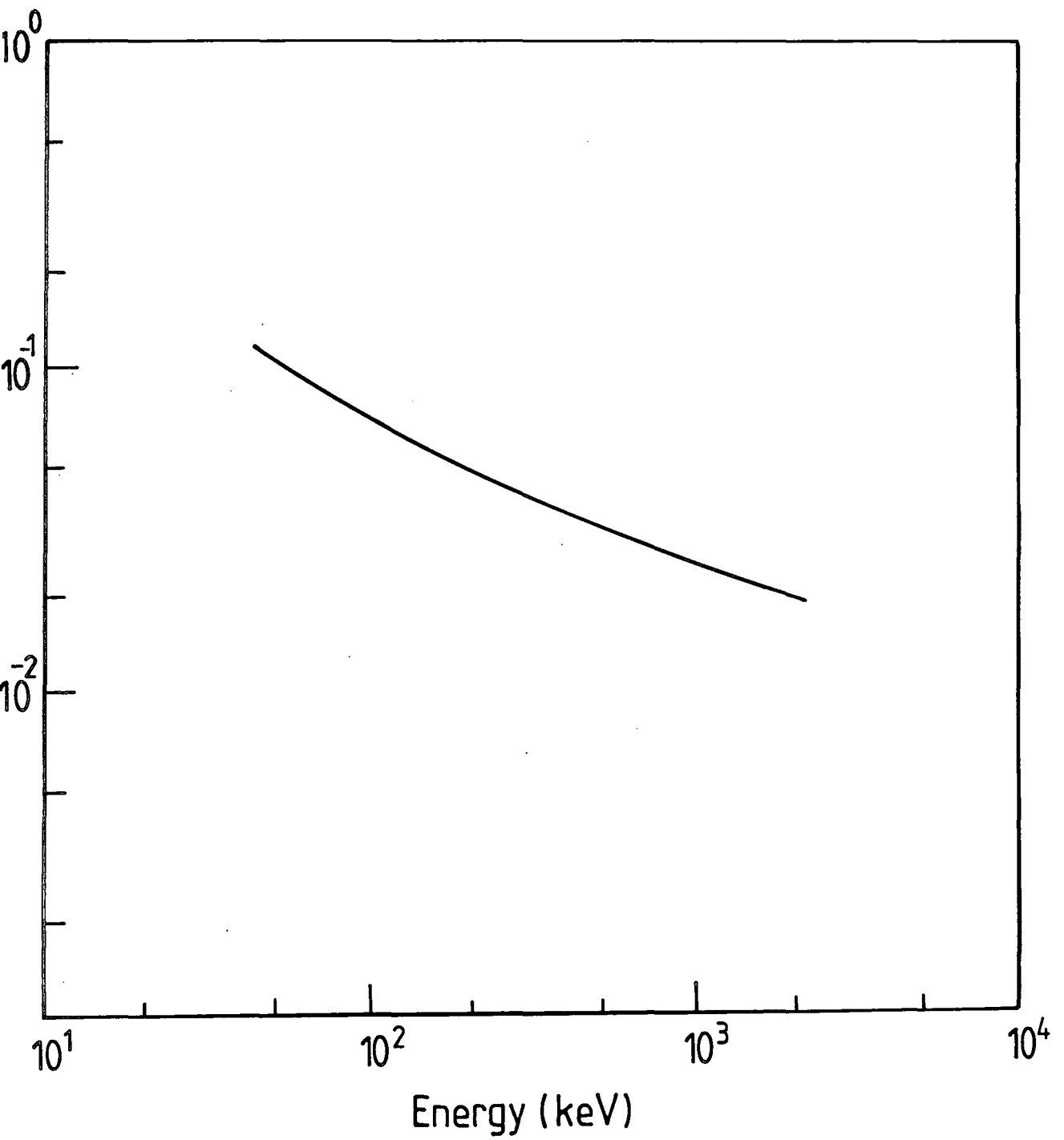
Figure E3. The maximum value of R_C/σ_S as a function of energy.

energy loss spectrum can be neglected.

APPENDIX F

DETERMINATION OF THE 'ON SOURCE' APERTURE FOR COLLIMATED γ-RAY TELESCOPES

F.1 INTRODUCTION

During a drift or raster scan of a celestial point source, the source makes a transit of the telescope collimator and thus the detector counting rate will reflect the effective collimator aperture. To determine the absolute source flux it is then necessary to sum the individual source fluxes at each orientation of the telescope axis with respect to the source, θ, after first correcting for the detector response at θ. Intuitively we can see that if we sum over too small a range of polar angles, $\Delta\theta = \theta - 0$, the signal to noise ratio will be poor because of insufficient source counts. Likewise if $\Delta\theta$ is too large, the decreasing effective collimator aperture will result in an increase in noise relative to the signal. Therefore there must exist a maximum polar angle θ_s (or 'on source' polar angle) for which the signal to noise ratio will be maximised when data are summed over the range 0 to θ_s. The definition of the 'on source' polar angle (or alternately, aperture) in the literature is vague and generally arbitary, being some fraction of the geometrical aperture (Ayre et al. 1983) or exposure factor (Dipper, 1979). In this appendix we will derive the on source aperture analytically and show that for a null source hypothesis it is dependant only on the FWHM collimator aperture and the relative source and background observing times.

F.2 PHENOMONOLOGY

Consider the observation of a celestial point source using a drift or raster scan. We define the signal to noise ratio to be,

$$SNR = r_s / \sigma_s \qquad \text{F.1}$$

where r_s is the source counting rate in energy interval $\Delta E = E_n - E_{n-1}$ and σ_s is its associated standard deviation. Assuming a trapezoidal approximation for the effective collimator aperture;

$$SNR = \frac{r_s}{\left[\dfrac{r_s}{\Sigma t_i} + r_b \left(\dfrac{1}{\Sigma \, t_i} + \dfrac{1}{t_b} \right) \right]^{\frac{1}{2}}} \qquad \text{F.2}$$

where

$$r_s = \frac{\displaystyle\sum_{j}^{\Delta E} \sum_{i}^{\Delta \theta} r(E)_j \left(1 - \frac{\theta_i}{\theta_m(E)_j} \right) t_i}{\Sigma \, t_i} \qquad \text{F.3}$$

and t_i is the exposure time at polar angle θ_i, r_b is the background counting rate, t_b is the background observing time, θ_m is the energy dependant FWHM aperture and $r(E)$ is the source counting rate in at energy E given by,

$$r(E) = \delta t (1 - 2 \Sigma r_{ai} \tau) \int_0^\infty A(\bar{E}) I(\bar{E}) \epsilon(\bar{E}) G(\bar{E}, E) B(\bar{E}, \theta, \phi) \, d\bar{E} \qquad \text{F.4}$$

where the symbols have been defined previously. The exposure time

for the Crab Nebula measurements described in this thesis can be well represented by the linear function,

$$t(\theta) = \begin{cases} 1462\ \theta, & \theta \le 2.6^{\circ} \\ \\ 6333-974\ \theta, & 2.6^{\circ} < \theta \le 6.5^{\circ} \end{cases}$$

F.5

Therefore we may rewrite Equations F.2 and F.3 as;

$$SNR = \frac{r_s}{\left[\dfrac{r_s}{\int k\theta d\theta} + r_b\left(\dfrac{1}{\int k\theta d\theta} + \dfrac{1}{t_b}\right)\right]^{\frac{1}{2}}}$$

F.6

where

$$r_s = \frac{\displaystyle\int_{E_{n-1}}^{E_n}\int_0^{\theta} r(E)\left(1 - \frac{\theta}{\theta_m(E)}\right)k\theta d\theta dE}{\int k\theta d\theta}$$

F.7

and $k = dt/d\theta$. Figure F.1 shows the calculated and experimentally determined signal to noise ratio's as a function of the maximum polar angle for accepted events, from which it can be seen there is good agreement. Assuming that the FWHM aperture is independant of energy, the integrals in Equation F.7 simplify considerably and an analytic solution for the polar angle, θ_s, which maximises the SNR may be found. Differentiating Equation F.6 with respect to θ and setting the result equal to zero we obtain,
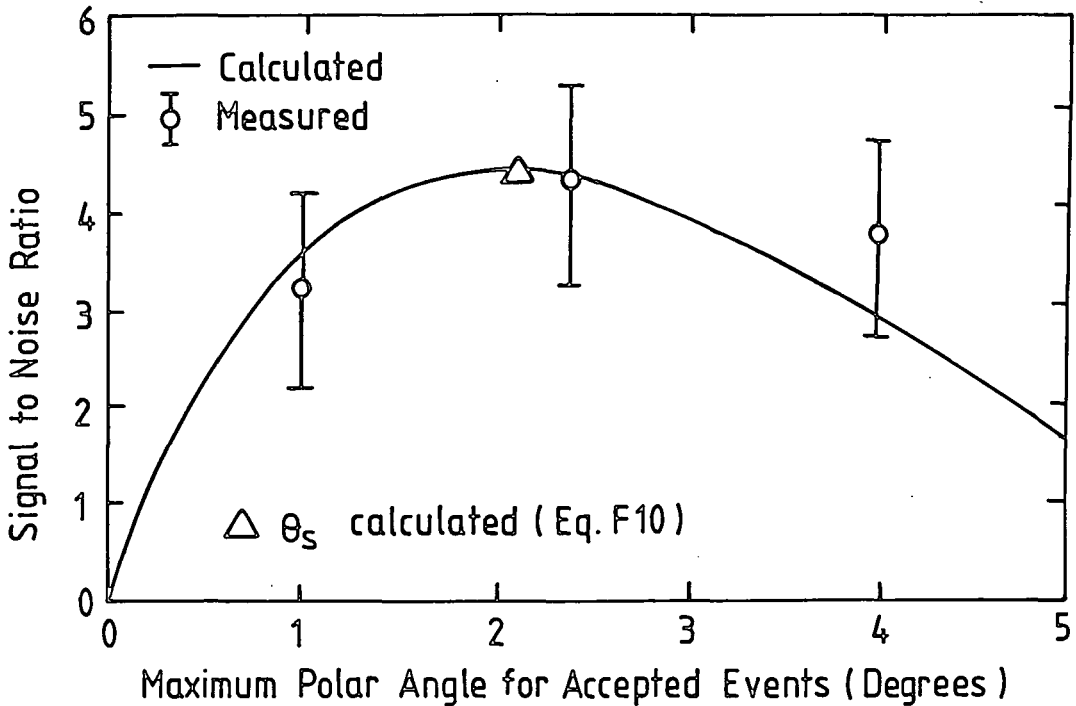
Figure F.1 The calculated and experimentally determined
signal to noise ratio's as a function of the
maximum polar angle for accepted events.
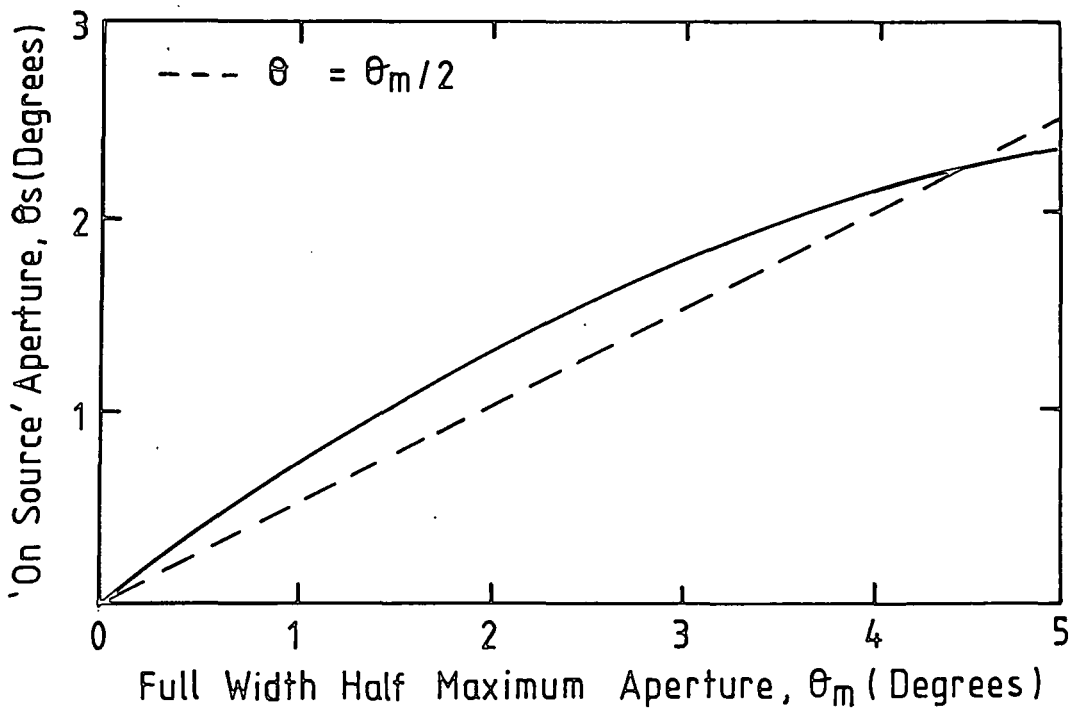
Figure F.2 The variation of the 'on source' polar angle, θ_s,
with FWHM aperture. Here θ_s is the value of
the maximum polar angle for accepted events for
which the signal to noise ratio is a maxium.

$$k\theta^3 - \frac{2r(\Delta E)t_b\theta_s^2}{\theta_m r_b} + 4t_b\left(1 + \frac{5r(\Delta E)}{4r_b}\right)\theta_s - 3\theta_m t_b\left(1 + \frac{r(\Delta E)}{r_b}\right) = 0 \qquad \text{F.8}$$

where $r(\Delta E)$ is given by integrating equation F.4 over ΔE. It should be noted that for physical values of t_b, θ_m, and $r(\Delta E)$, Equation F.8 has only one real root. For the present Crab Nebula measurements, $r_s = .13$ cts s^{-1} and $r_b = 2.16$ cts s^{-1} when integrated over the energy range 50 to 350 keV. Therefore we feel justified in assuming a null source hypothesis. In this case, Equation F.6 may be written;

$$\text{SNR} = \frac{r(\Delta E) \int (1 - \theta/\theta_m)k\theta d\theta / \int k\theta d\theta}{\left[r_b\left(\dfrac{1}{\int k\theta d\theta} + \dfrac{1}{t_b}\right)\right]^{\frac{1}{2}}} \qquad \text{F.9}$$

Solving for θ_s we obtain,

$$k\theta^3 + 4t_b\theta_s - 3\theta_m t_b = 0 \qquad \text{F.10}$$

This is a remarkable result in that it shows that for a particular source measurement the optimum polar angle for accepted events is independant of the detector counting rate and is therefore independant of energy. For the Durham MK2 telescope the solution of Equation F.10 yields $\theta_s = 2.1^O$, the other two roots being imaginary and therefore non-physical. Figure F.2 shows how θ_s varies with the FWHM aperture from which we deduce that for FWHM apertures $> 3.5^O$ a good approximation (within 10%) is given by $\theta_s = \theta_m/2$. Under this assumption the signal to noise ratio is given

by,

$$SNR_{max} = \begin{cases} r(\Delta E)\theta_m (k/18r_b)^{0.5} \, , & \theta_m k \ll 8t_b \\ \\ r(\Delta E)\theta_m (k/36r_b)^{0.5} \, , & \theta_m k = 8t_b \end{cases} \qquad F.11$$

For the present Crab measurements the evaluation of Equation F.12 yields $3.7 < SNR_{max} < 5.2$ for the energy interval 50 to 350 keV (c.f. Figure F.1).

The above formulations are quite general and are valid for all drift or raster scans such that $dt/d\theta$ is a constant. It should be noted, however, that for most drift scans $dt/d\theta = 0$, i.e. t_i at θ_i is a constant. Let τ be the exposure time per degree. Assuming the effective collimator is independant of energy, the on source polar angle is obtained from the solution of;

$$2r_b\tau\theta_s^2 + 3\theta_m t_b (r(\Delta E) + r_b)\theta_s - 2\theta_m t_b (r(\Delta E) + r_b) = 0 \qquad F.12$$

or for a null source hypothesis,

$$2\tau\theta_s^2 + 3t_b\theta_s - 2\theta_m t_b = 0 \qquad F.13$$

For a non-driven drift scan $\tau = nt'$, where n is the number of times the source makes a complete transit of the detector, and $t' = 480$ sec/degree. Under the condition that $2\theta_m\tau \leq t_b$, the solution of Equation F.13 yields $\theta_s = 2\theta_m/3$. At this value the signal to noise ratio is given by,

$$SNR_{max} = \begin{cases} (8r(\Delta E)^2 \theta_m \tau / 27r_b)^{0.5} , & \theta_m \tau \ll t_b \\ \\ (4r(\Delta E)^2 \theta_m \tau / 27r_b)^{0.5} , & \theta_m \tau = t_b \end{cases} \qquad \text{F.14}$$

REFERENCES

Allen, C.W.; Astrophysical Quantities, Athlone Press, London (1976) 220.

Apparao, K.M.V.; Astr. and Space Sci., 25 (1973) 3.

Armantrout, G.A., Thompson, H.W.; IEEE Trans. Nuc. Sci., NS-17, 3 (1970) 165.

Arnould, M., Norgaard, H., Thieleman, F.K., Hillebrandt, W.; Ap. J., 237 (1980) 931.

Audouze, J., Lequeux, J., Masnou, J.L., Puget, J.L.; Astr. and Ap. 80 (1979) 276.

Ayre, C.A., Bhat, P.N., Owens., A., Summers, W.M., Thompson, M.G.; Phil. Trans. R. Soc. of Lond., A301 (1981a) 687.

Ayre, C.A., Bhat, P.N., Owens., A., Summers, W.M., Thompson, M.G.; Proc. of the 17th Intl. Cosmic Ray Conf., Paris, 1 (1981b) 103.

Ayre, C.A., Bhat, P.N., Owens., A., Summers, W.M., Thompson, M.G.; Proc. of the 17th Intl. Cosmic Ray Conf., Paris, 1 (1981c) 107.

Ayre, C.A., Bhat, P.N., Ma, Y.Q., Myers, R.M., Thompson, M.G.; Mon. Not. R. Astr. Soc., 205 (1983) 285.

Ayre, C.A., Bhat, P.N., Ma, Y.Q., Myers, R.M., Thompson, M.G.; Nucl. Inst. and Meth.; 220 (1984) 549.

Baity, W.A., Rothschild, R.E., Lingenfelter, R.E., Stein, W.A., Nolan, P.L., Gruber, D.E., Knight, F.K., Matterson, J.L., Mushotzky, R.F., Tennet, A.F.; Ap. J., 244 (1981) 429.

Baker, R.E., Lovett, R.R., Orford, K.J., Ramsden, D.; Nature Phys. Sci., 245 (1973) 18.

Baker, R.E., Butler, R.C., Dean, A.J., Di Cocco, G., Dipper, N.A., Martin, S.J., Mount, K.E., Ramsden, D., Barbaglia, G., Barbarschi, L., Boella, G., Bussini, A., Igiuni, A., Inzani, P., Perotti, F., Vila, C.; Nucl. Instr. and Meth., 158 (1979) 595.

Basko, M.M., Sunyaev, R.A.; Astr. and Ap., 42 (1975) 311.

Bevington, P.R.; Data Reduction and Error Analysis for the Physical Sciences, McGraw Hill Publishing Co., New York (1969).

Bignami, G.F., Fichtel, C.E., Kniffen, D.A., Thompson, D.J.; Ap. J., 199 (1975) 54.

Bignami, G.F., Lichti, G.G., Paul, J.A.; Astr. and Ap., 68 (1978) L15.

Bignami, G.F., Caraveo, P.A., Paul, J.A.; Nature, 310 (1984) 464.

Bilger, H.R.; Phys. Rev., 163 (1967) 238.

Boldt, E.A., Holt, S.S., Serlenitscs., P.J.; Ap. J., <u>164</u> (1971) L9.

Borner, G., Cohen, J.M.; Ap. J. <u>185</u> (1973) 959.

Brauer, F.P., Kaye, J.H., Mitzlaff, W.A., Rieck, H.G.; Nucl. Instr. and Meth., <u>102</u> (1972) 223.

Brecher, K.; Gamma-Ray Spectroscopy in Astrophysics, ed. T.L Cline and R. Ramaty, NASA TM-79619 (1978) 275.

Brecher, K., Ulmar, M.P.; Nature, <u>271</u> (1978) 135.

Brown, J.C.; Solar Phys., <u>18</u> (1971) 489.

Brown, R.L.; Ap. J., <u>159</u> (1970) L187.

Buccheri, R., D'Amico, N., Scarsi, L., Kanbach, G., Masnou, J.L.; Proc. 12th ESLAB Sym., eds. R.D. Wills and B. Battrick, ESA SP-124 (1977) 309.

Bussard, R.W.; Ap. J., <u>237</u> (1980) 970.

Bussard, R.W., Ramaty, R., Drachman, R.J., Ap. J., <u>228</u> (1979) 928.

Cameron, A.G.W.; Space Sci. Rev., <u>15</u> (1973) 121.

Carlson, L.A., Morgan, P.S.; High Altitude Balloon Package Thermal Analysis, Texas Engr. Expt. Station Rept. No. TAMRF-921-7307 (1973).

Carpenter, G.F., Coe, M.J., Engel, A.R.; Nature, <u>259</u> (1976) 99.

Carter, J.N., Frye, G.M., Hall, C.J., Jenkins, T.L., Owens, A., Ramsden, D.; Adv. Space Res., <u>3</u> (1983) 49.

Cheng, A.F., Ruderman, M.A.; Ap. J., <u>216</u> (1977) 865.

Chupp, E.L.; <u>Gamma-Ray Astronomy</u>, Reidel Publishing Co., Dordmacht, Holland (1976).

Chupp, E.L., Forrest, D.J., Higbie, P.R., Suri, A.N., Tsai, C., Dunphy, P.P.; Nature, <u>241</u> (1973) 333.

Clayton, D.D., Colgate, S.A., Fishman, G.J.; Ap. J., <u>155</u> (1969) 75.

Clayton, D.D.; Nature, <u>234</u> (1971) 291.

Coe, M.J., Engel, A.R., Quenby, J.J., Dyer, C.S.; Nature, <u>268</u> (1977) 508.

Coe, M.J., Engel, A.R., Quenby, J.J., Dyer, C.S.; Nature, <u>274</u> (1978) 242.

Colgate, S.A.; Acta Physica Academiae Scientiarum Hungaricae, <u>29</u>, Supp. 1 (1970) 353.

Costa, E., Massaro, E., Salvati, M., Appolloni, A.; Ap. and Space Sci., 17 (1984) 165.

Daugherty, J.K., Bussard, R.W.; Ap. J., 238 (1980) 296.

Dean, A.J., Dipper, N.A.; Mon. Not. R. Astr. Soc., 194 (1981) 219.

Dipper, N.A.; PhD Thesis, The University of Southampton, Southampton, U.K. (1979).

Dolan, J.F.; Ap. and Space. Sci., 17 (1972) 325.

Dolan, J.F., Crannell, C.J., Dennis, B.R., Frost, K.J., Maurer, G.S., Orwig, L.E.; Ap. J., 217 (1977) 809.

East, L.V.; Nucl. Instr. and Meth, 93 (1971) 193.

Euler, B.A., Kaplan, S.N.; IEEE Trans. Nucl. Sci., NS-17, 1 (1970) 81.

Evans, R.D.; The Atomic Nucleus, McGraw Hill Book Co., New York (1955).

Fano, U.; Phys. Rev., 72 (1947) 26.

Fano, U.; Nucleonics, 11, no. 8 (1953a) 8.

Fano, U.; Nucleonics, 11, no. 9 (1953b) 55.

Fazio, G.G.; Ann. Rev. of Astron. and Ap., ed. L. Goldberg, Annual Reviews Inc., Palo Alto, California, 5 (1967) 481.

Fazio, G.G., Helmken, H.F., O'Mongain, E., Weekes, T.C.; Ap. J., 175 (1972) L117.

Felten, J.E., Morrison, P.; Ap. J., 146 (1966) 686.

Fichtel, C.E., Kniffen, D.A., Thompson, D.J.; Proc. of the 12th ESLAB Symp., eds. R.D. Wills and B. Battrick, ESA SP-124 (1977) 98.

Fishman, G.J.; Ap. J., 171 (1972) 163.

Fishman, G.J., Meegan, D.A., Watts, J.W., Derrickson, J.H.; Ap. J. 223 (1978) L13.

Freeman, J.M., Jenkins, J.G.; Nucl. Instr. and Meth., 43 (1966) 269.

Frye, G.M., Albats, P., Thompson, G.B., Hopper, V.D., Mace, O.B., Thomas, J.A., Staib, J.A.; The Context and Status of Gamma-Ray Astronomy, Proc. of the 9th ESLAB Symp., ed. B.G. Taylor, ESRO SP-106 (1974) 265.

Gehrels, N., Cline, T.L., Teegarden, B.J., Paciesas, W.S., Tueller, J., Durouchoux, Ph., Hameury, J.M.; Ap. J., 278 (1984) 112.

Gilman, D., Metzger, A.E., Parker, R.H., Trombka, J.I.; Ap. J., <u>229</u> (1979) 753.

Ginzberg, V.L.; <u>Elementary Processes for Cosmic-Ray Astrophysics</u>, Gordon and Breach Publ. Co., New York (1969).

Gnedin, Yu.N., Sunyaev, R.A.; Astr. and Ap., <u>36</u> (1974) 379.

Gorenstein, P., Gurslay, H., Garmire, G.; Ap. J., <u>153</u> (1968) 885.

Goret, P., Engelmann, J.J., Koch-Miramond, L. Meyer, J.P., Lund, N., Rasmussen, I.L., Perron, C.; Proc. of the 17th Intl. Cosmic Ray Conf., Paris, <u>1</u> (1981) 198.

Graml, F., Penningsfeld, F.P., Schonfelder, V.; Gamma-Ray Spectroscopy in Astrophysics, ed. T.L. Cline and R. Ramaty, NASA TM-79619 (1978) 207.

Graser, U., Schonfelder, V.; Ap. J., <u>263</u> (1982) 677.

Grindlay, J.E., Helmken, H.K., Hanbury-Brown, R., Davis, J., Allen, J.R.; Ap. J., <u>197</u> (1975) L9.

Gruber, D.E., Ling, J.C.; Ap. J., <u>213</u> (1977) 802.

Hajnal, F., Klusek, C.; Nucl. Instr. and Meth., <u>122</u> (1974) 559.

Hall, R.D., Meegan, C.A., Walraven, G.D., Djuth, F.T., Haymes, R.C.; Ap. J., <u>210</u> (1976) 631.

Hameury, J.M., Boclet, D., Durouchoux, Ph., Cline, T.L., Paciesas, W.S., Teegarden, B.J., Tueller, J., Haymes, R.C.; Ap. J., <u>270</u> (1983) 114.

Hansen, W., Goulding, F.S.; <u>Semi-Conductor Nuclear Particle Detectors</u>, Nat. Acad. of Sci., Washington, <u>871</u> (1968) 202.

Harvey, J.R.; Nucl. Instr. and Meth., <u>86</u> (1970) 189.

Haschick, A.D., Crane, P.C., Mathijs, van der Hulst, J.; Ap. J., <u>262</u> (1982) 81.

Hasinger, G., Pietsch, W., Reppin, C., Trumper, J.C., Voges, E., Kendziorra, E., Staubert, R.; in Accreting Neutron Stars, eds. W. Brinkmann and J. Trumper, MPI report 177 (1982) 130.

Haslam, C.G., Stoffel, T., Kearsey, S., Osbourne, J.L., Phillips, S.; Proc. of the 17th Intl. Cosmic Ray Conf., Paris, <u>1</u> (1981) 198.

Hayakawa, S.; <u>Cosmic Ray Physics</u>, Pub. Willey and Sons (1969).

Hayles, R.L.; PhD Thesis, The University of Southampton, Southampton, U.K. (1981).

Haymes, R.C., Glenn, S.W., Fishman, G.J., Harnden, Jr., F.R.; J. Geophys. Res., <u>74</u> (1969) 5792.

Haymes, R.C., Walraven, G.D., Meegan, C.A., Hall, R.D., Djuth, F.T., Shelton, D.H.; Ap. J., 201 (1975) 593.

Haymes, R.C., Meegan, C.A., Fishman, G.J.; Astr. and Ap., 79 (1979) 88.

Heitler, W.; The Quantum Theory of Radiation, Oxford University Press, London (1954).

Helmken, H.; Proc. of the 14th Intl. Cosmic Ray Conf., Munich, 1 (1975) 128.

Henck, R., Gutknecht, D., Siffert, P., De Laet, L., Schoenmaekers, W.; IEEE Trans. Nuc. Sci., NS-17, 3 (1970) 149.

Hermsen, W.; PhD Thesis, The University of Leiden, Holland (1980).

Holt, S.S., Mushotzsky, R.F.; NASA TM-80559 (1979).

Horstman, H.M., Cavallo, G., Moretti-Horstman, E.; Nuovo Cimento, 5, no. 2, (1975) 255.

Hudson, H.S., Bai, T., Gruber, D.E., Matterson, J.L., Nolan, P.I., Peterson, L.E.; Ap. J., 236 (1980) L91.

Imhof, W.L., Nakano, G.H.; Ap. J., 214 (1977) 38.

Jackson, J.D.; Classical Electrodynamics, Pub. John Willey and Sons, New York (1962).

Jackman, T.E., Schulte, C.W., Campbell, J.L., Lechtenberger, P.C., Mackenzie, I.K., Wormald, M.R.; J. Phys. F.: Metal Phys., 4 (1974) L1.

Jacobson, A.S.; Invited paper to the American Physical Society, Washington, D.C. (1977).

Jacobson, A.S., Bishop, R.J., Culp, G.W., Jung, L., Mahoney, W.A., Willet, J.B.; Nucl. Instr. and Meth., 127 (1975) 115.

Jacobson, A.S., Ling, J.C., Mahoney, W.A., Willet, J.B.; Gamma-Ray Spectroscopy in Astrophysics, ed. T.L. Cline and R. Ramaty, NASA TM-79619 (1978) 228.

Jennings, M.C., White, R.S.; Ap. J., 238 (1980) 110.

Johnson, J.R., Mann, K.C.; Nucl. Instr. and Meth., 112 (1973) 601.

Johnson, W.N., Harnden, F.P., Haymes, R.C.; Ap. J., 172 (1972) L1.

Johnson, W.N., Haymes, R.C.; Ap. J., 184 (1973) 103.

Jones, F.C.; Cosmic Gamma Rays from Suprathermal Photon Bremsstralung, GSFCX-641-71-372, Goddard Space Flight Center, Greenbelt, Maryland (1971).

Julien, P.F., Helmken, H.F.; Nature, 272 (1968) 699.

Kane, W.R., Mariscotti, M.A.; Nucl. Instr. and Meth., 56 (1967) 189.

Klein, O., Nishina, Y.; Z. Physik, 52 (1929) 853.

Knight, F.K.; Ap. J., 260 (1982) 538.

Lacy, J.H., Baas, F., Townes, C.H., Geballe, T.T.; Ap. J., 227 (1979) L17.

Lacy, J.H., Townes, C.H., Geballe, T.T., Hollenbach, D.J.; Ap. J., 241 (1980) 132.

Lampton, M., Margon, B., Boyer, S.; Ap. J., 208 (1976) 177.

Lebrun, F., Bennet, K., Bignami, G.F., Bloemen, J.B., Buccheri, R., Caraveo, P.A., Gottwald, M., Hermsen, W, Kanbach, G., Mayar-Hasselwander, H.A., Montmerle, T., Paul, J.A., Sacco, B., Strong, A.W., Wills, R.D.; Ap. J., 274 (1983) 231.

Lee, H.; Nucl. Instr. and Meth., 197 (1982) 411.

Leventhal, M.; Ap. J., 153 (1973) L149.

Leventhal, M., MacCallum, C.J., Stang, P.D.; Ap. J., 225 (1978) L11.

Leventhal, M., MacCallum, C.J., Watts, A.; Ap. J., 216 (1977) 491.

Leventhal, M., MacCallum, C.J., Huters, A.F., Stang, P.D.; Ap. J., 240 (1980) 338.

Li, T.P., Ma, Y.Q.; Ap. J., 272 (1983) 317.

Lichti, G.G., Buccheri, R., Caraveo, P., Gerardi, G., Hermsen, W., Kanbach, G., Masnou, J.L., Mayer-Hasselwander, H.A., Paul, J.A., Swanenburg, B.N., Wills, R.D.; Non-Solar Gamma-Rays, Advances in Space Exploration, Pergamon Press, 7 (1980) 49.

Ling, J.C., Gruber, D.E.; J. Geophys. Res., 82, no. 7 (1977) 1211.

Ling, J.C., Mahoney, W.A., Willet, J.B., Jacobson, A.S.; Nature, 370 (1977) 36.

Ling, J.C., Mahoney, W.A., Willet, J.B., Jacobson, A.S.; Ap. J., 231 (1979) 896.

Lingenfelter, R.E., Higdon, J.C., Ramaty, R.; Gamma-Ray Spectroscopy in Astrophysics, ed. T.L. Cline and R. Ramaty, NASA TM-79619 (1978) 252.

Lingenfelter, R.E., Ramaty, R.; High Energy Nuclear Reactions in Astrophysics, ed. B.S.P. Shen, W.A. Benjamin Inc., New York (1967) 99.

Lingenfelter, R.E., Ramaty, R.; The Structure and Content of the Galaxy and Galactic Gamma-rays, eds. C.E Fichtel and F.W. Stecker, GSFC, X 662-76-154 (1976) 264.

Lingenfelter, R.E., Ramaty, R.; Physics Today, <u>31</u> (1978) 40.

Lingenfelter, R.E., Ramaty, R.; <u>Gamma-Ray Transients and Related Astrophysical Phenomena</u>, ed. R.E. Lingenfelter, H.S. Hudson and D.M. Worrall, AIP, New York (1982).

Ljubicic, A., Carter, A.L., Clarke, R.L.; Phys. Rev. B, <u>10</u> (1974) 31.

Lust, R., Pinkau, K.; <u>Electromagnetic Radiation in Space</u>, ed. J.G. Emming, Springer Verlag, New York (1967) 231.

Mahoney, W.A., Ling, J.C., Jacobson, A.S.; Nucl. Instr. and Meth., <u>178</u> (1980) 363.

Mahoney, W.A., Ling, J.C., Jacobson, A.S.; J. Geophys. Res., <u>86</u> (1981) 11098.

Mahoney, W.A., Ling, J.C., Jacobson, A.S.; Nucl. Instr. and Meth., <u>185</u> (1981) 449.

Mahoney, W.A., Ling, J.C., Jacobson, A.S.; Ap. J., <u>278</u> (1984) 784.

Mahoney, W.A., Ling, J.C., Jacobson, A.S., Lingenfelter, R.E.; Ap. J., <u>262</u> (1982) 742.

Mahoney, W.A., Ling, J.C., Willet, J.B., Jacobson, A.S.; Gamma-Ray Spectroscopy in Astrophysics, ed. T.L. Cline and R. Ramaty, NASA TM-79619 (1978) 462.

Makowsky, L.L., Strokan, N.B., Tisnek, N.I.; IEEE Trans. Nucl. Sci., NS-15, <u>3</u> (1968) 304.

Manchanda, R.K.; Ap. and Space Sci., <u>50</u> (1977) 179.

Manchanda, R.K., Bazzano, A., La Padula, C.D., Polcaro, V.F., Ubertini, P.; Ap. J., <u>252</u> (1982) 172.

Mandrou, P.; These de Doctoral D'Etat no. 872, Universite Paul Sabatier, Toulouse, France (1979).

Marmier, P., Sheldon, E.; <u>Physics of Nuclei and Particles</u>, Academic Press, New York, <u>1</u> (1969).

Marscher, A.P., Brecher, K., Wheaton, W.A., Ling, J.C., Mahoney, W.A., Jacobson, A.S.; Ap. J., <u>281</u> (1984) 566.

Masnou, J.L., Bennett, K., Bignami, G.F., Bloemen, J.B., Buccheri, R., Caraveo, P.A., Hermsen, W., Kanbach, G., Mayer-Hasselwander, H., Paul, J.A., Wills, R.D.; Proc. of the 17th Intl. Cosmic Ray Conf., Paris, <u>1</u> (1981) 177.

Mather, R.L.; J. Ap. Phys., <u>28</u> (1957) 1200.

Matterson, J.L.; Proc. AIAA 16th Aerospace Sciences Meeting (1978).

Matterson, J.L., Nolan, P.L., Peterson, L.E.; IAU COSPAR Symp. on X-Ray Astronomy, Innsbruck, Space Research V III, Pergamon Press (1978).

Maurer, G.S.; PhD Thesis, The Catholic University of America, NASA TM-80285 (1979).

Mayer-Hasselwander, H.A.; Space Sci. Rev., 36 (1983) 223.

Mazets, E.P., Golenetskii, S.V., Aptekar, R.L., Guryan, Yu.A., Il'inskii, V.N.; Acad. of Sci. of USSR preprint, Leningrad (1980).

Mazets, E.P., Golenetskii, S.V., Aptekar, R.L., Guryan, Yu.A., Il'inskii, V.N.; Nature, 290 (1981) 378.

McMath, T.A., Martini, M.; Nucl. Instr. and Meth., 86 (1970) 245.

McNelles, L.A., Campbell, J.L.; Nucl. Instr. and Meth., 109 (1973) 241.

Meegan, C.A.; Gamma-Ray Spectroscopy in Astrophysics, eds. T.L. Cline and R. Ramaty, NASA TM-79619 (1978) 223.

Meszaros, P.; Astr. and Ap., 63 (1978) L19.

Metzger, F.E., Deutsch, M.; Phys. Rev., 78 (1950) 551.

Meyer, R.A., Tirsell, K.G., Armantrout, G.A.; Proc. ERDA X-Gamma-Ray Symp., Ann Arbor, MI, CONF-760539 (1976) 40.

Mowat, R.S.; Nucl. Instr. and Meth., 70 (1969) 237.

Nakano, G.H., Imhof, W.L., Reagan, J.B., Johnson, R.G.; Gamma-Ray Astrophysics, ed. F.W. Stecker and J.I. Trombka, NASA SP-339 (1973) 71.

Ore, A., Powell, J.L.; Phys. Rev., 75 (1949) 1696.

Paciesas, W.S., Cline, T.L., Teegarden, B.J., Tueller, J., Durouchoux, Ph., Ehrmann, C., Gehrels, N., Hameury, J.M.; The Galactic Centre, eds. G.R. Reigler and R.D. Blandford, Am. Inst. of Phys., New York (1982) 139.

Paciesas, W.S., Baker, R., Boclet, D., Brown, S., Cline, T.L., Costlow, H., Durouchoux, Ph., Ehrmann, C., Gehrels, N., Hameury, J.M., Haymes, R.C., Teegarden, B.J., Tueller, J.; Nucl. Instr. and Meth., 215 (1983) 261.

Paradellis, T., Hontzeas, S.; Nucl. Instr. and Meth., 73 (1969) 210.

Pehl, R.H., Goulding, F.S.; Nucl. Instr. and Meth., 81 (1970) 329.

Powell, C.F., Fowler, P.H., Perkins, D.H.; The Study of Elementary Particles by the Photographic Method, Pergamon Press, Oxford (1959).

Ramaty, R.; Gamma-Ray Spectroscopy in Astrophysics, ed. T.L. Cline and R. Ramaty, NASA TM-79619 (1978) 6.

Ramaty, R., Lingenfelter, R.E.; Solar Gamma, X and EUV Radiation, IAU Symp. no. 68, Reidel Pub. Co., Dordrecht, Holland (1975) 363.

Ramaty, R., Lingenfelter, R.E.; Ap. J., 213 (1977) L5.

Ramaty, R., Lingenfelter, R.E.; Nature, 278 (1979) 131.

Ramaty, R., Lingenfelter, R.E.; Phil. Trans. R. Soc. Lond., A301 (1981) 671.

Ramaty, R., Lingenfelter, R.E.; Annual Reviews of Nuclear and Particle Science, Annual Reviews Inc., Palo Alto, California, 32 (1982).

Ramaty, R., Kozlovsky, B., Lingenfelter, R.E.; Space Sci. Rev., 18 (1975) 341.

Ramaty, R., Kozlovsky, B., Lingenfelter, R.E.; Nuclear Gamma-Rays from Energetic Particle Reactions, NASA TM-79654 (1978).

Ramaty, R., Kozlovsky, B., Lingenfelter, R.E.; Ap. J., 40 (1979) 487.

Reigler, G.R., Mahoney, W.A., Ling, J.C., Prince, T.A., Jacobson, A.S.; paper presented at the Conf. on Cosmic Ray Astrophysics and Low Energy Gamma-Ray Astronomy, Univ. of Minnesota (1980).

Reigler, G.R., Ling, J.C., Mahoney, W.A., Wheaton, W.A., Willet, J.B., Jacobson, A.S., Prince, T.A.; Ap. J., 248 (1981) L13.

Roney, W.M., Searle, W.A.; preprint, Instituto de Fisica, Universidade de Sao Paulo (1978).

Rothschild, R.E., Baity, W.A., Marscher, A.P., Wheaton, W.A.; Ap. J., 243 (1981) L13.

Rothschild, R.E., Mushotzky, R.F., Baity, W.A., Gruber, D.E., Matterson, J.L., Peterson, L.E.; Ap. J., 269 (1983) 423.

Ruderman, M.A., Sutherland, P.G.; Ap. J., 196 (1975) 51.

Sakai, E.; IEEE Trans. Nucl. Sci., NS-15, 3 (1968) 310.

Sakai, E., McMath, T.A., Franks, R.G.; IEEE Trans. Nucl. Sci., NS-16, 1 (1969) 68.

Sanderson, T.R.; Nucl. Instr. and Meth., 105 (1972) 371.

Schonfelder, V.; Non Solar Gamma-Rays, COSPAR Advances in Space Exploration, Pergamon Press, 7 (1979) 3.

Schonfelder, V., Graser, U., Daugherty, J., Ap. J., 217 (1977) 306.

Schonfelder, V., Lichti, G., Moyano, C.; Nature, 257 (1975) 375.

Schwartz, R., Lin, R.P., Pelling, R., Hurley, K.; BAAS, 12 (1980) 542.

Schwinger, J.; Phys. Rev., 75 (1949) 1912.

Shafroth, S.M., Strait, E.N., Carpenter, R.T.; Nucl. Instr. and Meth., 3 (1958) 298.

Sher, A.H., Pate, B.D.; Nucl. Instr. and Meth., 71 (1969) 251.

Singh, R.; Nucl. Instr. and Meth., 136 (1976) 543.

Somorjai, E.; Nucl. Instr. and Meth., 131 (1975) 557.

Starrfield, S.G., Sparks, W.M., Truran J.W.; Structure and Evolution of Close Binary Systems, eds. P. Eggleton, S. Mitton and J. Whelan, IAU Symp., 73, Reidel Publ. Co., Dordrecht, Holland (1976) 155.

Starrfield, S.G., Truran, J.W., Sparks, W.M., Arnold, M.; Ap. J., 222 (1978) 600.

Stecker, F.W.; Ap. and Space Sci., 3 (1969) 579.

Stecker, F.W.; Ap. and Space Sci., 6 (1970) 377.

Stecker, F.W.; Cosmic Gamma-Rays, NASA SP-249 and Monobook Co., Baltimore, Md (1971).

Stecker, F.W.; Ap. and Space Sci., 20 (1973) 47.

Stephens, S.A.; Non Solar Gamma-Rays, COSPAR Advances in Space Exploration, Pergamon Press, 7 (1979) 223.

Steyn, J.J., Andrews, D.G., Dixmier, M.; Nucl. Instr. and Meth., 79 (1969) 123.

Strickman, M.S., Johnson, W.N., Kurfess, J.D.; Ap. J., 230 (1979) L15.

Strickman, M.S., Kurfess, J.D., Johnson, W.N.; Ap. J., 253 (1982) L23.

Strokan, N.B., Tisnek, N.I.; Phys. Tech. Semicond., 3 (1969) 769.

Strokan, N.B., Ajdacic, V., Lalovic, B.; Nucl. Instr. and Meth., 94 (1971) 147.

Strong, A.W., Bignami, G.F., Bloemen, J.B., Buccheri, R., Caraveo, P.A., Hermsen, W., Kanbach, G., Lebrun, F., Mayer-Hasselwander, H.A., Paul, J.A., Sacco, B., Scarsi, L., Wills, R.D.; Astr. and Ap., 115 (1982) 404.

Sturrock, P.A.; Ap. J., 164 (1971) 529.

Summers, W.M.; MSc Thesis, The University of Durham, Durham, U.K. (1983).

Swanenburg, B.N., Bennett, K., Bignami, G.F., Buccheri, R., Caraveo, P., Hermsen, W., Kanbach, G., Lichti, G.G., Masnou, J.L., Mayer-Hasselwander, H.A., Paul, J.A., Sacco, B., Scarsi, L., Wills, R.D.; Ap. J., 243 (1981) L69.

Teegarden, B.J.; Gamma-Ray Transients and Related Astrophysical Phenomena, ed. R.E. Lingenfelter, H.S. Hudson and D.M. Worrall, AIP, New York (1982) 123.

Tokcan, G., Cothern, C.R.; The Ohio J. Sci.; 69 (1969) 2.

Toor, A., Steward, F.D.; Ap. J., 79 (1974) 995.

Tomnovec, F.M., Mather, R.L.; J. Ap. Phys., 28 (1957) 1208.

Trammell, R., Walter, F.J.; Nucl. Instr. and Meth., 76 (1967) 317.

Trumper, J., Pietsch, W., Reppin, C., Sacco, B., Kendziorra, E., Staubert, R.; Texas Symposium on relativistic Astrophysics, Boston, paper 1 (1976).

Trumper, J., Pietsch, W., Reppin, C., Sacco, B., Kendziorra, E., Staubert, R.; Ann. N.Y. Acad. Sci., 302 (1977) 538.

Trumper, J., Pietsch, W., Reppin, C., Voges, W., Staubert, R., Kendziorra, E.; Ap. J., 219 (1978) L105.

Tueller, J., Cline, T.L., Paciesas, W., Teegarden, B.J., Boclet, D., Durouchoux, Ph., Hameury, J., Haymes, R.C.; Proc. of the 17th Intl. Cosmic Ray Conf., Paris, 1 (1981) 95.

Vano, F., Gonzalez, J., Gaeta, R., Gonzalez J.A.; Nucl. Instr. and Meth., 123 (1975) 573.

Vedrenne, G.; Non Solar Gamma-Rays, COSPAR Advances in Space Exploration, Pergamon Press, 7 (1979) 85.

Voges, W., Pietsch, W., Reppin, C., Trumper, J.; X-Ray Astronomy, ed. W.A. Baity and L.E. Peterson, Pergamon Press, Oxford (1979) 845.

Wallace, R.K., Woosley, S.E.; Ap. J. Suppl., 45 (1981) 220.

Walraven, G.D., Hall, R.D., Meegan, C.A., Coleman, P.L., Shelton, D.H., Haymes, R.C.; Ap. J., 202 (1975) 502.

Walraven, G.D., Haymes, R.C.; Nature, 264 (1976) 42.

Wang, H.T., Ramaty, R.; Solar Phys., 107 (1974) 1065.

Wang, H.T., Ramaty, R.; Ap. J., 202 (1975) 532.

Wdowczyk, J., Tkaczyk, W., Wolfendale, A.W.; J. Phys., A5 (1972) 1419.

Willet, J.B.; Radioactivity in Nuclear Spectroscopy, ed. J.H. Hamilton, Gordon and Breach Publ. Co., New York (1971) 1317.

Winkler, P.F., White, A.E.; Ap. J., 199 (1975) L139.

Womack, E.A., Overbeck, J.W.; J. Geophys. Res., 75 (1970) 1811.

Woosley, S.E., Weaver, T.A.: Ap. J., 238 (1980) 1017.

Yau, K.K.C.; MSc Thesis, The University of Durham, Durham, U.K. (1984).

Yoshimori, M., Watanabe, H., Okudaira, K., Hirasima, Y., Murakami, H.; Aust. J. Phys., 32 (1979) 375.

Zullinger, H.R.; High Energy Physics Laboratory Report no. 621, Stanford University (1970).

Zullinger, H.R., Middleman, L.M., Aitken, D.W.; IEEE Trans. Nucl. Sci., NS-16, 1 (1969) 47.

Zwicky, F.; Interim Report to the Committee for Research on Supernovae within Commission 28 of the IAU (1964).